

Copyright Undertaking

This thesis is protected by copyright, with all rights reserved.

By reading and using the thesis, the reader understands and agrees to the following terms:

- 1. The reader will abide by the rules and legal ordinances governing copyright regarding the use of the thesis.
- 2. The reader will use the thesis for the purpose of research or private study only and not for distribution or further reproduction or any other purpose.
- 3. The reader agrees to indemnify and hold the University harmless from and against any loss, damage, cost, liability or expenses arising from copyright infringement or unauthorized usage.

IMPORTANT

If you have reasons to believe that any materials in this thesis are deemed not suitable to be distributed in this form, or a copyright owner having difficulty with the material being included in our database, please contact lbsys@polyu.edu.hk providing details. The Library will look into your claim and consider taking remedial action upon receipt of the written requests.

DESIGN, ANALYSIS, AND TESTING OF BIOMIMETIC UNDERWATER ROBOTS

CHAO XU

PhD

The Hong Kong Polytechnic University

The Hong Kong Polytechnic University

Department of Mechanical Engineering

Design, Analysis, and Testing of Biomimetic Underwater Robots

Chao Xu

A thesis submitted in partial fulfilment of the requirements for the degree of Doctor of Philosophy

December 2024

CERTIFICATE OF ORIGINALITY

I hereby declare that this thesis is my own work and that, to the best of my knowledge and belief, it reproduces no material previously published or written, nor material that has been accepted for the award of any other degree or diploma, except where due acknowledgement has been made in the text.

<u>CHAO Xu</u> (Name of student)

Abstract

The ocean significantly impacts humanity by serving as a valuable source of energy and food, as well as an essential channel for maritime transport. Marine robots play an indispensable role in taking the place of human beings to carry out various activities in extreme underwater environments with respect to eliminating human risks and high adaptability to surrounding conditions. Over the decades, a variety of marine robots have been developed, including traditional thruster-driven ROVs and AUVs, as well as biomimetic swimming robots.

To carry out tasks with high effectiveness and efficiency, marine robots should have extended operational durations and high agility. These capabilities hinge on the robots' performance in energy efficiency, swimming speed, and maneuverability. It is worth noting that most fish are naturally endowed with the capability of efficient swimming as a result of millions of years' natural selection and evolution. Approximately 85% of fish adopt the body and/or caudal fin (BCF) propulsion method, which is also a popular biomimetic approach for driving underwater robots due to its feature in dexterous and efficient swimming. However, it is rare to find swimming robots whose performance is comparable to that of their biological counterparts. Consequently, the pursuit of creating high-performance marine robots to narrow the gap with the natural skillful swimmers, fish, remains a significant focus in marine robotics research. This study aims to explore novel strategies for constructing high-performance swimming robots.

In the first part, a robotic tadpole is constructed using a multi-joint-link mechanism and

a compliant fin to study the effects of the active-joint ratio and the geometry-related stiffness of the fin on its swimming performance. To thoroughly and conveniently investigate the robot's performance, the dynamic model with well-identified hydrodynamic parameters is derived. Extensive simulations and experiments are conducted to determine the optimal active-joint ratio among several designed tails, the optimal control parameters of each tail, and the optimal shape of the fin. The findings are also verified in water with currents to show the applicability in real marine environments with disturbances.

Secondly, a novel stiffness modulation mechanism without introducing extra power sources is proposed to enable robotic fish to adapt to various tail beat frequencies and maintain good performance. The tail body of the robot is composed of a parallel mechanism, a rigid link, an elastic steel strip, and a slider mechanism. By controlling the rhythmic swing trajectory of the parallel mechanism, the effective length of the spring steel spanning between the rigid link and the caudal fin can be adjusted, thereby enabling the tuning of the tail's stiffness. Numerous simulations and experiments based on the derived dynamic model demonstrate that the proposed method can effectively help the robot maintain optimal performance across a wide range of frequencies.

The final part focuses on exploring nonlinear structures in the design of robotic fish to achieve efficient and agile swimming. The design integrates a flexible spine with a lightweight, parallel-linkage structure. Theoretical models are derived to facilitate the control of the robot and the understanding of its nonlinear behaviors. By actively managing the endpoint of the flexible spine, the elastic tail is endowed with remarkable controllability and adjustable bistability. Consequently, the ability to switch between monostable and bistable operational states enables the robot to demonstrate superior swimming capabilities in terms of

swimming speed, energy efficiency, and maneuverability, which is validated by experimental results.

List of Publications

- Xu Chao, Imran Hameed, David Navarro-Alarcon, and Xingjian Jing. Performance
 Oriented Understanding and Design of a Robotic Tadpole: Lower Energy Cost, Higher
 Speed, *Journal of Field Robotics*, 2024. (Accepted)
- 2. **Xu Chao**, Imran Hameed, David Navarro-Alarcon, and Xingjian Jing. A Controllable Nonlinear Bistable "Fishtail" Boosting Robotic Swimmer with Excellent Maneuverability and High Energy Efficiency, *Soft Robotics*, 2024. (Accepted)
- 3. **Xu Chao**, David Navarro-Alarcon, and Xingjian Jing. Accurate Swing Trajectory Control of a Novel Fishtail Achieving Online Stiffness Modulation without Extra Power Sources, Submitted to *IEEE Transactions on Robotics*. (Under second round review)
- 4. **Xu Chao**, Imran Hameed, David Navarro-Alarcon, and Xingjian Jing. Untethered Bimodal Robotic Fish with Tunable Bistability, 2024 IEEE International Conference on Robotics and Automation (ICRA 2024), Yokohama, Japan, 2024, pp. 1491-1497.
- 5. Imran Hameed, Xu Chao, David Navarro-Alarcon, and Xingjian Jing. Training Dynamic Motion Primitives using Deep Reinforcement Learning to Control a Robotic Tadpole, 2022 IEEE/RJS International Conference on Intelligent Robots and Systems (IROS 2022), Kyoto, Japan, 2022, pp. 6881-6887.
- Imran Hameed, Xu Chao, David Navarro-Alarcon, and Xingjian Jing. Deep Reinforcement Learning Enabling a BCFbot to Learn Various Undulatory Patterns. Submitted to Ocean Engineering, 2025. (Accepted).
- 7. Zhengchao Li, **Xu Chao**, Imran Hameed, Jianan Li, Wen Zhao, and Xingjian Jing.

- Biomimetic Omnidirectional Multi-Tail Underwater Robot, *Mechanical Systems and Signal Processing*, vol. 173, p. 109056, 2022.
- 8. Xingjian Jing, Yuyang Chai, **Xu Chao**, and Jing Bian. In-situ Adjustable Nonlinear Passive Stiffness using X-shaped Mechanisms, *Mechanical Systems and Signal Processing*, vol. 170, p. 108267, 2022.
- 9. Yuyang Chai, Xingjian Jing, and **Xu Chao**. X-shaped mechanism based enhanced tunable QZS property for passive vibration isolation, *International Journal of Mechanical Sciences*, vol 218, p. 107077, 2022.

Acknowledgments

This thesis encapsulates the research I conducted during my four-year PhD study at the Hong Kong Polytechnic University (PolyU). I want to take this opportunity to thank everyone who supported and helped me during this period.

Firstly, I would like to express my heartfelt thanks to my chief supervisor, Prof. Jing Xingjian, whose constant guidance and support were pivotal throughout my research journey. He has deep expertise and visionary insight in scientific research. Without his patient mentorship and inspiration, the completion of this thesis would be impossible. Special thanks also to Prof. David Navarro-Alarcon for his kind help and support.

Then, I would like to thank the Laboratory of Nonlinear Dynamics, Vibration, and Control (NDVC), City University of Hong Kong, and the Hong Kong Polytechnic University for providing funding and facilities support through the course of my PhD study.

Next, my gratitude extends to my friends and colleagues, Dr. Imran Hameed, Dr. Li Zhengchao, Mr. M.A.A. Abdelkareem, Mr. Zhou Zengcheng, Dr. Zeng Lingwei, Dr. Liu Ze etc., for their generous help and advice in my study and life. Our friendship made my time in Hong Kong much more enjoyable and memorable.

Finally, my deepest gratitude is reserved for my family for their endless support, understanding, and love.

CHAO Xu, Hong Kong, August 2024

Table of Contents

CERTIFICATE OF ORIGINALITYi
Abstractiii
List of Publicationsvi
Acknowledgmentsviii
Table of Contentsix
List of Figuresxiii
List of Tablesxviii
List of Abbreviationsxix
Chapter 1
Introduction1
1.1 Research Background
1.2 Research Objectives
1.3 Research Contributions
1.4 Thesis Outline
Chapter 2
Literature Review11
2.1 Designs of Biomimetic Marine Robots
2.1.1 Robotic swimmers with rigid structures
2.1.2 Soft robotic swimmers
2.1.3 Robotic swimmers with nonlinear structures
2.1.4 Stiffness tuning mechanism
2.2 Kinematic Model of Fish Locomotion
2.3 Dynamic Modeling of Marine Robots
ix

2.4 Concluding Remarks	26
Chapter 3	29
Design of a Robotic Tadpole	29
3.1 Hardware Implementation	31
3.1.1 Mechanical system	31
3.1.2 Control system	33
3.2 Mathematical Modeling	36
3.2.1 Kinematic analysis	36
3.2.2 Dynamic modeling	38
3.3 Experimental Setup	41
3.4 Hydrodynamic Parameters Identification	42
3.5 Performance of the Tail with Different Active-Joint Ratios	47
3.6 Impact of the Dimension-Related Stiffness Distribution of the Caudal Fin	56
3.7 Verification in Water Currents	60
3.8 Comparisons with Other Robots	61
3.9 Concluding Remarks	63
Chapter 4	66
A Robotic Fish with Online Stiffness Modulation	66
4.1 Hardware Implementation	68
4.1.1 Mechanical design	68
4.1.2 Electronic components	69
4.1.3 Stiffness regulation principle	70
4.2 Mathematical Modeling	73
4.2.1 Coordinate system and notations	73
4.2.2 Kinematic analysis	75
4.2.3 Dynamic modeling	78
4.3 Hydrodynamic Parameters Identification	79

4.4 Simulation and Experimental Results	83
4.4.1 Forward swimming	83
4.4.2 Swimming efficiency	85
4.4.3 Underwater swimming test	90
4.4.4 Stiffness regulation rule	91
4.4.5 Turning performance	96
4.5 Comparison and Discussion	99
4.6 Concluding Remarks	103
Chapter 5	106
A Robotic Fish with Tunable Bistability	106
5.1 Hardware Implementation	108
5.1.1 Mechanical design	108
5.1.2 Electronic components	109
5.2 Mathematical Modeling	110
5.2.1 Inverse kinematics	110
5.2.2 Monostable mode	111
5.2.3 Bistable mode	117
5.3 Experimental Setup and Methods	121
5.3.1 Free swimming tests	121
5.3.2 Power consumption evaluation	121
5.3.3 Thrust measurement and trajectory tracking of point <i>E</i>	122
5.3.4 Statistical analysis	123
5.4 Simulation and Experimental Results	124
5.4.1 Stiffness coordination	124
5.4.2 Forward swimming	128
5.4.3 Turning performance	135
5.5 Comparisons with Reported Robotic Fish	141

5.6 Concluding Remarks	142
Chapter 6	145
Conclusions and Future Work	145
Appendix	149
Appendix A	149
Bibliography	153

List of Figures

Fig. 1.1	Unmanned underwater vehicles (UUV)	2
Fig. 1.2	Four classic BCF swimming modes in fishes	4
Fig. 2.1	Swimming robots constructed by multi-joint-link mechanisms	.12
Fig. 2.2	Robotic fish actuated by DC motors	.13
Fig. 2.3	Soft swimming robots	.15
Fig. 2.4	Swimming robots designed by nonlinear structures	.18
Fig. 2.5	Swimming robots with the capability of adjusting tails' stiffness	.19
Fig. 2.6	Demonstration of Central Pattern Generators (CPG) by the schematic of a salamander's body	.22
Fig. 2.7	Illustrative example of CPG model applied to a robotic salamander platform	.24
Fig. 3.1	Overview of the robotic tadpole	.31
Fig. 3.2	Schematic of remote control	.33
Fig. 3.3	CPG output signals for the robot with three active joints	.35
Fig. 3.4	Schematic of the coordinate systems	.35
Fig. 3.5	Position tracking system	.41
Fig. 3.6	Thrust measurement system	.42
Fig. 3.7	Comparison of fin-tip displacement amplitude and average thrust between simulations and experimental tests	.45
Fig. 3.8	Tails with different active-joint ratios	.46
Fig. 3.9	Simulation results of velocity with respect to different frequencies, amplitudes, and phase differences	.47
Fig. 3.10	Experimental and simulation results of velocity for four tails and the experimental CoT	.50
Fig. 3.11	Snapshots taken from videos of simulations and experiments	.51

Fig. 3.12	Experimental results of the maximum steady swimming velocity and the	
	related CoT of four tails under different frequencies	.52
Fig. 3.13	Heat maps of the dimensionless value δ	.53
Fig. 3.14	Optimal performance of the robot with different tails	.54
Fig. 3.15	Dimensional parameters of the flexible fin	.55
Fig. 3.16	Three cases of different dimensions of the flexible fin with the same surface area	.56
Fig. 3.17	(a) Performance results of the flexible fins with different dimensions from simulations and experiments. (b) Body shape of an eel	.58
Fig. 3.18	(a) Experimental setup for testing the robot in water current. (b) Flow rates of water in the swimming pool when the thrusters are in operation	.59
Fig. 3.19	Testing results of the robot in water currents	.61
Fig. 4.1	Design of the robotic fish with stiffness tuning mechanism	.68
Fig. 4.2	Remote control system and electronic components	.70
Fig. 4.3	Illustration of the stiffness modulation principle	.71
Fig. 4.4	Schematic diagram of the bending leaf spring under the force applied on the caudal fin	.71
Fig. 4.5	Stiffness of the fishtail under different values of L_s	.72
Fig. 4.6	Validation of stiffness model	.73
Fig. 4.7	Schematic illustration of coordinate frames and notations	.74
Fig. 4.8	Reachable space of control angles of two servos under different values of θ_1 and L_s	.76
Fig. 4.9	Motion tracking system	.80
Fig. 4.10	Comparisons between simulations and experimental results when $L_s = 25$ mm	.82
Fig. 4.11	Simulation results of velocity under different L_s and frequencies	.83
Fig. 4.12	Comparisons of experimental velocities between tunable L_s , a fixed L_s of high stiffness, and a fixed L_s of low stiffness under the amplitude of 40°	.85

Fig. 4.13	Force analysis of the parallel mechanism	86
Fig. 4.14	Simulation results of CoT under different L_s and frequencies	88
Fig. 4.15	Comparisons of experimental CoT between tunable L_s , a fixed L_s of high stiffness, and a fixed L_s of low stiffness under the amplitude of 40°	89
Fig. 4.16	Underwater swimming performance test of the robot	90
Fig. 4.17	Values of δ under different values of L_s and different frequencies	91
Fig. 4.18	Optimized values of L_s under different frequencies	92
Fig. 4.19	Swimming performance of the robot with the optimal L_s under different frequencies	93
Fig. 4.20	Experimental testing of the robot with online stiffness adjustment and multiple fixed values of L_s	94
Fig. 4.21	Time and energy costs of five testing cases	94
Fig. 4.22	Control inputs for turning motion	95
Fig. 4.23	Turning performance under different frequencies and different values of L_s	96
Fig. 4.24	Experimental turning trajectories when $L_s = 5 \text{ mm}$	96
Fig. 4.25	Demonstrations of constant turning radius under varying angular speeds	98
Fig. 4.26	Schematic illustrations of the basic stiffness modulation mechanisms for fish- like robots from the literature	98
Fig. 5.1	System design of the robot: it consists of a rigid head, an active controlled flexible tail, and a passive compliant caudal fin	107
Fig. 5.2	Overview of the remote-control system	109
Fig. 5.3	Defined parameters for the kinematics of parallel mechanism	110
Fig. 5.4	Monostable motion mode: the tail beat trajectory is defined by three parameters	112
Fig. 5.5	Coordinate frames for the monostable motion mode	113
Fig. 5.6	One cycle of monostable motion	116
Fig. 5.7	Bistable motion mode: compressing the spine to form a buckling beam	116

Fig.	5.8	One cycle of bistable motion	120
Fig.	5.9	Tracking setup for the swimming experiments	120
Fig.	5.10	(a) Thrust measurement system. (b) Trajectory tracking	122
Fig.	5.11	(a) Dimensions of the elastic spine and caudal fin. The unit is millimeters. (b) Different thickness combinations of the elastic spine and caudal fin	124
Fig.	5.12	(a) Swimming speed under different frequencies. (b) Cost of transport under different frequencies	125
Fig.	5.13	(a) Swimming speed under different frequencies. (b) Cost of transport under different frequencies	125
Fig.	5.14	Reachable space of control parameters for the monostable mode (Top) and the bistable mode (Bottom)	127
Fig.	5.15	Different control trajectories for forward swimming	127
Fig.	5.16	Comparisons between the demanded and resultant control trajectories	128
Fig.	5.17	Comparison of swimming speed between the bistable and monostable modes 1	130
Fig.	5.18	Comparison of energy consumption between the bistable and monostable modes	130
Fig.	5.19	Comparison of the swimming between the bistable mode (Top) and the monostable mode (Bottom)	132
Fig.	5.20	Thrust comparison between the bistable ($\Delta L=2$ cm) and monostable modes ($\gamma=2$ cm, $\alpha_c=60^\circ$)	134
Fig.	5.21	Relation of moment and passive rotational joint's angle	134
Fig.	5.22	Different control trajectories for turning	135
Fig.	5.23	Comparison of turning performance between the bistable and monostable modes	136
Fig.	5.24	Comparisons of the turning angle in the time domain between the trajectory of 2 cm γ and 60° α_c and the trajectory of 12 cm γ and 150° α_c when tail beat frequencies are 1 Hz (a) and 4 Hz (b) respectively	137
Fig.	5.25	Comparison of the turning between the trajectory of a large radius (a) and the trajectory of a small radius (b)	138 xvi

Fig. 5.26	point E for turning	.139
Fig. 5.27	Performance comparisons between the robotic fish in this study and similar robotic swimmers in literature	.140
Fig. A1	Comparison of the swimming velocity and CoT in the frequency domain between the robot with different thickness combinations of the elastic spine and the caudal fin for the monostable swimming mode	.149
Fig. A2	Comparison of the swimming velocity and CoT in the frequency domain between the robot with different thickness combinations of the elastic spine and the caudal fin for the bistable swimming mode	.150
Fig. A3	Comparison of the swimming velocity in the frequency domain between the robot with different tail beat amplitudes for each trajectory of monostable mode	.151
Fig. A4	Turning performance comparison between the robot with different tail beat amplitudes for each control trajectory	.152

List of Tables

Table 2.1	Comparison of bio-inspired swimming robots	26
Table 3.1	Physical parameters of the robotic tadpole used for simulation	32
Table 3.2	Identified hydrodynamic parameters	44
Table 3.3	Average errors between simulations and experiments	45
Table 3.4	Simulated maximum steady swimming velocity under different frequencies	48
Table 3.5	Optimal control parameters for four tails	54
Table 3.6	Comparison with other robotic fish	62
Table 4.1	Physical parameters of the robotic fish	81
Table 4.2	Identified hydrodynamic parameters	82
Table 4.3	Comparison with other online stiffness adjustable robotic fish	101
Table 5.1	Structural parameters of the robotic fish	108
Table 5.2	Swimming performance improvement of the bistable mode relative to the	122
	monostable mode	133

List of Abbreviations

Abbreviation Expansion

UUV Unmanned underwater vehicles

AUV Autonomous Underwater Vehicles

ROV Remotely Operated Vehicles

BCF Body and/or Pectoral Fin

MPF Median and/or Pectoral Fin

RPi Raspberry Pi

IMU Inertial Measurement Unit

UART Universal Asynchronous Receiver/Transmitter

CPG Central Pattern Generators

CoT Cost of Transport

SL Stride Length

BL Body Length

2D Two Dimensional

3D Three Dimensional

DRL Deep Reinforcement Learning

Chapter 1

Introduction

1.1 Research Background

The ocean has significant impact on various aspects of life on Earth. It is a vital source of seafood for human beings. Abundant aquatic creatures largely support the fishing industry and provides approximately 15% of average animal protein supply to around 2.9 billion people worldwide [1, 2]. The ocean is also a valuable source of energy resources. It contains a variety of mineral resources and renewable energy such as oil, natural gas, offshore wind, and tidal power [3-6]. Importantly, the ocean plays a crucial role in climate regulation. It helps stabilize global temperatures and mitigate the influences of climate change through absorbing lots of heat from the sun and the carbon dioxide emitted into the atmosphere [7-9]. Other than the above listed aspects, the ocean plays a key role in many other ways such as scientific research, transportation and trade, and so on [10-13]. It is essential for human beings to protect, explore, and exploit the ocean reasonably and adequately.

Although 71% surface area of the earth is covered by the ocean, more than 80% of the ocean still remains unexplored and mysterious to date [14, 15]. The reason is that the complex underwater environments present a multitude of difficulties [16], which are rather challenging for human to overcome. For example, the limited visibility as a result of lacking natural light makes it hard for humans to navigate and observe the marine environment. And humans cannot breathe underwater without oxygen supply equipment, making it difficult for divers to carry out missions for extended periods. The extremely high pressure in the deep ocean poses significant challenges for humans to explore without specialized equipment as

well. Additionally, the ocean is home to a wide variety of marine life, some of which can be dangerous to humans. Therefore, reliable and specialized tools and techniques are essential to aid in ocean exploration.

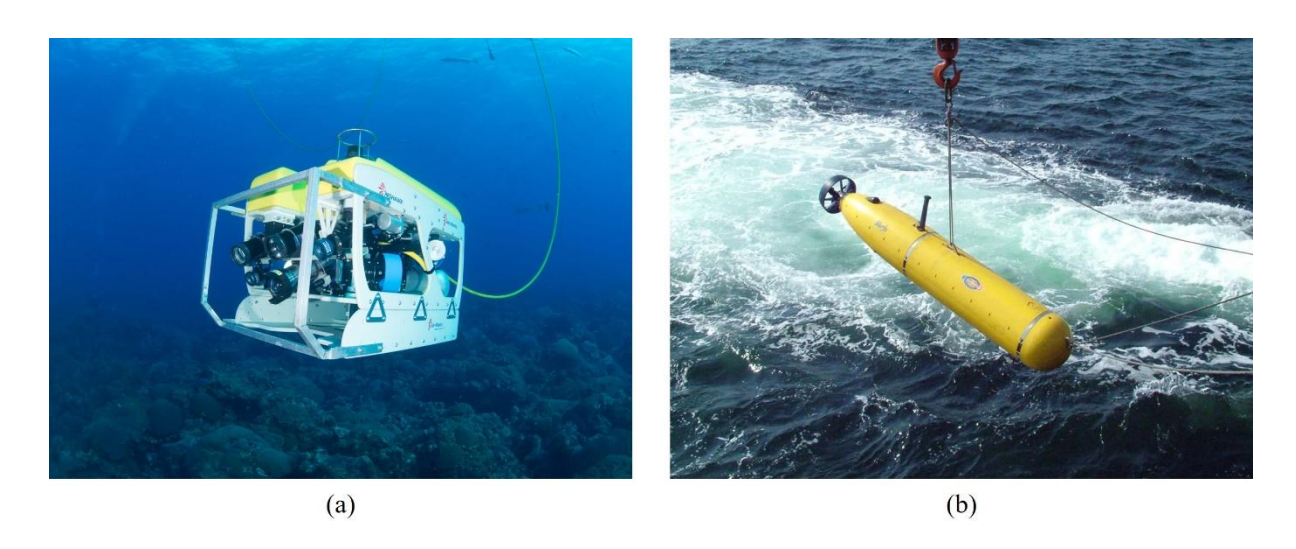


Fig. 1.1: Unmanned underwater vehicles (UUV). (a) Remotely operated vehicles (ROV). (b) Autonomous underwater vehicles (AUV).

Over the past half century, various unmanned underwater vehicles (UUVs) have been developed with advances in technology. These traditional underwater robots are driven by propellers or jet-based propulsion systems. They are basically classified into two categories including the remotely operated vehicles (ROVs) (Fig. 1.1(a)) and autonomous underwater vehicles (AUVs) (Fig. 1.1(b)), which are characterized by remote operation with a tether cable and wireless autonomous operation, respectively [17-20]. Equipped with a series of sensors for data acquisition, including high-resolution camera, acoustic sonar, doppler velocity log (DVL) etc. and specialized tools like manipulator, UUVs can effectively take the place of divers to perform those tough tasks in uncertain and complex underwater environments, such as inspection and maintenance of submarine infrastructures, undersea terrain exploration, marine biology studies, and so on [21-25].

Although humans made great progress in ocean exploration and exploitation with the help of UUVs, the application and deployment of these traditional propeller-based or jet-based underwater robots is still relatively limited due to some prominent drawbacks listed as follows.

- 1) Bulky underwater vehicles using one or two thrusters usually lack sufficient maneuverability, thus leading to big challenge on operation in narrow and unstructured underwater environments [14, 26].
- 2) To improve the agility of traditional underwater robots, multiple propellers are often utilized to achieve omnidirectional locomotion by following some intricate installment and control strategies. However, such a configuration generally causes high power consumption, which is not energy-efficient and largely limits the operation duration of robot [27].
- 3) Propellers or thrusters have low adaptability and are not environmentally friendly. They cannot work in unclear and dirty water because the blades are prone to be twined and blocked by seaweed and water refuses [28]. High-speed rotating propellers often generate substantial noise and turbulence, which has the potential to scare marine animals and affect their communication [29, 30]. Moreover, the sharped blades are dangerous for the possibility to kill or cause irreversible damage in marine animals.

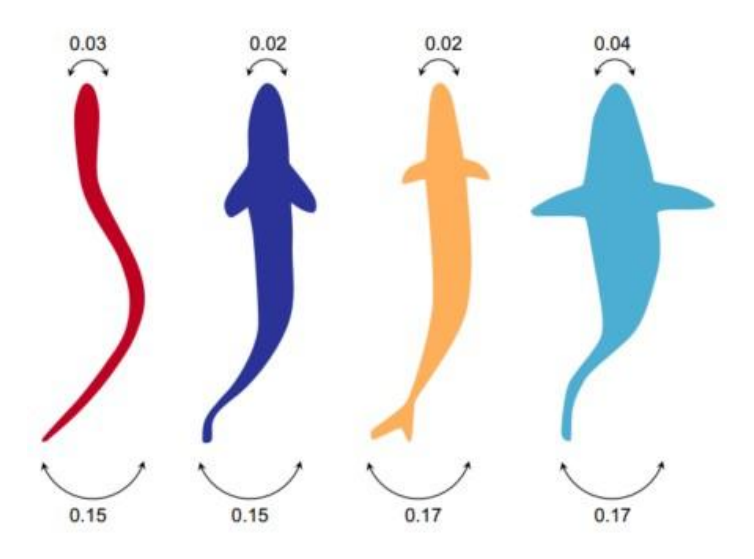


Fig. 1.2: Four classic BCF swimming modes in fishes, which are anguilliform, subcarangiform, carangiform, and thunniform from left to right [31].

How can we design a more adaptable underwater robotic swimmer? Nature could answer this question. In fact, lots of aquatic animals, especially fish, are naturally endowed with the remarkable capabilities of agile and high energy-efficient swimming after thousands of years natural selection and evolution [32, 33]. The locomotion of fish is mainly divided into two different types based on the propulsive morphologies, namely, median and/or paired fin (MPF) propulsion and body and/or caudal fin (BCF) propulsion [34-36]. A large portion of fish species (85%) adopt BCF locomotion for propulsion as a result of higher efficiency, speeds, and acceleration rates, which is related to the work in this thesis and can further be classified into four different modes based on the body ratio to generate undulation or the body propulsive wave length [37], i.e., anguilliform mode, subcarangiform mode, carangiform mode, and thunniform mode as shown in Fig. 1.2. Each mode has its own advantages and disadvantages, and no singly mode allows fish to achieve optimal swimming performance in all aspects, including cruising velocity, energy efficiency, and maneuverability. For example, anguilliform swimmers have good maneuverability with the

ability to move forward and backward through controlling the propulsive wave direction along their bodies, but they generally swim slowly. Carangiform swimmers are usually faster when compared to anguilliform swimmers, however, their turning abilities are worse than that of the anguilliform swimmers. All these locomotion modes broaden and provide extensive biomimetic alternatives to the marine robots' design. According to the specific operation requirements and environmental conditions, robotic swimmers can be designed to either swim with a certain locomotion mode or have the ability to select the most suitable mode through modes switch.

Bionic propulsors capable of imitating the undulatory motion of fish outperform traditional thrusters in terms of noiseless propulsion, higher energy efficiency, better adaptability, damage tolerance, and dexterous maneuverability, etc. [38-41], and consequently the potential applicable fields of marine robots can be greatly extended such as close-up observations of marine animals without disrupting their life and flexible navigating in particular areas of the sea including reef area and small crevices.

Over the past few decades, many researchers have made great efforts in the development of biomimetic underwater robots. As a result, various design, modeling, and control methods have been proposed as elaborated in Chapter 2. Although prominent progress has been achieved on narrowing the performance gap between bioinspired underwater vehicles and biological organisms, most existing swimming robots are still orders of magnitude slower and less efficient than their natural counterparts, as well as their maneuverability. Thus, it is still rather challenging and difficult to deploy these robots into the potential practical marine tasks. To endow robotic swimmers with similar swimming skills of fish is in need and could present new opportunities in ocean exploration and monitoring.

1.2 Research Objectives

According to the aforementioned background, there is a growing requirement for the agile and efficient robotic swimmers for ocean exploration and applications. Therefore, this thesis will look into the development of bioinspired marine robots with fast speed, high energy efficiency, and good maneuverability. And the main objectives of this work are summarized as follows.

- 1) The undulatory motion of fish can be effectively described by multi-segment models [42]. As a result, multi-joint mechanisms are commonly used in the design of robotic swimmers [43-45]. Its structure is simple to construct, and various swimming patterns are easy to realize and control. The flexible plate is often adopted as the caudal fin of robotic swimmers to replicate the efficient swimming of fish [46-48]. However, the propulsive performance of the robotic fish constructed by incorporating a hyper-redundant mechanism and a compliant fin under different configurations and control parameters remains largely unexplored. Thus, the swimming performance of a robotic swimmer with different tail configurations concerning the active-joint ratio in a large-scale control parameter space should be investigated.
- 2) Biological and bionic investigations on BCF fish have shown that the body's passive features, including stiffness and distribution, play a crucial influence in their swimming ability [49-51]. Many studies focus on the impact of different uniform or nonuniform stiffness distributions of a rectangular foil achieved by varying the thickness on the propulsive performance [52-55]. As a matter of fact, different geometries of a fin can lead to different stiffness distributions, which are simple and easy to achieve. Therefore, the influence of the shape-related stiffness distribution

- of the flexible fin on the swimming performance of a robotic fish deserves to be studied.
- 3) Over the past several decades, scientists and engineers have discovered that fish are capable of maintaining energy-efficient swimming across a wide range of swimming velocities by adjusting the stiffness of their tails through muscle activity [56-58]. The stiffness tuning strategy can also be applied equally to robotic fish to achieve optimal swimming performance under various control parameters. The stiffness tuning of robots can be achieved either offline by replacing passive structures with different stiffnesses or online by designing the stiffness adjustable mechanisms [59-67]. Compared to the offline method, the online tuning method is more beneficial for robots in maintaining high swimming efficiencies similar to those of fish. However, most existed stiffness tuning mechanisms of robotic swimmers usually have complex structures and need to use extra actuators or other types of power sources for the realization of stiffness adjusting, which impairs their usability in real practice. Thus, it is worth conceiving and designing a simple and effective variable stiffness mechanism without introducing extra actuation motors or energy cost for swimming robots.
- 4) Compared to traditional rigid robots, soft robots are more adaptive, safe, and friendly to various working environments [26, 68]. However, most soft robotic swimmers generally tend to produce weak thrust and slow response, thus leading to low speed and efficiency [69, 70]. Nonlinear structures often present some interesting properties for instance bistable or multi-stable structures, which can take advantage of elastic instability to amplify the reaction force and achieve fast motion. How the nonlinear structure can be leveraged to design a robotic swimmer that

possesses good maneuverability and high swimming efficiency is valuable to be studied as well.

1.3 Research Contributions

The main contributions and novelties of this thesis are concluded in four points as below.

- 1) To explore the influence of different active-joint ratios on the performance of swimming robots, a robotic tadpole that can perform multiple motion modes is developed with the combination of a rigid-joint-link mechanism and a flexible fin. Its dynamic model is well derived and validated to facilitate the swimming performance predictions. Extensive simulations and experiments are conducted to find the optimal active-joint ratio among several designed tails, and the optimal control parameters of each tail. This study provides an effective design and control optimization method based on the active-joint ratio for enhancing the performance of bio-inspired marine robots.
- Using the same platform in point (1), the impact of the geometry-related stiffness distribution of flexible fin is further studied through numerous simulations and experiments. The propulsive performance variational tendency of a flexible fin with its dimensions changing including the leading edge, trailing edge, and length is investigated in depth. Both simulation and experimental results indicate that, with the same surface area, a longer fin with a wide leading edge and a narrow trailing edge can achieve fast swimming speeds and low energy consumption, which conforms to the tail shape of naturally slender-bodied fish, such as eels. Thus, this study presents a novel and in-depth insight into the design of bio-inspired underwaters with compliant propulsion mechanisms.

- Then, a stiffness tuning mechanism is designed for robotic fish. The mechanism consists of a parallel mechanism, a rigid link, and a flexible spring steel. The tail's stiffness of the robot can be adjusted by controlling the rhythmic swing trajectory of the parallel mechanism which determines the effective length of the spring steel between the rigid link and the caudal fin. The dynamic model of the robot is derived to predict the swimming performance of the robot under various control parameters and tail's stiffness. Extensive experiments verify that the designed mechanism enables the robot to maintain optimal swimming performance over a wide range tail beat frequencies including forward swimming speed, energy efficiency, and turning performance. Therefore, this study proposes a simple and effective online stiffness adjustable mechanism without extra actuation sources for robotic swimmers.
- 4) Finally, a controllable nonlinear bi-stable "fishtail" is proposed, designed, and tested. The mechanism combines an elastic spine and a lightweight parallel linkage mechanism. Through active control of the endpoint of the elastic spine, the compliant tail can be empowered with exceptional controllability and tunable bistability for a much more efficient and also the first-ever accurately controlled bistable elastic propulsion system. As a result, the switchable motion mode between the monostable and bistable modes allows the robot to exhibit excellent swimming performance. Experimental results demonstrate that the new bi-stable fishtail can achieve faster speed of its size (up to an average speed of 0.8 m·s⁻¹) with associate higher energy efficiency (corresponding cost of transport (CoT) as low as 9 J·m⁻¹·kg⁻¹), and greater maneuverability (with an average turning speed of up to 107 °/s at a much smaller turning radius of 0.31 body length (BL)). This

study provides an efficient, controllable, and feasible approach to the design of nonlinear compliant propulsion systems for underwater vehicles by exploring nonlinear dynamics.

1.4 Thesis Outline

In this chapter, the research background, objectives, and contributions are introduced. And the rest of the thesis is organized as follows. In Chapter 2, the literature review is discussed including various designs of bioinspired marine robots and modeling methods of kinematics and dynamics. In Chapter 3, the swimming performance of a robotic tadpole with different tail configurations in terms of active-joint ratios and geometry-related stiffness distributions is studied based on the well-developed and validated dynamic model and experiments. In Chapter 4, an online tail stiffness tuning mechanism is proposed. The dynamic model of the robot is derived to evaluate swimming performance. And numerous experiments are conducted to validate the effectiveness of the proposed method. In Chapter 5, an untethered robotic fish with a novel propulsion system featuring the capability of tunable bistability is designed. The theoretical models are derived to facilitate the control of the robot and the understanding of nonlinear behaviors of the tail. And the performance of the new propulsion mechanism under various control parameters is studied through extensive experiments. In Chapter 6, the conclusions of this work are summarized, and some possible future research topics and directions are discussed.

Chapter 2

Literature Review

In this chapter, a comprehensive literature review on bio-inspired robotic swimmers is presented to introduce the current development of biomimetic marine robots, elaborate the related methodologies, and identify the main research gaps. The review focuses on three aspects, including various design methods of fish-like robots in Section 2.1, kinematic models commonly used for imitating fish-like locomotion and achieving different motion modes in Section 2.2, and several methods of dynamic modeling for swimming performance evaluation and prediction of marine robots in Section 2.3. Finally, Section 2.4 concludes the chapter.

2.1 Designs of Biomimetic Marine Robots

2.1.1 Robotic swimmers with rigid structures

One of the most common design methods of the bio-inspired swimming robots is to use multiple servo motors connected in series to form the tail body as shown in Fig. 2.1. Yang *et al.* [71] used three servos to construct a robotic shark (Fig. 2.1(a)) and two active controlled pectoral fins were adopted to realize the pitch and roll attitude adjustment. Through the embedded vision and stabilizer system, their robot can capture high-quality images in underwater environments when imitating the swimming motion of a fish for carrying out inspection tasks. Zhong *et al.* [72] built a snake-like swimming robot (Fig. 2.1(b)) by five servos, and they added two soft dorsal fins on the tail to investigate its impact on the swimming performance inspired from that the lampreys in nature utilize their posterior dual

dorsal fins to boost the thrust. Zhong *et al.* [73] took advantage of a five-joint robotic fish (Fig. 2.1(c)) to successfully verify that their derived general kinematic model enables the multi-joint swimming robots to be well versed in diverse fish-like locomotion modes. Thandiackal *et al.* [74] added a series of pressure sensors on both sides of the body of a lamprey-like robot (Fig. 2.1(d)) that has ten servo-actuated joints to endow the robot with the ability of generating robust self-organized undulatory movement leveraging its perception on the surrounding hydrodynamic force.

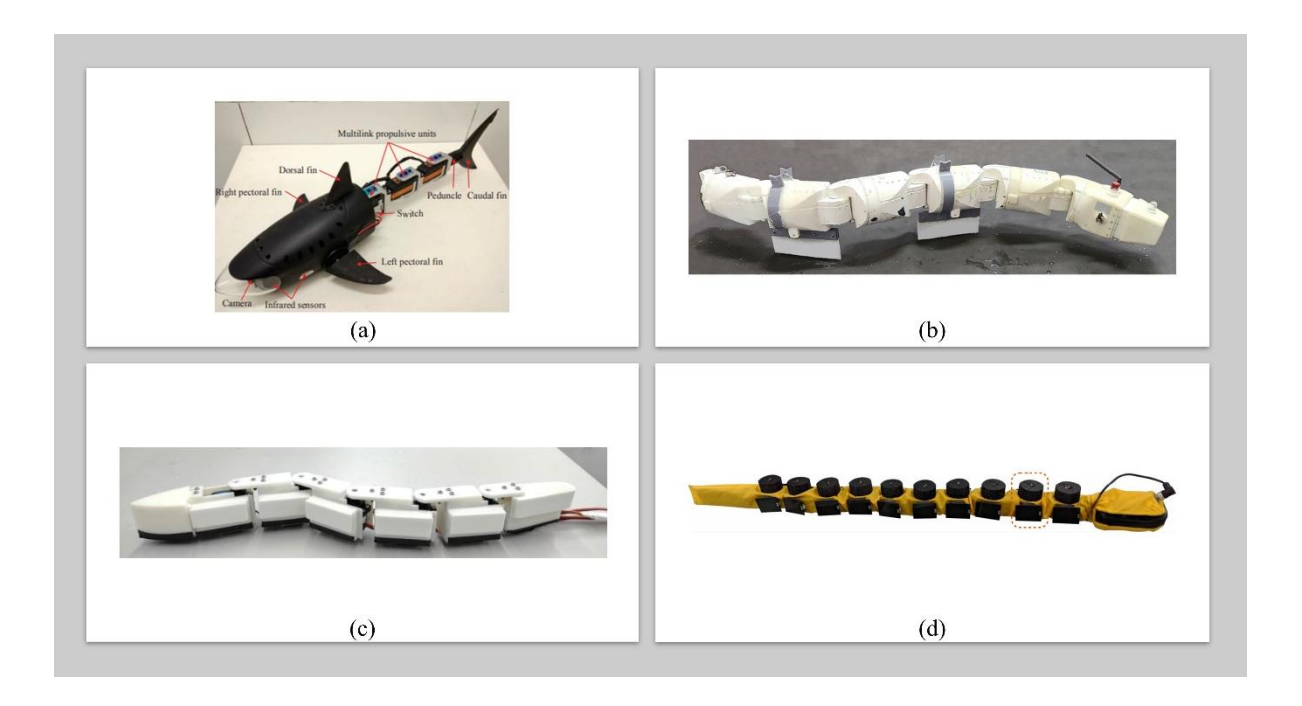


Fig. 2.1: Swimming robots constructed by multi-joint-link mechanisms. (a) Robotic shark. (b), (c), and (d) are snake-like or eel-like swimming robots.

Although multi-joint-link mechanism is prevalent in the design of marine robots owing to its prominent advantages of easy control and realizing multiple locomotion modes such as S shape swimming mode and C-shape turning mode, there are two key issues that cannot be neglected. One problem is that having many joints in the tail body places a significant burden on the servos during tail oscillation due to large inertia and substantial friction loss from dynamic sealing. As a result, the servos cannot perform high-frequency swing, creating a

bottleneck in improving swimming speed. Another drawback is that the entire robot composed of rigid links cannot replicate the smooth undulatory movement of the biological counterparts due to its discrete kinematics, which is also one main limitation on the further improvement of swimming performance.

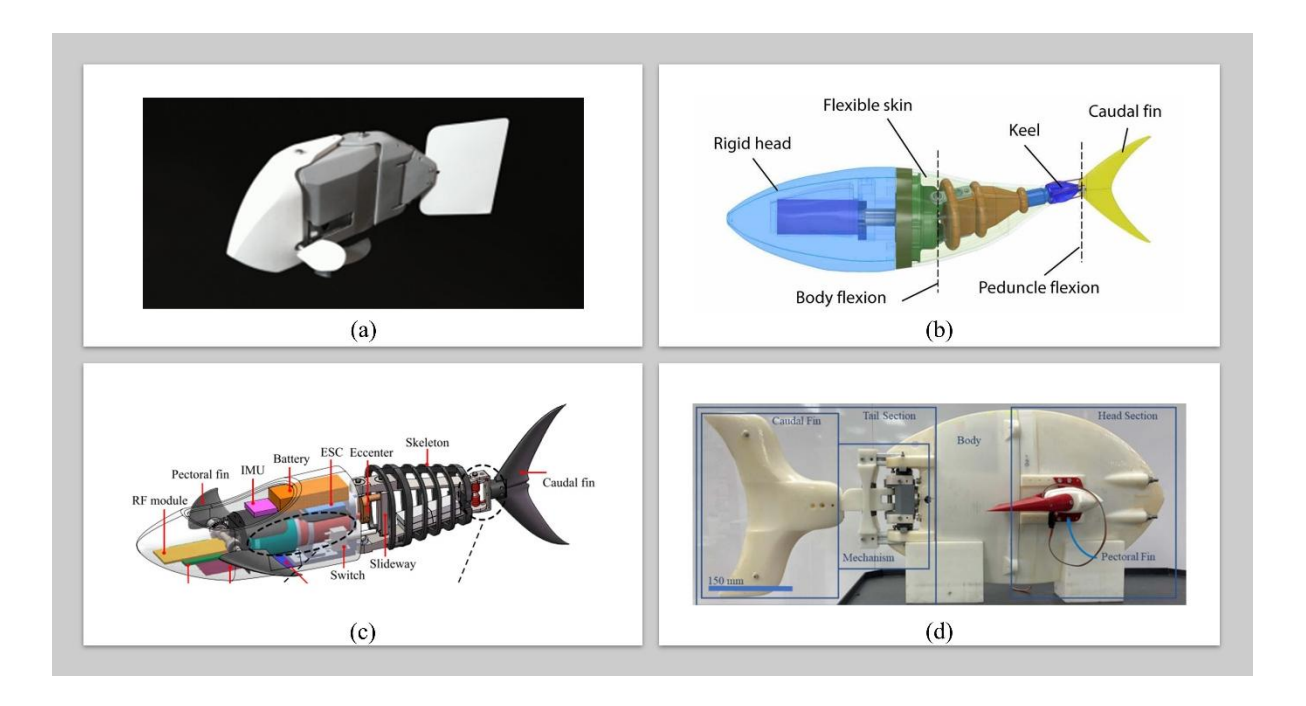


Fig. 2.2: Robotic fish actuated by DC motors. (a) iSplash-II. (b) Tunabot. (c) Leaping fish robot. (d) Snapp.

Cruising velocity is one of the vital indicators of swimming performance of underwater robots. Many fish such as Tuna and related scombrid fishes can achieve very fast swimming speed benefiting from high tail beat frequency which is usually in the range from 10 Hz to 20 Hz [75, 76]. Servos often used to actuate robotic fish have the limitation on the rotation speed as discussed above. Therefore, researchers and engineers have made great effort on designing robotic fish capable of high-frequency swimming through using DC motors. And some examples are listed in Fig. 2.2. Clapham and Hu [77] designed a robotic fish named iSplash-II (Fig. 2.2(a)) can achieve fast cruising speed (11.6 BL/s, 3.7 m/s) with the tail beat frequency up to 20 Hz relying on the transmission system of DC motor actuated single

bearing crank shaft. Zhu *et al.* [78] created a Tunabot (Fig. 2.2(b)) to simulate the body structure, kinematics, cruising velocity, and power expenditure of yellowfin tuna through a DC motor actuated transmission mechanism that is capable of converting single-directional continuous rotation to the oscillation movement of robot tail. Tunabot achieves its maximum swimming speed under the tail beat frequency of 15 Hz, which is about 1 m/s equivalent to 4 BL/s. Chen *et al.* [79] developed a robotic fish (Fig. 2.2(c)) using the similar actuation mechanism with Tunabot to take advantage of the feature of fast-speed swimming for mimicking the leaping motion of fish. Ng *et al.* [80] utilized the scotch-yoke mechanism to design the tail structure of a robotic fish named Snapp (Fig. 2.2(d)), which is also actuated by a DC motor and can realize fast swimming (maximum speed is 1.5 m/s, i.e. 1.7 BL/s) through high tail beat frequency as well.

The above discussed examples prove that high-frequency swing mechanisms actuated by DC motors can effectively improve the swimming speed of biomimetic swimming robots. However, these DC-motor actuated swimming robots perform poorly in maneuverability. The reason is that steering cannot be achieved by controlling tails' motion. And most of them rely on two actively controlled pectoral fins for turning. This way usually brings about a slow turning rate and a very large steering radius, consequently leading to poor flexibility and great difficulty when working in complex underwater environments. What's more, in order to amplify swimming speed as fast as possible, most of these kinds of robots generally have externally placed electronic components, which is unrealistic for practical applications.

2.1.2 Soft robotic swimmers

Compared to the robots with rigid structures, soft robots exhibit various merits in terms of compliant and smooth body motion, safer and more adaptable interactions with

surrounding environments, and bio-compatibility [81], which is able to greatly expand the potential application range. Hence, the topic of soft robots attracts lots of research interest. And in the recent ten years, there has been a rapid development in the field of soft robotics owing to the advancing in manufacturing and technology, which involves in the domain of biomimetic swimming robots as well.



Fig. 2.3: Soft swimming robots. (a) Robotic fish SoFi. (b) Soft robot eel. (c) Pressure-resilient soft robot fish (d) Bionic muscle actuated soft robotic fish. (e) Untethered artificial fish.

In general, there are two prominent design methods in soft robotic swimmers. The first one is to use soft materials such as silicon rubber to construct the soft bodies or tails of robots, and these soft bodies or tails are actuated by hydraulic or pneumatic pumps [26, 82-85]. To control the fluid or air filling and draining in or out from different chambers of soft body can generate side-to-side undulating motion thus leading to propelling the robot to move like fish. SoFi is the most representative of soft robotic fish designed by Katzschmann *et al.* [26] as shown in Fig. 2.3(a). It has a gear pump inside the robot body to fluidically actuate its soft

fish tail. The robot was successfully applied to swim with marine creatures through the acoustic remote control in the deep ocean for the close-up view. The highest average swimming velocity of SoFi is around 0.24 m/s (0.5 BL/s), and its average turning rate is about 0.18 m/s with the steering radius of 0.78 m approximately. Nguyen and Ho [82] designed a soft robotic eel that consists of four soft segments and each segment is a pair pneumatic soft actuator as shown in Fig. 2.3(b). Through the proper setting of phase difference in the control signals of four actuators, this robotic eel can simulate the anguilliform locomotion mode of elongated body fish. At the control frequency of 1.25 Hz, it achieves the maximum swimming speed which is about 0.19 m/s (0.36 BL/s) and the corresponding CoT is 10.72.

Designing swimming robots by soft smart materials such as shape memory alloy (SMA), macro fiber composites (MFCs), dielectric elastomers (DEs), and so on is another one popular method [40, 86-92]. Li *et al.* [90] proposed a snailfish-like soft robot that is actuated by DEs as shown in Fig. 2.3(c). The most striking feature of their robot is the capability to withstand extremely high pressure benefiting from the protection of the entire body from the silicone-based matrix. Thus, the robot is able to operate in very deep ocean environments, such as the Mariana Trench. From the testing results, its maximal swimming speed is around 3.89 cm/s (0.34 BL/s). Wang *et al.* [91] designed a cylindrical DE actuator by flexible electrodes and compression spring, which was harnessed to actuate the tail of fish robot as shown in Fig. 2.3(d). The maximum swimming velocity of the robot reaches up to 76 mm/s (0.76 BL/s). Gravert *et al.* [92] created a kind of electrohydraulic actuator and they used their actuators to design a robotic fish as shown in Fig. 2.3(e). When the robot is actuated at the frequency of 2 Hz, it reaches its maximal swimming speed of 0.04 m/s (0.14 BL/s)

approximately.

Noticeably, soft robots usually have some shortcomings like that they tend to produce relatively weak reaction force and slow response time. These deficiencies determine that most soft swimming robots generally swim at an ultra-low speed and possess poor maneuverability, as a result, most of them may remain at the concept level yet and far away from performing tasks in the real applications. Therefore, great efforts are still in need for overcoming the fatal weaknesses of robots with soft actuators thus enhancing their applicability.

2.1.3 Robotic swimmers with nonlinear structures

Many nonlinear structures can generate interesting behaviors or phenomena related to force and kinematics. Thus, they can be utilized in the design of robots to satisfy some special requirements. For example, elastic instability of bistable or multi-stable structures can induce the phenomenon of snapping as a result of quickly storing and releasing strain energy [93-97]. During the process of snapping, remarkable force amplification and rapid morphing can be achieved as two characteristics of the elastic instability, and these features have extensive applications such as energy harvesting [98, 99].

Recently, the elastic instabilities have attracted tremendous interest of researchers in the field of biomimetic soft swimming robots, which can apparently overcome the inherent drawbacks of soft robots as discussed above and enable them a further step to approach the real applications. Tang *et al.* [70] utilized the bistable linkages as the spine of a soft aquatic robot (Fig. 2.4(a)) to improve its speed and force of locomotion. This robot achieves a fast-swimming speed of 0.78 BL/s at the actuated frequency of 1.3 Hz. Chen *et al.* [100] designed a soft and untethered robot (Fig. 2.4(b)) by using shape memory polymers (SMPs) and

exploited bistable actuation for amplifying its directional propulsion. Xiong *et al.* [69] adopted a hair-clip mechanism as the tail of a robotic fish (Fig. 2.4(c)) that also take advantage of bistable actuation to increase swimming speed. The swimming test of HCM robotic fish shows that its velocity reaches up to 0.44 m/s (2.03 BL/s). Chi *et al.* [101] utilized the hair-clip mechanism as well to design a bistable flapping robotic swimmer (Fig. 2.4(d)). And they prove that the snapping enables the robot to exhibit butterfly swimming mode with high speed and high energy efficiency (maximal velocity is 3.78 BL/s, and St = 0.25).

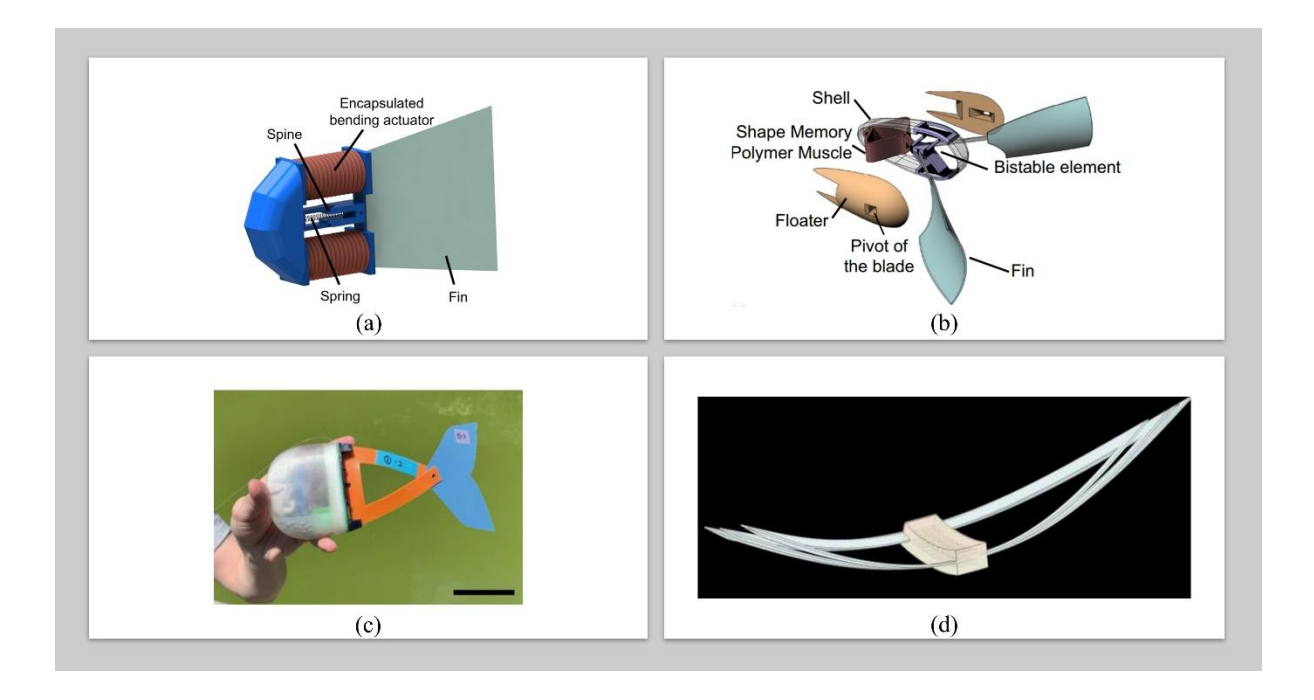


Fig. 2.4: Swimming robots designed by nonlinear structures. (a) Bistable fish-like robot. (b) Untethered bistable propulsor. (c) HCM robotic fish. (d) Bistable flapping robotic swimmer.

Despite the studies referenced above having indeed enhanced the performance of soft swimming robots, they are all related to the elastic instabilities without the competence of tunability, and the snap-through movement is difficult to be controlled precisely, which is a major limitation for further performance improvement of fish robots during performing practical tasks. As a matter of fact, fish usually cruise smoothly in water and only exhibit

suddenly rapid movement when necessary. Such a behavior should also be endowed to robotic fish so that they can swim dexterously.

2.1.4 Stiffness tuning mechanism

In nature, fish are able to keep energy-efficient swimming in a broad spectrum of velocities through tails' flexibility adjusting based on muscle activity [56]. Inspired by this phenomenon, researchers and engineers come up with an idea which is to endow the biomimetic swimming robots with the same capability via designing and adding stiffness tuning mechanisms in the structures of the flapping tails.

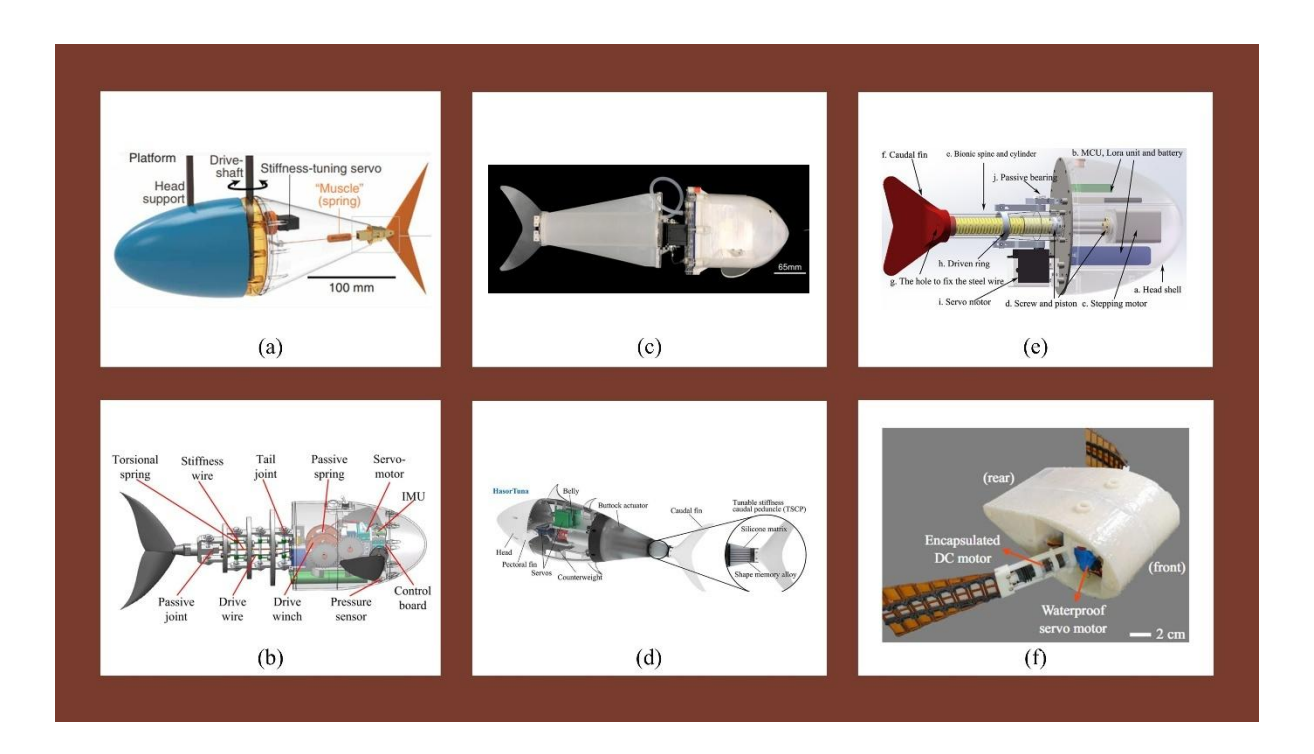


Fig. 2.5: Swimming robots with the capability of adjusting tails' stiffness. (a) Tunabot with stiffness tuning mechanism. (b) Variable-stiffness tendon-driven robotic fish. (c) Soft robotic fish with hydraulic variable-stiffness mechanism. (d) Hydraulic Autonomous Soft Robotic Tuna (HasorTuna). (e) Robotic fish with compressible flexible bionic spine. (f) Swimming robot with paddles.

Fig. 2.5 demonstrates several robotic fish with the ability to tune their tails' stiffness for achieving high performance swimming. Zhong *et al.* [64] used a linear spring driven by a

servo and connected to the peduncle of Robotic tuna's tail to simulate the muscle of tuna as shown in Fig. 2.5(a), thus realizing tail's stiffness adjusting ability of Tunabot by controlling the pretension of the spring. Their results suggest that robotic fish with high tail beat frequency could gain more performance enhancing in terms of swimming velocity and energy efficiency via stiffness adjusting. Qiu et al. [66] designed a tendon-actuated fish robot (Fig. 2.5(b)) which relies on regulating the pretension of the spring by a servo to achieve variable stiffness for high performance swimming as well. Ju and Yun [65] proposed a hydraulic stiffness tuning mechanism for a soft fish-like robot as shown in Fig. 2.5(c). The motion of the soft tail is controlled by a servo, and its stiffness is adjusted by a pump that controls the injection volume of water inside the chamber of the tail. And this mechanism enables the robot to obtain better maneuverability. Liu et al. [67] built a hydraulic actuated tuna robot as shown in Fig. 2.5(d) and they embedded shape memory alloy (SMA) wire into the soft peduncle of the robot's tail. The elastic modulus of SMA can be regulated by temperature control. In their work, the current is utilized to heat SMA, and as a result, the tail's stiffness of the robot can be tuned. And their proposed stiffness regulation mechanism effectively improved the swimming speed and energy efficiency of HasorTuna. Zhu et al. developed a robotic fish with a compressible bionic spine (Fig. 2.5(e)) [102]. The compression of the soft spine can be controlled by a stepping motor actuated screw-piston mechanism, thus leading to variable stiffness for maintaining efficient swimming under various frequencies. The swimming performance of the robot were investigated within a tail beat frequency range of 0-3 Hz, which exhibited a maximum speed of 1.07 BL/s. The robot designed by Kwak et al., as shown in Fig. 2.5(f), relied on two stiffness-adjustable articulated paddles to swim [103]. Each paddle consisted of a trapezoidal substrate paddle and a sliding laminate. The flapping motion of the paddle was actuated by a servo, and a DC motor was employed to control the

displacement of the sliding laminate for inducing stiffness change. This proposed paddle was experimentally demonstrated that it enabled a rowing robot to achieve enhancement of both speed and energy efficiency in frequency-varying swimming (0-1.75 Hz).

The capability of tuning stiffness is crucial for maintaining high performance of swimming robots. But most existing tuning mechanisms are complicated and need to consume extra power to achieve stiffness adjusting. These shortcomings could cause non-ignorable burdens on robots. Because more complex structures usually lead to more malfunctions and need more maintenance. And extra energy consumption is not good for high energy efficiency. Therefore, a simple mechanism for regulating stiffness without extra energy consumption will be more beneficial to marine robots.

2.2 Kinematic Model of Fish Locomotion

To simulate the swimming locomotion of fish, one key point is to mimic the undulatory motion of the fish tail. And during the past several decades, several kinematic models have been proposed and applied on the control of robotic fish by scientists and researchers.

Referring to [104], Lighthill derived the traveling wave model that can be used to describe the swimming mode of BCF swimmers as follows.

$$y(x,t) = (c_1 x + c_2 x^2) \sin(kx + \omega t)$$
 (2.1)

where y denotes the transverse displacement of the midline of the tails' body, x represents the distance along the horizontal direction, c_1 and c_2 are the linear and quadratic wave amplitude envelope respectively, k relates to the body wave number, and ω means the body wave frequency. Through the selection of different set of c_1 , c_2 , and k, different BCF swimming modes can be achieved.

Traveling wave equation is one of the most popular models to be used for replicating the tails' motion of robotic fish. And to apply the traveling wave equation on the control of fish-like robots with multi-link-joint mechanisms, the trajectory approximation method is often be adopted [105-107]. First, the motion equation needs to be discretized for the trajectory approximation of the robots' tails in the following form.

$$\begin{cases} y(x,i) = (c_1 x + c_2 x^2) \sin\left(kx + \frac{2\pi}{M}i\right) \\ i = \{0,1,2,...,M-1\} \end{cases}$$
 (2.2)

And the trajectory approximation method can be expressed by the following equations.

$$\begin{cases} \theta_{j} = \arctan\left(\frac{y_{j} - y_{j-1}}{x_{j} - x_{j-1}}\right) \\ \left(x_{j} - x_{j-1}\right)^{2} + \left(y_{j} - y_{j-1}\right)^{2} = l_{j}^{2} \\ y_{j}(x_{j}, i) = \left(c_{1}x_{j} + c_{2}x_{j}^{2}\right) \sin\left(kx_{j} + \frac{2\pi}{M}i\right) \\ y_{j-1}(x_{j-1}, i) = \left(c_{1}x_{j-1} + c_{2}x_{j-1}^{2}\right) \sin\left(kx_{j-1} + \frac{2\pi}{M}i\right) \end{cases}$$

$$(2.3)$$

where θ_i is the control angle of jth joint, and l_i is the length of the connected link.

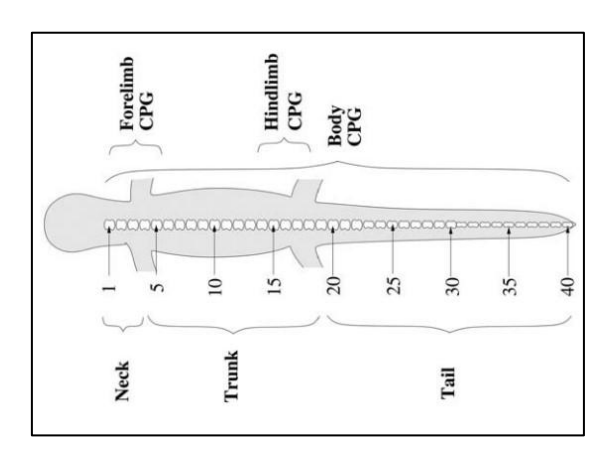


Fig. 2.6: Demonstration of Central Pattern Generators (CPG) by the schematic of a salamander's body [108].

Other than traveling wave equation, researchers proposed the central pattern generators (CPG) inspired by the neural circuits in vertebrate animals [109, 110] as shown in Fig. 2.6.

CPG are capable of generating the coordinated output signals for realizing locomotion of rhythmic patterns even though with very simple input commands [111], which are widely used in controlling bio-inspired marine robots and terrestrial robots as shown in Fig. 2.7. There are a variety of CPG models and modified forms to be used for the control of different robots. And one most common adopted to control biomimetic marine robots can be described in the following differential equations.

$$\begin{cases} \dot{\gamma}_{i} = 2\pi f_{i} + \sum_{j} \left(C_{ij} a_{j} \sin(\gamma_{j} - \gamma_{i} - \Gamma_{ij}) \right) \\ \ddot{a}_{i} = \lambda_{1} \left(\frac{\lambda_{1}}{4} (A_{i} - a_{i}) - \dot{a}_{i} \right) \\ \ddot{b}_{i} = \lambda_{2} \left(\frac{\lambda_{2}}{4} (B_{i} - b_{i}) - \dot{b}_{i} \right) \\ \theta_{i} = b_{i} + a_{i} \sin(\gamma_{i}) \end{cases}$$

$$(2.4)$$

where γ_i , a_i , and b_i are phase, amplitude, and bias of the *i*th oscillator respectively. C_{ij} and Γ_{ij} are the coupling weight and the phase difference between the *i*th oscillator and the *j*th oscillator correspondingly. λ_1 and λ_2 are just the constants or gains. f_i , A_i , and B_i are the target frequency, amplitude, and bias of the *i*th oscillator. θ_i is the rhythmic output signal of the oscillator.

Traveling-wave-model based trajectory approximation approach is very simple and can easily achieve various swimming modes of BCF swimmers by adjusting its several parameters, however, it is difficult to straightforwardly generate the non-straight cruising motion gaits and directly obtain the input signals such as joint's amplitude and phase lag, potentially leading to uncertainty and difficulty in the maneuvering control of fish robots such as turning motion control [73] and causing trouble in comprehensively optimizing motion performance just based on control parameters. The CPG model can solve these problems and provides an alternative to the traveling-wave-model based trajectory

approximation approach, which can realize multifarious rhythmic motions freely and precisely just relying on very simple and straightforward input signals.

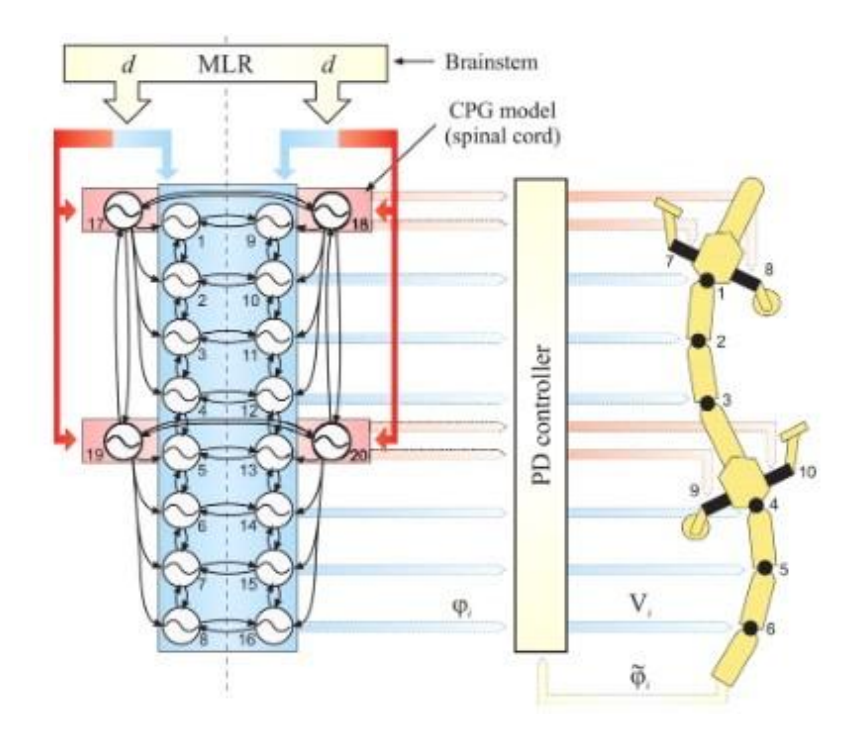


Fig. 2.7: Illustrative example of CPG model applied to a robotic salamander platform [112].

2.3 Dynamic Modeling of Marine Robots

Dynamic models are crucial for the structural design and control optimization of a swimming robot. They can be used to predict and evaluate robots' performance, providing useful references or guidance for experiments and control. However, deriving dynamic models for marine robots is not easy due to the complex interaction between the robot's body and surrounding fluid environments. How the fluid forces can be described precisely and adequately is one of the most important points.

During long time development of marine robots, various methods of dynamic modeling have been proposed. CFD (Computational Fluid Dynamics) is a very accurate numerical method to calculate hydrodynamics, but it needs large computational source and costs long time due to the complicated differential equations, namely Navier-Stokes equations [113,

114]. To avoid complexity, researchers have developed some simplified models to describe hydrodynamics, which can be used to compute hydrodynamic forces efficiently. And these models are extensively adopted for the performance analysis and control purpose of marine robots by researchers and engineers.

A suitable approach to derive the dynamic model of a biomimetic marine robot needs to be considered in accordance with its constructed mechanism. For instance, Kopman *et al*. [115] used Kirchhoff's equations and Euler-Bernoulli beam theory to model a robotic fish with a compliant tail, and Morison's equations were used to describe the hydrodynamic forces, which includes the drag forces and added mass effect. Chen *et al*. [116] derived the dynamic model of a robotic fish with three rigid links by the Lagrangian dynamics. They also made use of Morrison equation to calculate fluid forces on the robot's body, and for the caudal fin with a lunate shape, the lift and drag forces model was utilized. Wang and Tan [117] took advantage of the elongated-body theory (EBT) to derive the dynamic model of a fish-like robot, which can be used to obtain the average thrust conveniently and quickly. Wiens and Nahon [118] formulated the dynamics of a swimming robot constructed by redundant mechanism utilizing Newton-Euler dynamic equations, and the hydrodynamic forces were estimated by linearly combining drag and added mass effects, in accordance with the approach presented by Jordan in [119].

There are some hydrodynamic parameters in those simplified hydrodynamics equations, and to obtain proper hydrodynamic coefficients is another key point. CFD simulation is one method to determine these parameters [120]. In most studies [116, 121, 122], the hydrodynamic parameters were identified through the matching method between the experimental data and simulation results. And computation tool, i.e. the system identification

toolbox, is often used for the hydrodynamic parameters identification [116].

Table 2.1: Comparison of bio-inspired swimming robots

Category	Mechanisms	References	Advantages	Limitations
Rigid swimming robots	Multi-link-joint mechanisms	[71-74]	Capable of simulating various swimming gaits of fish.	Low swimming speed and efficiency due to discrete rigid body and high friction loss.
	DC motor actuated transmission mechanisms	[77-80]	Fast speed owing to high oscillation frequency.	Pool maneuverability.
	Hydraulic or pneumatic actuated mechanisms	[26, 82]	Safer and more adaptive to surrounding environments.	Weak force and slow response speed.
Soft swimming robots	Smart materials	[90-92]	Safer and more adaptive to surrounding environments.	Weak force and slow response speed.
	Elastic unstable mechanisms	[69, 70, 100, 101]	Enhanced force and fast response speed.	Only unstable motion and most are tethered, leading to difficulty in control and limitations in real applications.
Swimming robots with stiffness adjusting mechanisms	Mechanically controlled stiffness mechanisms	[64, 66]	Capable of maintaining efficient swimming under various inputs and fast response for tuning stiffness.	Increased energy consumption and more complex structures due to additional actuators solely for stiffness adjusting.
	Structurally controlled stiffness and intrinsic rigidity tuning mechanisms	[65, 67, 102, 103]	Capable of maintaining efficient swimming under various inputs.	Slow response for tuning stiffness, and increased energy consumption and more complex structures due to additional actuators solely for stiffness adjusting.

2.4 Concluding Remarks

In this chapter, a relatively comprehensive literature review is presented. According to the extensive investigation on the above research works, the following remarks can be drawn. Firstly, various design and construction methods of biomimetic swimming robots have been illustrated including rigid mechanisms, soft structures, nonlinear structures, and variable stiffness mechanisms. Various design approaches have their advantages and disadvantages as shown in Table 2.1. For example, the robotic fish built by multi-link-joint mechanism have superiorities of the ability to achieve diverse swimming patterns and control modes, but the propulsive efficiency and speed level of these robots are limited by the fully rigid structures and need to be further improved. Indeed, most existed biomimetic swimming robots only focus on improving a certain function such as swimming speed, power efficiency, or maneuverability. And rare robots can perform well in all these three aspects, which makes the performance of bio-inspired marine robots is still far away from their biological counterparts thus leading to difficulty in carrying out tasks in the complex underwater environments.

Secondly, two frequently adopted kinematic models for bio-inspired underwater robots to simulate locomotion of real fish have been elaborated, namely traveling wave model and CPG model. Although traveling wave model is proficient in replicating four different BCF swimming modes, it is weak in directly generating non-straight swimming gaits. Compared to the traveling-wave-model based trajectory approximation method for fish robots' control, CPG model is more suitable for the flexible maneuvering control and motion optimization of fish robots owing to its capability of freely producing various rhythmic motion gaits just relying on simple and straightforward input signals.

Finally, some methods to derive dynamic models of underwater robots have been introduced. Dynamic models are necessary for conducting optimizations related to structures and control. However, the fluid mechanics is very complex. To avoid the complexity of hydrodynamics, a variety of simplified modeling methods have been proposed and validated.

And for the swimming robots built by different mechanisms and materials, different proper modeling methods can be selected.

Chapter 3

Design of a Robotic Tadpole

Swimming robots designed with multi-joint mechanisms continue to be highly favored by scientists and engineers for research in the field of biomimetic robotics. This preference is attributed to their controllable multiple degrees of freedom, which facilitate ease of control and enable the replication of diverse locomotion modes observed in natural fish. But discrete kinematics of the multi-joint mechanism due to rigid body restricts swimming efficiency. Although increasing the number of joints could enhance the tails' flexibility of swimming robots, it also imposes an additional burden on the motors and consumes more power during undulation, consequently, further leading to lower swimming efficiency. Therefore, it is crucial and worthwhile to investigate effective measures for improving propulsion efficiency of multi-joint swimming robots. Incorporating the passive compliant fin in the design of a swimming robot is a simple and effective way to boost the swimming performance. According to a multitude of biological and bionic research on the passive compliance of fish body, the tail's compliance and its stiffness distribution significantly influence the propulsion performance. It is noted that although there are some existing studies about propulsion efficiency with compliant fins, very few results have been reported on the optimal integration of compliant fins and multi-joint mechanisms to achieve high-performance propulsion. To this aim, we develop a robotic tadpole by combining a multi-joint mechanism with a flexible fin, and its swimming performance is thoroughly investigated with different tail configurations concerning several key design parameters including active-joint ratios and dimension-related stiffness distributions of the flexible fin. A dynamic model with identified

hydrodynamic parameters is established to predict propulsive performance, and it is validated through extensive experiments. An optimization function is also defined to evaluate the optimal control performance for different designs. Interestingly, it reveals that (a) tails with different active-joint ratios can achieve their best performance at a small phase difference, while the tail with a larger active-joint ratio tends to perform worse than a small active-joint ratio when a larger phase difference is used; (b) the optimal active-joint ratio can enable the robot to achieve superior performance in terms of swimming velocity and energy efficiency; and (c) with the same surface area, a longer fin with a wide leading edge and a narrow trailing edge can achieve higher swimming speeds with lower energy consumption. This work presents a novel and in-depth insight into the design of robotic swimmers with bioinspired fish-like propulsion mechanisms.

The rest of this chapter is structured as follows. Section 3.1 presents the detailed construction of the robot, including its mechanical system and control architecture. Mathematical modeling, involving kinematic analysis and dynamic modeling, is described in Section 3.2. Section 3.3 introduces experimental setups, such as the trajectory tracking system and the thrust measurement system. Section 3.4 illustrates the detailed procedures of hydrodynamic parameters identification for the robot's dynamic model. The impact of active joint ratios on the swimming performance of the robot is investigated in Section 3.5. And then in Section 3.6, the impact of geometry-related stiffness distributions of the caudal fin on the swimming performance of the robot is explored. In Section 3.7, the robot is tested in water currents to verify the applicability in real environments. Comparisons with other swimming robots from the literature are discussed in Section 3.8. Finally, Section 3.9 summarizes the chapter.

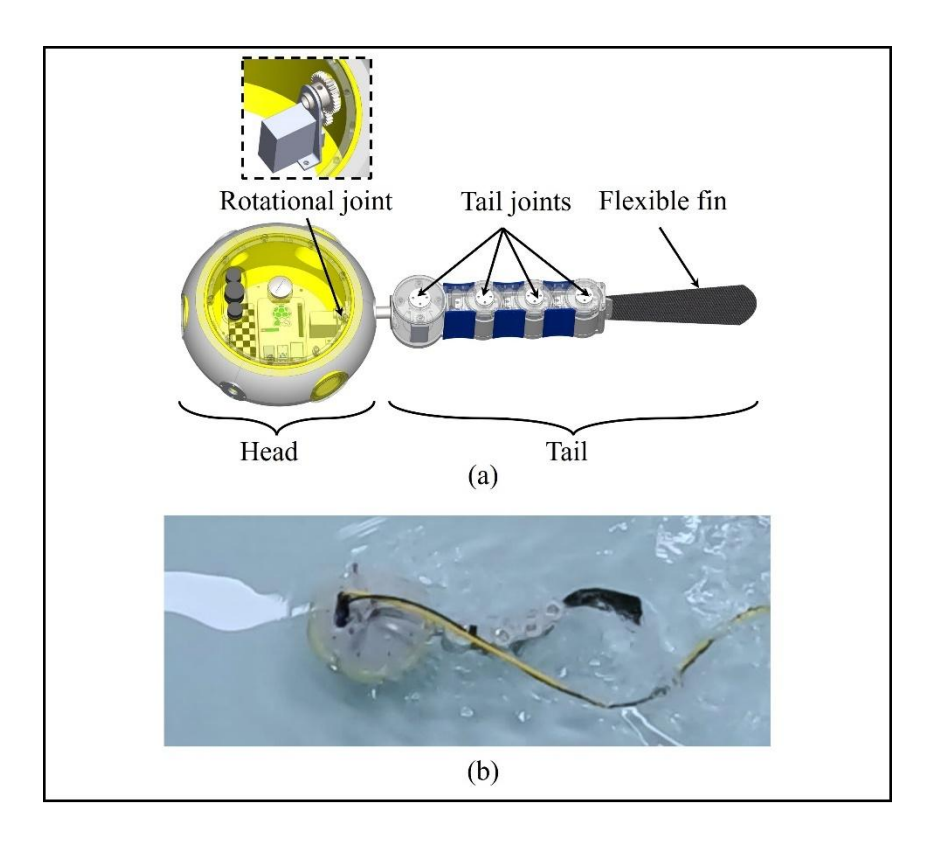


Fig. 3.1: Overview of the robotic tadpole. (a) Overall structure. (b) Experimental platform.

3.1 Hardware Implementation

3.1.1 Mechanical system

The full system of the robot is shown in Fig. 3.1. The robotic tadpole mainly consists of two parts: a rigid head and a tail. The head is shaped like an ellipsoid, which, although not identical to a real tadpole's head, is beneficial for stable swimming motion. In field applications, the robot needs to carry various electronics including the microcontroller, communication board, sensors, and battery. Therefore, the head should have ample space. Its dimensions are 260 mm × 260 mm × 150 mm. The tail is composed of several active joints connected in series and a passive flexible fin at the end. The size of each joint and link is as compact as possible to ensure smoother tail motion. Each joint is actuated by a servo with a maximum no-load rotational speed of 65 rpm and a stall torque of 5 Nm. The first joint, which has a large allowable rotation range, is used to adjust the bias angle of the entire tail

and the remaining joints are used to perform the undulatory motion. The allowable range of the first joint and the remaining joints are $\pm 120^{\circ}$ and $\pm 80^{\circ}$, respectively. The diameters of the first joint and the remaining joints are 70 mm and 50 mm correspondingly. The distance between the first joint and second joint is 85 mm, and for the others, the distance is 65 mm. The height of all joints is 80 mm.

Table 3.1: Physical parameters of the robotic tadpole used for simulation

Parameters	Value	Parameters	Value	
m_0	3.635 kg	l_n	0.038 m	
m_1	0.333 kg	$S_{0,x}$	0.1606 m^2	
$m_2 \sim m_{n-1}$	0.316 kg	$S_{0,y}$	0.0327 m^2	
m_n	0.200 kg	$S_{1,x}$	0.0238 m^2	
I_0	$3.1\times10^{-2} \text{ kg}\cdot\text{m}^2$	$S_{1,y}$	0.0068 m^2	
I_1	$2.0\times10^{-4} \text{ kg}\cdot\text{m}^2$	$S_2 \sim S_{n-1}$	0.0156 m^2	
$I_2 \sim I_{n-1}$	$1.0\times10^{-4}~\mathrm{kg\cdot m^2}$	$S_2 \sim S_{n-1}$	0.0052 m^2	
I_n	$2.0 \times 10^{-5} \text{ kg} \cdot \text{m}^2$	$S_{n,x}$	0.0055 m^2	
l_0	0.185 m	$S_{n,y}$	0.0018 m^2	
l_1	0.085 m	E	200 Gpa	
$l_2 \sim l_{n-1}$	0.065 m	c_k	0.02 s	

The head and the rigid tail body are fabricated CNC machining, and the material is ABS plastic. The flexible fin should have an appropriate Young's modulus for sufficient elasticity, high strength, and light weight. Thus, commonly used carbon fiber is selected as the material of the flexible fin. And its shape is produced through laser cutting. The tail is connected to the

head by an active joint capable of rotating in roll direction. The static sealing of the whole system uses silicon rubber rings, and the dynamic sealing is achieved by the glyd ring on each rotational shaft. With the help of the rotational joint, the robot is capable of three-dimensional swimming. The experimental prototype is shown in Fig. 1B. The detailed physical parameters of the robot are listed in Table 3.1.

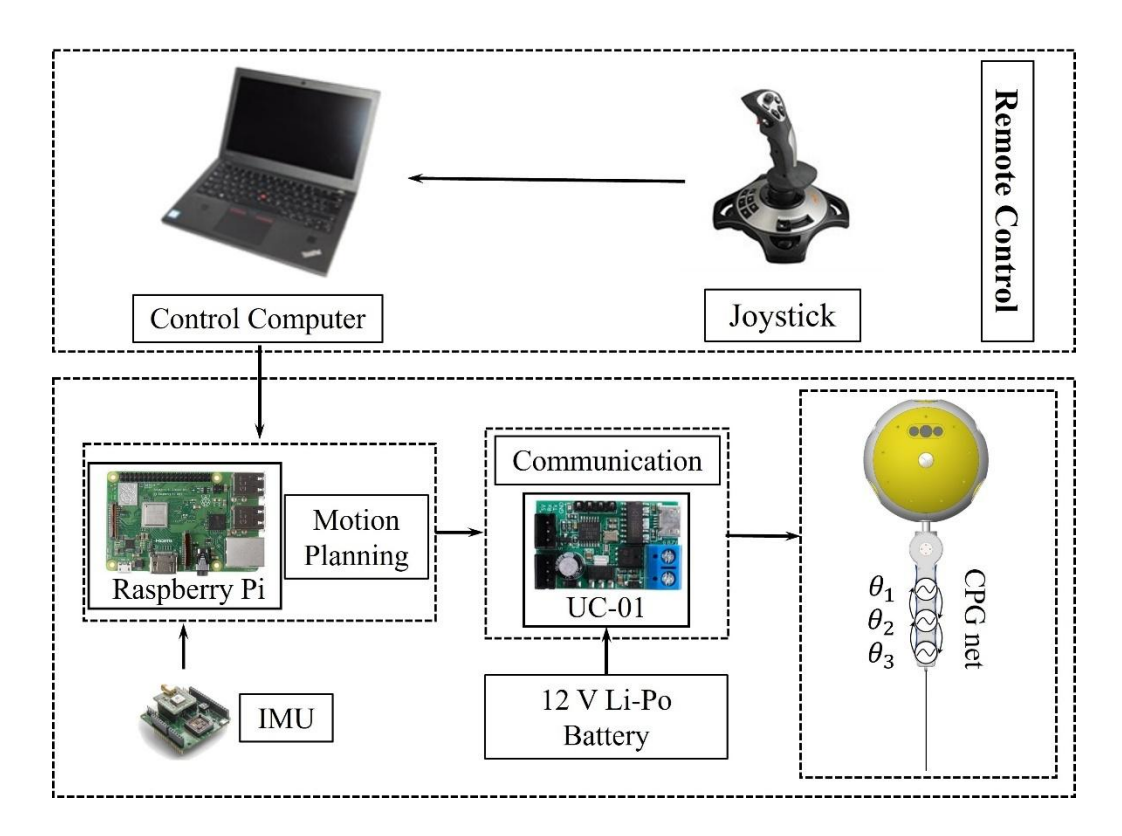


Fig. 3.2: Schematic of remote control.

3.1.2 Control system

The control system of the robotic tadpole is depicted in Fig. 3.2. The Main controller inside the head is Raspberry Pi (RPi) 4 B+, which is responsible for communication with a remote computer, motor control, and data acquisition from the sensors. The remote computer communicates with the microcontroller of the robot through a Lan or Ethernet cable. The communication between the main controller and servo motors, namely the universal asynchronous receiver/transmitter (UART) and serial communication link, relies on a

TTL/USB converter (UC-01). The power source is a rechargeable Li-Po battery with a voltage of 12 V and a capacity of 4900 mAh. The inertial measurement unit (IMU) can estimate the attitude of the robot. A joystick connected to the computer is used to send locomotion mode commands.

The CPG model is used to control the robot. The block diagram of the robot in Fig. 3.2 illustrates the CPG network of a phase oscillator model. The circle on each joint indicates an oscillator, and the arrows between two adjacent circles denote phase couplings. The remote-control laptop solves the differential equations of the CPG model based on the required amplitude, bias angle, phase difference between adjacent joints, and frequency to obtain the output signals for each joint. Subsequently, the data is transmitted to the microcontroller Raspberry Pi via the local area network using a LAN cable. The microcontroller then communicates control commands to the servos within the joints through serial communication, with the servos utilizing low-level PD-controllers to track their individual position commands. The CPG model implemented on this robot is presented in the following form,

$$\begin{cases} \dot{\gamma}_{i} = 2\pi f_{i} + \sum_{j} \left(C_{ij} a_{j} \sin(\gamma_{j} - \gamma_{i} - \Gamma_{ij}) \right) \\ \ddot{a}_{i} = \lambda_{1} \left(\frac{\lambda_{1}}{4} \left(A_{i} - a_{i} \right) - \dot{a}_{i} \right) \\ \ddot{b}_{i} = \lambda_{2} \left(\frac{\lambda_{2}}{4} \left(B_{i} - b_{i} \right) - \dot{b}_{i} \right) \\ \theta_{i} = b_{i} + a_{i} \sin(\gamma_{i}) \end{cases}$$

$$(3.1)$$

where γ_i , a_i , and b_i are phase, amplitude, and bias of the *i*th oscillator respectively. C_{ij} and Γ_{ij} are the coupling weight and the phase difference between the *i*thoscillator and the *j*th oscillator correspondingly. λ_1 and λ_2 are just the constants or gains. f_i , A_i , and B_i are the target frequency, amplitude, and bias of the *i*th oscillator. θ_i is the rhythmic output signal of

the oscillator. Fig. 3.3 shows one example of CPG output signals for the robot with three active joints when the amplitude, frequency, phase lag, and bias are 30 degrees, 1.7 Hz, 90 degrees, and 0 degree, respectively.

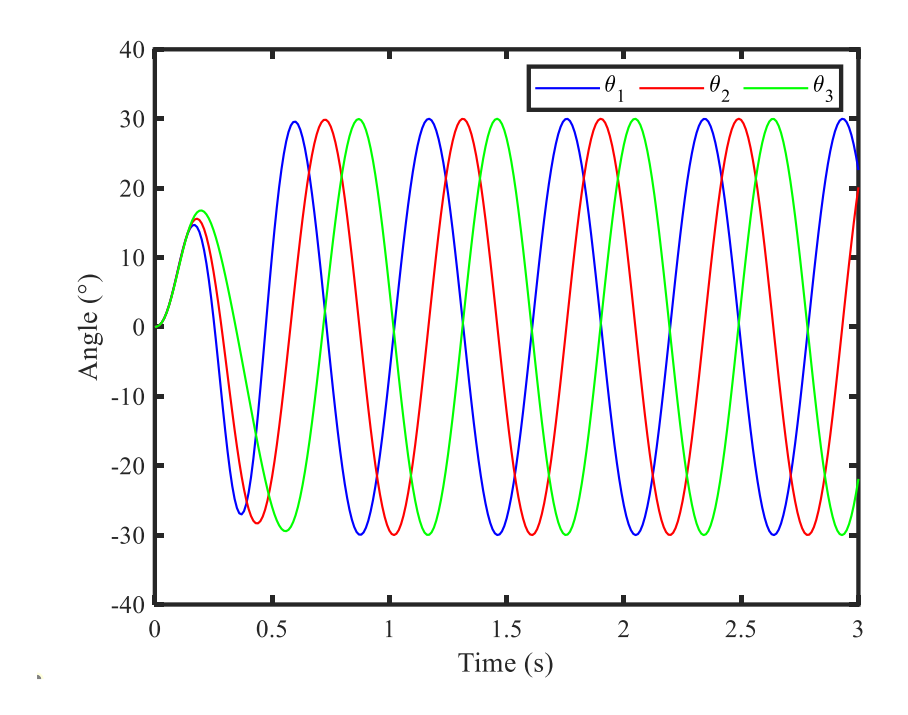


Fig. 3.3: CPG output signals for the robot with three active joints.

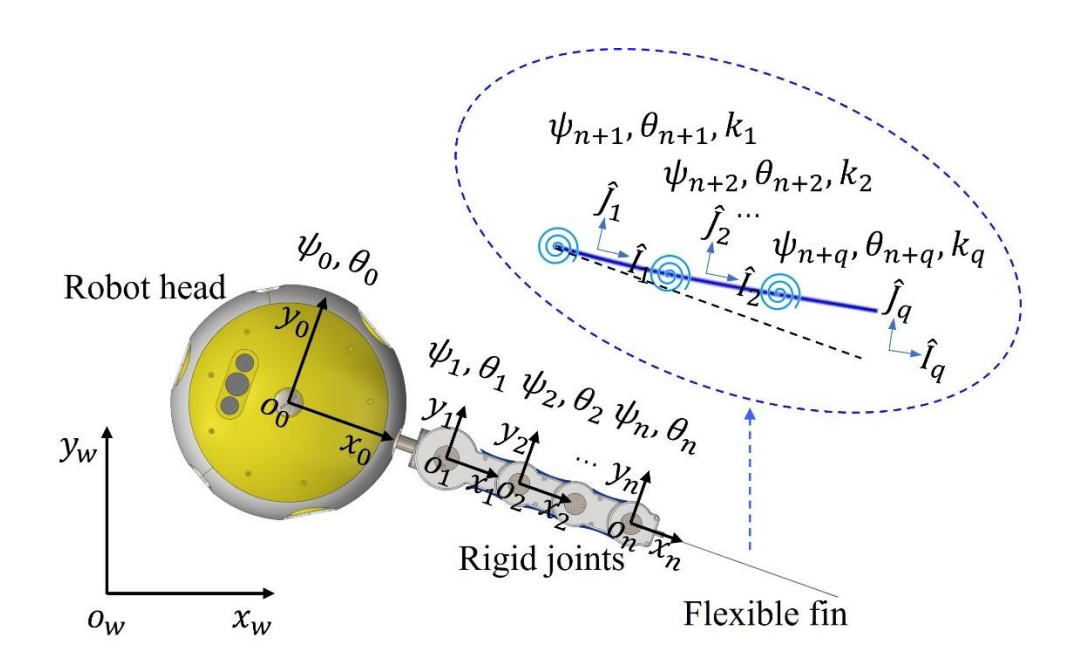


Fig. 3.4: Schematic of the coordinate systems.

3.2 Mathematical Modeling

3.2.1 Kinematic analysis

To facilitate the motion analysis of the robot, the coordinate systems are defined as shown in Fig. 3.4. $o_w - x_w y_w z_w$ indicates the inertial coordinate frame. $o_0 - x_0 y_0 z_0$ is the head-fixed coordinate frame located at the mass centre of the robot head. $o_i - x_i y_i z_i$ (i = 1, 2, ..., n) denotes the joints-fixed frames, and n is the number of the joints. θ_i and ψ_i represent the yaw angle between the current frame to the previous frame and the yaw angle between the current frame to the inertial coordinate frame, respectively. The relationship between θ_i and ψ_i is $\psi_j = \sum_{i=0}^j \theta_i$, (i = 0,1,...,j). l_{i-1} is the distance between o_{i-1} and o_i along the axis x_{i-1} . The position vector P_i^w of the ith coordinate origin o_i in the inertial coordinate frame can be expressed as

$$P_i^w = P_0^w + \sum_{j=1}^i R_{j-1}^w P_j^{j-1}$$
(3.2)

where P_0^w denotes the position vector of the robot head, R_{j-1}^w is the rotating matrix of the (j-1)th coordinate relative to the inertial coordinate, and P_j^{j-1} is the position vector of the jth coordinate origin o_j in the (j-1)th coordinate. The rotating matrix R_i^w and position vector P_i^{i-1} are defined as

$$R_{i}^{w} = \begin{pmatrix} \cos\psi_{i} & -\sin\psi_{i} & 0\\ \sin\psi_{i} & \cos\psi_{i} & 0\\ 0 & 0 & 1 \end{pmatrix}, P_{i}^{i-1} = \begin{pmatrix} l_{i-1}\\ 0\\ 0 \end{pmatrix}$$
(3.3)

Then the position vector r_i of the mass centre of ith rigid link in the inertial coordinate system can be obtained by

The linear velocity and angular velocity of the mass centre of *i*th rigid link in the inertial coordinate system can be further obtained by

$$v_i^w = \dot{r}_i = \dot{R}_i^w c_i + \dot{P}_i^w \tag{3.5}$$

$$\omega_i^w = \omega_{i-1}^w + R_i^w \omega_i \tag{3.6}$$

For the analysis of the flexible fin, it is divided into q rigid segments [123]. These segments connect to each other through torsional springs and dampers. \hat{I}_i and \hat{J}_i (i = 1, 2, ..., q) are the unit vectors in the inertial coordinate frame, which are parallel and perpendicular to the ith segment respectively, and are given as $\hat{I}_i = [\cos\psi_{n+i}, \sin\psi_{n+i}, 0]^T$, $\hat{J}_i = [-\sin\psi_{n+i}, \cos\psi_{n+i}, 0]^T$. Therefore, the position vector of the mass centre of the ith segment in the inertial coordinate system can be expressed as

$$r_{n+i} = R_n^w P_{n+1}^n + P_n^w + \zeta \cdot \left(\sum_{j=1}^{i-1} \hat{I}_j\right) + \tau \hat{I}_i$$
 (3.7)

where ζ is the length of each segment, and τ is the length between the start point and the mass centre of each segment.

Then the perpendicular component of the velocity of the mass centre on the *i*th segment can be expressed as

$$v_{n+i,\perp} = \dot{P}_0^w \cdot \hat{J}_i + \sum_{j=1}^{n+1} l_{j-1} \dot{\psi}_{j-1} \cos(\psi_{j-1} - \psi_{n+i}) + \zeta \cdot \left(\sum_{j=1}^{i-1} \dot{\psi}_{n+j} \cos(\psi_{n+j} - \psi_{n+i})\right) + \tau_i \dot{\psi}_{n+i}$$
(3.8)

3.2.2 Dynamic modeling

1) Robot Head Dynamics: Kirchhoff's equations are widely adopted to derive the motion equations of the rigid body in an inviscid fluid [124]. Thus, the motion equations of the head of the robotic tadpole in the head-fixed coordinate system can be expressed as

$$\begin{cases}
(m_0 - A_{ax})\dot{v}_{0,x} = (m_0 - A_{ay})v_{0,y}\omega_0 + F_{0,x} \\
(m_0 - A_{ay})\dot{v}_{0,y} = -(m_0 - A_{ax})v_{0,x}\omega_0 + F_{0,y} \\
(I_0 - A_{az})\dot{\omega}_0 = (A_{ay} - A_{ax})v_{0,x}v_{0,y} + M_0
\end{cases}$$
(3.9)

where m_0 is the mass of the head and I_0 is its inertial about axis z_0 . $v_{0,x}$ and $v_{0,y}$ are the linear velocities expressed in the head-fixed frame $o_0 - x_0 y_0 z_0$. ω_0 is the angular velocity. $F_{0,x}$, $F_{0,y}$, and M_0 are the external force components and moments acting on the head. A_{ax} , A_{ay} , and A_{az} are the terms to describe the effect of the fluid added mass, which can be obtained by Lamb's k-factors and mass as the following equations [124].

$$\begin{cases}
A_{ax} = -k_1 m_0 \\
A_{ay} = -k_2 m_0 \\
A_{az} = -k' I_0
\end{cases}$$
(3.10)

 $F_{0,x}$, $F_{0,y}$, and M_0 can be expressed as

$$\begin{cases}
F_{0,x} = F_{t,x}^0 + F_{d0,x} \\
F_{0,y} = F_{t,y}^0 + F_{d0,y} \\
M_0 = M_t^0
\end{cases}$$
(3.11)

where $F_{t,x}^0$, $F_{t,y}^0$, and M_t^0 are the force components and moment generated by the tail and are expressed in the head frame. $F_{d0,x}$ and $F_{d0,y}$ are the drag forces from surrounding fluid, which can be calculated by

$$\begin{cases}
F_{d0,x} = -0.5\rho C_{f0} S_{0,x} v_{0,x} || v_{0,x} || \\
F_{d0,y} = -0.5\rho C_{d0} S_{0,y} v_{0,y} || v_{0,y} ||
\end{cases}$$
(3.12)

where ρ is the density of the fluid. C_{f0} and C_{d0} are the friction coefficient and drag coefficient. $S_{0,x}$ and $S_{0,y}$ denote the characteristic areas with respect to axis x and axis y of the coordinate system $o_0 - x_0 y_0 z_0$, respectively.

2) Tail Dynamics: The tail of the robot comprises two parts, the rigid body and the flexible fin. The rigid body is a multi-joint mechanism. To simplify the analysis, all forces and moments are assumed to act on the mass centre of each link, and the dynamics can be derived by Newton-Euler equations as follows,

$$\begin{cases}
F_{i} + F_{fluid} - R_{i+1}^{i} F_{i+1} = m_{i} a_{i} \\
M_{i} - R_{i+1}^{i} M_{i+1} + r_{i,i} \times F_{i} - r_{i,i+1} \times \left(R_{i+1}^{i} F_{i+1} \right) \\
= I_{i} \dot{\omega}_{i} + \omega_{i} \times \left(I_{i} \omega_{i} \right)
\end{cases} (3.13)$$

where F_i and M_i are the force and moment exerted on the *i*th link by the (i-1)th link, and all these items are described in the *i*th coordinate system. F_{fluid} are the hydrodynamic forces including drag force and added mass force based on the simplified Morison equation, which can be calculated by

$$F_{di} = \begin{pmatrix} F_{di,x} \\ F_{di,y} \\ 0 \end{pmatrix} = \begin{pmatrix} -0.5\rho C_{f1} S_{i,x} v_{i,x} \| v_{i,x} \| \\ -0.5\rho C_{d1} S_{i,y} v_{i,y} \| v_{i,y} \| \\ 0 \end{pmatrix}$$
(3.14)

$$F_{ai} = \begin{pmatrix} F_{ai,x} \\ F_{ai,y} \\ 0 \end{pmatrix} = \begin{pmatrix} -0.25\rho\pi h_i^2 l_i C_{m1} \dot{v}_{i,x} \\ -0.25\rho\pi h_i^2 l_i C_{m1} \dot{v}_{i,y} \\ 0 \end{pmatrix}$$
(3.15)

where h_i is the depth of the cross section of each link, C_{m1} is the added mass coefficient. C_{f1} and C_{d1} are the friction coefficient and drag coefficient of the rigid joints. $S_{i,x}$ and $S_{i,y}$ are the characteristic areas with respect to axis x and axis y of the joint-fixed coordinate frame $o_i - x_i y_i z_i$, respectively.

The multi-segment method is employed for the analysis of the flexible fin as described in the previous section. In the inertial coordinate frame, the interactions between adjacent segments can be described as

$$\begin{cases} F_{\delta_{i}} = F_{\tau_{i}} + F_{\delta_{i+1}} \\ M_{\delta_{i}} = M_{\tau_{i}} + M_{\delta_{i+1}} + \zeta \hat{I}_{i} \times F_{\delta_{i+1}} \end{cases}$$
(3.16)

where F_{δ_i} and M_{δ_i} are the force and moment exerted by the *i*th segment on the (i-1)th segment. F_{τ_i} and M_{τ_i} are the hydrodynamic forces and moments from surrounding fluid,

$$F_{\tau_i} = \left(-0.5C_{df}\rho S_{n+i}v_{n+i,\perp} ||v_{n+i,\perp}||\right) \hat{J}_i + \left(-m_{afi}\frac{d}{dt} \left(v_{n+i,\perp} \cdot \hat{J}_i\right)\right)$$
(3.17)

$$M_{\tau_i} = \tau_i \hat{I}_i \times F_{\tau_i} \tag{3.18}$$

where $m_{af,i}$ is the added mass and equals to $0.25\rho\pi h_{fi}^2\zeta C_{mf}$. C_{df} is the drag coefficient of each segment of the fin. h_{fi} is the span at the mass centre of the *i*th segment. C_{mf} is added mass coefficient.

The moments on the *i*th segment generated by the torsional spring and damper are defined as M_{k_i} and M_{d_i} correspondingly,

$$M_{k_i} = \begin{pmatrix} 0 \\ 0 \\ k_i(\psi_{n+i} - \psi_{n+i-1}) \end{pmatrix}$$
 (3.19)

$$M_{d_i} = \begin{pmatrix} 0 \\ 0 \\ c_{ki}k_i(\dot{\psi}_{n+i} - \dot{\psi}_{n+i-1}) \end{pmatrix}$$
 (3.20)

where k_i is the stiffness of the torsional spring on the *i*th segment, and it can be evaluated by $k_i = EI_i/\zeta$ [125]. c_k is the constant of stiffness proportionality for damping [126]. The rotation angles of each segment can be obtained by solving the moment balance equations as

follows.

$$M_{\delta_i} = M_{k_i} + M_{d_i} \tag{3.21}$$

3.3 Experimental Setup

The swimming tests of the robot are conducted in a laboratory swimming pool with dimensions of 4 m (L) \times 2 m (W) \times 0.8 m (H) as shown in Fig 3.5. Four tracking cameras (OptiTrack) are placed on four corners of the pool with a height of 2.5 m for tracking the robot's swimming trajectory through the infrared reflective markers fixed on the robot's head. A laptop is connected to the tracking cameras by an Ethernet switch and cables for controlling the cameras and acquiring tracking data. Then the motion states of the robotic tadpole including swimming velocity and angular speed can be calculated through the obtained data.

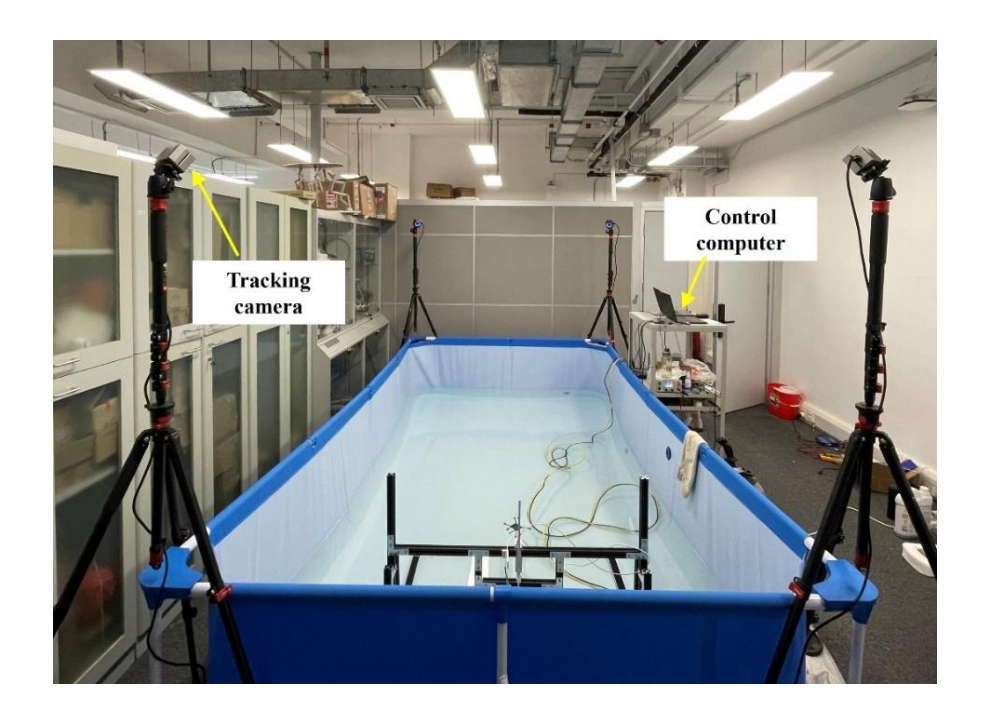


Fig. 3.5: Position tracking system.

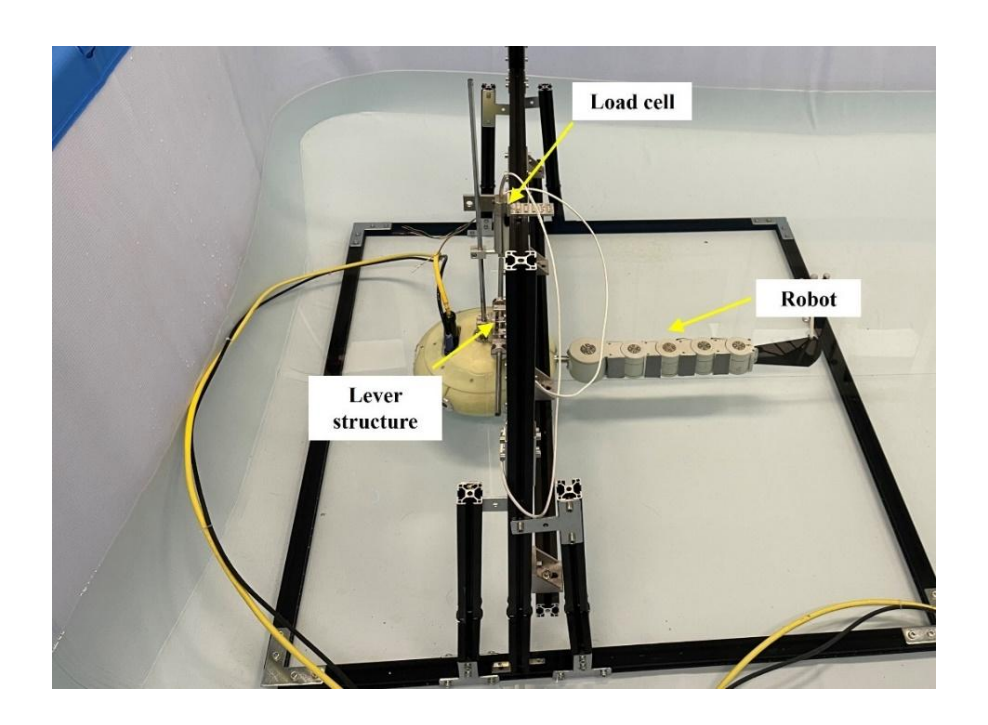


Fig. 3.6: Thrust measurement system.

A static frame is made up of aluminum alloy sections and is placed inside the swimming pool for measuring thrust and tracking the fin-tip trajectory as shown in Fig. 3.6. The thrust measurement is achieved by a lever mechanism that is constructed by a series of rods and rolling bearings. A horizontal rod is fixed on the static frame, and it is connected with a vertical rod by the rolling bearings, which allows the vertical rod to rotate around axis x. One side of the vertical rod is fixed on the robot's head, and another side is attached to a load cell. Thus, the thrust force can be measured while the tail of the robot performs undulatory motion in water. Meanwhile, the infrared reflective markers are attached on the fin's tip. And the displacement of the fin's tip can be tracked by the tracking cameras.

3.4 Hydrodynamic Parameters Identification

The physical parameters of the robot in the derived dynamic model including mass, dimensions, etc. can be easily obtained from the software SolidWorks as shown in Table 3.1. However, it is difficult to determine the hydrodynamic parameters, which are related to the geometry and motion state of the robot. In most studies, hydrodynamic parameters are

estimated by tuning these parameters to match the results of velocity obtained from simulation with experimental data [61, 116]. But this approach is not suitable for the case in this study. The tail of the robotic tadpole consists of rigid joints and links and a flexible fin. The derived simulation results using the estimated hydrodynamic parameters not only need to match the result of velocity with experimental data but also are required to satisfy the deformation of the flexible fin. Hence, we used the experimental platform as depicted in Figs. 3.5 and 3.6 to measure the tips' displacement of the flexible fins and the thrust force of the tails. The experimental results are used to estimate the hydrodynamic parameters by comparison with the simulation results according to equations (3.22) and (3.23). The detailed identification procedure of tail hydrodynamic parameters is given as follows:

For each tail, fifteen tests are performed with different joint control parameters $A=\{20^\circ,30^\circ,40^\circ\}$, $f=\{0.8$ Hz, 1.1 Hz, 1.4 Hz, 1.7Hz, 2.0 Hz $\}$, $\xi=90^\circ$. And the tip's displacement of the flexible fin for each case is recorded by the tracking system. At the same time, the thrust force of four tails is measured by the thrust measurement system.

The drag coefficient C_{df} and the added mass coefficient C_{mf} of the flexible fin are set within a certain range according to the empirical values, which are [0.01, 3] and [0.01, 1], respectively. The dynamical simulations of the flexible fin under the same control parameters in the first procedure are run for all values of C_{df} and C_{mf} in their own range with a step of 0.01 to acquire the tip's displacement of the fin. The root-mean-square error between the simulation results of the displacement and the experimental data is calculated for each step. The values of C_{df} and C_{mf} that satisfy the minimum root-mean-square error for all testing cases are selected as the final values by following the equation (3.22).

Similarly, the drag coefficient C_{d1} , the friction coefficient C_{f1} , and the added mass

coefficient C_{m1} of the rigid joints and links of the tails are restricted in the range [0.01, 3], [0.01, 1], and [0.01, 1] correspondingly. The results of the thrust force obtained from the simulations are compared with the measured thrust data. And the parameters within the restricted range that can obtain the best match between simulations and experiments by solving the equation (3.23) are chosen as the identified values for the tails' dynamics model.

$$\min \Delta d = \min \frac{1}{\chi} \sum_{\chi} \sqrt{\frac{1}{N} \sum_{i=1}^{N} (d_e(i) - d_s(i))^2}$$
 (3.22)

$$\min \Delta F = \min \frac{1}{\chi} \sum_{\chi} \sqrt{\frac{1}{N} \sum_{i=1}^{N} (F_e(i) - F_s(i))^2}$$
(3.23)

In equations (3.22) and (3.23), d_e and d_s are the tip's displacements of the flexible fin acquired from experiments and simulations, correspondingly. F_e and F_s are the theoretical and the experimental thrust force, respectively. N is the total samples' number, and χ denotes the number of all testing cases.

Table 3.2: Identified hydrodynamic parameters

Parameters	C_{d0}	C_{f0}	C_{d1}	C_{f1}	C_{m1}	C_{df}	C_{mf}
Value	0.22	0.12	1.20	0.03	0.05	2.00	0.10

By following the procedure above, all the hydrodynamic parameters of the robot's tail can be obtained. The drag coefficient C_{d0} and the friction coefficient C_{f0} of the robot's head are determined using computational fluid dynamics (CFD) simulations due to its regular geometry. All the identified hydrodynamic parameters are listed in Table 3.2 and are used in

the following simulations. Fig. 3.7 demonstrates the comparison between the results of simulations and experiments. The average errors for all tail beat frequencies at each amplitude, comparing simulations and experiments, are presented in Table 3.3. All errors are within 20%, demonstrating the high accuracy of the dynamic model for predicting the propulsion performance of the robot.

Table 3.3: Average errors between simulations and experiments

	Fin-tip's	Thrust	Fin-tip's	Thrust
Amplitude	displacement of tail N2	force of tail N2	displacement of tail N3	force of tail N3
	112	112	113	113
$A = 20^{\circ}$	9.1%	15.5%	6.8%	8%
$A = 30^{\circ}$	9.6%	17.2%	6.6%	8.5%
$A = 40^{\circ}$	11%	9.8%	6.3%	8%

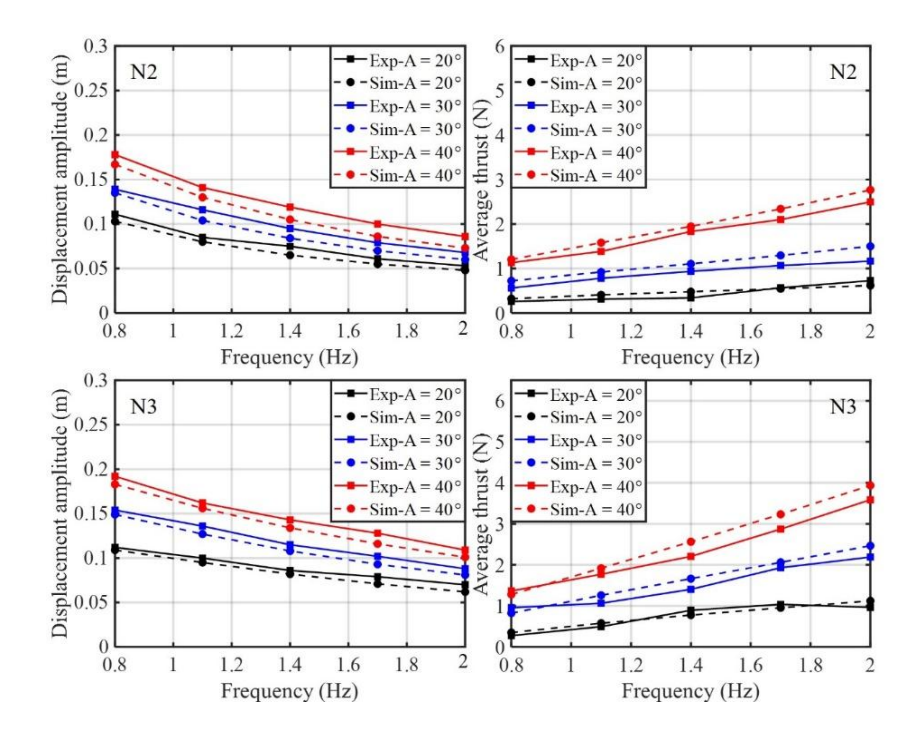


Fig. 3.7: Comparison of fin-tip displacement amplitude and average thrust between simulations and experimental tests.

Remark 1. A reliable and effective dynamic model is crucial for the analysis and control of a robotic fish. However, most existing work focuses on either only rigid-linkage tail [116, 127] or tails made up of flexible materials [115, 123, 128], and no literature results are related to a rigid-linkage-with-flexible fin system of any linkage number and fin materials/shapes. In this study, using the Newton-Euler equations of the tail rigid body and the simplified multi-segment method of the flexible fin, the complex dynamics of a tail consisting of a multi-joint mechanism and a flexible fin can be established. This model can greatly facilitate performance exploration in a large-scale control parameter space, and it should be noted that:

(1) the model is generic for the propulsive performance prediction of a tail consisting of an arbitrary number of active joints, and (2) the model can be used for the flexible fin undergoing large deformation. These can therefore ensure the following structure and control parameters optimization.

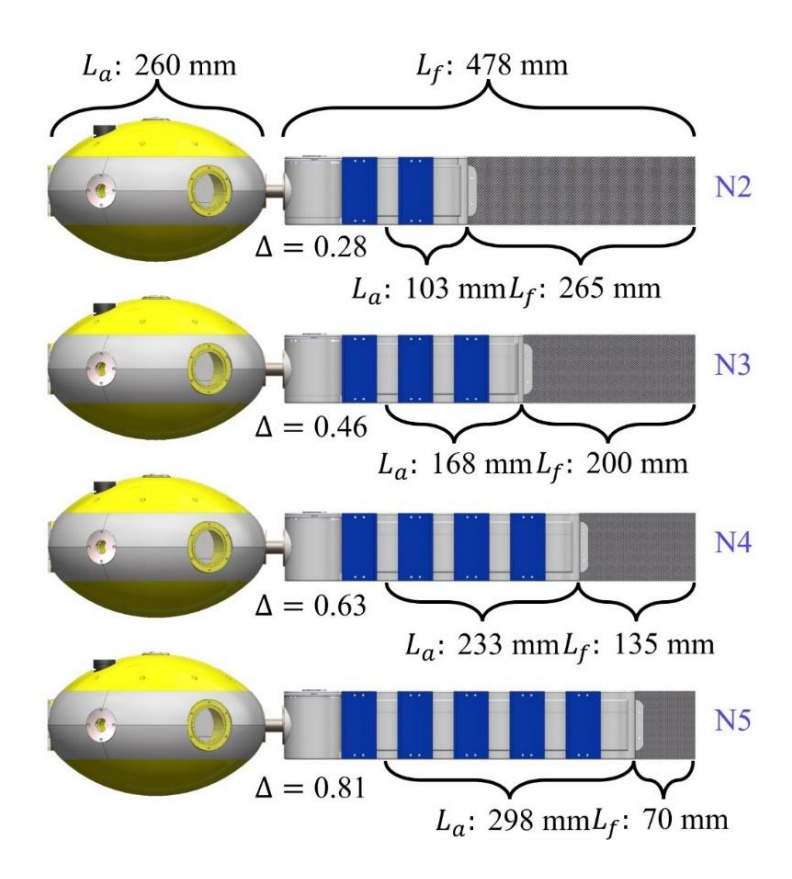


Fig. 3.8: Tails with different active-joint ratios.

3.5 Performance of the Tail with Different Active-Joint Ratios

In this part, the well-developed dynamic model in the previous sections is used to evaluate the swimming performance and optimize the control parameters of the tail with different active-joint ratios as shown in Fig. 3.8. The performance of different tails, in terms of steady swimming speed and swimming efficiency under different control parameters including frequency, amplitude and phase difference, is compared. The simulation results are further validated by the experiments.

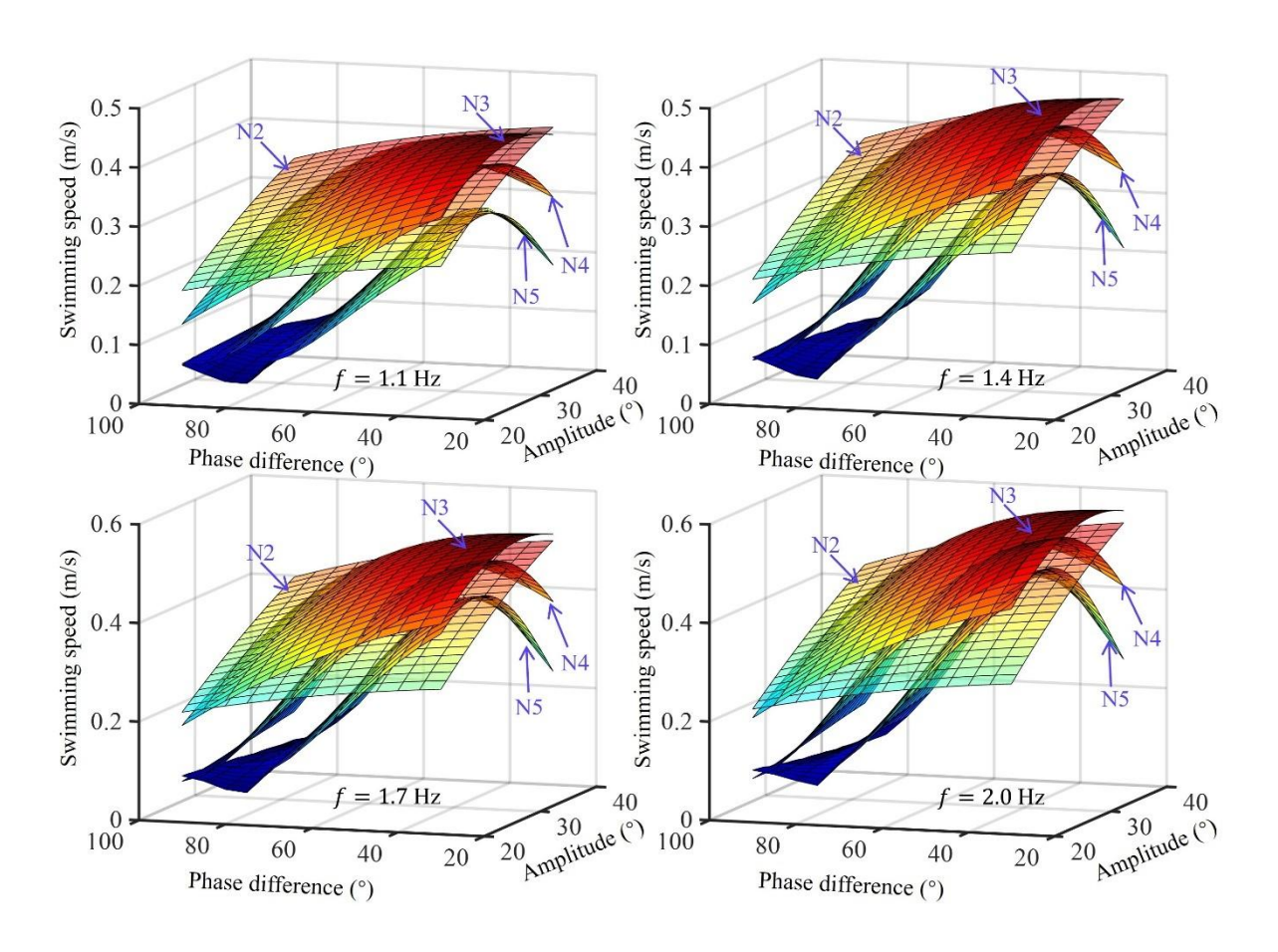


Fig. 3.9: Simulation results of velocity with respect to different frequencies, amplitudes, and phase differences.

The steady swimming velocities of four tails under different control parameters, as investigated by the theoretical model, are shown in Fig. 3.9. Based on the competence of the real adopted motors, with a maximum no-load rotational speed is 65 rpm, the tail beat

frequency and amplitude for the performance exploration are limited within 2 Hz and 40°, respectively. Real fish with slender bodies usually exhibit the smooth and compliant undulatory movement, which benefits from the movement phase lag along the tail body during the rhythmic oscillation. To simulate this feature, the phase difference starts from a small value 30°. Therefore, the explored ranges of frequency, amplitude and phase difference are from 0.8 Hz to 2 Hz, from 20° to 40°, and from 30° to 90°, correspondingly. From the results, it is clear to see that the influences of changes in control parameters on four tails are different. With changes of control parameters, the velocities of tail N2 and tail N3 vary gently, while the velocities of tail N4 and tail N5 show dramatic changes. At small phase differences, all tails achieve their maximum velocities, as shown in Table 3.4, and the differences are not significant. However, tail N4 and tail N5 perform significantly worse than tail N2 and tail N3 when the phase difference is large. Among all tails, tail N3 generates the fastest speed.

Table 3.4: Simulated maximum steady swimming velocity under different frequencies

Frequency	Tail N2	Tail N3	Tail N4	Tail N5
1.1 Hz	0.41 m/s	0.42 m/s	0.39 m/s	0.31 m/s
1.4 Hz	0.46 m/s	0.48 m/s	0.46 m/s	0.38 m/s
1.7 Hz	0.50 m/s	0.53 m/s	0.51 m/s	0.45 m/s
2.0 Hz	0.53 m/s	0.57 m/s	0.56 m/s	0.51 m/s

To verify the reliability of the simulation results above and further compare energy consumption, the free-swimming experiments of the robot with four different tails at different control parameters were conducted. According to the simulation results, the influence of phase difference is significant. Therefore, to simplify the experiments for the verification, a

medium value of amplitude, namely 30°, and three different phase differences 40°, 60°, and 80° were selected as the control parameters of tails, which represent small, medium, and large phase differences, correspondingly. The results are presented in Fig. 3.10. For swimming speed, the results match well and clearly show consistent conclusions of different tails between simulations and experiments. The Cost of Transport (CoT) calculated by equation (3.24) is used to quantify the swimming efficiency [129], defined as

$$CoT = \frac{P}{mgU} \tag{3.24}$$

where P is the average input electrical power measured by an external power supply, U is the steady cruising speed, m is the mass of the robot, and g is the acceleration of gravity. When measuring the power consumption, we used a separate battery to power the rotating joint inside the head, and the external power supplier was only used to power the tail. Thus, the power consumption of the rotating joint was excluded for the computation of CoT.

From the results of the CoT, it can be observed that as the number of active joints increases, the energy consumption also increases. The CoT of tail N3 is a slightly higher than that of tail N2. And the variations in CoT for tail N2 and tail N3 are very small. In contrast, tail N4 and tail N5 show significant variations with changes in phase difference. At a large phase difference, the energy consumption of these two tails is much higher than that of tail N2 and tail N3. Fig. 3.11 demonstrates the snapshots of the robot's free swimming when the robot is configured with different tails in both simulations and experiments. By comparing the results between simulations and experiments, it can be concluded that the theoretical model is reliable enough for the robot with different tails under various control parameters.

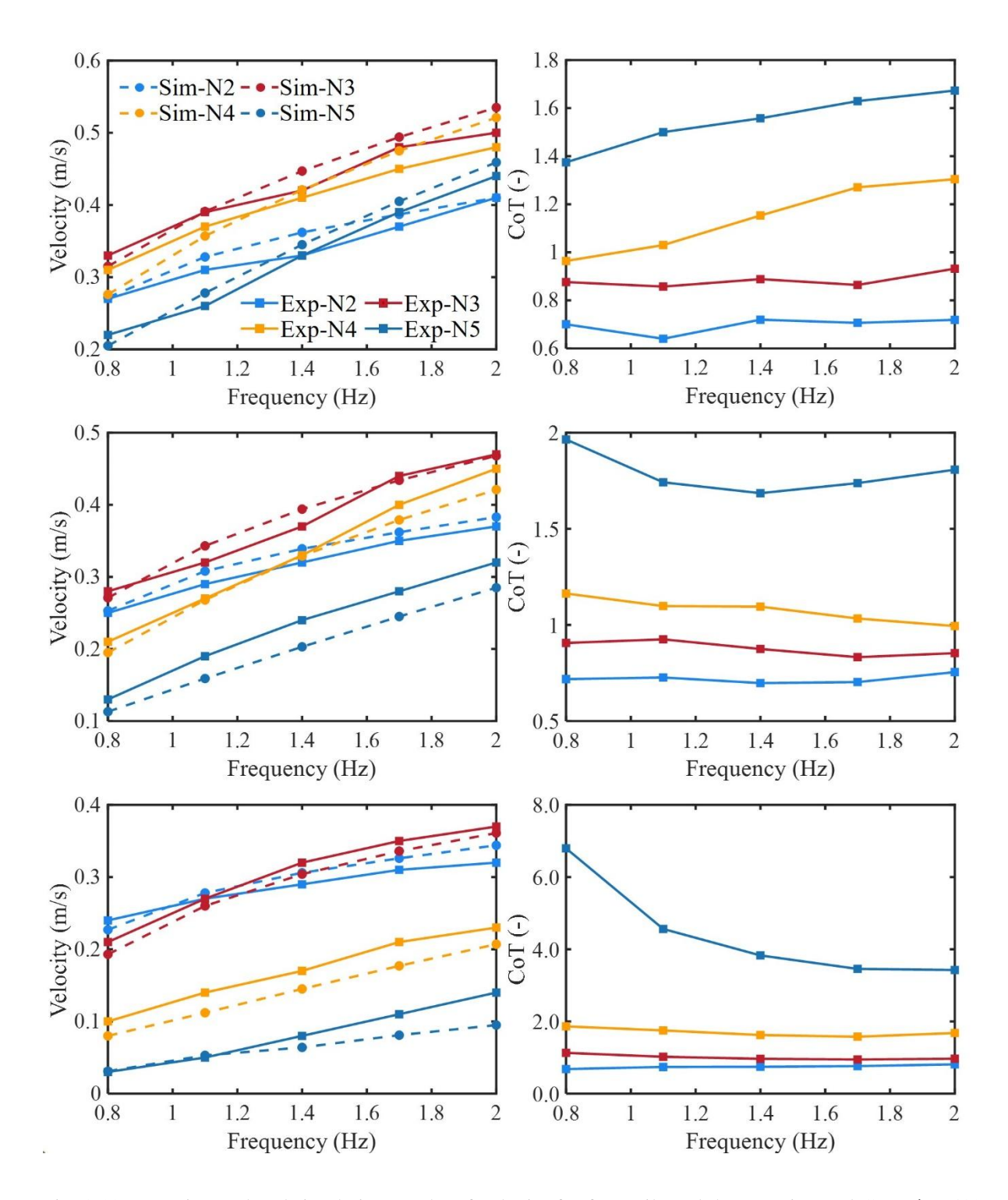


Fig. 3.10: Experimental and simulation results of velocity for four tails and the experimental CoT: $\xi = 40^{\circ}$ (Top), $\xi = 60^{\circ}$ (Middle), $\xi = 80^{\circ}$ (Bottom).

The experimental results of the maximum steady swimming velocities and the corresponding CoT of four tails at different frequencies are compared in Fig. 3.12. The

experimental results of the maximum velocities are close to the simulation results as shown in table 3.4. As the active-joint ratio increases, the achievable maximum speed initially rises and then starts to decline. However, the trend of the CoT at the maximum velocities continuous to rise exponentially. The results indicate that fewer joints result in insufficient power to actuate the flexible fin, while too many active joints lead to discrete kinematics and dramatically increased energy consumption to power the additional active joints. Thus, a proper active-joint ratio needs to be determined. The robot with tail N3 ($\Delta = 0.46$) is the fastest, and its related energy consumption is just slightly higher than that of the robot with tail N2.

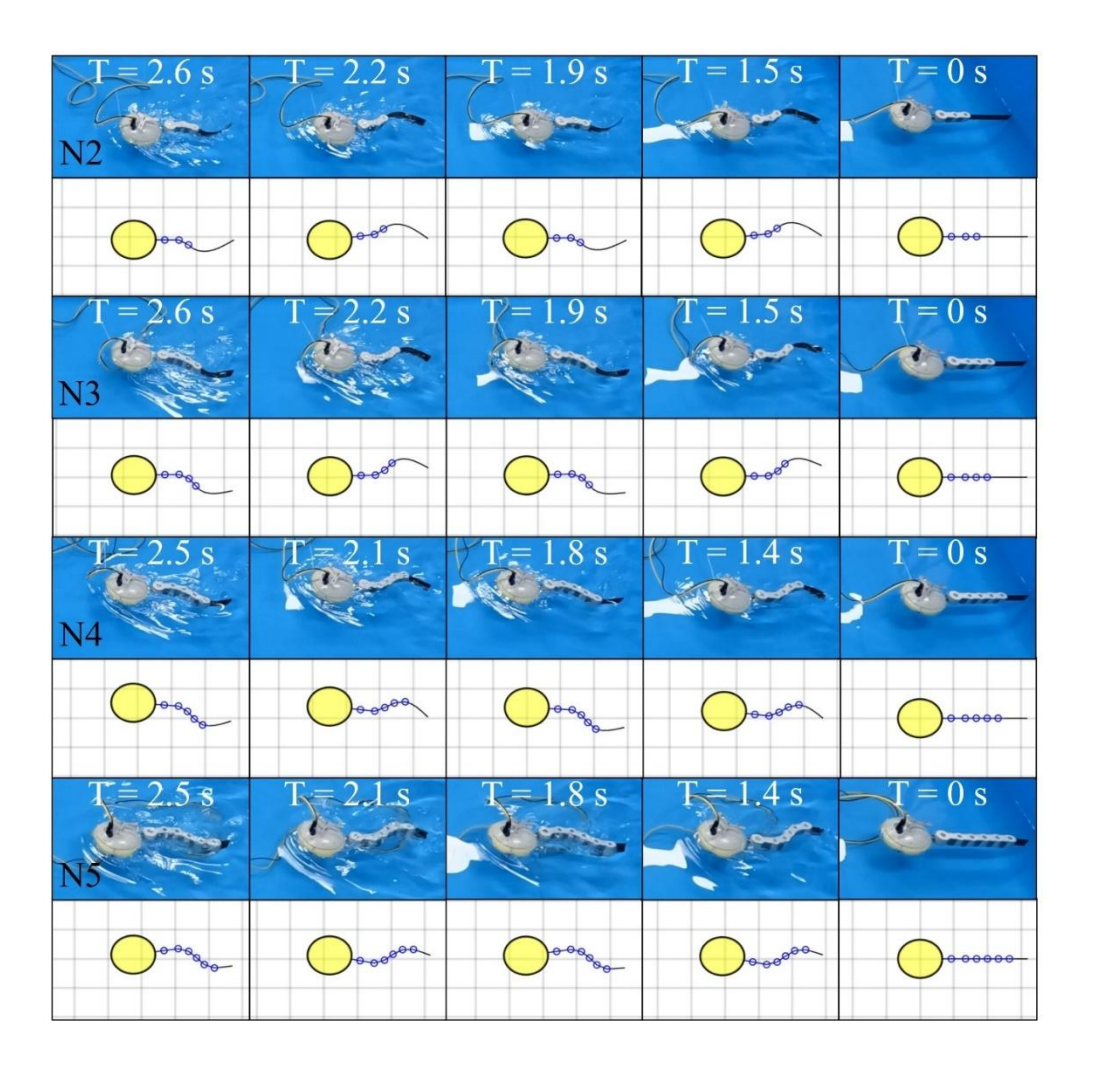


Fig. 3.11: Snapshots taken from videos of simulations and experiments. (A = 30° , $\xi = 60^{\circ}$, f = 1.4 Hz).

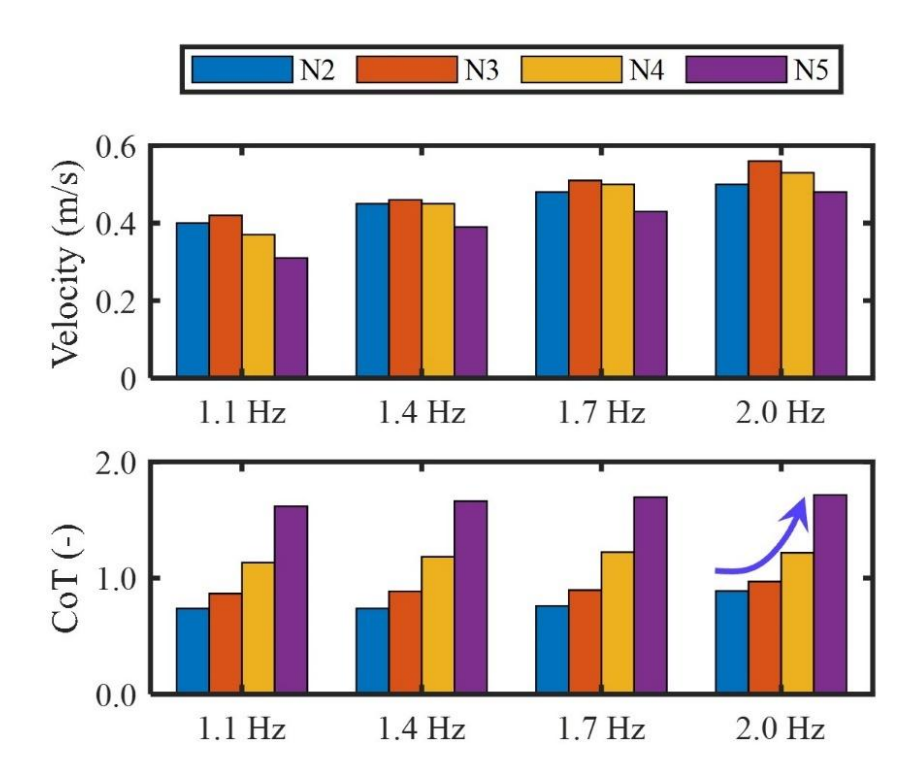


Fig. 3.12: Experimental results of the maximum steady swimming velocity and the related CoT of four tails under different frequencies.

The swimming performance analysis across a wide spectrum of various control parameters shows that the robot with different tail configurations performs very differently with the variation of control parameters, and the optimal set of control parameters for different tails is different. To find the optimal control parameters for each tail, parameter optimization for control should be conducted. The assessment of the forward swimming performance of the robotic tadpole includes the swimming speed and power consumption. Hence, the optimization function in this study is defined as follows.

$$\max \delta = c_1 \left\| \frac{v}{v_{max}} \right\| + c_2 \left\| \frac{P_{min}}{P} \right\|$$

$$\text{s. t.} \begin{cases} A_i \in [20^\circ, 40^\circ] \\ \xi \in [30^\circ, 90^\circ] \\ f \in \{1.1 \text{ Hz}, 1.4 \text{ Hz}, 1.7 \text{ Hz}, 2.0 \text{ Hz} \} \end{cases}$$

where δ is a dimensionless value to indicate the synthesized swimming performance, c_1 and c_2 denote the weight coefficients of the normalized speed and power consumption. c_1 and c_2 should satisfy $c_1 \in [0,1]$, $c_2 \in [0,1]$, and $c_1 + c_2 = 1$. The normalization of three performance indicators enables the consistency of the value scales. In most papers [116, 118], the torque M_i and angular speed $\dot{\theta}_i$ of the active joints are used to predict the power consumption numerically as shown in equation (3.26).

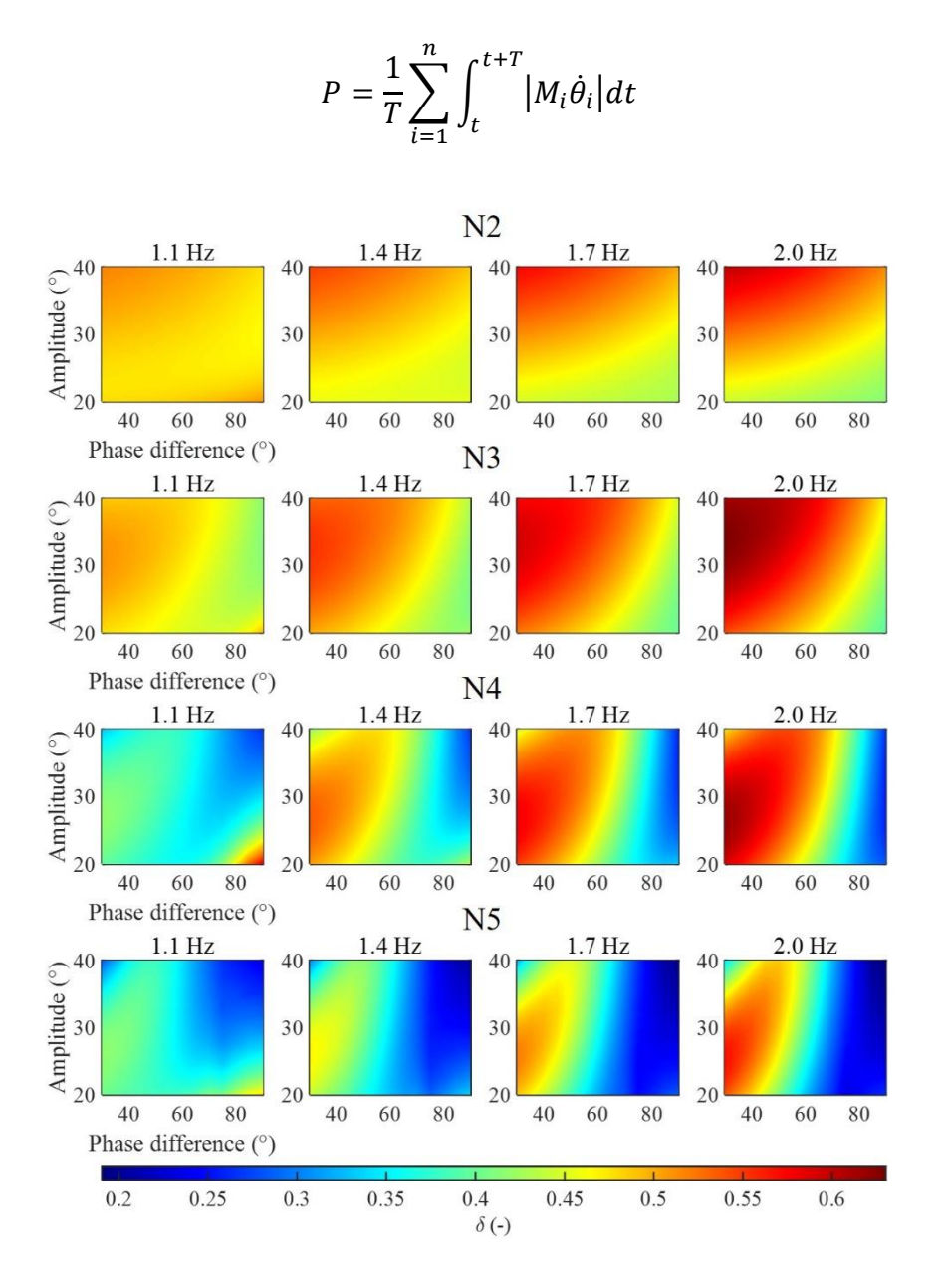


Fig. 3.13: Heat maps of the dimensionless value δ .

(3.26)

Different values of c_1 and c_2 result in different optimization objectives. For example, a large value c_1 indicates that velocity is the primary objective, while a large value c_2 signifies that the control parameters are set to enable the robot to swim more energy-efficiently. To balance the trade-off between the swimming velocity and energy consumption, the weight coefficients are set as $c_1 = 0.5$ and $c_2 = 0.5$, which means both speed and energy efficiency are equally prioritized. With the selected weight coefficients, the dimensionless value δ was calculated under the constrained control parameters. The results are shown in Fig. 3.13, and the optimal control parameters to achieve the maximum δ are listed in Table 3.5.

Table 3.5: Optimal control parameters of four tails

Tail configurations	δ_{max}	A (°)	f (Hz)	ξ (°)
Tail N2	0.60	40	2.0	30
Tail N3	0.63	32	2.0	30
Tail N4	0.62	23	2.0	30
Tail N5	0.57	21	2.0	30
Valocity (m/s)			CoT()	

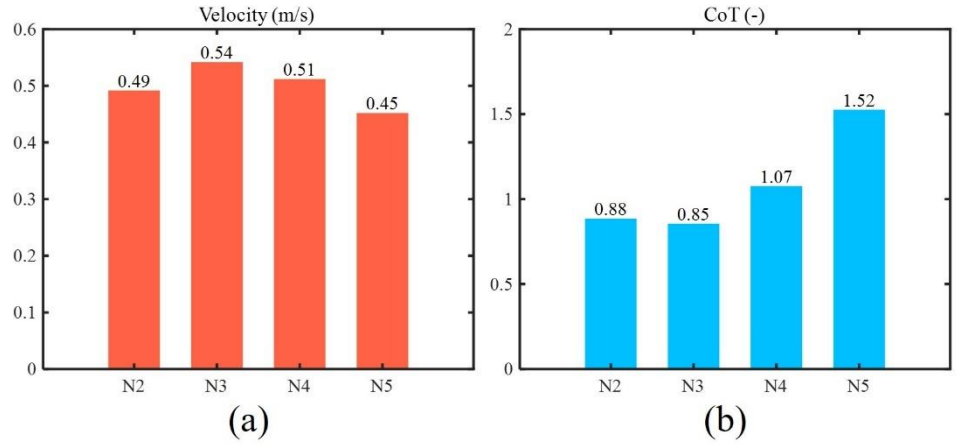


Fig. 3.14: Optimal performance of the robot with different tails: (a) Swimming speed. (b) CoT.

The swimming performances of four tails under their optimal control parameters are

demonstrated in Fig. 3.14. From the comparisons, the best performance in terms of the fastest speed and lowest CoT can be achieved by tail N3 ($\Delta = 0.46$). The swimming speed and CoT of tail N3 under its optimal control parameters are 0.54 m/s and 0.85, respectively.

Based on the above analysis, the following remarks can be drawn.

- a) The obtained dynamic model is effective and accurate in predicting the propulsive performance of the robot.
- b) At a small phase difference, tails with various active-joint ratio can all achieve optimal performance, however, when the phase difference is large, the swimming performance of the tail with a large active-joint ratio is worse than that of the tail with a small active-joint ratio.
- c) The maximum speed rises initially and then falls as the active-joint ratio increases, while the CoT at the maximum velocities tends to grow exponentially. And the robot can achieve greater performance through the optimized active-joint ratio of the tail.

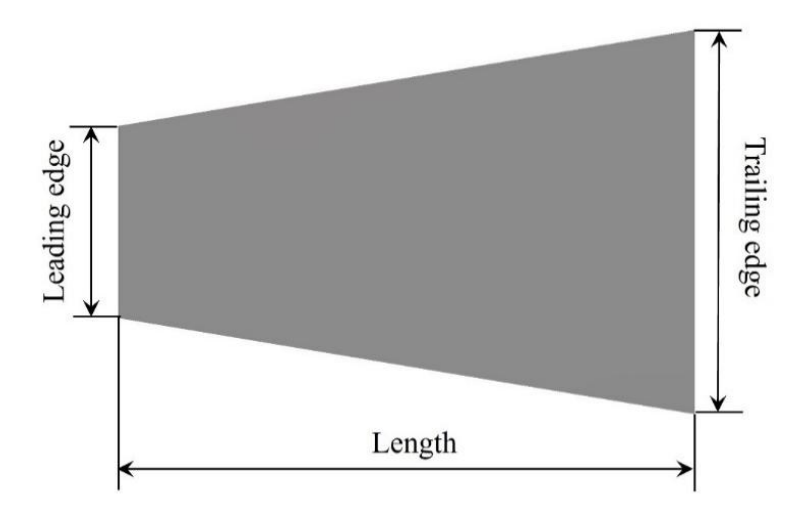


Fig. 3.15: Dimensional parameters of the flexible fin.

3.6 Impact of the Dimension-Related Stiffness Distribution of the Caudal Fin

In this subsection, the impact of the dimension-related stiffness distribution of the flexible fin with the same surface area is explored through simulations and experiments. The dimensions mainly include the span of the leading edge, the span of the trailing edge, and the length as shown in Fig. 3.15. The leading edge $L_1 \in \{40:10:80\}$ mm, the length $L \in \{100:20:260\}$ mm, and the trailing edge $L_2 = 2S/L - L_1$. S is a constant value of the surface area of the fin to make sure that the wet area for propulsion is same for all cases. The tail with three active joints was chosen for the simulations and experiments. Based on the above results, the robot with three active joints can achieve better performance at a phase difference of 30° and an amplitude in the range from 30° to 40°. To simplify the experiments, the control parameters were selected as $A = 35^{\circ}$, $f = \{1.0 \text{ Hz}, 1.5\text{Hz}, 2.0 \text{ Hz}\}$, $\xi = 30^{\circ}$.

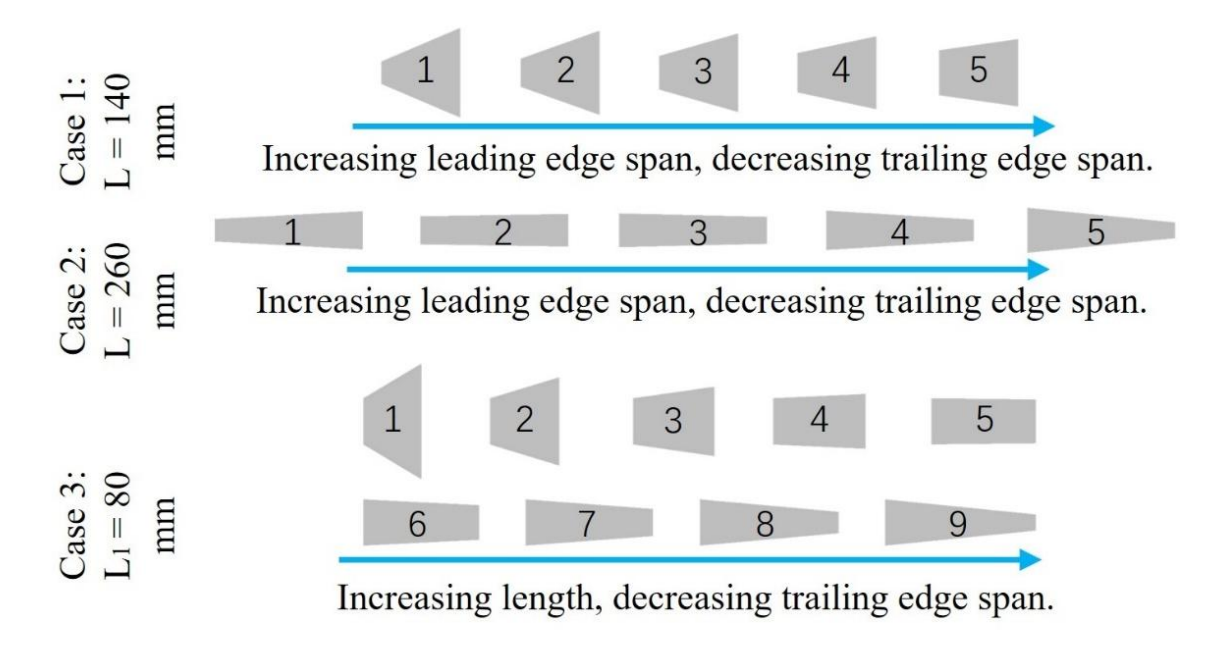


Fig. 3.16: Three cases of different dimensions of the flexible fin with the same surface area.

Three different cases are selected for discussion, as shown in Fig. 3.16. Case 1, case 2,

and case 3 explore the propulsive performance of a short fin with different leading and trailing edge spans, a long fin with different leading and trailing edge spans, and fins with the same leading-edge span but different lengths and trailing edge spans, respectively. The results are demonstrated in Fig. 3.17. The same trend can be observed for both short and long fins: both velocity and CoT rise with the increasing leading-edge span and the decreasing trailing edge span, while the CoT variance is very small. For fins with the same leading-edge span, when the length increases and the trailing edge span decreases, the velocity initially goes up and then gradually converges to a stable value at 1 Hz, with almost no change in velocity at 1.5 Hz and 2 Hz. However, the CoT for all frequencies drops significantly at first and then gradually converges to a stable value, starting from fin 6 in case 3, where the active-joint ratio is 0.46. Compared to the leading and trailing edge spans, the length has a much more significant impact on energy efficiency. The stiffness of a short fin with a wide trailing edge is higher, resulting in a large fluid drag force when the tail swings. However, the ratio between the thrust component and the overall drag force is small, leading to higher energy consumption. Increasing the length of the fin and decreasing the width of the trailing edge can result in a gradually reduced stiffness distribution from the leading edge to the trailing edge. Although the fluid drag force produced under the same control parameters is smaller, the thrust-to-drag ratio is larger due to increased bending. Consequently, it consumes less energy to maintain nearly the same speed level. This conclusion is consistent with the stiffness distribution observed in fish bodies, where the bending stiffness decreases along the anterior-posterior axis [52]. The findings can serve as guidelines for designing compliant caudal fins for multi-joint swimming robots.

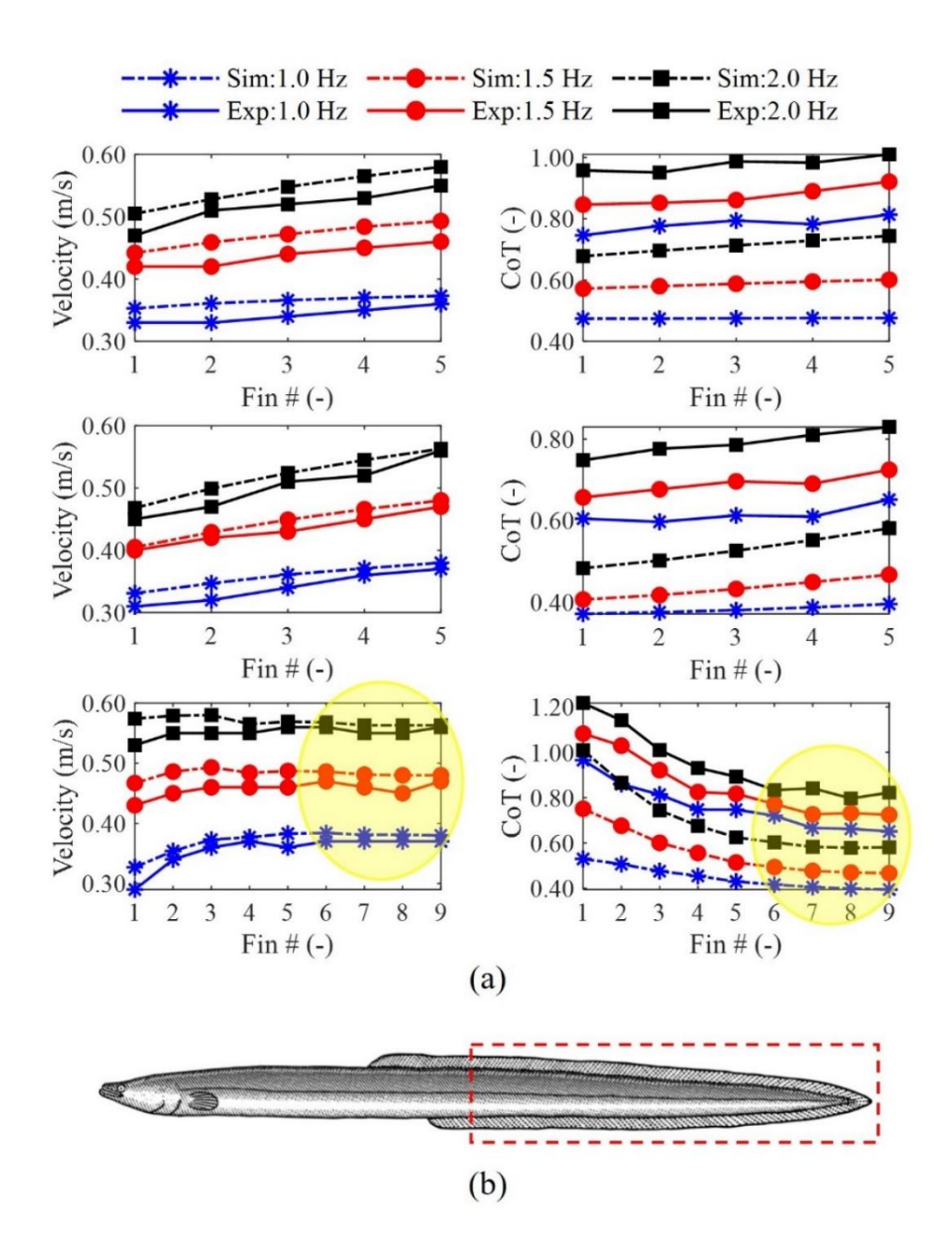


Fig. 3.17: (a) Performance results of the flexible fins with different dimensions from simulations and experiments: case 1 (Top), case 2 (Middle), case 3 (Bottom). (b) Body shape of an eel.

According to the above results, the following points can be drawn:

a) For fins with the same surface area and length, increasing leading edge span and decreasing the trailing edge span can improve the speed and slightly reduce energy efficiency. b) Increasing the length and narrowing the trailing edge of the fin can significantly reduce energy consumption while maintaining the same speed. It indicates that decreasing stiffness along the length can improve propulsion efficiency. Thus, a longer fin with a wide leading edge and a narrow trailing edge can achieve higher swimming speeds with low energy consumption, which conforms to the tail shape of slender-bodied fish in nature that swim with low tail beat frequencies, like eels, as shown in Fig. 3.17b.

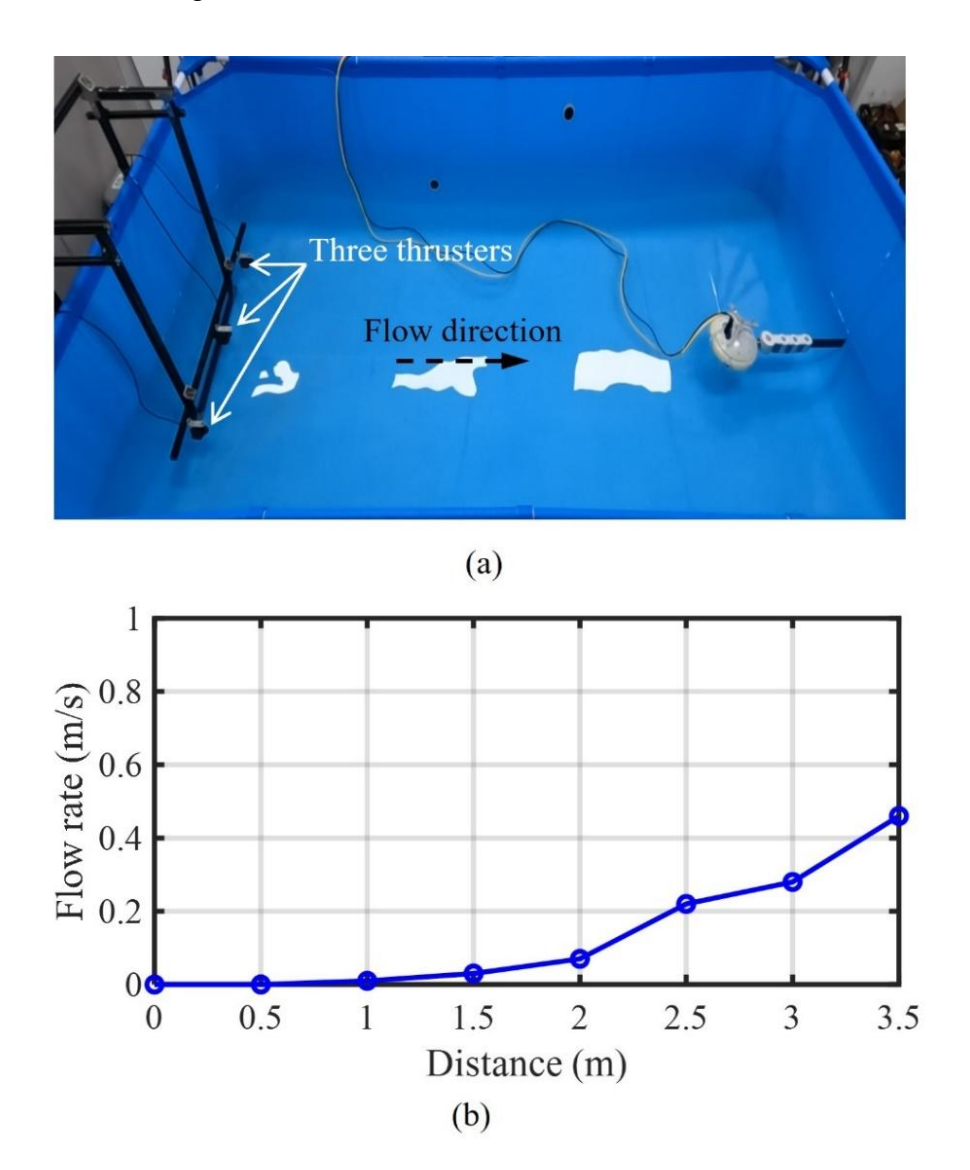


Fig. 3.18: (a) Experimental setup for testing the robot in water current. (b) Flow rates of water in the swimming pool when the thrusters are in operation.

3.7 Verification in Water Currents

In order to verify the applicability of the results in marine environments with disturbances, we built a setup to test the robot in water with currents.

Three thrusters T200 are fixed on a static structure at one side of the pool, just below the water surface, to create currents in the water as shown in Fig. 3.18(a). The waves in the ocean are very complex, and the flow direction can be arbitrary. However, if the robot is tested in water with currents from random directions, backflow and vortices will exist, and the flow might push the robot, making it difficult to compare and determine better configurations of the robot. Thus, here we just simulate the current opposite to the robot's swimming direction. To ensure uniform water flow disturbance opposite to the swimming direction of the robot, three thrusters are placed equidistantly on the opposite side of the pool. The thrusters are powered by an external power supply, with easily adjustable voltage and current. Fig. 3.18(b) demonstrates the flow rate with respect to the distance from the opposite side of the thrusters under around 40% power of the thrusters. To measure the flow rate at different positions in the pool, the entire pool is divided into seven equally spaced sections. A float with infrared reflective markers attached to its top is used to measure the flow rate in each section, which is tracked by motion tracking cameras. For instance, the distance from 0.33 m to 0.38 m from the side opposite the thrusters is considered one section, and the average flow rate of this section is used to represent the flow rate at the position of 0.35 m. The average speed of robot swimming from one side to another side and the corresponding CoT are compared.

Fig. 3.19(a) shows the results of four different tails under their optimal control parameters in water currents. Tail N3 achieves the fastest speed and the lowest value of CoT,

which are 0.38 m/s and 1.22, respectively. This indicates that despite being disturbed by the water flow, tail N3 remains the optimal tail configuration. Tail N5 performs the worst in both swimming speed and energy efficiency. Fig. 3.19(b) illustrates the performance of the robot with tail N3 and various fins, as in Case 3 of Fig. 3.16, under a tail beat frequency of 2 Hz. The results show that all velocities are around 0.4 m/s, while the value of CoT decreases firstly and then converges to around 1.16 from fin 6. Due to the drag force caused by the current that are not considered in the simulation, there are discrepancies between the experimental results with the above simulation results. But the testing results of the robot in water currents show the same trend with the above conclusions, demonstrating the findings' applicability in the real-world environments.

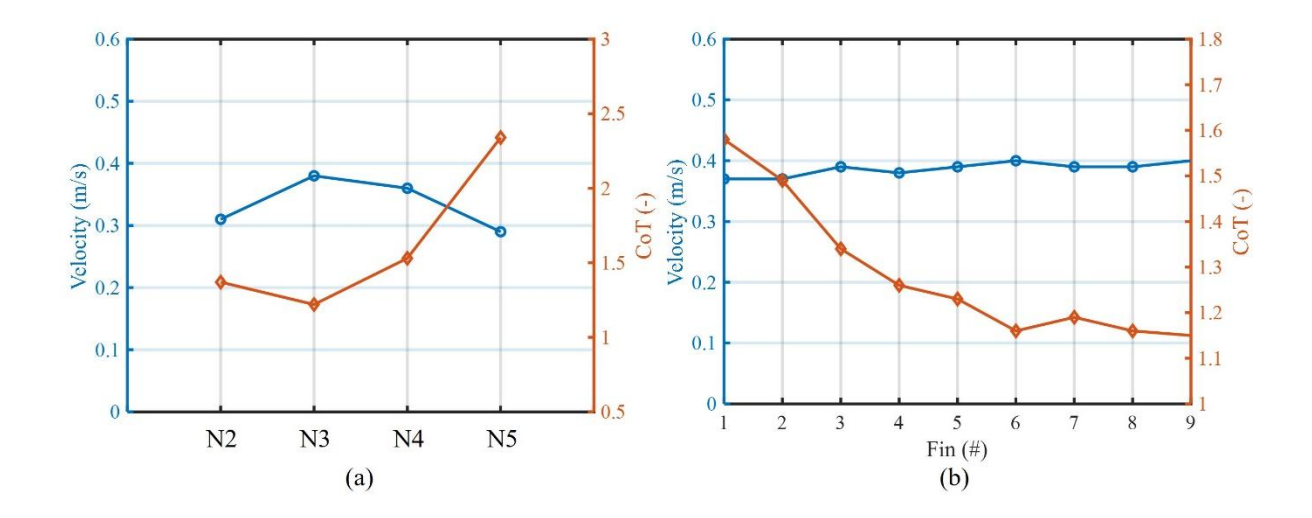


Fig. 3.19: Testing results of the robot in water currents. (a) Swimming performance of the robot with four different tails under the optimal control parameters in water currents. (b) Swimming performance of the robot with tail N3 and different fins in Case 3 of Fig. 3.16 (f = 2 Hz) in water currents.

3.8 Comparisons with Other Robots

Comparisons between the robotic tadpole and other robotic swimmers in the literature are summarized in Table 3.6. To ensure fair comparisons, the selected robots share similar features, such as long body length, the same propulsion method (BCF swimming mode), and

a driven frequency within 2 Hz. The eel-inspired soft robot [82] is composed of four pairs of pneumatic actuators that can produce undulatory movement. Its total length is 0.53 m. The snake-like robot [72] consists of five rigid joints actuated by servos. It has two dorsal fins, and its body length is 0.9 m. The multi-joint robotic fish [73] has five motor-actuated joints as well and the last joint connects with a caudal fin. The body length of multi-joint robotic fish is about 0.57 m.

Table 3.6: Comparison with other robotic fish

Platform	Max. velocity	СоТ
Eel-inspired soft robot [82]	0.19 (0.36 BL/s)	11
Snake-like robot [72]	0.30 (0.33 BL/s)	1.5
Multi-joint robotic fish [73]	0.43 (0.75 BL/s)	-
Robotic tadpole (Tail N3, Fin 9)	0.56 (0.75 BL/s)	0.82

The eel-inspired soft robot [82] can effectively replicate the continuous body motion of real fish. However, its maximum speed is only 0.19 m/s (0.36 BL/s), and its cost of transport (CoT) is significantly higher, reaching up to 11. There remains a substantial gap for soft robots to achieve efficient swimming. The snake-like robot [72] relies on two dorsal fins to boost its swimming efficiency, achieving a maximum speed of 0.30 m/s (0.33 BL) and a CoT of about 1.5. Dorsal fins primarily serve as boosters for propulsion, with the thrust mainly produced by the tail and caudal fin, resulting in limited performance improvement for the snake-like robot. The performance of multi-joint robotic fish [73] is enhanced through kinematic optimization, reaching a speed of up to 0.43 m/s (0.75 BL/s). Kinematics significantly impact the swimming performance of robotic fish as they determine the

locomotion mode. However, relying solely on the motion control of active joints offers limited improvements in energy efficiency. Comparative analysis indicates that our robot, when using tail N3 and fin 9, achieves the fastest swimming speed of 0.56 m/s (0.75 BL/s) with a corresponding CoT value of 0.82, which is much lower than that of other robots. Although the multi-joint robotic fish achieves the same speed when expressed in body lengths per second, the robotic tadpole's ellipsoid head results in a much larger drag force. If the head were designed to be streamlined like that of real fish, the robotic tadpole could swim much faster and more energy-efficiently than the other listed robots. The comparison further confirms that the combination of a multi-link mechanism and a flexible fin with a longer length, wide leading edge, and narrow trailing edge can effectively improve swimming efficiency.

3.9 Concluding Remarks

In this chapter, the swimming performance of a robotic tadpole with different tail configurations was explored. First, a dynamic model was established and validated through simulation and experiments. A critical assessment indicator, i.e., active-joint ratio, is proposed and thus the impact of control parameters on the performance of the tail with different active-joint ratios was thoroughly investigated based on the well-developed dynamic model with extensive experiments. Noticeably, the optimal control parameters of all tails can be obtained through the deliberately defined optimization function, and the optimal performance of each tail was compared. Importantly, the geometry-related stiffness distribution of the flexible fin was also studied in this study. Several remarkable conclusions can be drawn as follows.

The hydrodynamic parameters identified by the proposed method based on simulations and experimental data of the fin tip's displacement and the thrust force generated by the tail

are very reliable for the developed dynamic model to predict the propulsive performance of a tail consisting of a multi-joint mechanism and a flexible fin, which can greatly facilitate the structure and control parameters optimization. In consideration of most of the existing work concerning on either the wholly rigid-linkage tail or the fully flexible tail, it should be noted that no literature results are available for establishing or providing a comprehensive model for such a rigid-linkage-with-flexible-fin system of any linkage number and fin materials/shapes.

Although tails with different active-joint ratios can all be optimized to achieve their best performance at a small phase difference subject to the same tail length, it is noted that, for a large phase difference, the tail with a large active-joint ratio will perform worse than a small active-joint ratio both in velocity and CoT. This gives an important guideline for structural parameter design in practice.

As the active-joint ratio increases, the achievable maximum speed rises first and then decreases, however, the CoT at the maximum velocities tends to keep increasing exponentially. It is noted that, the tail with a ratio of active joints of 0.46 in this study performs much better than all other tails in terms of swimming velocity and energy efficiency --- implying the existence of the best parameter setting for a given length of tails, which is useful for the design of flexible fins of such kind of bio-inspired robots.

With the same surface area and length of the flexible fin, both velocity and CoT rise with the increasing leading-edge span and decreasing trailing edge span; but noteworthily, the variance of the CoT is very small. This implies that a larger leading-edge span with a decreasing trailing edge span is better to improve velocity with basically the same energy cost, another important point to be claimed with this study.

Compared to the leading and the trailing edge span, the length has a greater impact on energy efficiency. With the same surface area and leading edge, a longer fin can achieve smaller energy consumption while maintaining almost the same velocity. For the case of three active joints, the value of CoT tends to a smaller value with the increase of fin length, which covers the case of ratio of active joints $\Delta = 0.46$ for a fixed entire tail length and thus also agrees with the conclusion in (3). Also note that, the shape of the fin that exhibits good propulsive performance matches the known knowledge about the tail shape of eels in nature.

Note that, only the forward swimming performance of the robotic tadpole was studied in this work. In future work, the turning performance will be explored. And the dynamic model will be extended to the three dimensions by including the angle of the rotational joint. The three-dimensional swimming performance of the robot will be further investigated both in simulation and experiment. Apart from tail optimization, the head shape and the fins at different positions also have a crucial influence on swimming performance, which deserves investigation in the future. In addition, as the tadpole grows, it relies on different ways of swimming, which could be a potential direction for future research to develop a multi-modal swimming robot or an amphibious robot through combining legs and tails.

Chapter 4

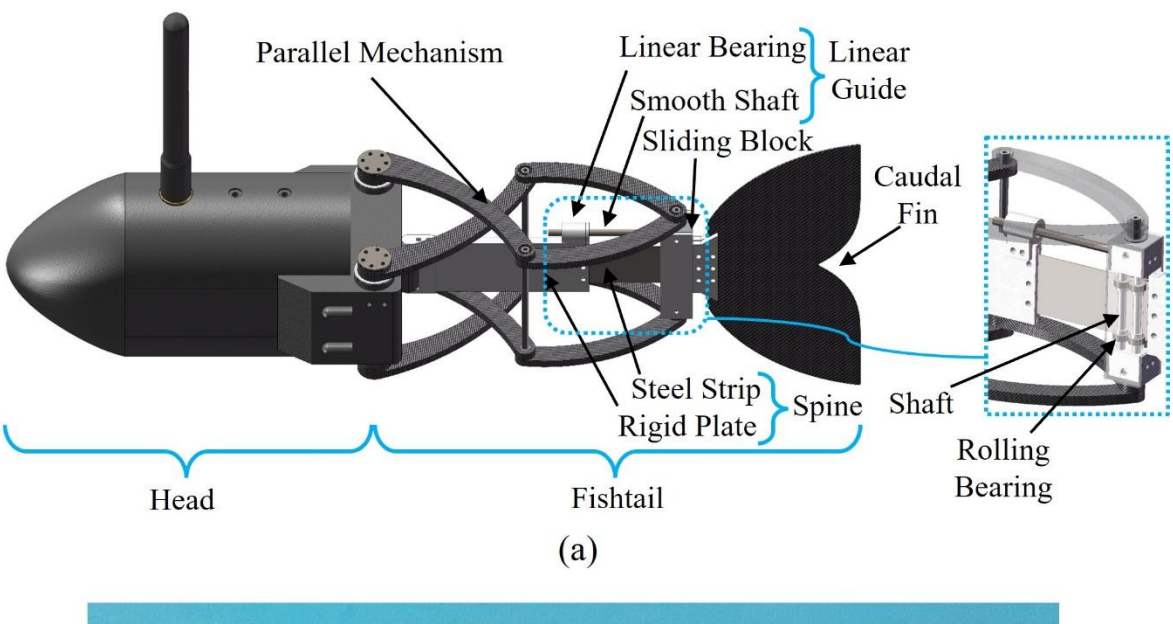
A Robotic Fish with Online Stiffness Modulation

The passive compliance of fish body is one crucial property determining the skillful swimming of fish [62, 130]. Fish body is a complex mechanism consisting of muscle, spine, skin, and so on [131-133]. Their intricate muscular systems are capable of behaving like a spring [134]. Fish take advantage of such a trait of flexibility to enhance propulsion force and lower drag as a result of produced phase offset and reorienting forces [135-137]. More importantly, based on numerous biological studies, fish can make use of muscle to modulate stiffness of tail to adapt to the actuation inputs like tail beat frequency, thus leading to maintaining efficient swimming under various cruising velocity [138]. For instance, sunfish enhance their tails' flexural rigidity through muscle activity to counteract more hydrodynamic loads when swimming fast [58]. Inspired from this point, some variable stiffness mechanisms have been proposed and adopted on the construction of robotic fish. However, the existed stiffness modulation mechanisms have one common feature that extra actuators or power sources need to be applied just for tuning stiffness, which brings about more energy consumption and complicated structures. The complexity of mechanisms further causes drawbacks in the difficulty of waterproofing, reduced durability, and increased burden on the robotic fish. According to [64], high-frequency platform could benefit more from tuning stiffness. Greater burden leads to a low tail beat frequency in most servo-actuated robots, i.e., around 1 or 2 Hz [65, 66]. Although those DC actuated robotic fish can exhibit high frequency oscillation, the maneuverability is poor. Thereout, we raise the question of whether we can achieve tunable stiffness for swimming robots without introducing extra actuators or other types of power sources. Hence, this study aims to address this question by proposing a fish-like robot featuring all servos contributing to tail swing, as well as regulating stiffness with no more energy consumption.

The main contributions of this work are summarized as follows. Firstly, we take advantage of a parallel mechanism, a rigid link, an elastic steel strip, and a slider mechanism to build the tail body of a robotic fish, which can realize tuning stiffness by end point trajectory control of the parallel mechanism without any extra actuator. Then, the dynamic model of the robot is derived by the Lagrangian dynamics for the robot's performance prediction. Thirdly, extensive experiments are conducted to validate the theory model and investigate the effectiveness of the proposed mechanism and method on the performance enhancement in terms of swimming speed, energy efficiency, and maneuverability. Finally, the stiffness regulating rule is explored to optimize the performance based on the balanced trade-off between swimming velocity and power consumption. The results articulated within this article offer a novel and alternative perspective on the design of stiffness modulation mechanisms for swimming robots.

The rest of this article is organized as follows. Section 4.1 describes the design of the robotic fish with the stiffness tuning mechanism including mechanical and electronical components, and the stiffness modulation principle is explained. In Section 4.2, the kinematic analysis and dynamic modeling of the robot are presented. Section 4.3 demonstrates the identification of hydrodynamic parameters for the derived dynamic model, and comparisons between simulations and experiments are conducted to verify reliability. Section 4.4 illustrates simulation and experimental results of the performance investigation including swimming speed, energy efficiency, and turning performance, and the stiffness regulation rule

is formulated. In Section 4.5, comparisons between the proposed method and the methods from the literature are discussed. Section 4.6 concludes this chapter.



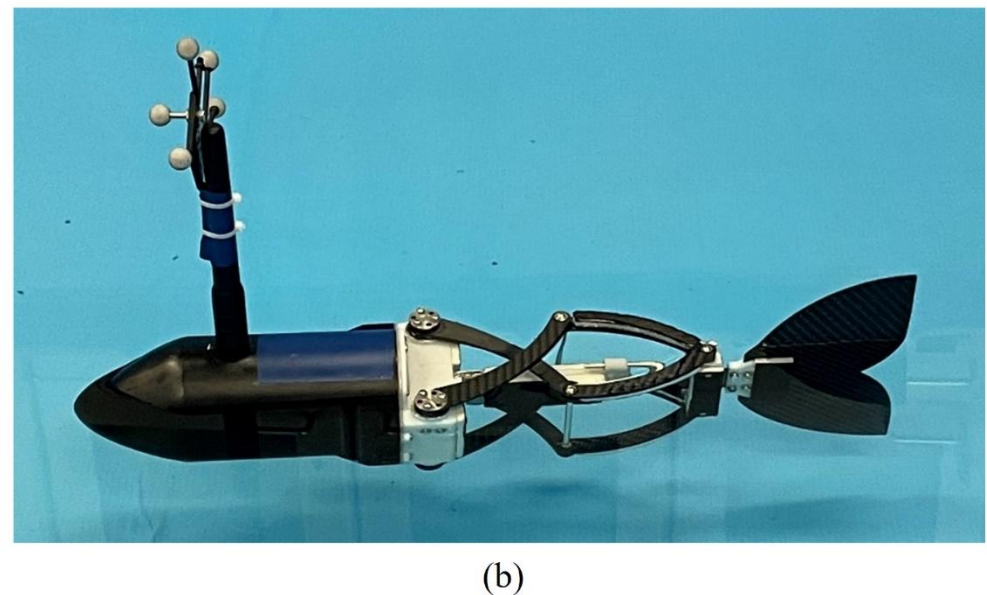


Fig. 4.1: Design of the robotic fish with stiffness tuning mechanism. (a) Mechanical structures. (b) Experimental prototype.

4.1 Hardware Implementation

4.1.1 Mechanical design

The design of the robotic fish is illustrated in Fig. 4.1. It comprises a rigid head, an

actively controlled tail, and a rigid caudal fin. The head is water-resistant to house all electronic components securely. The tail features a parallel mechanism and a spine, which consists of a rigid plate and a flexible steel strip, functioning as a leaf spring. One side of the rigid plate is connected to the head via a pivot joint, while the other side is fixed with the leaf spring with screws. The caudal fin is attached to the end of the leaf spring. The parallel mechanism is connected to the head by two active joints at one end, and to a slider mechanism at the other. This slider mechanism moves along the surface of the leaf spring using eight rolling bearings. A linear bearing fixed on the rigid plate and a smooth shaft serve as a linear motion guide. The overall dimensions of the robot are 500 mm in length, 106 mm in width, and 120 mm in height, with a total weight of 1.8 kg.

4.1.2 Electronic components

The electronic components are demonstrated in Fig. 4.2. The microcontroller inside the head is a Raspberry Pi 4B, which is responsible for controlling the motors and acquiring data from the sensors. The active rotational joints are actuated by two servos, each providing a normal torque of 2.5 N·m. Communication between the microcontroller and the two motors is facilitated by a TTL/USB converter. Two ACS712 sensors are employed to measure the current of the motors, with the data being read by an Arduino nano. Power is supplied by two rechargeable batteries, providing 5 V for the controller and 12 V for the motors. Wireless communication between the Raspberry Pi and a computer for remote control is established via a 2.4 GHz transmitter and receiver.

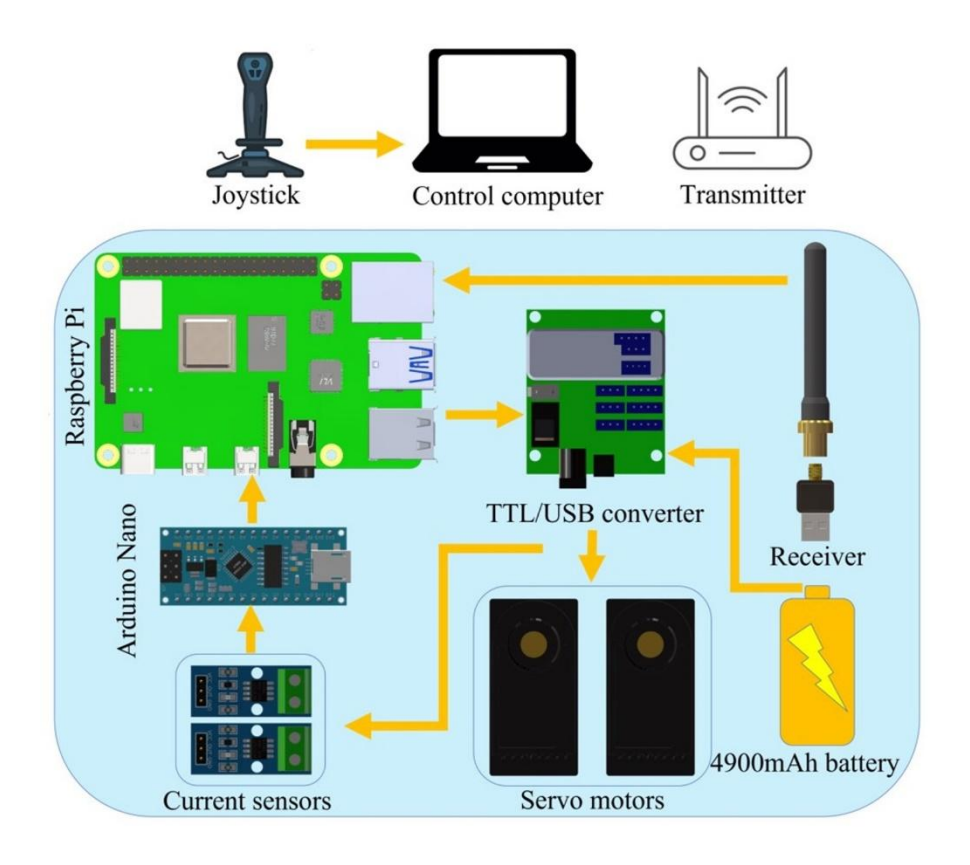


Fig. 4.2: Remote control system and electronic components.

4.1.3 Stiffness regulation principle

Fig. 4.3 Illustrates the realization of stiffness modulation. The slider block divides the leaf spring into two segments with distinct constraints: a fully constrained section, which acts as a rigid plate, and a free section, which functions as a cantilever beam. The flexural stiffness varies with the length of the free section, allowing stiffness modulation by adjusting the length of the cantilever beam portion of the leaf spring. This length adjustment is achieved by controlling the swing motion of the tail according to a predefined endpoint trajectory of the parallel mechanism. The trajectory follows a circular arc, with control parameters including the angle θ_1 and the radius d_0 . By varying the radius d_0 , the length of the free section of the leaf spring changes, resulting in different stiffness levels. The adjustable range for the cantilever beam portion of the leaf spring is from 5 mm to 45 mm.

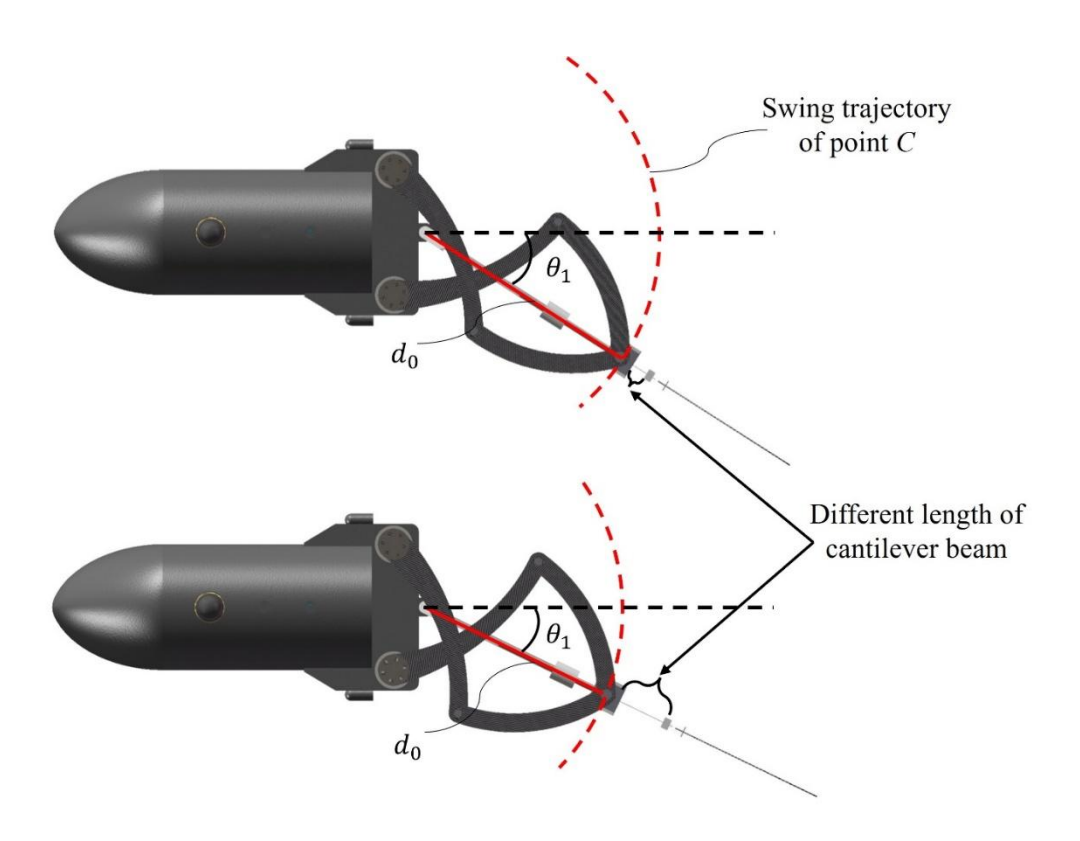


Fig. 4.3: Illustration of the stiffness modulation principle.

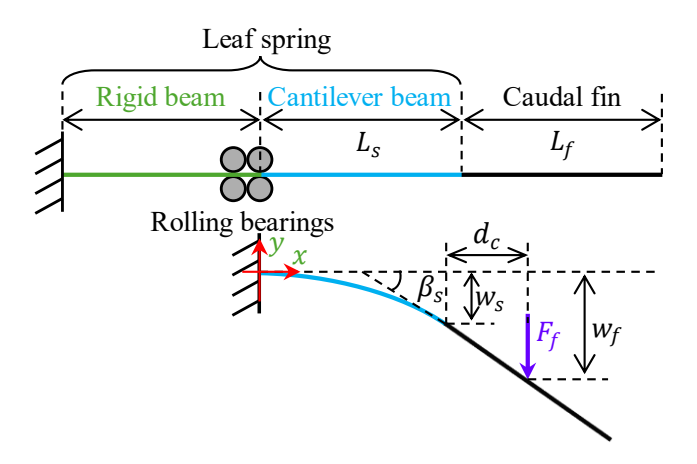


Fig. 4.4: Schematic diagram of the bending leaf spring under the force applied on the caudal fin.

To quantify the variable stiffness of the fishtail, we assumed to apply a force in vertical direction on the mass center of the caudal fin as shown in Fig. 4.4. According to the cantilever beam model, the moment M(x) along the length of the beam can be expressed as follows.

$$M(x) = E_s I_s w''(x) \tag{4.1}$$

When the free end of the cantilever beam is subjected to both concentrated force and moment, the deflection w(x) and the rotational angle $\beta(x)$ can be derived as

$$w(x) = \iint \frac{M(x)}{E_s I_s} dx = \frac{Mx^2}{2E_s I_s} + \frac{Fx^2}{6E_s I_s} (3L_s - x)$$
 (4.2)

$$\beta(x) = \int \frac{M(x)}{E_s I_s} dx = \frac{Mx}{E_s I_s} + \frac{Fx}{3E_s I_s} (3L_s - x) - \frac{Fx^2}{6E_s I_s}$$
(4.3)

Then, the deflection w_s and the rotational angle β_s at the free end of the cantilever beam can be calculated as follows.

$$w_{s} = \frac{F_{f}L_{s}^{3}}{3E_{s}I_{s}} + \frac{F_{f}d_{c}L_{s}^{2}}{2E_{s}I_{s}}$$
(4.4)

$$\beta_s = \frac{F_f L_s^2}{2E_s I_s} + \frac{F_f d_c L_s}{E_s I_s} \tag{4.5}$$

Thus, the stiffness of the fishtail can be estimated by the following equation.

$$K_T = \frac{F_f}{w_f} = \frac{F_f}{w_s + d_c \tan \beta_s} = \frac{3E_s I_s}{L_s^3 + 3d_c L_s^2 + 3d_c^2 L_s}$$
(4.6)

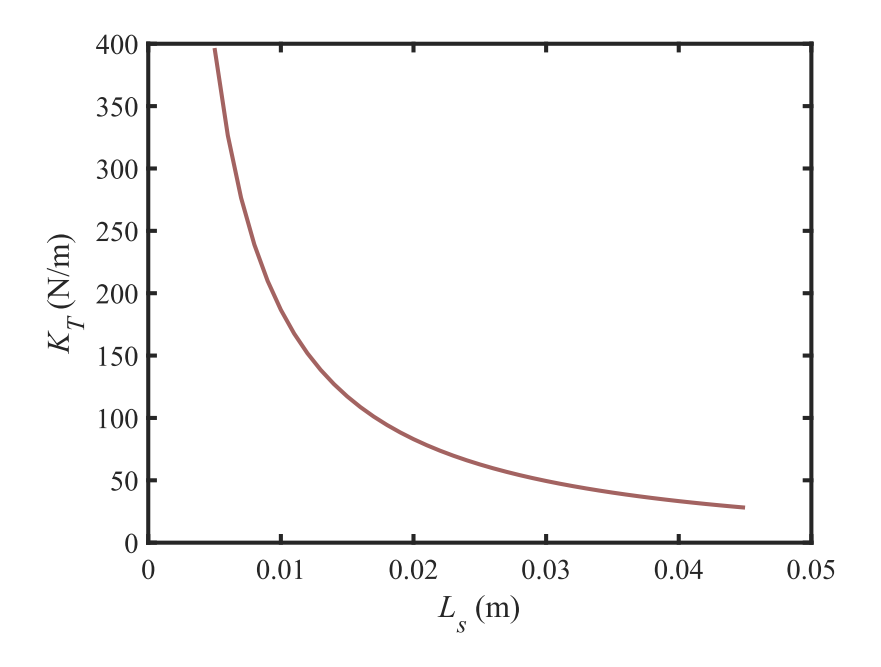


Fig. 4.5: Stiffness of the fishtail under different values of L_s .

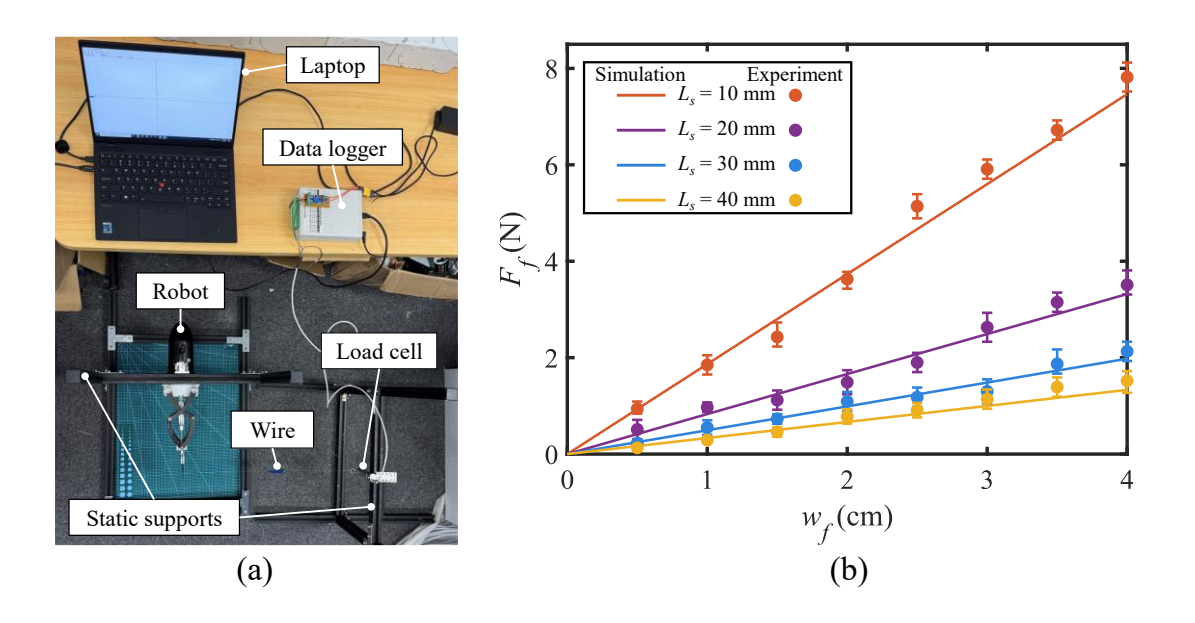


Fig. 4.6: Validation of stiffness model. (a) Experimental setup for measuring the stiffness of the fishtail. (b) Force comparisons between simulations and experiments under different values of L_s .

The simulated stiffness results are depicted in Fig. 4.5, showing an adjustable stiffness range from 28.1 N/m at $L_s=45$ mm to 396.6 N/m at $L_s=5$ mm. To verify the derived model of the tail's stiffness, an experimental setup was constructed to measure the static force exerted by the tail, as shown in Fig. 4.6(a). Two static supports were used to secure the robot and the load cell (Omegadyne LC601-5), respectively. The tail was connected to the load cell via a wire. The load cell, with a measurement range of approximately 20 N, was employed to capture the force data. A data logger, interfaced with a laptop, was utilized to record force measurements. Fig. 4.6(b) presents the measured results alongside a comparison with the simulation results, demonstrating a good agreement between the simulation and experimental outcomes across different values of L_s .

4.2 Mathematical Modeling

4.2.1 Coordinate system and notations

To estimate the swimming performance of the robot, the dynamic model is essential to

be derived. To facilitate the analysis, the coordinate frames and some relevant parameters are defined as shown in Fig. 4.7. $O_w - x_w y_w z_w$ is the inertia coordinate frame. $O_i - x_i y_i z_i$, L_i , and C_i (i = 0,1,2) denote the body-fixed coordinate frame, length, and mass center of ith link, respectively. θ_i (i = 0,1,2) is the angle between the ith link and its previous link. $^w P_0$ is the position vector of the origin O_0 with respect to the inertia frame. $O_p x_p y_p$ denotes the body-fixed coordinate frame on the center of $A_1 B_1$. d_1 represents the distance of $A_1 A_2$ and $B_1 B_2$. d_2 is the distance of $A_2 C$ and $B_2 C$. d_3 and d_4 are the distance of $A_1 C$ and $B_1 C$, respectively. δ denotes the distance between the origin of $O_p x_p y_p$ and the pivot joint of the spine.

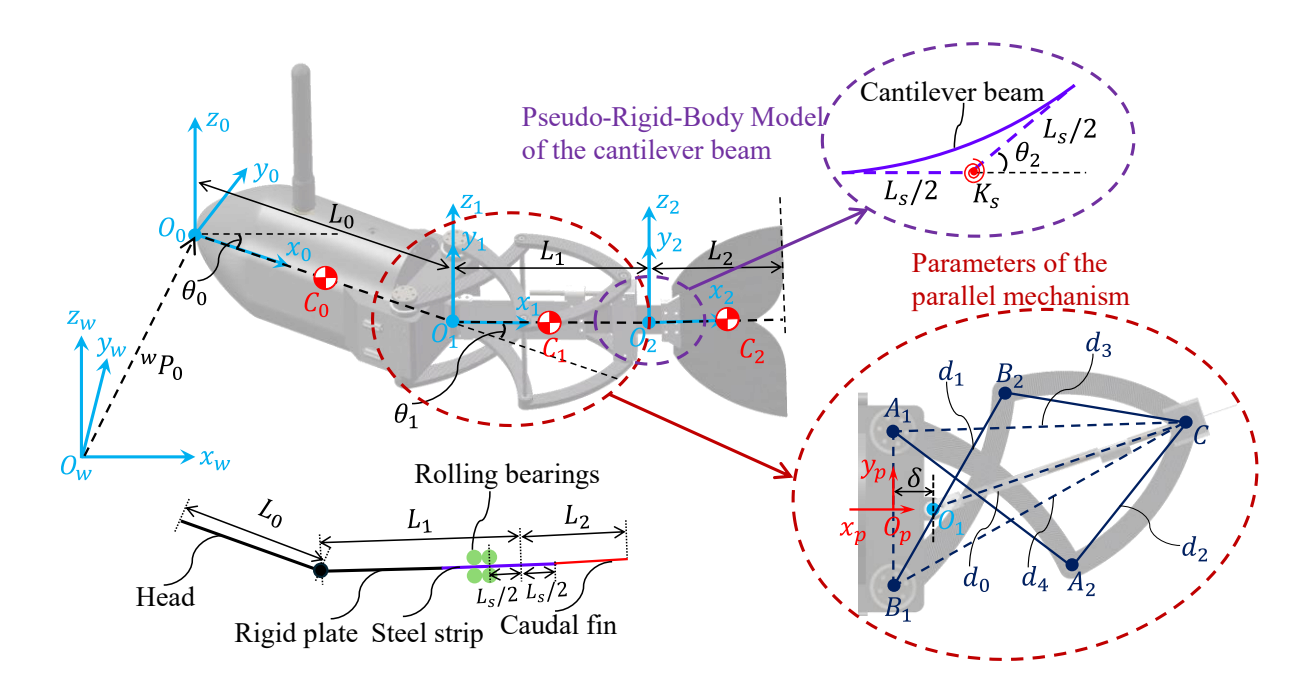


Fig. 4.7: Schematic illustration of coordinate frames and notations.

Additionally, some parameters and symbols are defined for the convenience of deriving the model in the subsequent section, which are not shown in Fig. 4.7. $\psi_i(i=0,1,2)$ is the angle between the *i*th link and the axis $O_w x_w$. And it can be computed by

$$\psi_j = \sum_{i=0}^j \theta_i \,, (i = 0, 1, ..., j) \tag{4.7}$$

 $\{\phi_1,\phi_2,\phi_3,\phi_4,\phi_5,\phi_6\}$ are the angles between O_px_p and $\{A_1A_2,B_1B_2,A_2C,B_2C,A_1C,B_1C\}$, respectively.

4.2.2 Kinematic analysis

The motion of the tail is controlled by the predefined trajectory of the end point of parallel mechanism. Thus, the inverse kinematics of the parallel mechanism is applied to derive the control laws of two servo motors. The parameters of the structure are defined as shown in Fig. 4.7 (red circle). The trajectory is derived by

$$\begin{cases} {}^{p}x_{C} = \delta + d_{0}\cos\theta_{1} \\ {}^{p}y_{C} = d_{0}\sin\theta_{1} \end{cases}$$

$$(4.8)$$

The rhythmic oscillation of the tail can be controlled by the following equation of θ_1 .

$$\theta_1 = A\sin 2\pi f t + B \tag{4.9}$$

where A, f, and B are amplitude, frequency, and bias angle, respectively.

The vector loop-closure equations of the parallel mechanism can be obtained as

$$\begin{cases}
d_3 e^{i\phi_5} = d_1 e^{i\phi_1} + d_2 e^{i\phi_3} \\
d_4 e^{i\phi_6} = d_1 e^{i\phi_2} + d_2 e^{i\phi_4}
\end{cases}$$
(4.10)

where d_3 , d_4 , ϕ_5 , and ϕ_6 can be calculated by

$$\begin{cases} d_{3} = \sqrt{(px_{C} - px_{A1})^{2} + (py_{C} - py_{A1})^{2}} \\ d_{4} = \sqrt{(px_{C} - px_{B1})^{2} + (py_{C} - py_{B1})^{2}} \\ \phi_{5} = \arctan \frac{py_{C} - py_{A1}}{px_{C} - px_{A1}} \\ \phi_{6} = \arctan \frac{py_{C} - py_{B1}}{px_{C} - px_{B1}} \end{cases}$$
(4.11)

The above equations can be simplified and then we can obtain the following equations.

$$\begin{cases}
2d_1 d_3 \cos(\phi_1 - \phi_5) + d_2^2 - d_1^2 - d_3^2 = 0 \\
2d_1 d_4 \cos(\phi_2 - \phi_6) + d_2^2 - d_1^2 - d_4^2 = 0
\end{cases}$$
(4.12)

The control laws of two motors can be obtained as

$$\begin{cases} \phi_{1} = - \left\| \arccos\left(\frac{d_{3}^{2} + d_{1}^{2} - d_{2}^{2}}{2d_{1}d_{3}}\right) \right\| + \phi_{5} \\ \phi_{2} = \left\| \arccos\left(\frac{d_{4}^{2} + d_{1}^{2} - d_{2}^{2}}{2d_{1}d_{4}}\right) \right\| + \phi_{6} \end{cases}$$

$$s.t. \begin{cases} \phi_{1} \geq -86^{\circ} \\ \phi_{2} \leq 86^{\circ} \\ d_{3} < d_{1} + d_{2} \\ d_{4} < d_{1} + d_{2} \end{cases}$$

$$\phi_{1} \text{ Non-reachable Space}$$

$$\phi_{2} \text{ 80}$$

$$\phi_{2} \text{ 80}$$

$$\phi_{3} \text{ 60}$$

$$\phi_{4} \text{ 60}$$

$$\phi_{2} \text{ 60}$$

$$\phi_{3} \text{ 60}$$

$$\phi_{4} \text{ 60}$$

$$\phi_{3} \text{ 60}$$

$$\phi_{4} \text{ 60}$$

$$\phi_{3} \text{ 60}$$

$$\phi_{4} \text{ 60}$$

$$\phi_{5} \text{ 60}$$

$$\phi_{6} \text{ 60}$$

$$\phi_{7} \text{ 60}$$

$$\phi_{8} \text{ 60}$$

Fig. 4.8: Reachable space of control angles of two servos under different values of θ_1 and L_s .

Based on the inverse kinematics, the reachable space of control parameters can be calculated as shown in Fig. 4.8, which determines the selection of control parameters for simulation and experiment.

The Pseudo-Rigid-Body Model (PRBM) [139] is used to simplify the modeling of the cantilever beam part of the spring steel as shown in Fig. 4.7 (purple circle). The cantilever part is separated into two rigid segments with equal length $L_s/2$, and two segments are

connected with each other by a torsional spring. Thus, L_1 and L_2 can be obtained as

$$L_1 = d_0 + \frac{d_R}{2} + \frac{L_S}{2} \tag{4.14}$$

$$L_2 = \frac{L_s}{2} + L_f \tag{4.15}$$

where d_R is the distance between the centers of two rolling bearings at one side, and L_f is the length of the caudal fin. The stiffness of the torsional spring can be calculated by

$$K_{s} = \frac{E_{s}I_{s}}{L_{s}} \tag{4.16}$$

where E_s is the Young's modulus, and I_s is the area moment of inertia that can be expressed as $I_s = w_s t_s^3 / 12$. w_s and t_s are the width and thickness of the spring steel respectively.

The position vector ${}^{w}P_{Ci}$ of each link's mass center C_{i} in the inertial frame can be calculated by

$$\binom{{}^{w}P_{Ci}}{1}_{4\times 1} = \binom{{}^{w}R_i & {}^{w}P_i}{0_{1\times 3} & 1}\binom{C_i}{1} \tag{4.17}$$

where ${}^{w}R_{i}$ and ${}^{w}P_{i}$ denote the rotation matrix and translation vector of the local frames' origin O_{i} with respect to the inertial frame respectively, and are expressed as

$${}^{w}R_{i} = \begin{pmatrix} \cos\psi_{i} & -\sin\psi_{i} & 0\\ \sin\psi_{i} & \cos\psi_{i} & 0\\ 0 & 0 & 1 \end{pmatrix}$$
(4.18)

$${}^{w}P_{i} = {}^{w}P_{0} + \sum_{j=1}^{i} {}^{w}R_{j-1}{}^{j-1}P_{j}$$

$$(4.19)$$

where $^{j-1}P_j$ is the translation vector of the current frame's origin O_j with respect to the previous frame's origin O_{j-1} , and can be expressed as

$$^{j-1}P_{j} = (L_{j-1} \quad 0 \quad 0)^{T}$$
 (4.20)

The linear velocity, linear acceleration, angular velocity, and angular acceleration of the mass center of *i*th rigid link in the inertial coordinate system can be obtained as

$${}^{w}v_{i} = {}^{w}\dot{P}_{Ci} = {}^{w}\dot{R}_{i}C_{i} + {}^{w}\dot{P}_{i}$$
 (4.21)

$$^{w}a_{i} = {}^{w}\ddot{P}_{Ci} = {}^{w}\ddot{R}_{i}C_{i} + {}^{w}\ddot{P}_{i}$$
 (4.22)

$$^{w}\omega_{i} = (0 \quad 0 \quad \dot{\psi}_{i})^{T} \tag{4.23}$$

$${}^{w}\dot{\omega}_{i} = (0 \quad 0 \quad \ddot{\psi}_{i})^{T} \tag{4.24}$$

4.2.3 Dynamic modeling

The Lagrangian function $\mathcal{L}(q, \dot{q}, t)$ can be expressed as

$$\mathcal{L}(q, \dot{q}, t) = T(q, \dot{q}, t) - V(q, \dot{q}, t) \tag{4.25}$$

where q is the generalized coordinates and is expressed as $q = \{q_1 = {}^w x_0, q_2 = {}^w y_0, q_3 = \psi_0, q_4 = \theta_2\}$. $T(q, \dot{q}, t)$ and $V(q, \dot{q}, t)$ are the kinetic energy and potential energy correspondingly, which can be obtained by

$$T(q, \dot{q}, t) = \sum_{i=0}^{2} \frac{1}{2} {}^{w} v_{i}^{T} M_{i}{}^{w} v_{i} + \sum_{i=0}^{2} \frac{1}{2} {}^{w} \omega_{i}^{T} I_{i}{}^{w} \omega_{i}$$
 (4.26)

$$V(q, \dot{q}, t) = \frac{1}{2} K_s \theta_2^2$$
 (4.27)

where M_i and I_i are the mass matrix and inertia matrix.

Then the Lagrange-Euler equation can be derived by

$$\frac{d}{dt}\frac{\partial \mathcal{L}}{\partial \dot{q}} - \frac{\partial \mathcal{L}}{\partial q} = Q \tag{4.28}$$

where $Q = \{F_X, F_Y, T_0, T_s\}$ is the generalized forces and moments. The generalized forces and moments can be derived by the following equations.

$$\begin{pmatrix} F_X \\ F_Y \\ 0 \end{pmatrix} = \sum_{i=0}^2 {}^{w}F_{a,i} + \sum_{i=0}^2 {}^{w}F_{d,i}$$
(4.29)

$$\begin{pmatrix} T_0 \\ T_s \end{pmatrix} = \begin{pmatrix} \sum_{i=0}^{2} M_{a0,i} + \sum_{i=0}^{2} M_{d0,i} \\ \sum_{i=0}^{2} M_{as,i} + \sum_{i=0}^{2} M_{ds,i} \end{pmatrix} = \begin{pmatrix} \sum_{i=0}^{2} ({}^{w}P_{Ci} - {}^{w}P_{0}) \times ({}^{w}F_{a,i} + {}^{w}F_{d,i}) \\ ({}^{w}P_{C2} - {}^{w}P_{2}) \times ({}^{w}F_{a,2} + {}^{w}F_{d,2}) \end{pmatrix}$$
(4.30)

where ${}^wF_{a,i}$ and ${}^wF_{d,i}$ are the added mass force and drag force from the surrounding fluid on the *i*th link. $M_{a0,i}$ and $M_{d0,i}$ are the moments generated by the fluid forces on the head joint. $M_{as,i}$, and $M_{ds,i}$ are the moments generated by the fluid forces on the spring steel joint. ${}^wF_{a,i}$ ${}^wF_{d,i}$ can be expressed as the following equations.

$${}^{w}F_{a,i} = \begin{pmatrix} {}^{w}F_{ax,i} \\ {}^{w}F_{ay,i} \\ 0 \end{pmatrix} = \begin{pmatrix} -m_{ai}{}^{w}a_{ix} \\ -m_{ai}{}^{w}a_{iy} \\ 0 \end{pmatrix}$$
 (4.31)

$${}^{i}F_{d,i} = \begin{pmatrix} {}^{i}F_{dx,i} \\ {}^{i}F_{dy,i} \\ 0 \end{pmatrix} = \begin{pmatrix} -\frac{1}{2}\rho C_{fi}S_{ix}{}^{i}v_{ix} \| {}^{i}v_{ix} \| \\ -\frac{1}{2}\rho C_{di}S_{iy}{}^{i}v_{iy} \| {}^{i}v_{iy} \| \\ 0 \end{pmatrix}$$
(4.32)

$${}^{w}F_{d,i} = {}^{w}R_{i}{}^{i}F_{d,i} \tag{4.33}$$

4.3 Hydrodynamic Parameters Identification

To obtain reliable simulation results for the performance analysis, some parameters involved in the derived dynamic model need to be provided. The physical parameters related

to the mass, length of link, etc. can be directly obtained or calculated as shown in Table 4.1. But the parameters related to hydrodynamics such as drag coefficients, friction coefficients and so on are difficult to acquire. In this article, we conducted experimental trials first and collected the results. These experimental results were then compared to those computed by the dynamic model using presupposed hydrodynamic parameters. The parameters that yielded the minimum error were determined to be the identified values. Thus, the process is to solve the following equation.

$$c_{pp} = \arg\min_{c_p} \frac{1}{\chi} \sum_{\chi} \sqrt{\frac{1}{N} \sum_{i=1}^{N} (v_e(i) - v_s(i))^2}$$
 (4.34)

where c_p and c_{pp} present the presupposed and identified hydrodynamic parameters. v_e and v_s are the swimming speeds acquired from experiments and simulations, respectively. N is the total samples' number and χ denotes the number of testing cases.

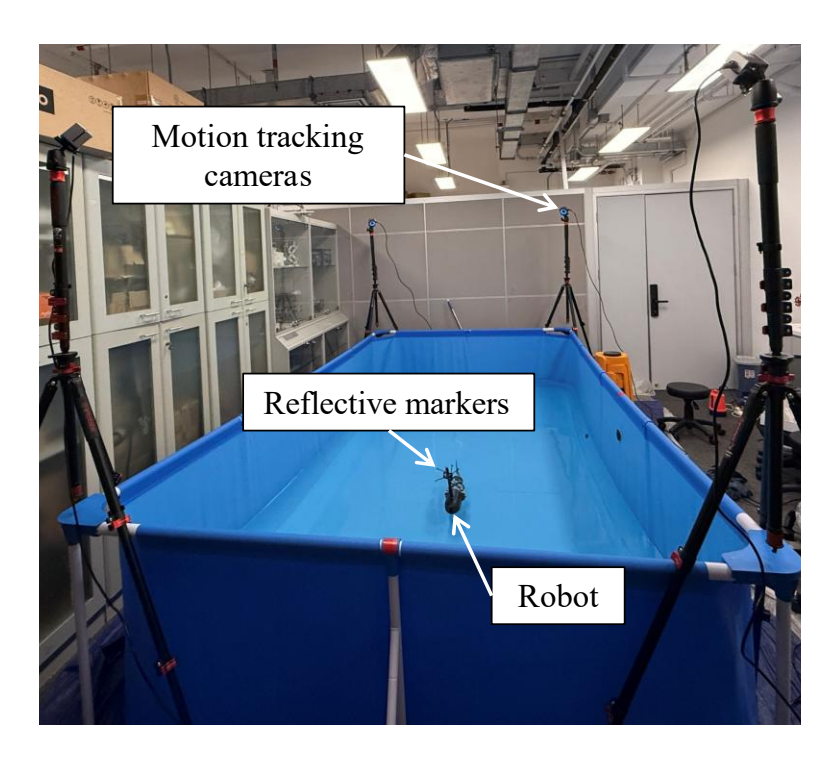


Fig. 4.9: Motion tracking system.

The experiments were conducted in a laboratory swimming pool, as depicted in Fig. 4.9. The robot's swimming trajectory was measured using four motion capture cameras strategically positioned at the corners of the pool. These cameras tracked the robot by detecting several infrared reflective markers affixed to the head of the robot. A computer, connected to the cameras via an Ethernet switch, managed the tracking process and facilitated data collection. This setup enabled precise monitoring of the robot's movements. From the tracked trajectory information, detailed analyses of the robot's swimming state, including calculations of linear and angular velocities, can be performed.

Table 4.1: Physical parameters of the robotic fish

Parameters	Value	Parameters	Value
m_0	1.62 kg	D_{rp}	$106.5 \times 5 \times 40 \text{ mm}^3$
m_1	0.18 kg	D_{es}	$61 \times 0.3 \times 30 \text{ mm}^3$
L_{0}	237 mm	W_{s}	8.2 mm
δ	20 mm	L_f	80 mm
d_0	158-118 mm	d_1	115 mm
E_{s}	200 GPa	d_2	95 mm

 D_{rp} and D_{es} denote the dimensions of the rigid plate and the elastic steel strip.

The identified results of the hydrodynamic parameters are presented in Table 4.2. Fig. 4.10 provides a detailed comparison of swimming speeds between simulations and experiments when the cantilever beam section of the leaf spring measures 25 mm in length. Fig. 4.10(a) depicts the time history of swimming speeds at a frequency of 2 Hz, showing that both the simulation and experimental results display the same variation trend and achieve similar average velocities of approximately 0.32 m/s. Fig. 4.10(b) illustrates the average swimming speeds across a range of frequencies, with differences between simulation and

experimental average velocities remaining within 5 cm/s (error within 10%). The error in the numerical simulation arose from the use of a simplified hydrodynamic force model to derive the robot's dynamic model, as well as the omission of disturbances in the pool. Although the simulation results do not exactly match the experimental outcomes, they are in close alignment with reasonable accuracy, and the observed trends are consistent. Consequently, the identified dynamic model can reliably evaluate the impact of stiffness on swimming performance and provide effective guidance for robot control.

Table 4.2: Identified hydrodynamic parameters

Parameters	Value	Parameters	Value
C_{f0}	0.24	C_{d1}	1.86
C_{d0}	2.32	C_{d2}	2.13
C_{f1}	0.20	\mathcal{C}_m	0.01

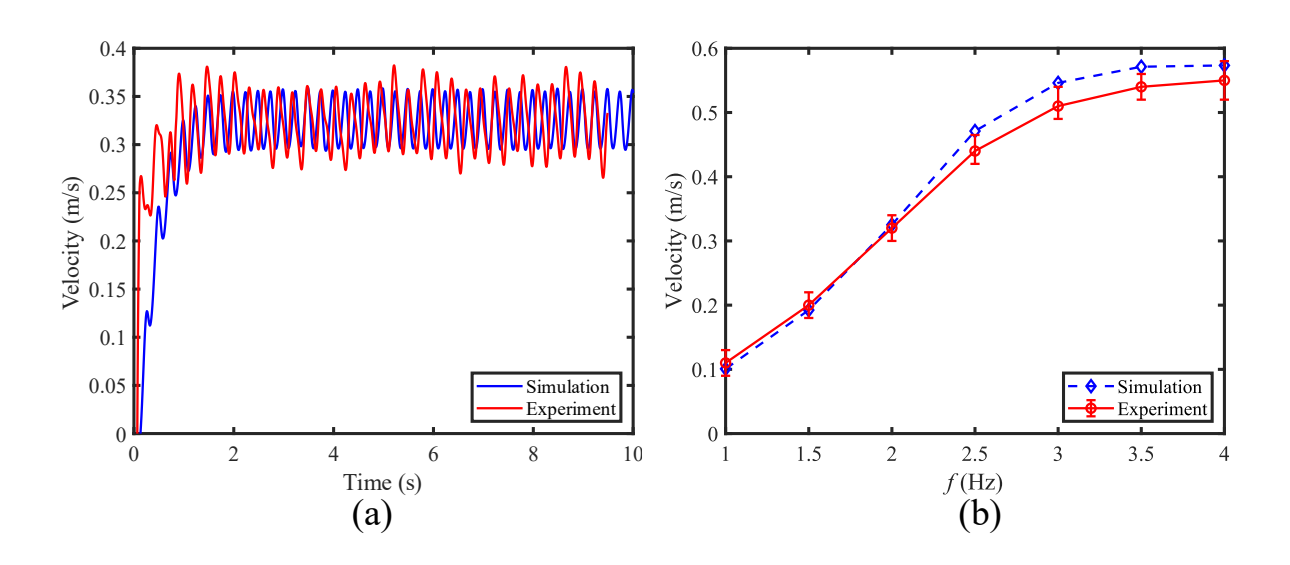


Fig. 4.10: Comparisons between simulations and experimental results when $L_s = 25$ mm. (a) Swimming speed under f = 2 Hz. (b) Average swimming speed under different frequencies.

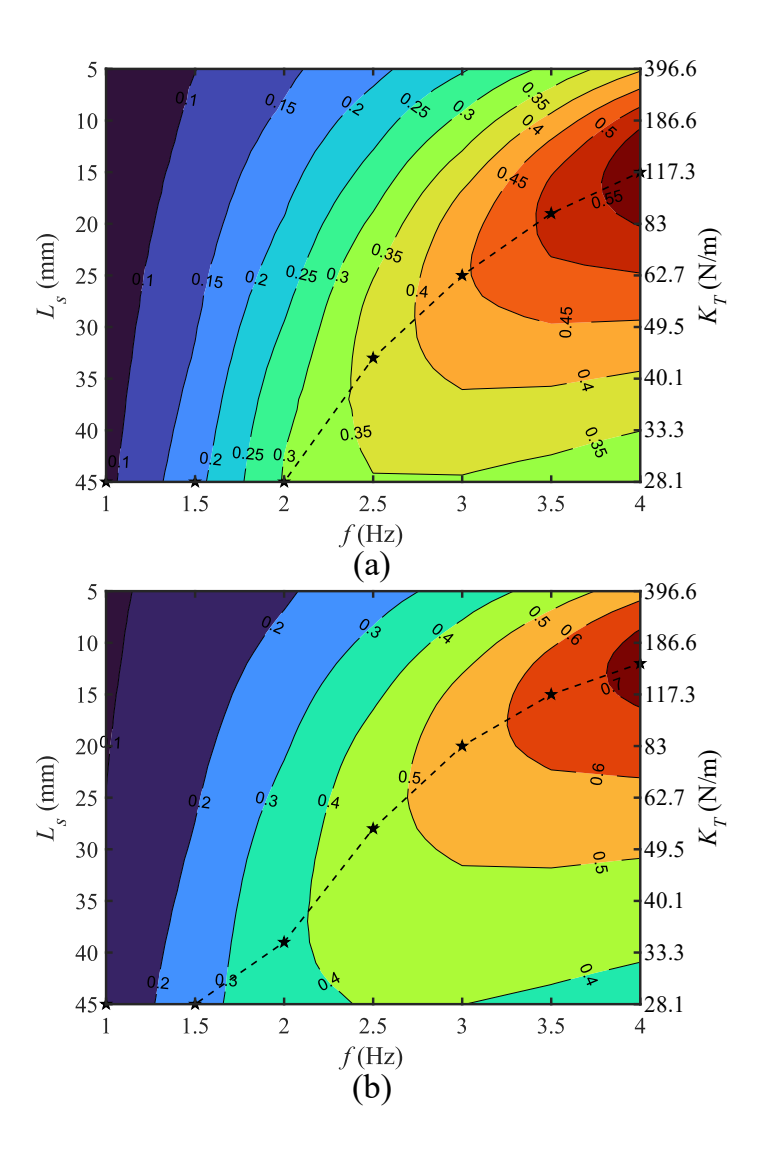


Fig. 4.11: Simulation results of velocity under different L_s and frequencies. (a) Amplitude $A = 30^{\circ}$. (B) Amplitude $A = 40^{\circ}$.

4.4 Simulation and Experimental Results

4.4.1 Forward swimming

To explore the impact of the length of the cantilever beam part of the leaf spring on the swimming speed of the robot, the simulations were conducted under different frequencies and different values of L_s . A small tail beat amplitude results in a small deflection of the tail, which inadequately demonstrates the impact of the tail's passive element on swimming performance and leads to very slow speeds. Conversely, a very large amplitude requires

substantial energy input, rendering it inefficient. Furthermore, as indicated by the reachable space analysis of the control parameters shown in Fig. 4.8, the angle limit for θ_1 is 45°, allowing the adjustable value of L_s to traverse the entire range from 5 to 45 mm. Consequently, two moderate amplitudes, 30° and 40°, are selected for subsequent performance investigations in both simulations and experiments. Figs. 4.11(a) and (b) depict the simulation results at the tail beat amplitudes of 30° and 40°, respectively. The black five-point stars in the figures represent the value of L_s at each frequency for obtaining the maximum speed of the robotic fish. The decreasing value of L_s is equivalent to the increasing stiffness. When the amplitude is 30°, the optimal value of L_s is 45 mm for the frequency within 2 Hz. And then it decreases gradually with the rising frequency. And the achieved maximum swimming speed of the robot for the amplitude of 30° is 0.58 m/s when the frequency is 4 Hz and the value of L_s is 15 mm. For the amplitude of 40°, 45 mm is the optimal value of L_s when the frequency is within 1.5 Hz. Afterwards, the value falls off with the frequency increasing. And at the frequency of 4 Hz and the L_s 's value of 12 mm, the robot achieves the fastest speed, which is 0.74 m/s.

To further validate the importance of the tunable stiffness on the swimming speed of the robot, we carried out forward swimming tests with a tunable value of L_s , a fixed value of L_s (5 mm) representing high stiffness, and a fixed value of L_s (45 mm) representing low stiffness under various frequencies and an amplitude of 40°. The testing results are depicted in Fig. 4.12. From the results, we find that both the tunable L_s and the fixed L_s of 5 mm enable the swimming speed to keep rising with increasing the tail beat frequency, while the swimming speed rises firstly from 1 Hz to 2.5 Hz and then declines for the fixed L_s of 45 mm, which indicates that the tail with soft stiffness flexes too much to provide enough thrust when facing

the large load at high frequencies. At low frequencies, the swimming speed of the soft stiffness is higher than that of the stiff stiffness, while it is opposite at high frequencies. At all frequencies, the swimming speed of the tunable L_s is the fastest. This is because the adjustable stiffness of the tail can maximize the thrust-to-drag ratio, thus leading to high swimming speed. The results demonstrate the effectiveness of the proposed mechanism and the importance of the tunable stiffness on improving the swimming speed. The maximum experimental swimming speed of the robot is about 0.7 m/s at the frequency of 4 Hz. And comparing Fig. 4.12 with Fig. 4.11(b), we can see that the simulation and experimental results match well.

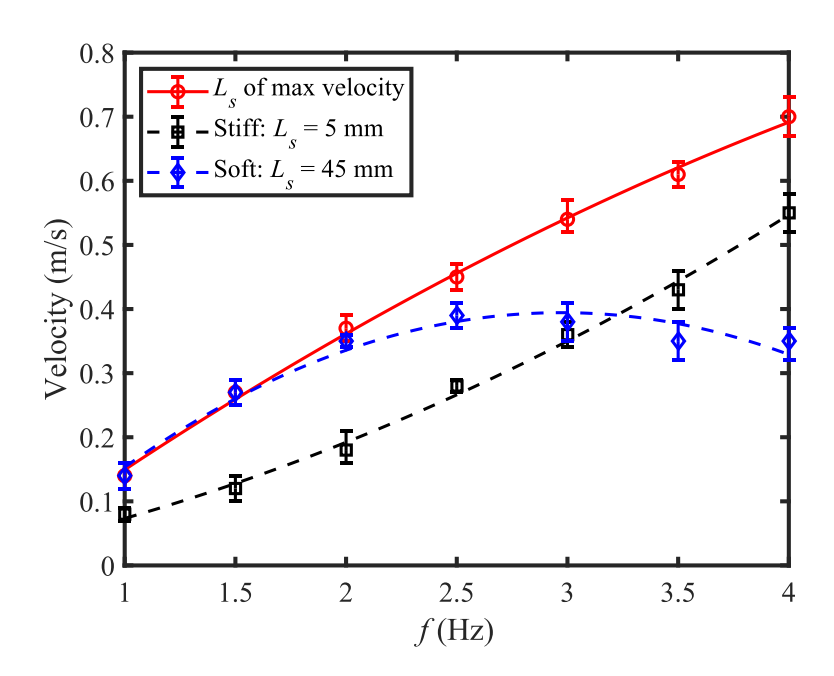


Fig. 4.12: Comparisons of experimental velocities between tunable L_s , a fixed L_s of high stiffness, and a fixed L_s of low stiffness under the amplitude of 40°.

4.4.2 Swimming efficiency

Besides the swimming velocity, the swimming efficiency is a crucial performance indicator for underwater robots. In this section we investigated the effect of the length of the

cantilever beam portion of the steel strip on energy efficiency. The cost of transport [78] is used to compare the swimming efficiency, which can be expressed as

$$CoT = \frac{P}{mV} \tag{4.35}$$

where P is the total power consumption of two servos, and V is the average swimming velocity. To calculate power consumption, the force analysis of parallel mechanism needs to be conducted.

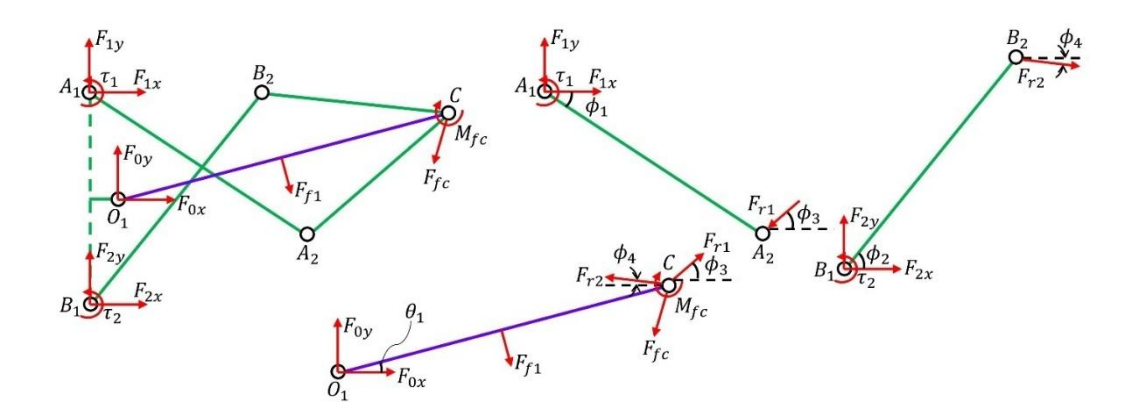


Fig. 4.13: Force analysis of the parallel mechanism.

To derive the torque of two motors, the force analysis of the parallel mechanism is conducted as shown in Fig. 4.13. For the bar A_1A_2 , the following force and moment equilibrium equations can be obtained.

$$F_{1x} - F_{r1}\cos\phi_3 = 0 \tag{4.36}$$

$$F_{1y} - F_{r1}\sin\phi_3 = 0 (4.37)$$

$$\tau_1 - F_{r_1} d_1 \sin \phi_1 \cos \phi_3 - F_{r_1} d_1 \cos \phi_1 \sin \phi_3 = 0 \tag{4.38}$$

Based on the analysis of bar B_1B_2 , the force and moment equilibrium equations can be obtained as

$$F_{2x} + F_{r2}\cos\phi_4 = 0 \tag{4.39}$$

$$F_{2v} - F_{r2}\sin\phi_4 = 0 \tag{4.40}$$

$$\tau_2 - F_{r_2} d_1 \sin \phi_2 \cos \phi_4 - F_{r_2} d_1 \cos \phi_2 \sin \phi_4 = 0 \tag{4.41}$$

For the rigid link of tail, the force and moment equilibrium equations can be derived as

$$F_{0x} + F_{f1}\sin\theta_1 - F_{fc,H} + F_{r1}\cos\phi_3 - F_{r2}\cos\phi_4 = 0 \tag{4.42}$$

$$F_{0v} - F_{f1}\cos\theta_1 - F_{fc,V} + F_{r1}\sin\phi_3 + F_{r2}\sin\phi_4 = 0 \tag{4.43}$$

$$-\frac{F_{f1}L_{1}}{2} - M_{fc} + F_{fc,H}d_{0}\sin\theta_{1} - F_{fc,V}d_{0}\cos\theta_{1} - F_{r1}d_{0}\cos\phi_{3}\sin\theta_{1} + F_{r1}d_{0}\sin\phi_{3}\cos\theta_{1} + F_{r2}d_{0}\cos\phi_{4}\sin\theta_{1} + F_{r2}d_{0}\sin\phi_{4}\cos\theta_{1} = 0$$
 (4.44)

According to the constraint condition of the slider, the following equation can be obtained.

$$F_{r_1}\cos(\phi_3 - \theta_1) - F_{r_2}\cos(\phi_4 + \theta_1) - F_{f_{c,H}}\cos\theta_1 - F_{f_{c,V}}\sin\theta_1 = 0 \tag{4.45}$$

Combining the motion equations of the robot with the above equations, we can obtain two motors' torque separately. And the power consumption can be calculated by [118, 140]

$$P = \frac{1}{T} \sum_{i=1}^{2} \int_{t}^{t+T} |\tau_{i} \dot{\phi}_{i}| dt$$
 (4.46)

Through the derived dynamic model and the torque analysis of two servos, the CoT of the robotic fish under different frequencies and different values of L_s was computed for the amplitudes of 30° and 40°, and the results are illustrated in Figs. 4.14 (a) and (b), respectively. The black five-point stars in the figures represent the value of L_s at each frequency for obtaining the minimum CoT of the robotic fish. For the amplitude of 30°, the optimal value

of L_s to obtain the minimum CoT within 2 Hz is 45 mm, and when the frequency is greater than 2 Hz, it keeps gradually descending with the ascending frequency. The minimum CoT among all cases for the amplitude of 30° is 7.5 J/m/kg at the frequency of 2.5 Hz and the L_s 's value of 38 mm. When the amplitude is 40°, the optimal value of L_s for achieving the minimal CoT within 1.5 Hz is 45 mm, and then, as the frequency increases, the optimal value of L_s drops bit by bit. For all cases under the amplitude of 40°, the minimal CoT occurs when the frequency is 2.5 Hz and the value of L_s is 36 mm, which is 8.49 J/m/kg.

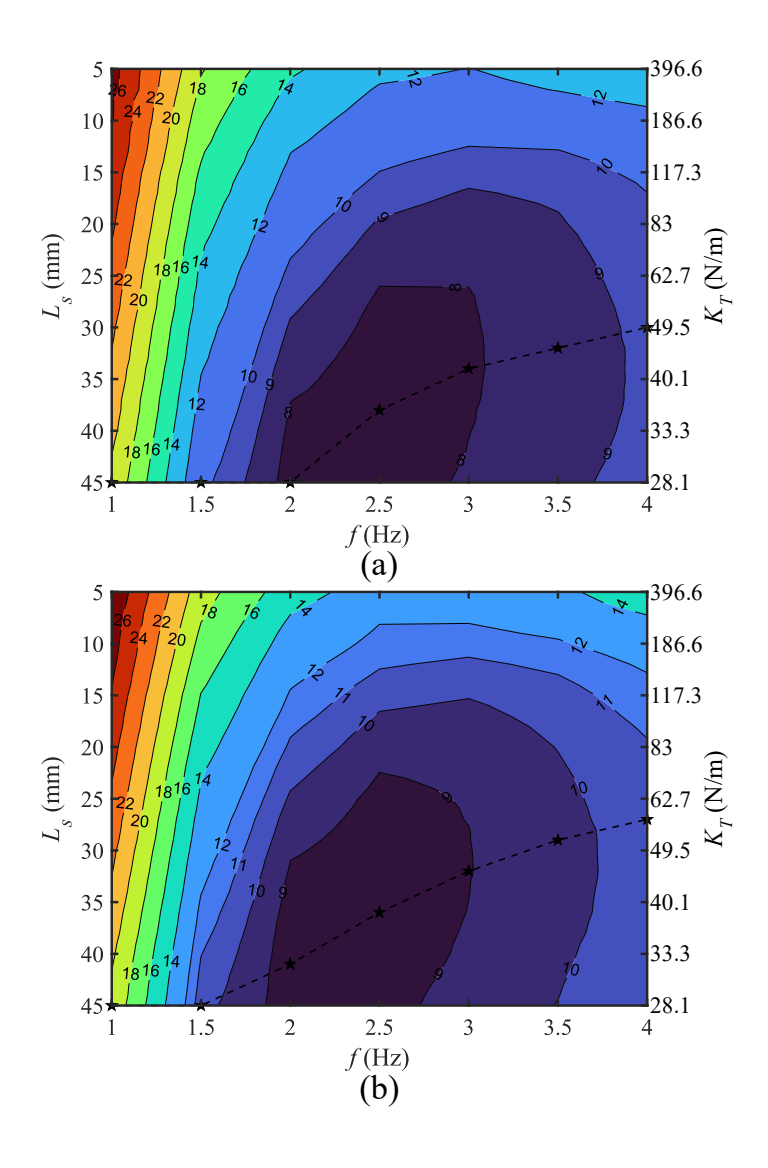


Fig. 4.14: Simulation results of CoT under different L_s and frequencies. (a) Amplitude $A = 30^\circ$. (b) Amplitude $A = 40^\circ$.

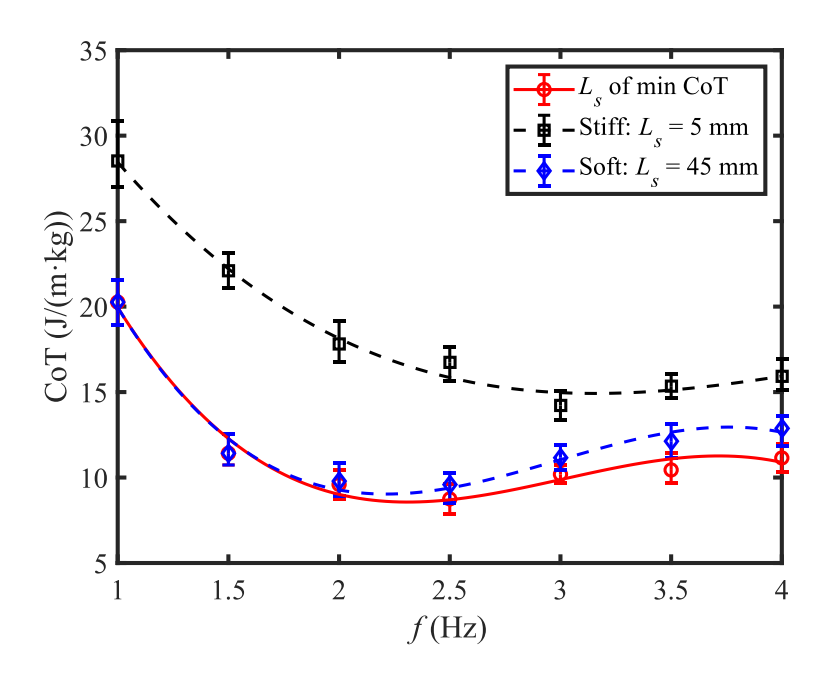


Fig. 4.15: Comparisons of experimental CoT between tunable L_s , a fixed L_s of high stiffness, and a fixed L_s of low stiffness under the amplitude of 40°.

Then we conducted experimental investigations to assess the impact of the adjustable length L_s on swimming efficiency. The experiments compared the CoT among three configurations: a tunable L_s , a fixed L_s of 45 mm representing soft stiffness, and a fixed L_s of 5 mm representing high stiffness, under various frequencies and an amplitude of 40°. The power consumption of the two motors was estimated by using two current sensors inside the robot's head and the battery voltage. The current sensors were read by an Arduino nano, and the read data was then transmitted to the Raspberry Pi via serial communication. The results, presented in Fig. 4.15, indicate that the CoT for all three configurations initially decreases dramatically and then slightly increases as the frequency rises. At all frequencies, the CoT for the fixed L_s of 5 mm is significantly higher than that for both the tunable L_s and the fixed L_s of 45 mm. The tunable L_s achieves the lowest CoT across various tail beat frequencies, with a minimum CoT of approximately 8.75 J/m/kg occurring at a frequency of 2.5 Hz.

4.4.3 Underwater swimming test

To examine the performance of the robot when it swims underwater, experimental testing was conducted as shown in Fig. 4.16(a). The buoyancy of the robot is adjusted to be totally neutral by adding 200 grams of weight in the robot so that the robot can hover at any depth. In order to ensure reliable communication between the robot and the remote-control computer for underwater operation, a remote antenna was connected to the robot via a long cable. A camera was utilized to record the testing. And the recorded video can be further processed to track the robot through detecting the color marker pasted on the robot head. Then the motion information of the robot can be obtained.

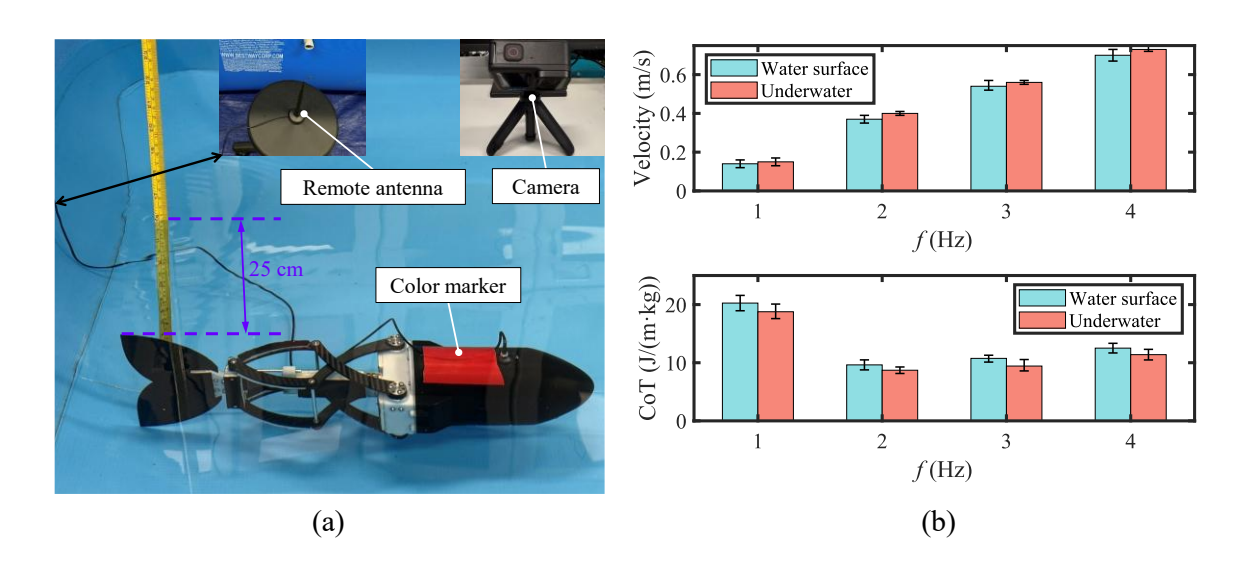


Fig. 4.16: Underwater swimming performance test of the robot. (a) Experimental setup. (b) Comparison between robot swimming on the water surface and underwater.

The results of the underwater testing, including the velocity and the CoT under the values of L_s for achieving the maximum swimming speed under various frequencies, are presented in Fig. 4.16(b). The outcomes reveal that both the swimming velocity and the CoT of the robot swimming underwater are a bit better than those of the robot swimming on the water surface. Less disturbance from water current leads to a bit higher swimming speed.

Higher speeds and more weight for ensuring the neutral buoyancy cause the smaller values of CoT. Thus, the system is effective for working underwater.

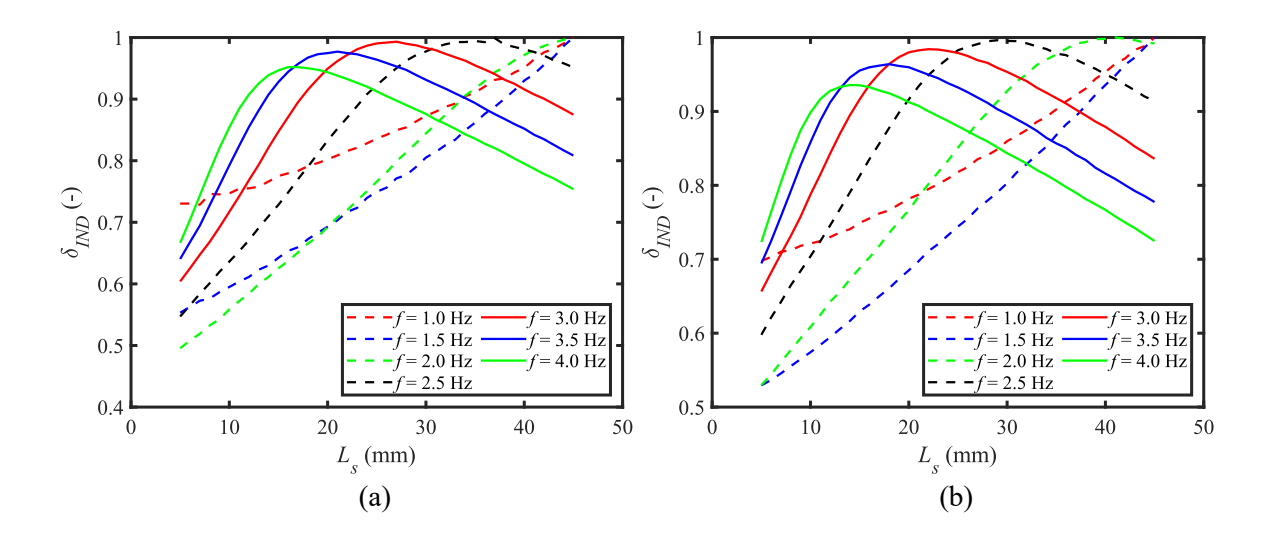


Fig. 4.17: Values of δ under different values of L_s and different frequencies. (a) Amplitude $A = 30^{\circ}$. (b) Amplitude $A = 40^{\circ}$.

4.4.4 Stiffness regulation rule

According to the above results, the optimal lengths of the cantilever beam portion of the steel strip enabling the robotic fish to achieve the fastest speed and the minimal CoT are not always same under various frequencies. In order to find the proper value of L_s for achieving fast and energy-efficient swimming of the robot, we define a performance indicator δ_{IND} as shown in the following equation, which takes the swimming speed and CoT into account.

$$\delta_{IND} = c_1 \left\| \frac{v}{v_{\text{max}}} \right\| + c_2 \left\| \frac{CoT_{\text{min}}}{CoT} \right\|$$
(4.47)

where c_1 and c_2 denote the weight coefficients of the normalized velocity and CoT. c_1 and c_2 should satisfy $c_1 \in [0,1]$, $c_2 \in [0,1]$, and $c_1 + c_2 = 1$. The normalization of the speed and CoT enables the consistency of the value scales. Different values of c_1 and c_2 result in different optimization objectives. For instance, a large value c_1 signifies that the speed is the

Primary objective, while a large value of c_2 indicates that the CoT is the major objective. Here, we want to balance the trade-off between the swimming speed and the CoT. Thus, the coefficients are set as $c_1 = c_2 = 0.5$. The value of L_s to maximize the value of δ denotes the optimal length of the cantilever beam part of the steel strip for the robot to achieve fast and energy-efficient swimming, which is symbolized by L_{ss} as shown in the following equation.



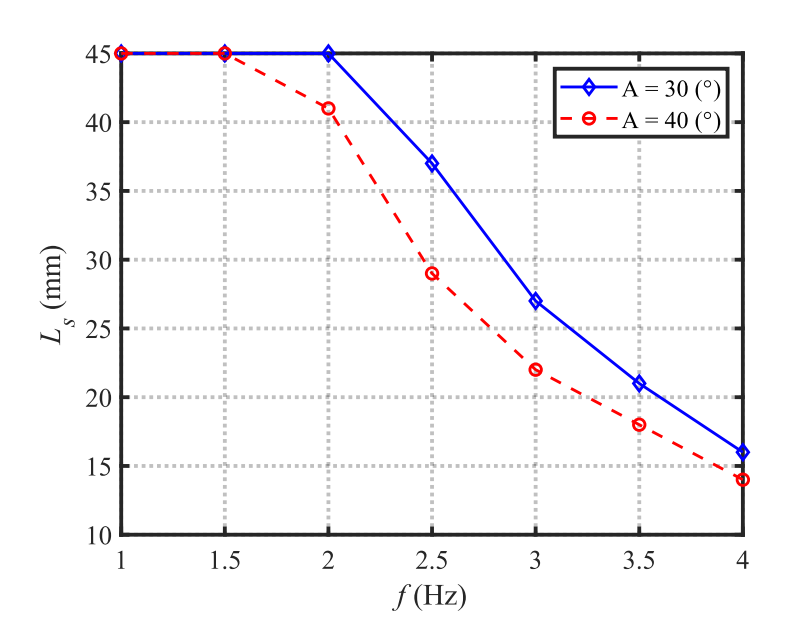


Fig. 4.18: Optimized values of L_s under different frequencies.

Figs. 4.17(a) and (b) depict the calculated results of δ under different frequencies and different values of L_s when the tail beat amplitudes are 30° and 40°, respectively. For the frequency within 2 Hz under the amplitude of 30° and the frequency within 1.5 Hz under the amplitude of 40°, the value of δ keeps rising with the value of L_s going up until the maximum adjustable length. When the frequency exceeds 2 Hz under the amplitude of 30° and the frequency is over 1.5 Hz under the amplitude of 40°, the value of δ with the increasing value of L_s shows the initially increasing and then decreasing trend. The optimal

values of L_s for the amplitudes of 30° and 40° at various frequencies are demonstrated in Fig. 4.18. The optimal L_s of the amplitude of 40° are slightly higher than that of the amplitude of 30° when the frequency is from 2 Hz to 4 Hz.

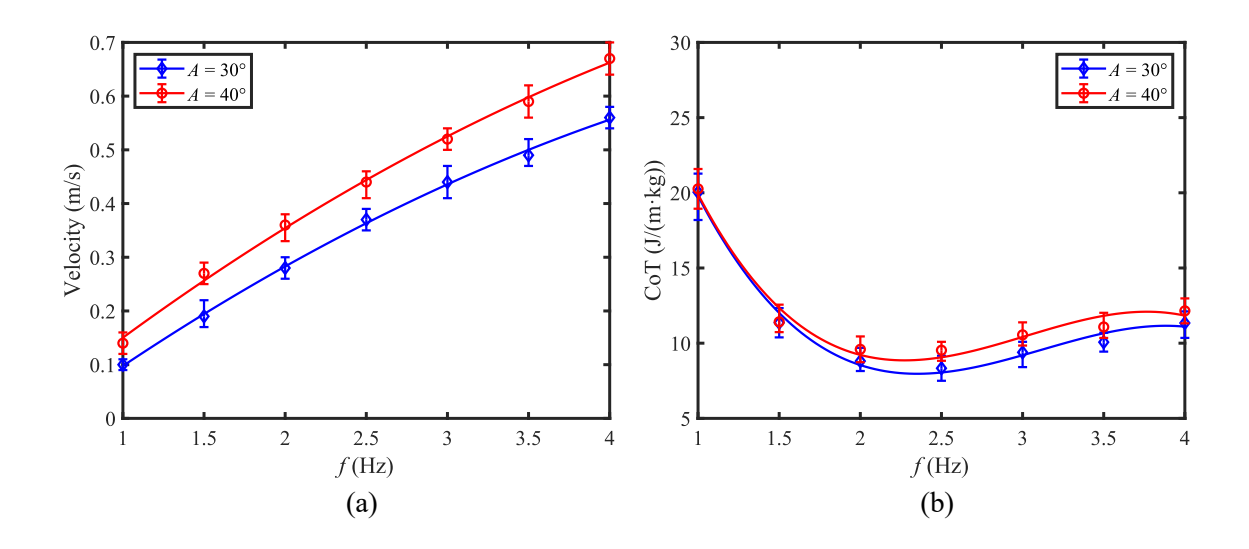


Fig. 4.19: Swimming performance of the robot with the optimal L_s under different frequencies. (a) Average swimming speed. (b) CoT.

The swimming performances including swimming speed and CoT of the robotic fish with the optimal values of L_s under the amplitudes of 30° and 40° are presented in Figs. 4.19 (a) and (b). Both the swimming speeds under two amplitudes increase almost linearly with the increasing frequency. The velocity under the amplitude of 40° is higher than that under the amplitude of 30°. The maximum speeds under the optimal value of L_s for the amplitudes of 30° and 40° are 0.56 m/s and 0.67 m/s respectively, both achieved at the frequency of 4 Hz. The CoT under two amplitudes decreases as the frequency rises from 1 Hz to 2.5 Hz and then is somewhat increasing. The CoT under the amplitude of 30° is a bit lower than that under the amplitude of 40°. The minimum values of CoT under the optimal value of L_s for the amplitudes of 30° and 40° are 8.33 and 9.53 correspondingly, happened at the frequency of 2.5 Hz.

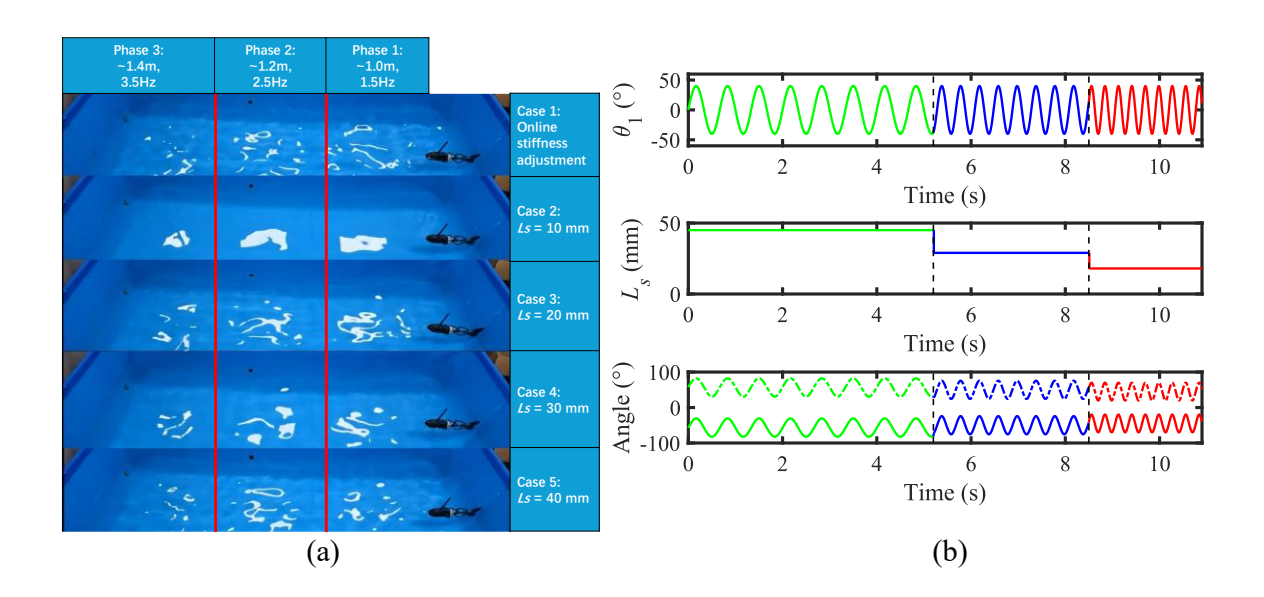


Fig. 4.20: Experimental testing of the robot with online stiffness adjustment and multiple fixed values of L_s . (a) Testing protocol for the comparison of five cases. (b) Control inputs for online stiffness adjustment.

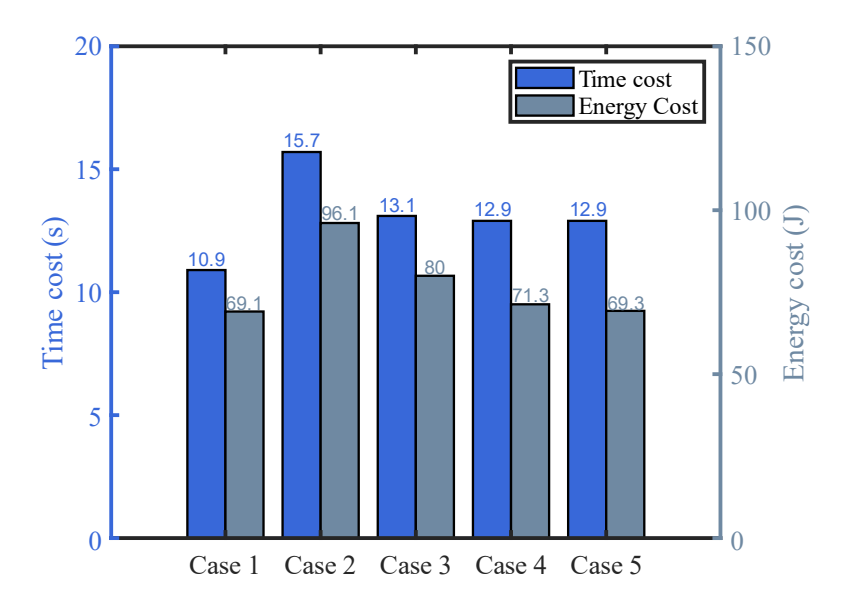


Fig. 4.21: Time and energy costs of five testing cases.

The optimized results can be utilized to guide the online stiffness modulation of the robot. To demonstrate the advantages of this strategy, experimental tests were conducted to compare the robot's performance under five different conditions, as illustrated in Fig. 4.20(a): online stiffness modulation (Case 1), and fixed L_s values of 10 mm (Case 2), 20 mm (Case 3), 30 mm (Case 4), and 40 mm (Case 5). The testing was separated into three phases: Phase 1

involved swimming approximately 1 m with a tail beat frequency of 1.5 Hz; Phase 2 covered about 1.2 m with a frequency of 2.5 Hz; and Phase 3 spanned approximately 1.4 m with a frequency of 3.5 Hz. The performance metrics assessed were total time and energy consumption. Based on the optimized values of L_s under various frequencies, the endpoint trajectory control for online modulating stiffness of tail between two adjacent swimming phases is demonstrated in Fig. 4.20(b). Using the inverse kinematics, the control angles of the two active joints can be derived when the angle θ_1 and the trajectory radius d_0 are known. The results, shown in Fig. 4.21, indicate that Case 1 achieved the lowest time and energy costs, at 10.9 s and 69.1 J, respectively. In contrast, Case 2 recorded the highest time and energy costs, at 15.7 s and 96.1 J, respectively. These findings demonstrate that the online stiffness modulation strategy significantly enhances the swimming performance of the robotic fish across various tail beat frequencies, a feat unattainable with any fixed tail stiffness.

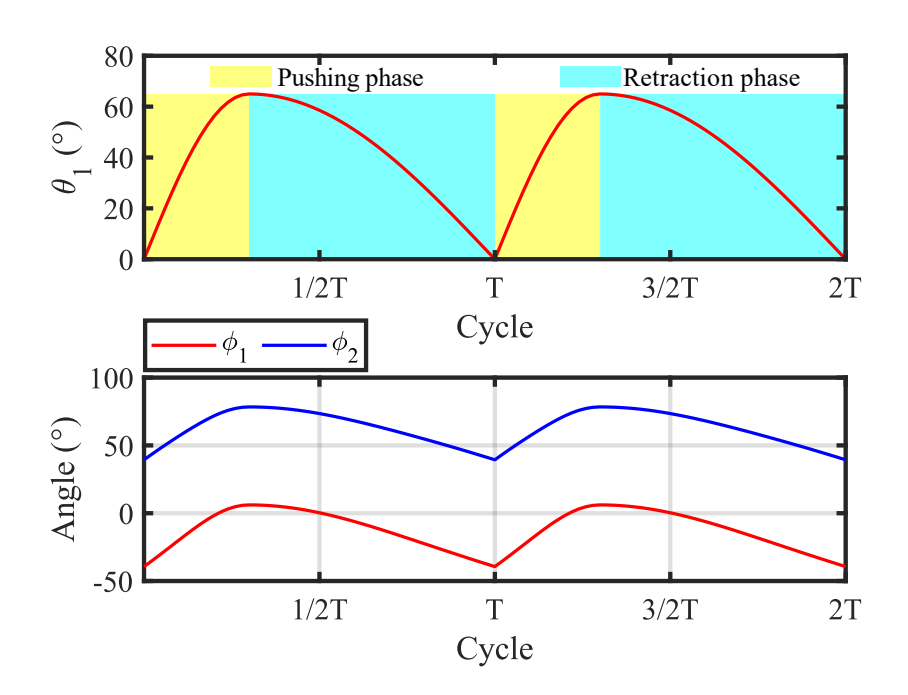


Fig. 4.22: Control inputs for turning motion when $L_s = 5$ mm.

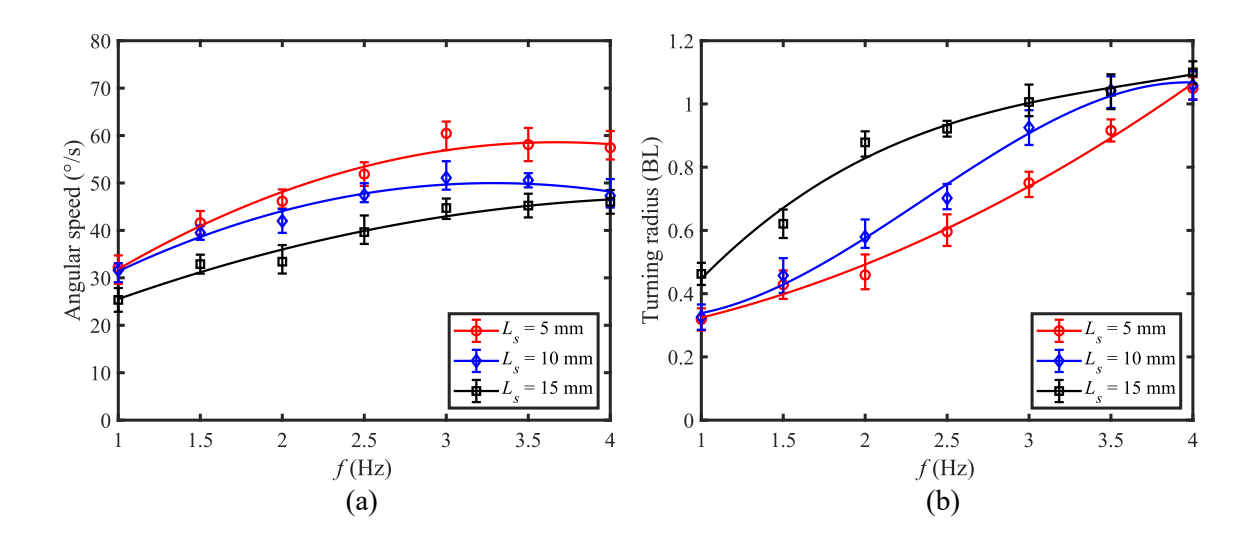


Fig. 4.23: Turning performance under different frequencies and different values of L_s . (a) Average turning rate. (b) Turning radius.

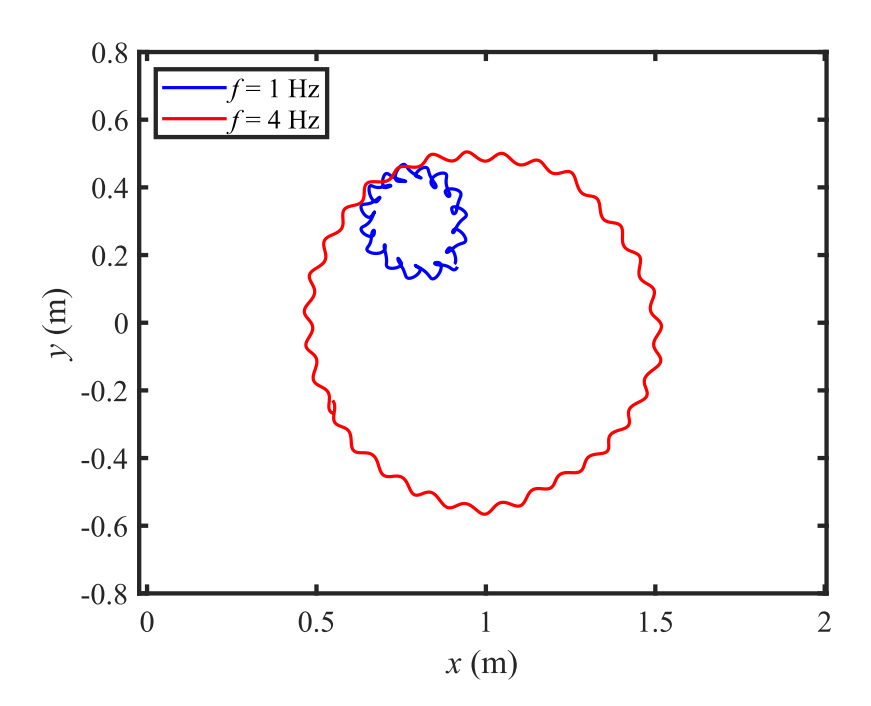


Fig. 4.24: Experimental turning trajectories under frequencies of 1 Hz and 4 Hz when $L_s=5$ mm.

4.4.5 Turning performance

Apart from swimming speed and CoT, maneuverability is also very crucial for underwater robots. In this section, the turning performance of the robotic fish is

experimentally investigated. Fig. 4.22 illustrates the control inputs for the turning locomotion mode. To produce a larger hydrodynamic force for the turning of the robotic fish, the tail's beating speed of the pushing phase is faster as twice as that of the retraction phase during one cycle. The amplitude of θ_1 is 65°, and the control laws of two motors can be obtained through the inverse kinematics as shown in Fig. 4.22(bottom).

According to the reachable space analysis of the control parameters in the previous section, the adjustable length range of L_s is from 5 mm to 15 mm. Thereby, the turning experiments are conducted under three values of L_s , namely 5 mm, 10 mm, and 15 mm. The testing results, including the turning rate and turning radius under various frequencies, are demonstrated in Figs. 4.23(a) and (b), respectively. We find that the average angular speed increases with the value of L_s decreasing, while it is opposite for the turning radius. The maximum average angular speed is around 61°/s when the frequency is 3 Hz and the value of L_s is 5 mm. And the minimum turning radius is about 0.32 BL (15.9 cm) under the frequency of 1 Hz and the L_s of 5 mm. Thus, the stiffness modulation mechanism proposed in this study not only enables the robotic fish to achieve fast and efficient swimming but also ensures good maneuverability. Fig. 4.24 shows the turning trajectories at frequencies of 1 Hz and 4 Hz, indicating that the robotic fish can turn in very narrow spaces at a low frequency.

A notable advantage of the tail's adjustable stiffness is its ability to maintain a consistent turning radius at different turning speeds, as shown in Figs. 25(a) and (b). The robot achieves a same turning radius of approximately 0.46 BL with an L_s of 15 mm at a frequency of 1 Hz and with an L_s of 5 mm at a frequency of 2 Hz, while the turning rate of the former case is just about half that of the latter case. Similarly, the robot maintains a turning radius of about 0.93 BL with an L_s of 15 mm at a frequency of 2.5 Hz and with an L_s of 5 mm at a frequency

of 3.5 Hz, whereas the latter turning speed is approximately 1.6 times as fast as that of the former.

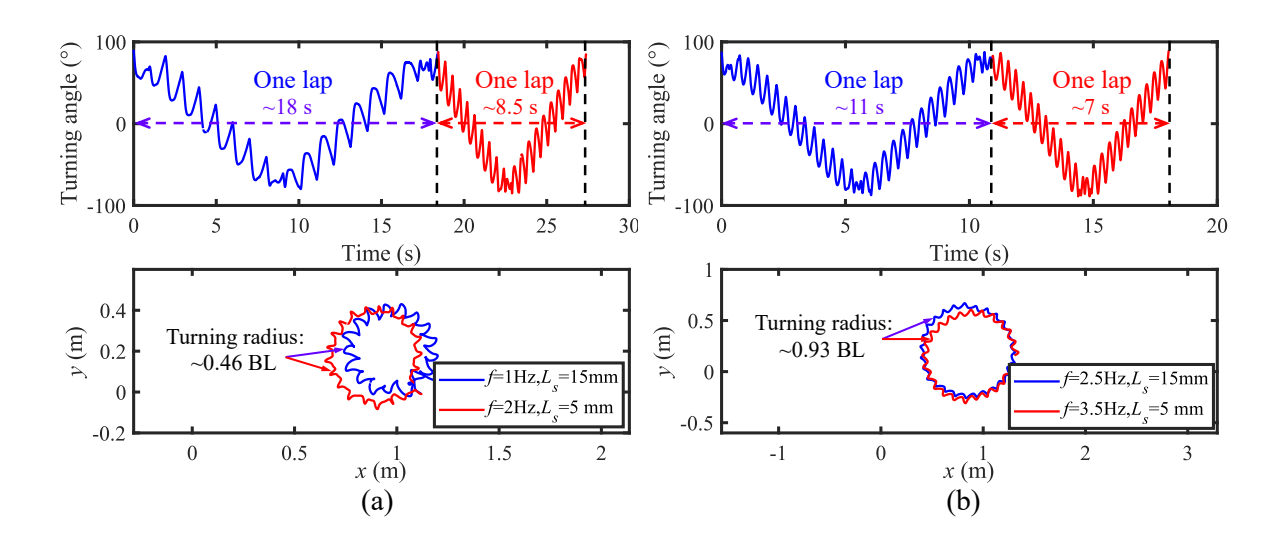


Fig. 4.25: Demonstrations of constant turning radius under varying angular speeds. (a) Small turning radius. (b) Large turning radius.

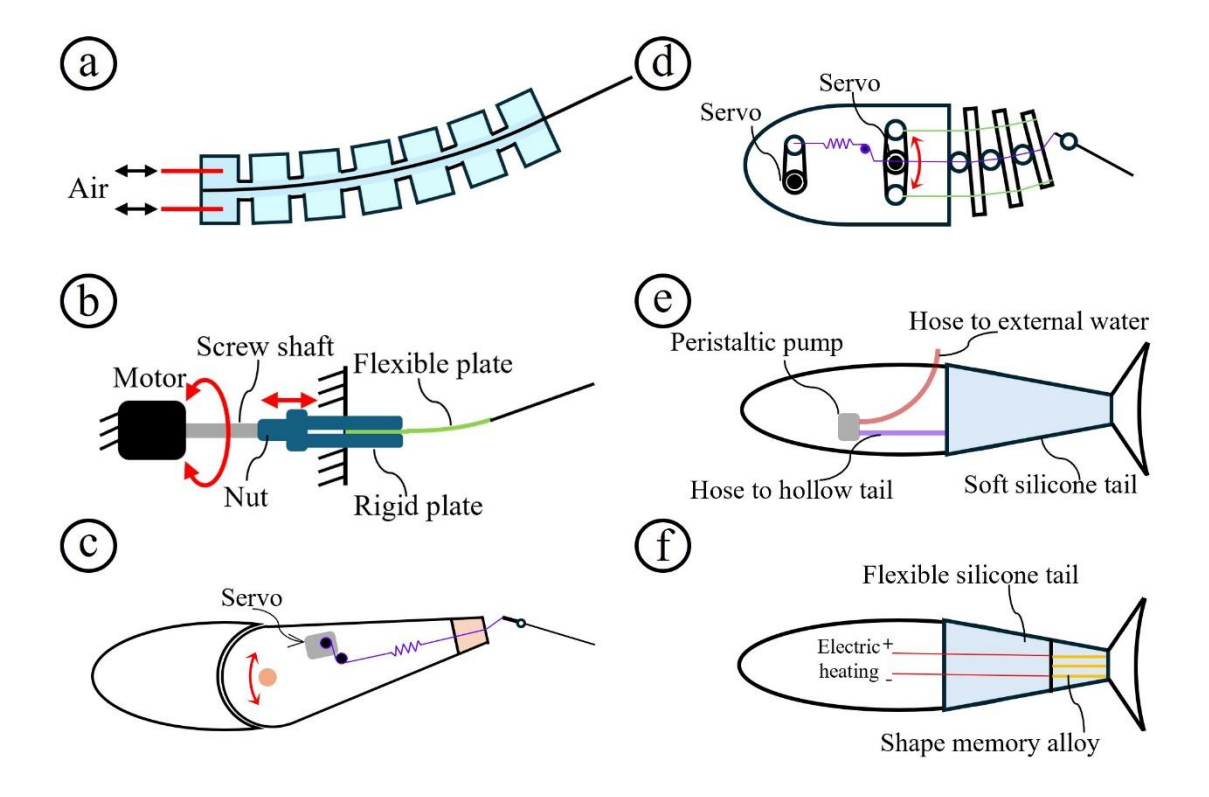


Fig. 4.26: Schematic illustrations of the basic stiffness modulation mechanisms for fish-like robots in the literature.

4.5 Comparison and Discussion

The simplest method for the realization of changing stiffness is to design robotic fishtails with replaceable passive compliant components, which is also known as offline modulation strategy and has been studied for many years. For example, Low *et al.* [46] developed a robotic fish with a linear spring connected peduncle of caudal fin and investigated influence of diverse parameters including the spring constant on the propulsion performance. Chen *et al.* [116] designed a passive joint using two torque springs for a three-joint fish-like robot to explore its swimming performance under various stiffnesses of the spring. Lu *et al.* [60, 63] adopted two spring steels to construct robotic fish and the swimming performance wad optimized by changing the spring steels with different thicknesses. Chen and Jiang [62, 141] designed tensegrity robotic fish that can achieve variable body stiffness through adjusting the cables' tension. Although these methods can effectively boost the performance of swimming robots, the offline replacing the flexible parts cannot realizing stiffness modulation when the robots swim and is not employable to real-timely adapt to the changing actuation inputs in the real applications.

Modulating stiffness online like a natural fish is more attractive and practical for the swimming robots. Researchers and engineers proposed some stiffness tuning mechanism for robotic fish. And several representative ones are shown in Fig. 4.27. Wolf *et al.* [142] built a soft robotic fishtail (Fig. 4.27(a)) by attaching a pair of pneumatic soft actuators to a compliant foil. The body stiffness is controlled by the soft actuators caused antagonistic forces. They conducted the thrust experiments under the tail beat frequencies from 0.25 to 1Hz and showed that as the tail becomes stiffer, increasing the frequency has a greater influence on thrust generation. Nakabayashi *et al.* [143] developed a fin (Fig. 4.27(b)) that can adjust the effective length of a plate spring to tune stiffness through a motor actuated

screw drive mechanism. Their findings showed that the ideal effective length for maximizing thrust efficiency changes with different oscillation amplitude and frequency, and the fin with tunable stiffness demonstrated better efficiency in comparison to the fin of constant stiffness. Zhong et al. [64] used a linear spring driven by a servo and connected to the peduncle of Tunabot's tail (Fig. 4.27(c)) to simulate the muscle of tuna, thus realizing tail's stiffness adjusting ability of Tunabot by controlling the pretension of the spring. They concluded that adjusting stiffness can greatly enhance swimming efficiency at frequencies (0 to 6 Hz) and velocities (0 to 2 BL/s) similar to those of tuna, and robotic fish with high oscillation frequency can benefit more in efficient swimming from stiffness controlling. Qiu et al. [66] designed a tendon-actuated fish robot (Fig. 4.27(d)) which relies on regulating the pretension of the spring by a servo to achieve variable stiffness as well. The robot achieved its maximal speed (1.04 BL/s) at 2.2 Hz through stiffness adjustment. Ju and Yun [65] proposed a hydraulic stiffness tuning mechanism for a soft fish-like robot (Fig. 4.27(e)). The motion of the soft tail is controlled by a servo, and its stiffness is adjusted by a pump that controls the injection volume of water inside the chamber of the tail. The performance of the robot was examined in the frequency range from 0.3 to 1.25 Hz. Owing to tuning stiffness, both the linear and angular velocities were effectively improved, i.e., reaching to 0.63 BL/s and 94.1° /s. Liu et al. [67] built a hydraulic actuated tuna robot (Fig. 4.27(f)) and they embedded shape memory alloy (SMA) wire into the soft peduncle of the robot's tail. The elastic modulus of SMA can be regulated by current-based temperature control. They took the energy consumption associated with tuning stiffness into account for the computation of the robot's cost of transport to prove that it deserves to apply adjustable stiffness to fish-like robot for performance improvement.

The capability of tuning stiffness is crucial for swimming robots to maintain high performance. The existing stiffness modulation mechanisms have one common feature that extra actuator or power source need to be applied just for tuning stiffness, which brings about more energy consumption and complicated structures. The complexity in mechanism further causes drawbacks in difficulty of waterproof, lower durability, and more burden to robotic fish. According to [64], high-frequency platform could benefit more from tuning stiffness. More burden leads to low tail beat frequency for most servo-actuated robots, i.e., around 1 or 2 Hz [65, 66]. Although those DC actuated robotic fish can exhibit high frequency oscillation, the maneuverability is poor. The detailed comparisons between our proposed robotic fish with several representative robotic fish featuring tunable stiffness of tail from the literature are shown in Table 4.3.

Table 4.3: Comparison with other online stiffness adjustable robotic fish

Platforms	Frequency range (Hz)	Max average velocity (BL/s, m/s)	Min CoT (J/m/kg)	Max average turning rate (°/s)	Min turning radius (BL)	Types and quantities of motors for tail actuation	Extra power sources	Response for Tuning stiffness	Self- contained
Robotic tuna [64]	0-6	2, 0.7	N/A	N/A	N/A	1 DC motor	Yes	Fast	No
Tendon-driven robotic fish [66]	0-2.2	1.04, 0.47	N/A	30.9	0.31	1 servo motor	Yes	Fast	Yes
HVS robotic fish [65]	0-1.25	0.63, 0.39	N/A	94.1	0.14	1 servo motor	Yes	Slow	Yes
HasorTuna [67]	0-6	0.63, 0.36	13.7	N/A	N/A	2 servo motors	Yes	Slow	Yes
Robotic fish [144]	0-3	0.86, 0.35	N/A	N/A	N/A	1 servo motor	Yes	Fast	No
Robotic dolphin [145]	0-2.88	1.12, 0.74	28.1	N/A	N/A	1 DC motor	Yes	Fast	Yes
Swimming robot [103]	0-1.75	1.67 , 0.25	25	N/A	N/A	2 servo motors	Yes	Slow	Yes
Robotic fish [102]	0-3	1.07, 0.43	13.3	N/A	N/A	1 servo motor	Yes	Slow	Yes
Our robot	0-4	1.46, 0.73	8.3	61	0.32	2 servo motors	No	Fast	Yes

Partial data is estimated with the information provided by authors. The notation "N/A" is used to indicate that specific information is unavailable. Items highlighted in bold represent those ranked among the top three in that particular aspect of performance. The term 'self-contained' refers to robots in which all mechatronic components are integrated within the robots' body.

Based on the comparison, several key points can be identified and are listed as follows:

- a) High-frequency swimming robots benefit significantly from tuning stiffness. Our robot exhibits a wider tail beat frequency range compared to most platforms in the literature, with only the robotic tuna [64] and HasorTuna [65] demonstrating broader frequency ranges. Although the DC-motor-actuated mechanism in robotic tuna facilitates high-frequency oscillation, it suffers from limited turning capability, resulting in poor maneuverability. Similar to our robot, HasorTuna employs two servos to hydraulically drive its soft tail, achieving a wider frequency range. However, both the swimming speed and energy efficiency of HasorTuna are considerably lower than those of our robot. Another major drawback of HasorTuna is its stiffness tuning mechanism, which has a slow response time for adjusting stiffness, making it unsuitable for real-time adjustments.
- b) Whether speed is measured in body lengths per second (BL/s) or meters per second (m/s), our robot ranks among the top three, specifically No. 3 in BL/s and No. 2 in m/s. In terms of BL/s, the speeds of the robotic tuna [64] and another swimming robot [103] exceed that of our robot. However, it is noteworthy that the robotic tuna is not self-contained, as its electronic components are external. Additionally, the swimming robot utilizes four motors, resulting in significantly higher energy consumption and suffers from a slow response in stiffness tuning. When speed is measured in m/s, the robotic dolphin [145] is slightly faster than our robot, but its torque-controlled caudal fin for simulating stiffness adaptation requires more energy. Compared to all robots in the literature, our robot achieves the highest energy efficiency.

- c) Most studies in the literature have not emphasized the turning capabilities of robotic fish. The HVS robotic fish [65] is one of the few that demonstrates better maneuverability in terms of both turning rate and radius compared to our robot, owing to the flexibility of its long, soft tail. However, its swimming speed is significantly slower than that of our robot, and its stiffness adjusting mechanism is unable to fully contribute to fast and efficient swimming due to a very limited frequency range. Besides, the response time for stiffness adjustment is slow as well.
- d) A key distinction between the robotic fish in this study and other platforms is that all other robots require additional power sources to achieve stiffness modulation. In contrast, the servos in our robot are responsible for both driving the tail and adjusting stiffness.

Overall, the comparison indicates that the proposed stiffness modulation mechanism enhances the robotic fish's general performance in terms of swimming speed, energy efficiency, maneuverability, and response time for tuning stiffness.

4.6 Concluding Remarks

In this chapter, we developed a novel robotic fish with the capability of modulating stiffness. And then we derived the dynamic model of the robot and validated its reliability by experiments. Finally, numerous simulations and experiments were carried out to examine the performance of the robot and to verify the effectiveness of the proposed method. Based on the above results and discussions, the following conclusions can be drawn.

1) The designed fishtail, which integrates a parallel mechanism, an elastic leaf spring, and a slider mechanism, achieves stiffness adjustment without the need for additional actuators or power sources. This represents a significant distinction from

other existing robotic fish capable of tuning stiffness. Furthermore, it exhibits a wider tail beat frequency range than most servo-actuated platforms, as both servos in the robot contribute to tail swinging and stiffness adjustment. Consequently, greater benefits can be derived from stiffness modulation.

- 2) The proposed stiffness modulation mechanism effectively enhances swimming speed and energy efficiency across various control inputs. But the fastest speed and the minimum CoT do not always occur at the same length as the cantilever beam part of the leaf spring. Therefore, the optimization function that considers both speed and CoT is necessary to determine the optimal value of L_s for maintaining fast and energy-efficient swimming. Experiments demonstrate that the performance improvements achieved through online stiffness modulation cannot be replicated by any fixed tail stiffness. The robot achieves a maximum average swimming speed of 1.46 BL/s, and the minimum CoT is 8.3 J/m/kg.
- 3) Turning experiments indicate that a small value of L_s allows the robotic fish to achieve a faster average angular velocity and a smaller turning radius, suggesting that higher stiffness is necessary for optimal maneuverability. The robot's maximum average turning rate is approximately 61°/s, and the minimum turning radius is around 0.32 BL (15.9 cm). Additionally, the ability to adjust stiffness enables the robot to maintain a consistent turning radius across various turning rates, demonstrating enhanced flexibility in turning.

The robot's overall design lacks streamlining due to the open structure of its tail, leading to flow separation at the rear of the robot's head. Consequently, a large wake region forms, creating a vacuum zone that generates significant pressure drag, thereby adversely affecting

both speed and efficiency. Future work should focus on optimizing the robot's structure. For instance, redesigning the connection between the head and the tail could effectively reduce the formation of a vacuum zone, and covering the tail with an appropriate soft material could streamline the robot. Three-dimensional swimming is essential for underwater robots; therefore, incorporating a pair of pectoral fins on the robot's head or integrating a movable mass within the head could be beneficial. Additionally, the impact of variable swing trajectories within a single period on the robot's swimming performance warrants further investigation.

Chapter 5

A Robotic Fish with Tunable Bistability

High maneuverability and energy efficiency are crucial for underwater robots to perform tasks in engineering practice. In nature, fish are excellent swimmers owing to their flexible and precise control of the tail, which allows them to freely transform between the smooth flapping and the motion of rapid response so that they can move with dexterity. And this can all be deliberately employed for better robotic swimmers. A critical issue for efficient robotic swimmers is the appropriate design and control of an appropriate propulsion system. In this chapter, we propose a highly controllable elastic tail for an untethered robotic swimmer, which is composed of a parallel linkage mechanism and an elastic spine. Through the accurate trajectory control of the endpoint of the spine via the parallel mechanism, the tail possesses tunable bistability, consequently leading to the ability of flexible switching between motion modes. The robot can perform smooth swing motion of the monostable mode and rapid impulsive motion of the bistable mode. With controllable bistability, the propulsion system can demonstrate higher forward and turning speeds, a smaller turning radius, and lower energy consumption across a wide range of speeds through motion mode switching. It is also noted that the continuous morphology of tail allows the robot to steer with the most effective tail beating trajectory, thus leading to good maneuverability.

The rest of this chapter is structured as follows. Section 5.1 illustrates the hardware implementation of the robot including mechanical design and electronic components. In Section 5.2, inverse kinematics and theoretical models of both monostable and bistable

modes are derived and analyzed to assist the motion control of robot and predict the nonlinear behaviors of the elastic spine. Section 5.3 introduces detailed experimental setups involving tracking system and thrust measurement system. Besides, the method of statistical analysis is also provided. Section 5.4 presents some simulation and experimental results to explore the impact of different control trajectories on the propulsion performance of the robot. The comparisons between our robot with the reported robotic fish from the literature are presented in Section 5.5 to demonstrate the effectiveness of the proposed method on swimming performance improvement of fishlike robots. Finally, Section 5.6 concludes the chapter.

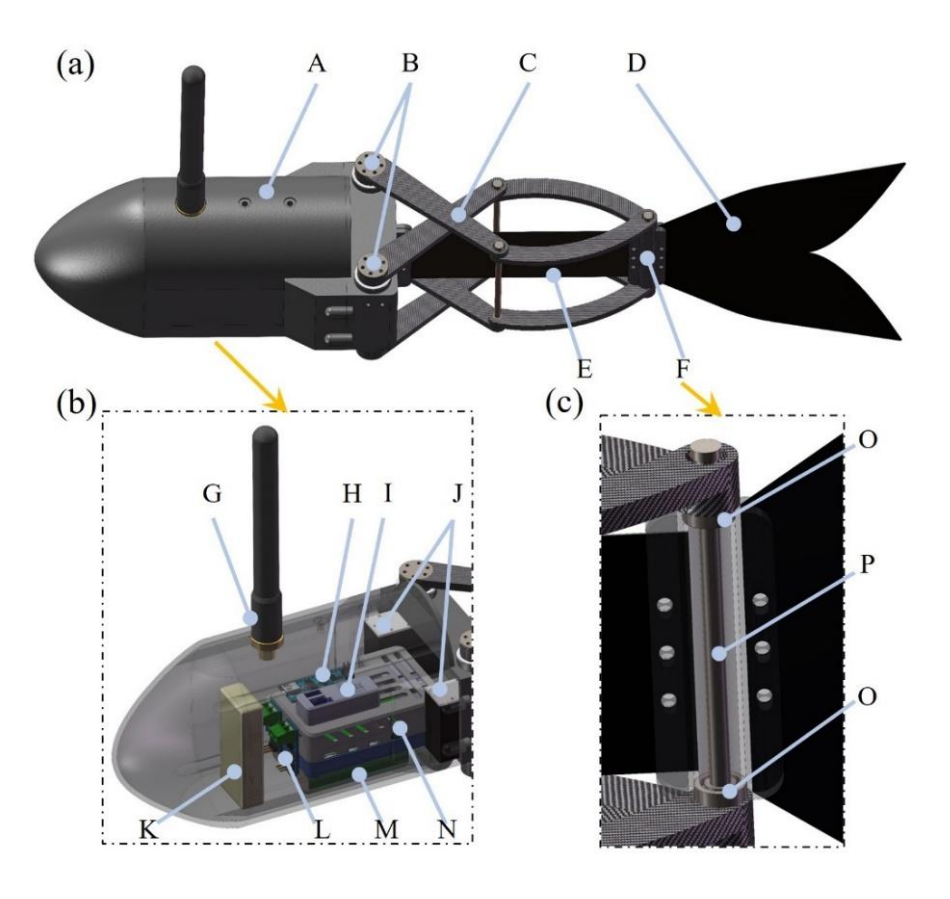


Fig. 5.1: System design of the robot: it consists of a rigid head, an active controlled flexible tail, and a passive compliant caudal fin. (a) Mechanical structure. (b) Electronic components. (c) Structure of passive joint. A: robot head, B: active joints, C: parallel mechanism, D: caudal fin, E: elastic spine, F: passive rotational joint, G: antenna of the receiver, H: Arduino nano, I: TTL/USB converter, J: servo motors, K: battery for micro-controller, L: current sensors, M: battery for motors, N: micro-controller, O: bearing, P: shaft.

5.1 Hardware Implementation

5.1.1 Mechanical design

The designed robotic fish is shown in Fig. 5.1. The robot mainly consists of three parts: a rigid robotic head, an elastic tail, and a compliant caudal fin. The rigid head is a waterproof container to house the electronic components. For the tail, a steel strip connected to the head is adopted as the elastic spine and is actively actuated by a parallel linkage mechanism which is a double-layer X structure composed of eight bars. One side of the parallel mechanism is connected to the head by two active rotational joints, and another side is connected to the spine by a passive rotational joint. The caudal fin is fixed on the end side of the passive rotational joint. The dimensions of the entire robot are 550(L) x 106(W) x 120(H) mm³ and it weighs 1.8 kg. The rigid head was printed with the material of ABS plastic by the 3D printer and was sealed by silicon rubber. Each bar of the parallel mechanism was fabricated by CNC and was made up of carbon fiber, which is lightweight but has high strength. The materials of the elastic spine and the caudal fin are 65Mn steel and carbon fiber respectively, and both shapes of them were produced by laser cutting. The water resistance of two active rotational joints was promised by the rotary sealing ring (Trelleborg Turcon). The values of the main structural parameters of the robot, which are defined and used in the theoretical models in the subsequent sections, are summarized in Table 5.1.

Table 5.1: Structural parameters of the robotic fish

Parameters	Value	Parameters	Value
L_1	10.5 cm	$\mathcal{Y}^h_{\mathcal{C}}$	0.04 m
L_2	10 cm	N	14
L_{s}	14 cm	$T_{\scriptscriptstyle S}$	0.35 mm
d_1	2.6 cm	$E_{\scriptscriptstyle S}$	200 GPa
\mathcal{Y}_A^h	-0.04 m	$I_{\scriptscriptstyle S}$	$1.79 \times 10^{-5} \mathrm{cm}^4$

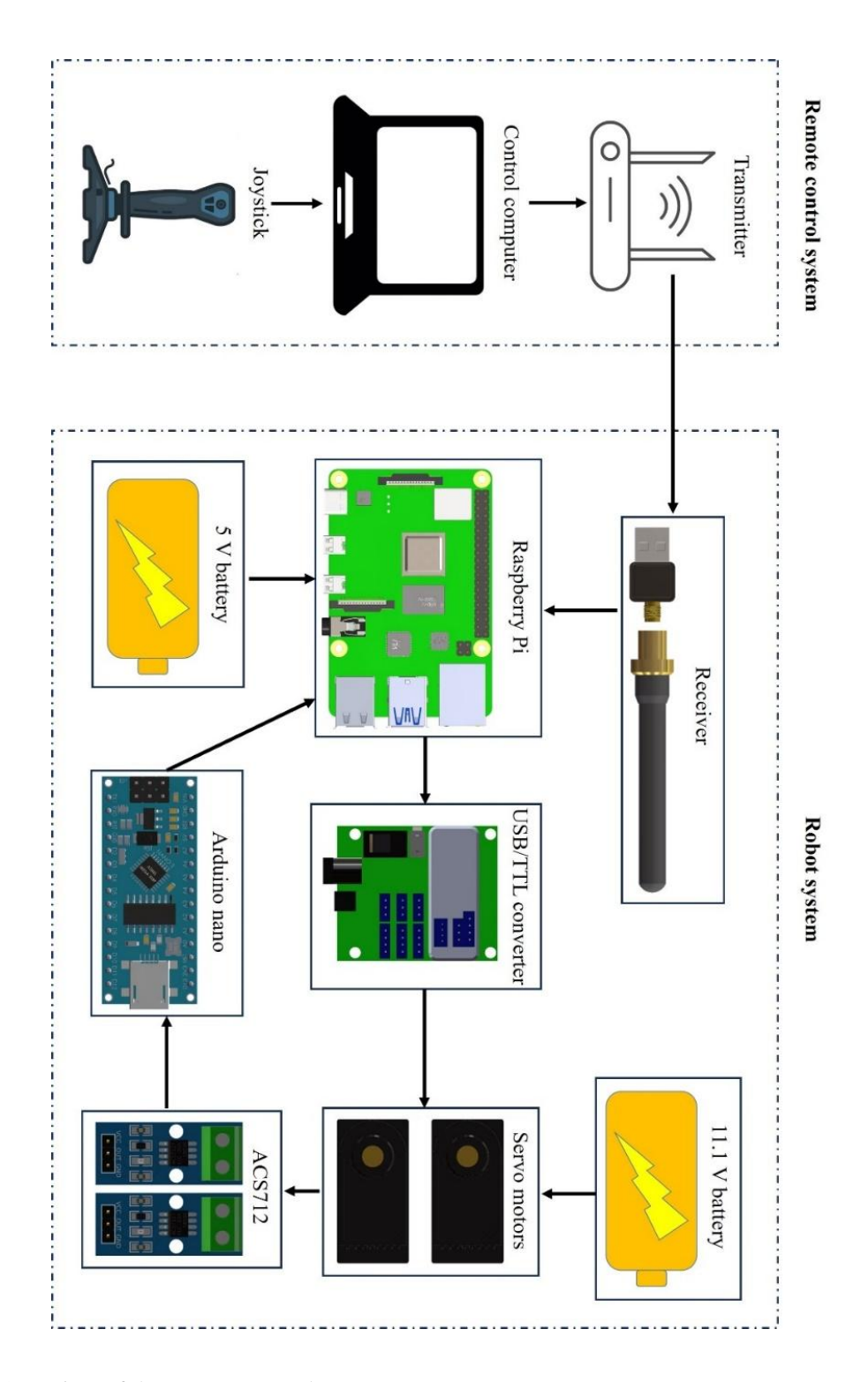


Fig. 5.2: Overview of the remote-control system.

5.1.2 Electronic components

The flow diagram of the electronic components is presented in Fig. 5.2. The main microcontroller is a Raspberry Pi 4B, which is used to control motors and acquire data from

sensors. The active rotational joints are actuated by two servo motors with the normal torque of 2.5 Nm. The communication between the main controller and the motors relies on one TTL/USB converter. Two sensors ACS712 are able to measure the current of two motors and the data is read by the Arduino nano. Two rechargeable batteries are used to power the controller (5 V) and the motors (11.1 V). Wireless communication between the Raspberry Pi and the computer is achieved by the 2.4 GHz transmitter and receiver.

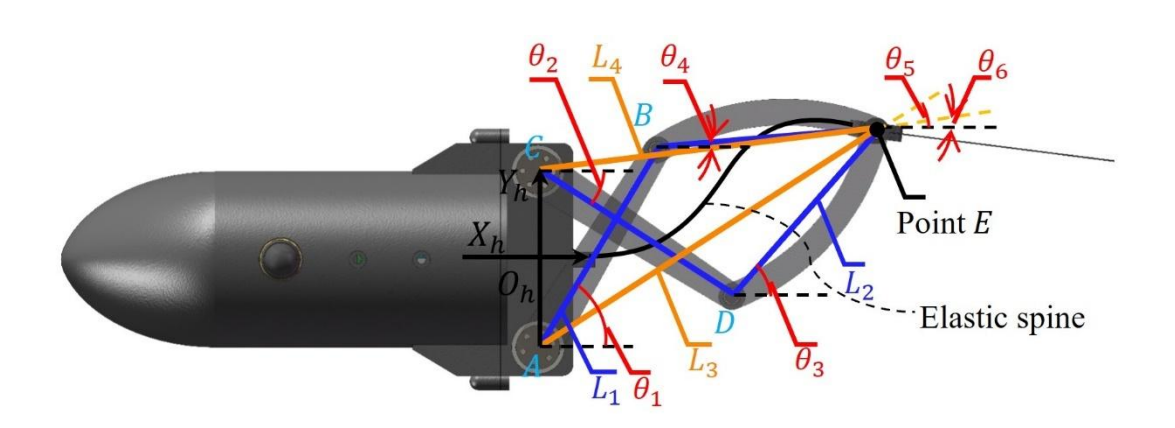


Fig. 5.3: Defined parameters for the kinematics of parallel mechanism.

5.2 Mathematical Modeling

5.2.1 Inverse kinematics

The motion of the tail is controlled by the predefined trajectory of point E to realize different swimming modes. Thus, the inverse kinematics of the parallel mechanism was applied to derive the control laws of two servo motors. The parameters of the structure are prescribed in Fig. 5.3. $O_h X_h Y_h$ denotes the body-fixed coordinate frame on the center of AC. L_1 represents the distance of AB and CD. L_2 is the distance of BE and DE. L_3 and L_4 are the distance of AE and CE, respectively. $\{\theta_1, \theta_2, \theta_3, \theta_4, \theta_5, \theta_6\}$ denote the angles between the axis $O_h X_h$ and $\{AB, CD, DE, BE, AE, CE\}$, respectively. The vector loop-closure equations of the

parallel mechanism can be obtained as

$$\begin{cases}
L_3 e^{i\theta_5} = L_1 e^{i\theta_1} + L_2 e^{i\theta_4} \\
L_4 e^{i\theta_6} = L_1 e^{i\theta_2} + L_2 e^{i\theta_3}
\end{cases}$$
(5.1)

where L_3 , L_4 , θ_5 , and θ_6 can be calculated by

$$\begin{cases} L_{3} = \sqrt{(x_{E}^{h} - x_{A}^{h})^{2} + (y_{E}^{h} - y_{A}^{h})^{2}} \\ L_{4} = \sqrt{(x_{E}^{h} - x_{C}^{h})^{2} + (y_{E}^{h} - y_{C}^{h})^{2}} \\ \theta_{5} = \arctan \frac{y_{E}^{h} - y_{A}^{h}}{x_{E}^{h} - x_{A}^{h}} \\ \theta_{6} = \arctan \frac{y_{E}^{h} - y_{C}^{h}}{x_{E}^{h} - x_{C}^{h}} \end{cases}$$
(5.2)

The above equations can be simplified and then we can obtain the following equations.

$$\begin{cases}
2L_1L_3\cos(\theta_1 - \theta_5) + L_2^2 - L_1^2 - L_3^2 = 0 \\
2L_1L_4\cos(\theta_2 - \theta_6) + L_2^2 - L_1^2 - L_4^2 = 0
\end{cases}$$
(5.3)

By solving equations (5.3), the control laws of two motors can be obtained as

$$\begin{cases} \theta_{1} = \left\| \arccos\left(\frac{L_{3}^{2} + L_{1}^{2} - L_{2}^{2}}{2L_{1}L_{3}}\right) \right\| + \theta_{5} \\ \theta_{2} = -\left\| \arccos\left(\frac{L_{4}^{2} + L_{1}^{2} - L_{2}^{2}}{2L_{1}L_{4}}\right) \right\| + \theta_{6} \end{cases}$$
(5.4)

5.2.2 Monostable mode

Fig. 5.4 demonstrates the trajectory generation of the monostable mode, which is part of a circle and controlled by three parameters as follows. Here, γ is the length between the circle center and the start point of the elastic spine. The distance from the circle center to the controlled rotational joint (point E) is the radius of the trajectory, denoted by r. The angle α_c is between the midline of the robot and the radius connected to the endpoint of the trajectory and used to control the tail beat amplitude. To realize this mode, we need to derive the

swinging trajectory for point E of the parallel mechanism first. Based on the defined parameters γ , r, and α_c , the trajectory can be calculated by the following equations.

$$\begin{cases} {}^{h}X_{E} = d_{1} + \gamma + r \cos \alpha_{c} \\ {}^{h}Y_{E} = r \sin \alpha_{c} \end{cases}$$
 (5.5)

where d_1 is the distance between the starting point of the elastic spine and the origin of the head frame $O_h X_h Y_h$.

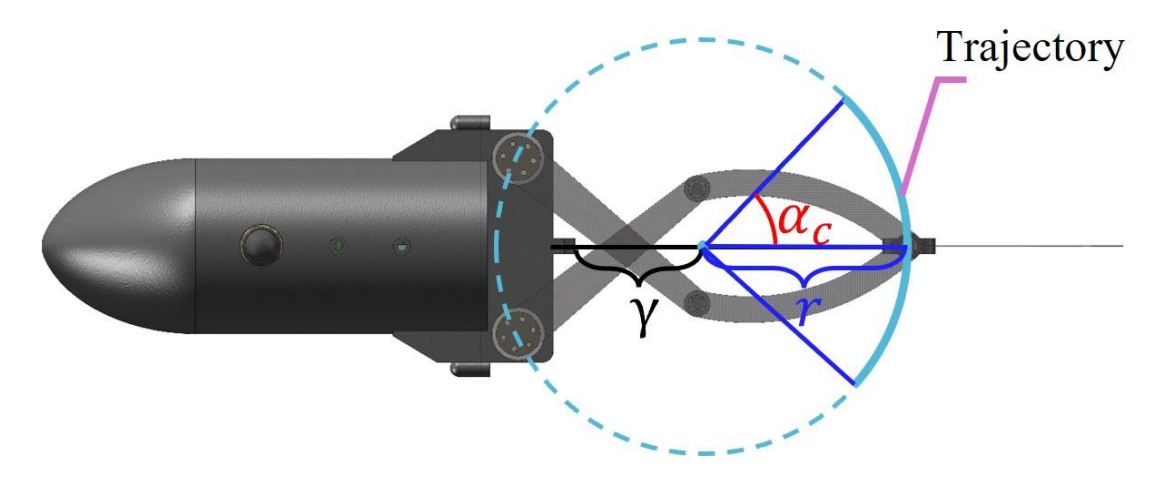


Fig. 5.4: Monostable motion mode: the tail beat trajectory is defined by three parameters $(\gamma, r, \text{ and } \alpha_c)$.

The rhythmic oscillation of the tail can be controlled by the following equation.

$$\alpha_c = a \sin 2\pi f t + b \tag{5.6}$$

where a, f, and b are amplitude, frequency, and bias angle, respectively.

Substituting equations (5.5) and (5.6) into the equations of the inverse kinematics, the control angles of two motors for the monostable mode can be obtained as shown in equations (5.4).

The mathematical model to calculate the deformed shape, strain energy, etc. of the elastic spine for the monostable was derived by the chained beam constraint model (CBCM) [146, 147]. Using the chained beam constraint model, the elastic spine is separated equally

into N segments as shown in Fig. 5.5. Each segment can be assumed as a cantilever beam. And a local coordinate system $O_{\zeta}X_{\zeta}Y_{\zeta}$ is attached to the start point of the ζ -th segment. $F_{\zeta X}$, $F_{\zeta Y}$, and M_{ζ} are transverse force, axial force, and moment respectively subject to the free end of the ζ -th segment, which results in translation and rotation displacements X_{ζ} , Y_{ζ} , and β_{ζ} . And then we can obtain the following equations about the relation between the force and displacement for the elastic spine.

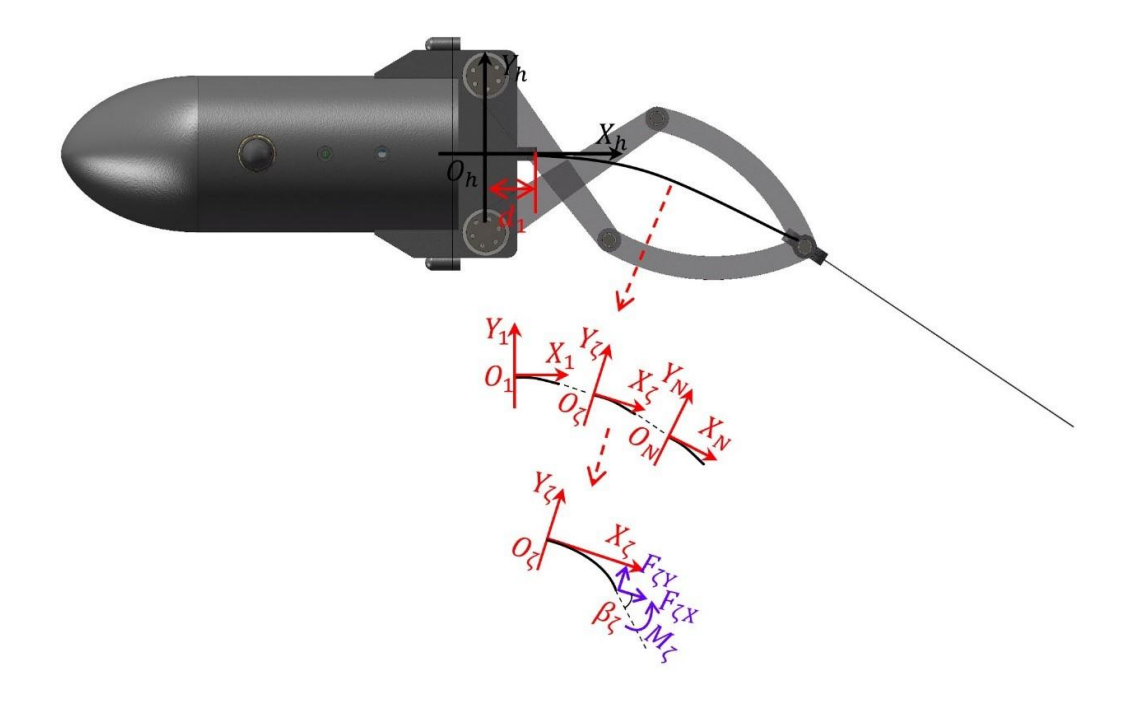


Fig. 5.5: Coordinate frames for the monostable motion mode.

$$\begin{cases}
\begin{bmatrix} f_{\zeta y} \\ m_{\zeta} \end{bmatrix} = R_{1} \begin{bmatrix} y_{\zeta} \\ \beta_{\zeta} \end{bmatrix} + f_{\zeta x} R_{2} \begin{bmatrix} y_{\zeta} \\ \beta_{\zeta} \end{bmatrix} + f_{\zeta x}^{2} R_{3} \begin{bmatrix} y_{\zeta} \\ \beta_{\zeta} \end{bmatrix} \\
x_{\zeta} = \frac{t_{s}^{2} f_{\zeta x}}{12} - \frac{1}{2} [y_{\zeta} \quad \beta_{\zeta}] R_{2} \begin{bmatrix} y_{\zeta} \\ \beta_{\zeta} \end{bmatrix} - f_{\zeta x} [y_{\zeta} \quad \beta_{\zeta}] R_{3} \begin{bmatrix} y_{\zeta} \\ \beta_{\zeta} \end{bmatrix}
\end{cases} (5.7)$$

where all the parameters are normalized as

$$t_{s} = \frac{NT_{s}}{L_{s}}, x_{\zeta} = \frac{NX_{\zeta}}{L_{s}}, y_{\zeta} = \frac{NY_{\zeta}}{L_{s}}, f_{\zeta X} = \frac{F_{\zeta X}L_{s}^{2}}{N^{2}EI}, f_{\zeta Y} = \frac{F_{\zeta Y}L_{s}^{2}}{N^{2}EI}, m_{\zeta} = \frac{M_{\zeta}L_{s}}{NEI}$$
(5.8)

And T_s is the thickness of the elastic spine. E is the Young's modulus. I is the moment of

inertial. R_1 , R_2 , and R_3 are the matrices of non-dimensional beam characteristic coefficients listed as follows.

$$R_{1} = \begin{bmatrix} 12 & -6 \\ -6 & 4 \end{bmatrix}, R_{2} = \begin{bmatrix} \frac{6}{5} & -\frac{1}{10} \\ -\frac{1}{10} & \frac{2}{15} \end{bmatrix}, R_{3} = \begin{bmatrix} -\frac{1}{700} & \frac{1}{1400} \\ \frac{1}{1400} & -\frac{11}{6300} \end{bmatrix}$$
 (5.9)

The strain energy stored in each segment of the deflected spine can be obtained by

$$v_{\zeta} = \frac{1}{2} \frac{t_s^2 f_{\zeta X}^2}{12} + \frac{1}{2} [y_{\zeta} \quad \beta_{\zeta}] R_1 \begin{bmatrix} y_{\zeta} \\ \beta_{\zeta} \end{bmatrix} - \frac{1}{2} f_{\zeta X}^2 [y_{\zeta} \quad \beta_{\zeta}] R_3 \begin{bmatrix} y_{\zeta} \\ \beta_{\zeta} \end{bmatrix}$$
 (5.10)

Then the total strain energy stored in the elastic spine can be calculated by the sum of the strain energy stored in each segment as

$$V_{s} = \sum_{1}^{N} \frac{v_{\zeta} NEI}{L_{s}} \tag{5.11}$$

The force equations of the ζ -th segment are expressed as

$$\begin{bmatrix} \cos \varphi_{\zeta} & -\sin \varphi_{\zeta} \\ \sin \varphi_{\zeta} & \cos \varphi_{\zeta} \end{bmatrix} \begin{bmatrix} F_{\zeta X} \\ F_{\zeta Y} \end{bmatrix} = \begin{bmatrix} F_{EX_h} \\ F_{EY_h} \end{bmatrix}$$
 (5.12)

where φ_{ζ} is the angle between the coordinate frame on the ζ -th segment and the coordinate frame on the robot head and is expressed as

$$\varphi_{\zeta} = \sum_{\kappa=1}^{\zeta-1} \beta_{k} \tag{5.13}$$

The moment equations of each segment can be derived as

$$\begin{cases}
M_{\zeta} = 0, \ \zeta = N \\
M_{\zeta} = M_{\zeta-1} - F_{\zeta X} Y_{\zeta} - F_{\zeta Y} \left(\frac{L_s}{N} + X_{\zeta}\right), \zeta \neq N
\end{cases}$$
(5.14)

Then we can obtain the following displacement equations of the elastic spine in the monostable motion mode.

$$\sum_{\zeta=1}^{N} \left(\begin{bmatrix} \cos \varphi_{\zeta} & -\sin \varphi_{\zeta} \\ \sin \varphi_{\zeta} & \cos \varphi_{\zeta} \end{bmatrix} \begin{bmatrix} L_{s} \\ N \\ Y_{\zeta} \end{bmatrix} \right) + \begin{bmatrix} d_{1} \\ 0 \end{bmatrix} = \begin{bmatrix} {}^{h}X_{E} \\ {}^{h}Y_{E} \end{bmatrix}$$
 (5.15)

The deformed shape of the ζ -th segment of the elastic spine can be calculated by the following equations.

$$y_{s\zeta}(x_{s\zeta}) = \begin{cases} a_1 + a_2 x_{s\zeta} + a_3 \sin\left(\sqrt{-f_{\zeta x}} x_{s\zeta}\right) + a_4 \cos\left(\sqrt{-f_{\zeta x}} x_{s\zeta}\right), \ f_{\zeta x} < 0 \\ b_1 + b_2 x_{s\zeta} + b_3 e^{\sqrt{f_{\zeta x}} x_{s\zeta}} + b_4 e^{-\sqrt{f_{\zeta x}} x_{s\zeta}}, \ f_{\zeta x} > 0 \\ c_1 + c_2 x_{s\zeta} + c_3 x_{s\zeta}^2 + c_4 x_{s\zeta}^3, \ f_{\zeta x} = 0 \end{cases}$$
 (5.16)

where $x_{s\zeta} \in [0, 1]$. a_i, b_i , and c_i is the coefficient and can be calculated by substituting the boundary conditions of a cantilever beam into equations (5.16) as follows.

$$y_{s\zeta}(0) = 0, y'_{s\zeta}(0) = 0, y_{s\zeta}(1) = y_{\zeta}, y'_{s\zeta}(1) = \beta_{\zeta}$$
 (5.17)

Then the deformed shape of the elastic spine can be obtained by the coordinate transformation between the local coordinate frame and the coordinate frame on the robot head as follows.

$$\begin{bmatrix}
{}^{h}X_{s\zeta} \\
{}^{h}Y_{s\zeta}
\end{bmatrix} = \begin{bmatrix}
\cos \varphi_{\zeta} & -\sin \varphi_{\zeta} \\
\sin \varphi_{\zeta} & \cos \varphi_{\zeta}
\end{bmatrix} \begin{bmatrix}
x_{s\zeta} \left(\frac{L_{s}}{N} + X_{\zeta}\right) \\
\underline{y_{s\zeta}L_{s}} \\
N
\end{bmatrix} + \begin{bmatrix}
{}^{h}X_{s\zeta_{0}} \\
{}^{h}Y_{s\zeta_{0}}
\end{bmatrix}$$
(5.18)

where $\begin{bmatrix} {}^h X_{s\zeta 0} & {}^h Y_{s\zeta 0} \end{bmatrix}^T$ is the coordinate of the start point of each segment in the robot head frame.

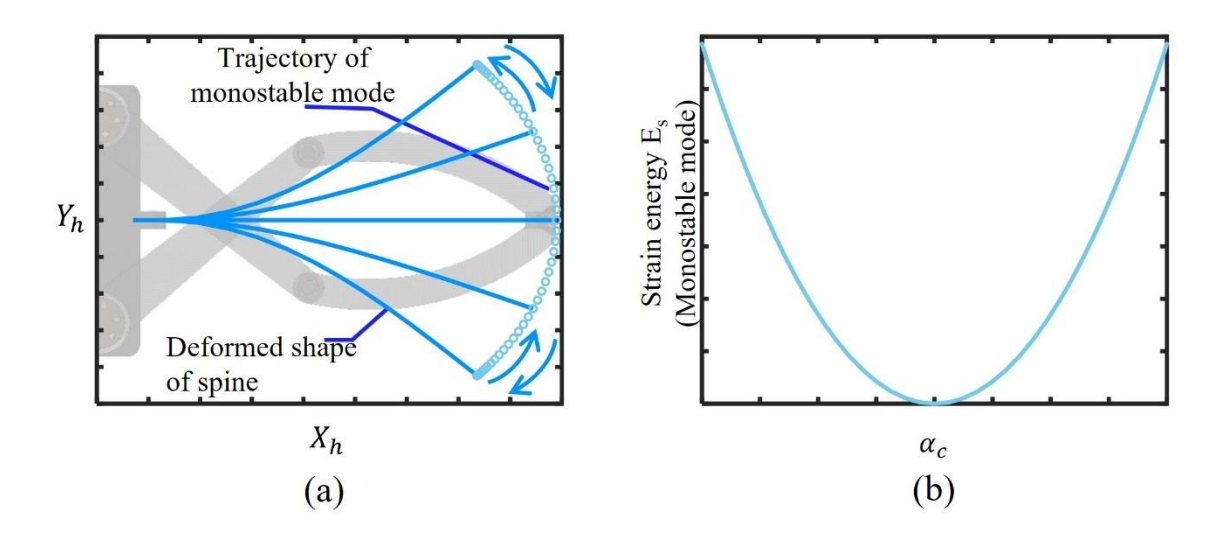


Fig. 5.6: One cycle of monostable motion: (a) Deformed shape. (b) Strain energy.

With the help of the above derived theoretical model, the deformed shape and strain energy of the elastic spine can be computed during one cycle of monostable motion. The deformed shape of the elastic spine during the motion of the monostable mode is presented in Fig. 5.6(a). For each motion cycle of monostable mode, point E passes the point where the elastic spine is in the undeformed state. Hence, the minimum strain energy of the elastic spine is 0 and is located at only one point of the trajectory of the monostable mode as seen in Fig. 5.6(b).

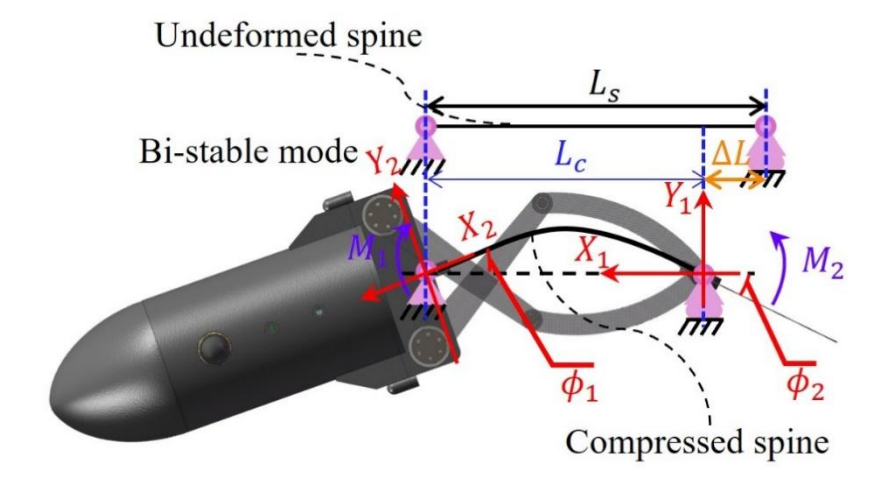


Fig. 5.7: Bistable motion mode: compressing the spine to form a buckling beam.

5.2.3 Bistable mode

The bistable mode can be achieved by precompressing the elastic spine as shown in Fig. 5.7. When the endpoint E of the parallel mechanism is assumed to be fixed at one point and the head is assumed to rotate around a fixed point, the elastic spine can be regarded as a pinned-pinned buckled beam. In the initial stage of the bistable locomotion mode, there is a prestored strain energy of the elastic spine due to the precompression. It is known that there are two stable positions of this mechanism, which are symmetrical about the horizontal line. When the input pivot (ϕ_1 or ϕ_2) of the elastic spine is actuated by rotation, a phenomenon of instantaneous and rapid change in position and speed i.e., snap-through, would be triggered between the switch of two stable states. In order to get the control trajectory of the bistable locomotion mode, three frames $(O_1X_1Y_1, O_2X_2Y_2, \text{ and } O_hX_hY_h)$ were established. Through the position and rotation transformations between the frames $O_1X_1Y_1, O_2X_2Y_2$, and $O_hX_hY_h$, the trajectory of the bistable mode can be obtained by solving the following equations.

$$\begin{cases} {}^{h}P_{E} = {}^{h}P_{2} + {}^{h}R_{2}{}^{2}P_{E} \\ {}^{1}P_{F} = {}^{1}R_{2}{}^{2}P_{F} \end{cases}$$
 (5.19)

where 1P_E , 2P_E , and hP_E denote the coordinates of the point E in the frames $O_1X_1Y_1$, $O_2X_2Y_2$, and $O_hX_hY_h$, respectively. hP_2 is the position vector of the origin of the frame $O_2X_2Y_2$ in the frame $O_hX_hY_h$. hR_2 and 1R_2 are the rotation matrices between the frames $O_hX_hY_h$ and $O_2X_2Y_2$ and between the frames $O_1X_1Y_1$ and $O_2X_2Y_2$, respectively. hP_2 , hR_2 , and 1R_2 are expressed as

$${}^{h}P_{2} = \begin{bmatrix} \delta \\ 0 \end{bmatrix}, {}^{h}R_{2} = \begin{bmatrix} -1 & 0 \\ 0 & 1 \end{bmatrix}, {}^{1}R_{2} = \begin{bmatrix} \cos\phi_{1} & -\sin\phi_{1} \\ \sin\phi_{1} & \cos\phi_{1} \end{bmatrix}$$
 (5.20)

In equation (5.20), only ϕ_1 is unknown. To obtain the angle ϕ_1 , we need to derive the theory model of the elastic spine during its movement of bistable mode. The CBCM method

cannot provide an analytical result for ϕ_1 , and only numerical results can be obtained by solving multiple equations. As a result, the control trajectory of point E cannot be straightforwardly determined, which is inefficient and not ideal for controlling the robot. As mentioned above, the spine can be regarded as the pinned-pinned buckled beam. Thus, the Euler-Bernoulli beam theory can be applied to derive the analytical solutions for many parameters, including ϕ_1 [148]. Then we can get the following equation of the bending moment.

$$M(\epsilon) = -F_{X_1}Y_1(\epsilon) + F_{Y_1}X_1(\epsilon) + M_2$$
 (5.21)

where ϵ is the arclength of the elastic spine.

The motion characteristics of the spine including ϕ_1 , the strain energy, etc. can be derived by equation (5.21). $X_1(\epsilon)$ in equation (5.21) can be linearized in the following form.

$$X_1(\epsilon) \cong \frac{L_c}{L_s} \epsilon \tag{5.22}$$

And the boundary conditions of the pinned-pinned beam are expressed as follows.

$$Y_1(\epsilon = 0) = 0, Y_1(\epsilon = L_s) = 0, Y_1''(\epsilon = 0) = 0$$
 (5.23)

By substituting the equation (5.22) and the boundary conditions (5.23) into equation (5.21), we can obtain the following equation.

$$Y_1(\epsilon) = Q\left(\sin\left(\frac{aL_s\epsilon}{L_s}\right) - \frac{\sin(aL_s)\epsilon}{L_s}\right)$$
 (5.24)

where $a = \sqrt{\frac{F_{X_1}}{EI}}$, and Q can be derived by the precompression length of the elastic spine as follows.

$$\Delta L = L_s - L_c = \frac{1}{2} \int_0^{L_s} (Y_1')^2 d\epsilon$$
 (5.25)

Thus Q can be expressed as

$$Q = \pm 2L_s \sqrt{\frac{\Delta L}{L_s}} \left((aL_s)^2 + aL_s \frac{\sin(2aL_s)}{2} + \cos(2aL_s) - 1 \right)^{-\frac{1}{2}}$$
 (5.26)

Then we can derive two pivots' angles as

$$\begin{cases} \phi_1 = Y_1'(L_s) = \frac{Q}{L_s} (aL_s \cos(aL_s) - \sin(aL_s)) \\ \phi_2 = Y_1'(0) = \frac{Q}{L_s} (aL_s - \sin(aL_s)) \end{cases}$$
 (5.27)

The strain energy of the elastic spine can be obtained by

$$V_s = \frac{EI}{2} \int_0^{L_s} \left(\frac{d^2 Y_1}{d\epsilon^2} \right) d\epsilon = \frac{1}{4} \frac{EI}{L_s} \left(\frac{Q}{L_s} \right)^2 (aL_s)^3 \left(aL_s - \frac{\sin(2aL_s)}{2} \right)$$
 (5.28)

Various nonlinear behaviors of the elastic spine during one cycle of the bistable motion can be predicted by using the above derived theoretical model as shown in Fig. 5.8. Figs. 5.8(a) and (b) show the deformed shape of the elastic spine and its strain energy variation during this process. When the instantaneous and rapid release of the strain energy occurs, the elastic spine snaps from shape II to shape III or from shape IV to shape I. The gap between the maximum energy and the minimum energy is defined as the energy barrier that needs to be overcome to achieve snapping. Fig. 5.8(c) illustrates the relation between the angles of the two pivots of the elastic spine during one motion cycle. Fig. 5.8(d) shows that different precompressions and thicknesses of the elastic spine can lead to different energy barriers.

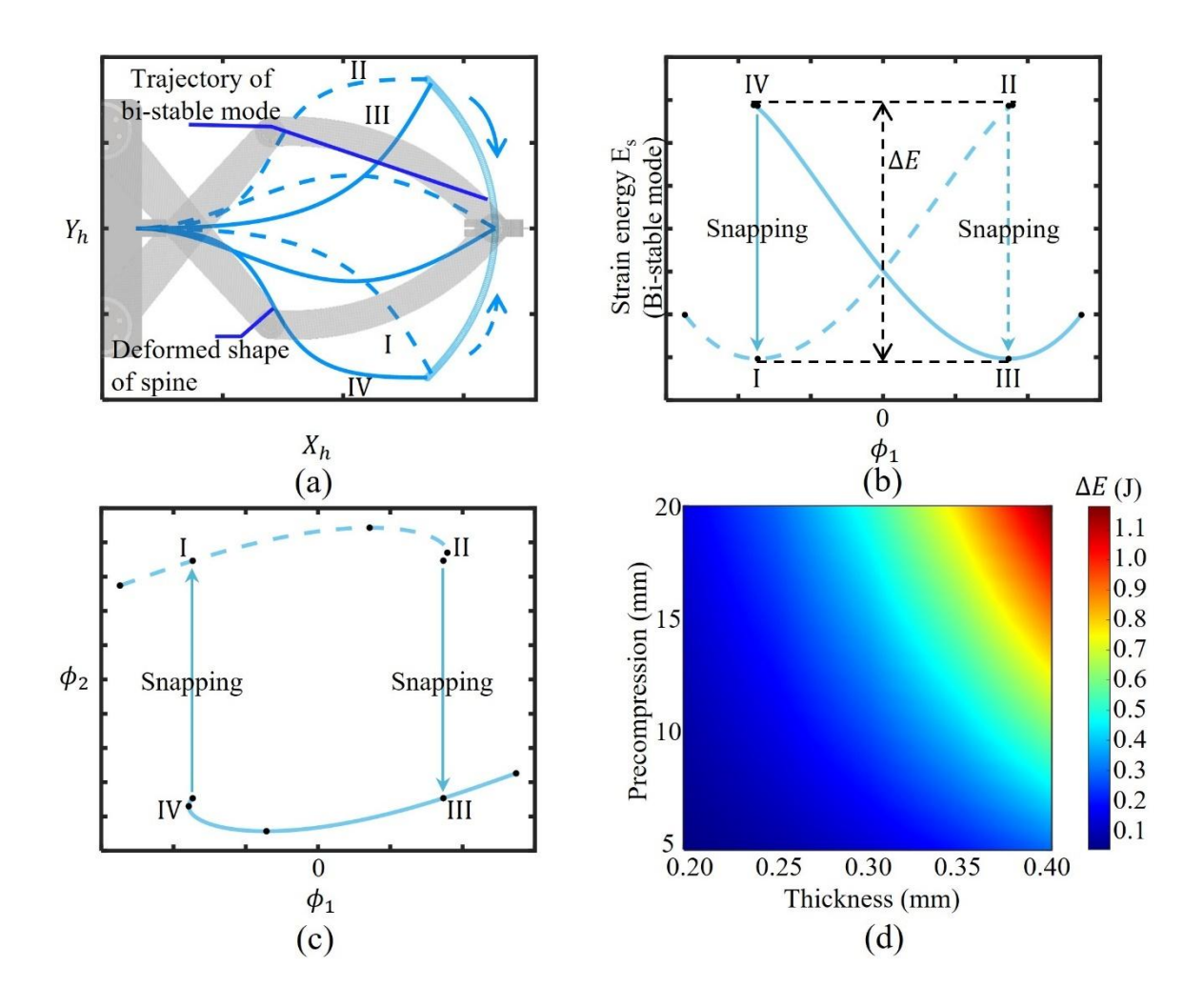


Fig. 5.8: One cycle of bistable motion: (a) Deformed shape. (b) Strain energy. (c) Angles relation. (d) Different compression and thickness of the spine result in different energy barrier ΔE for snapping.

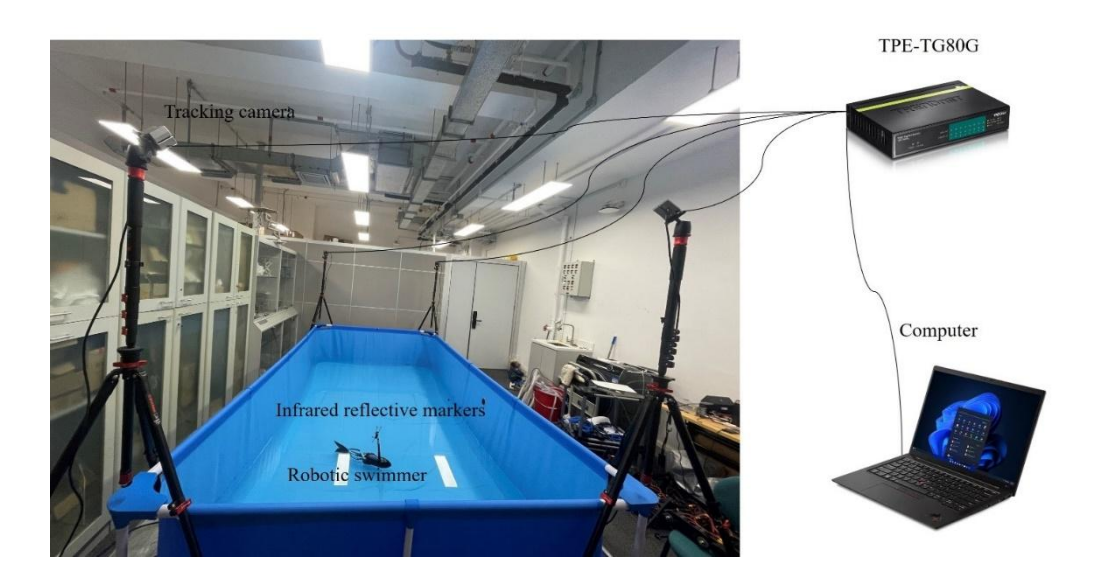


Fig. 5.9: Tracking setup for the swimming experiments.

5.3 Experimental Setup and Methods

5.3.1 Free swimming tests

Free swimming tests were conducted in a small laboratory swimming pool with the dimensions of $4 \text{ m} \times 2 \text{ m} \times 1 \text{ m}$ as shown in Fig. 5.9. On the corners of the pool, four tracking cameras were installed at 3 m height. The tracking cameras were connected to the laptop by an 8-port Ethernet switch (TPE-TG80g) and cables. Infrared reflective markers were installed on the head of the robot. The setup can track the position of the robot while it swims in the pool. The tracking data was then used to get the trajectory and velocity information of the robot.

5.3.2 Power consumption evaluation

A separate rechargeable Li-ion battery with a voltage of 11.1 v and a capacity of 4900 mAh was used to power two servo motors. The servos used in the robotic fish are capable of providing feedback on a series of parameters including voltage and current. The sampling rate of the motor's feedback on voltage and current is about 10 Hz. According to the battery duration test, one fully charged battery can power the robot around 6 hours. For each testing case, a fully charged battery was used for around 30 minutes before being replaced by another fully charged battery. The voltage drop was small. The sampling rate of motor feedback on voltage is sufficient to collect accurate results. However, the current shows significant changes during testing because it is related to the output torque of motors. Therefore, the additional current sensors (ACS712 with a current range of 5 A) with high sampling rate (50 Hz) were decided to be used for ensuring high accuracy of current measurement. We connected two current sensors into the electric circuit to measure the current of the motors separately. The output of the current sensor is analog data, and the

Raspberry Pi does not have the analog-to-digital converter (ADC), thus an Arduino nano was utilized to read the current sensors through its built-in ADC and then the data was sent to and stored in the Raspberry Pi. Finally, the power can be evaluated by the voltage and current.

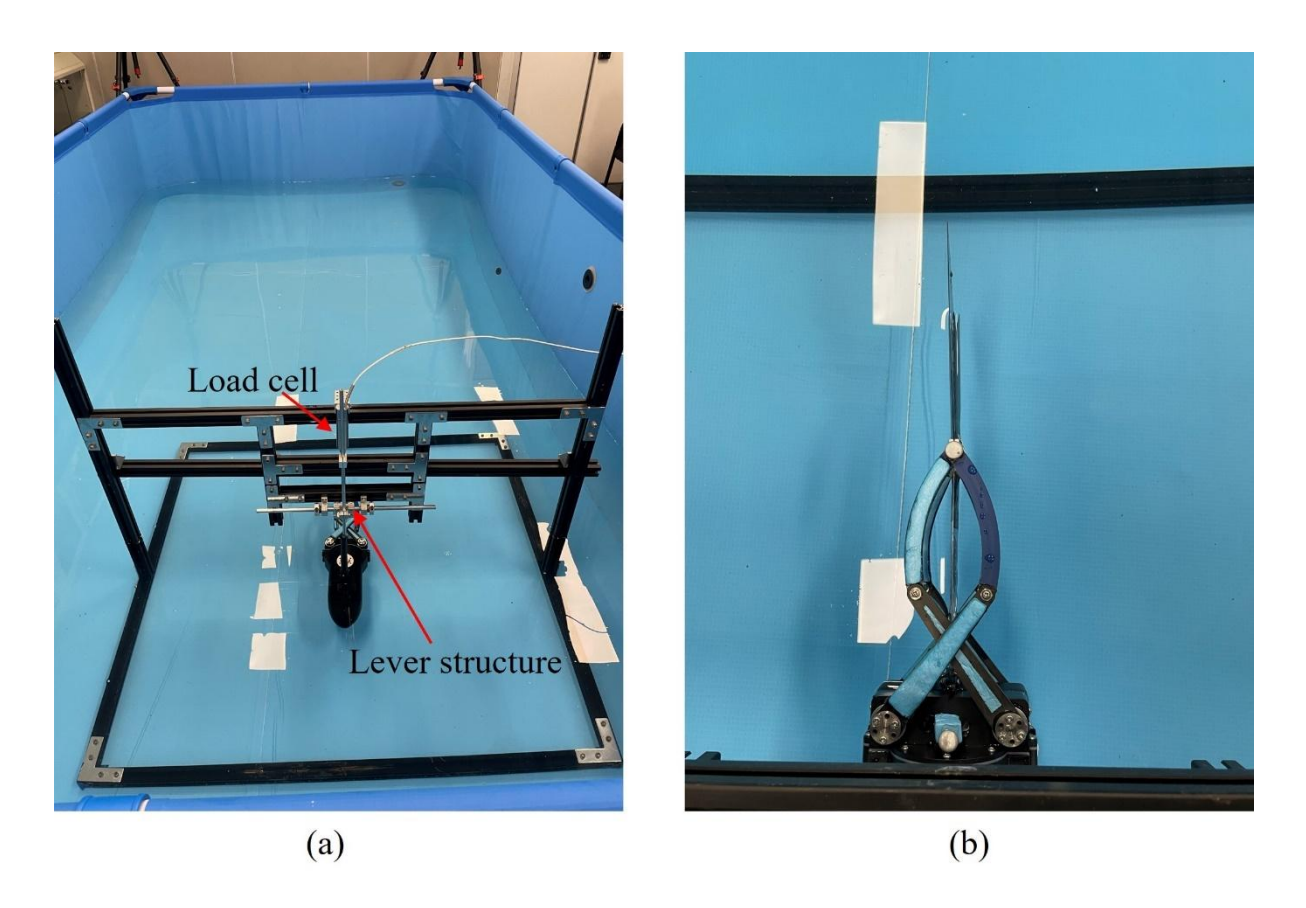


Fig. 5.10: (a) Thrust measurement system. (b) Trajectory tracking.

5.3.3 Thrust measurement and trajectory tracking of point E

A static frame, made up of the aluminum alloy sections, was used to fix the robot for measuring the thrust force (Fig. 5.10(a)) and tracking the trajectory of tail's endpoint E (Fig. 5.10(b)). The thrust measurement was achieved by a lever mechanism that was constructed by a series of rods and rolling bearings. A horizontal rod was fixed on the static frame, and it was connected to a vertical rod by the rolling bearings, which allows the vertical rod to rotate around the horizontal rod. One side of the vertical rod was fixed on the robot's head, and

another side was attached to a load cell (Omegadyne LC601-5). The measuring range of the load cell is around 20 N. A data acquisition card with the sampling rate of 200 Hz was used to collect the thrust data and is connected to a laptop. The infrared reflective markers were attached to the robot, and four tracking cameras, as shown in Fig. 5.9, were used to track the trajectory of the tail's endpoint E.

5.3.4 Statistical analysis

Testing was repeated for each measurement, and the average values represented the final results shown in figures. The uncertainty of the reported results contained in some figures was determined using the tested maximum and minimum values obtained from the repeated tests. To quantitatively analyze the performance improvement of the bistable mode compared to the monostable mode, the following indicators were defined.

$$IND_V = \frac{V_B - V_M}{V_M} \times 100\%$$
 (5.29)

$$IND_C = \frac{\text{CoT}_M - \text{CoT}_B}{\text{CoT}_M} \times 100\%$$
 (5.30)

$$IND_T = \frac{T_B - T_M}{T_M} \times 100\%$$
 (5.31)

$$AVG_{IND_T} = \frac{\sum IND_T(f)}{N_f}, f = 1, 1.5, ..., 4 \text{ Hz}$$
 (5.32)

where IND_V , IND_C , and IND_T are the quantitative indicators of the performance improvement of average velocity, CoT, and average thrust, respectively. AVG_{IND_T} represents the average value of the thrust improvement of all tested frequencies. N_f is the total number of testing cases. $\{V_B, V_M\}$, $\{\text{CoT}_B, \text{CoT}_M\}$, and $\{T_B, T_M\}$ denote the average velocity, CoT, and average thrust of bistable and monostable modes, respectively.

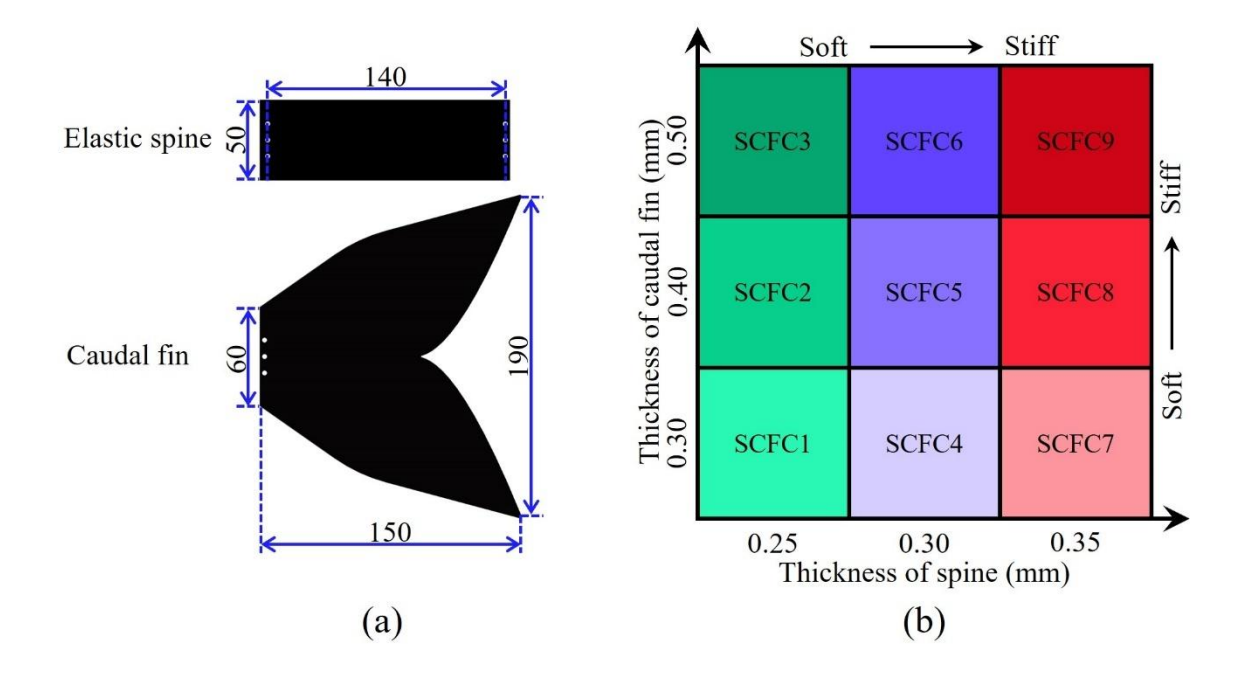


Fig. 5.11: (a) Dimensions of the elastic spine and caudal fin. The unit is millimeters. (b) Different thickness combinations of the elastic spine and caudal fin. SCFC is the abbreviation of Spine-Caudal-Fin Combination.

5.4 Simulation and Experimental Results

5.4.1 Stiffness coordination

The stiffness plays a crucial role in achieving efficient swimming of fish. In the proposed fishtail, two compliant elements need to be considered, including the elastic spine and the compliant caudal fin. The stiffness of the spine is not only one of the dominant factors in the energy barrier of the bistable locomotion mode but also together with the compliance of the caudal fin determines the kinematics of the tail during swimming. Therefore, the stiffness coordination between the spine and the caudal fin is important for the swimming performance of the robot and its influence is explored for both the monostable and bistable locomotion modes firstly. The stiffness is adjusted by varying the thickness, and other dimensions of the elastic spine and the caudal fin remain unchanged as shown in Fig.

5.11(a). The thickness sets of the spine and the caudal fin are {0.25 mm, 0.30 mm, 0.35 mm} and {0.3 mm, 0.4 mm, 0.5 mm} respectively. So, 9 cases in total of thickness combinations for the spine and the caudal fin are tested as presented in Fig. 5.11(b). Here, only three cases (SCFC1, SCFC5, and SCFC8) are selected for comparison, representing the best swimming performance of the robot with the elastic spine of three different thicknesses. More comparisons are provided in Figs. A1 and A2 (see Appendix A).

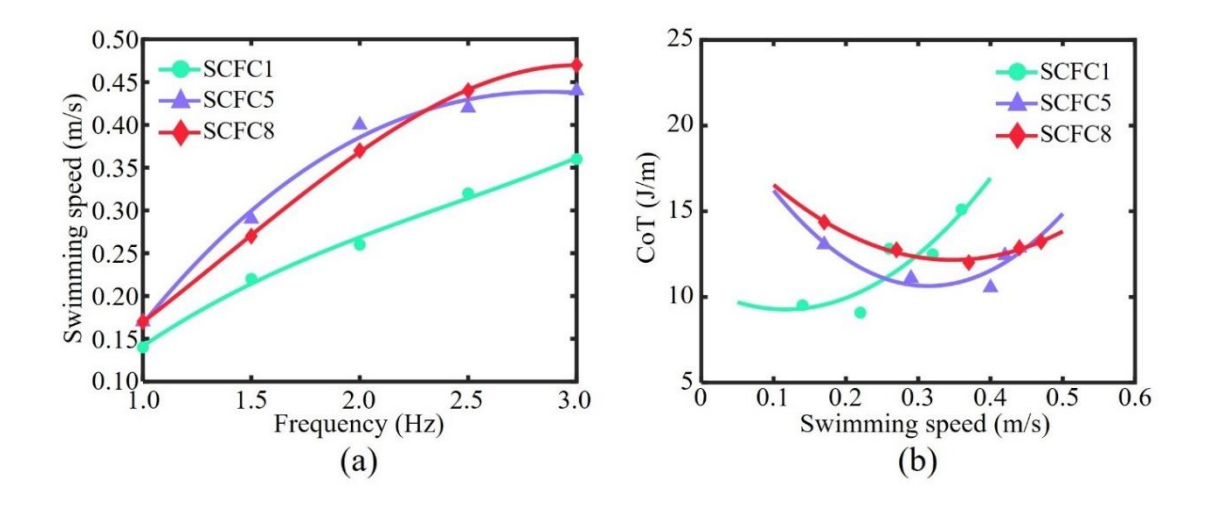


Fig. 5.12: (a) Swimming speed under different frequencies. (b) Cost of transport under different frequencies. The control parameters of the monostable mode are given as $\gamma = 2$ cm, $\alpha_c = 40^\circ$.

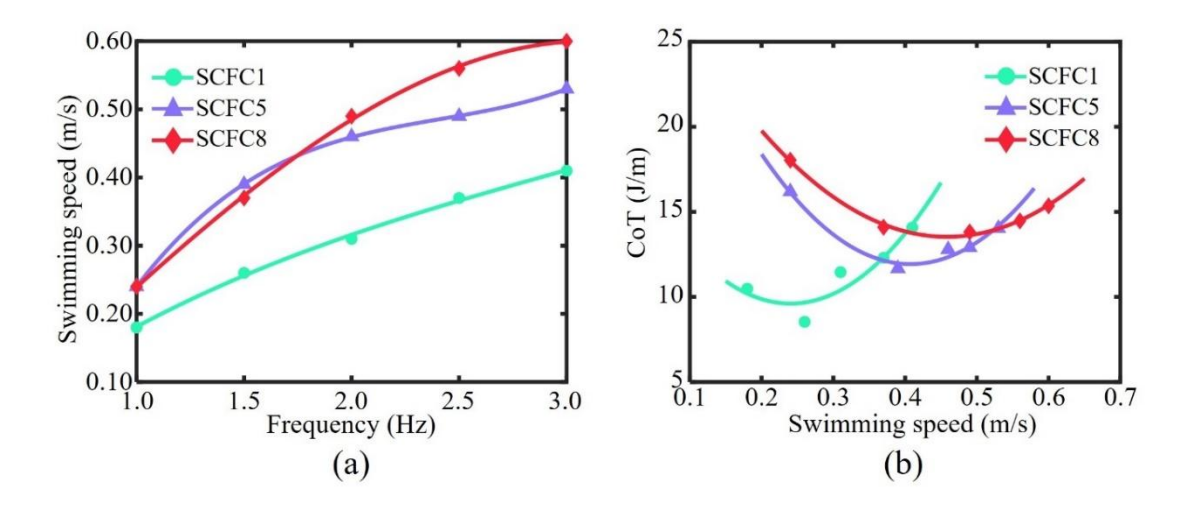


Fig. 5.13: (a) Swimming speed under different frequencies. (b) Cost of transport under different frequencies. The precompression length of the elastic spine of the bistable mode is set as $\Delta L = 10$ mm.

Figs. 5.12(a) and (b) demonstrate the results of the average swimming speed and the cost of transport for the monostable mode. The robot with SCFC1 swims the slowest under different tail beat frequencies. Before the frequency of 2.5 Hz, the robot with SCFC5 is the fastest, however, the speed of the robot with SCFC8 surpasses that of SCFC5 when the frequency rises above 2.5 Hz, and the SCFC8 achieves the highest speed among all cases for the monostable mode at the frequency of 3 Hz. For the results of CoT, no one case is always the most energy efficient. When the swimming velocity is under 0.25 m/s, the CoT of the robot with SCFC1 is the lowest. When the speed is in the range between 0.25 m/s and 0.44 m/s, the most energy efficient one turns into SCFC5. And as the speed continues to increase, the best one is SCFC8.

Figs. 5.13(a) and (b) show the average swimming speed and the cost of transport for the bistable mode. Similar conclusions about the effect of different cases of stiffness combinations on the monostable swimming mode can be found with the bistable mode, but the differences between different cases are more obvious. When the tail beat frequency is below 2 Hz, the swimming speeds of the robot with SCFC5 and SCFC8 are close to each other, and the robot with SCFC5 is slightly faster than the case of SCFC8, while SCFC8 performs much better on the velocity than the other two cases when the frequency is over 2 Hz. And the maximum speed is achieved with SCFC8 as well, which is about 0.60 m/s at the frequency of 3 Hz. When it comes to CoT, SCFC1 achieves the minimum CoT at speeds below 0.37 m/s. From the speed of 0.37 m/s to 0.53 m/s, the CoT of the robot with SCFC5 is minimal. When the speed exceeds 0.53 m/s, SCFC8 is most energy efficient.

According to the analysis above, no case can achieve the best performance in both swimming speed and CoT across the studied range of tail beat frequencies. However, SCFC8

enables the robot to obtain the maximum speed and the lowest CoT at high speed. Thus, for the subsequent tests, SCFC8 is selected for the robot.

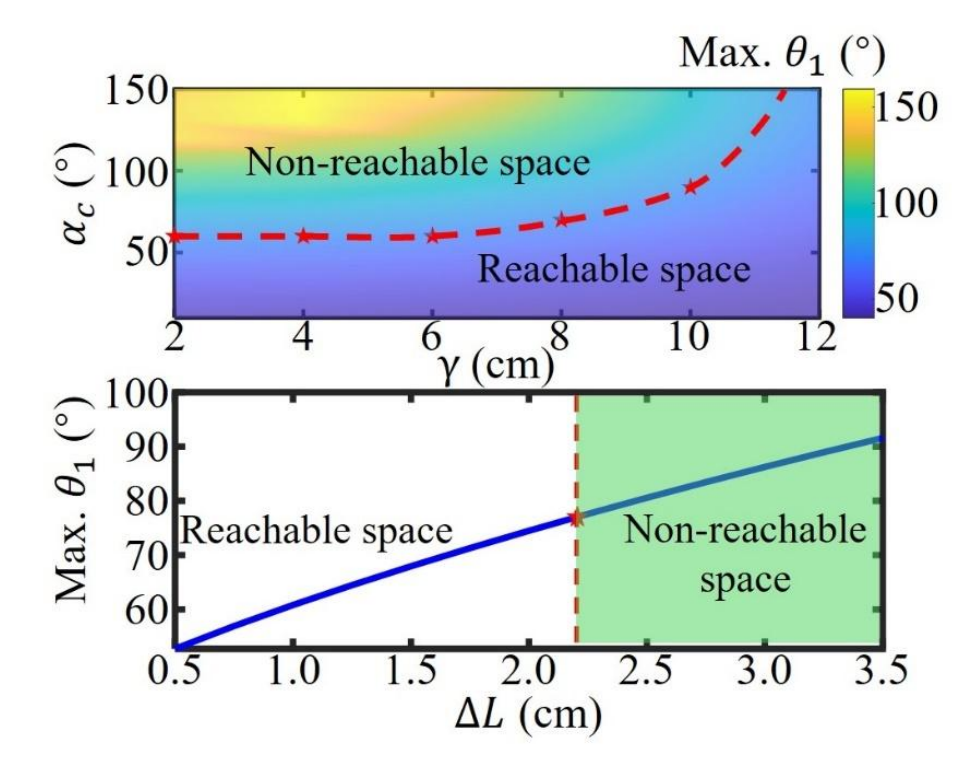


Fig. 5.14: Reachable space of control parameters for the monostable mode (Top) and the bistable mode (Bottom).

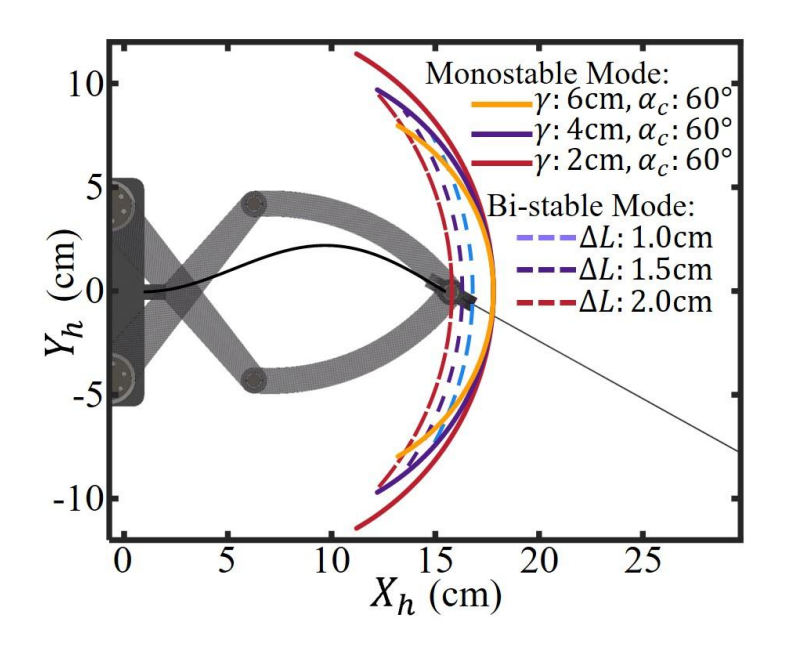


Fig. 5.15: Different control trajectories for forward swimming.

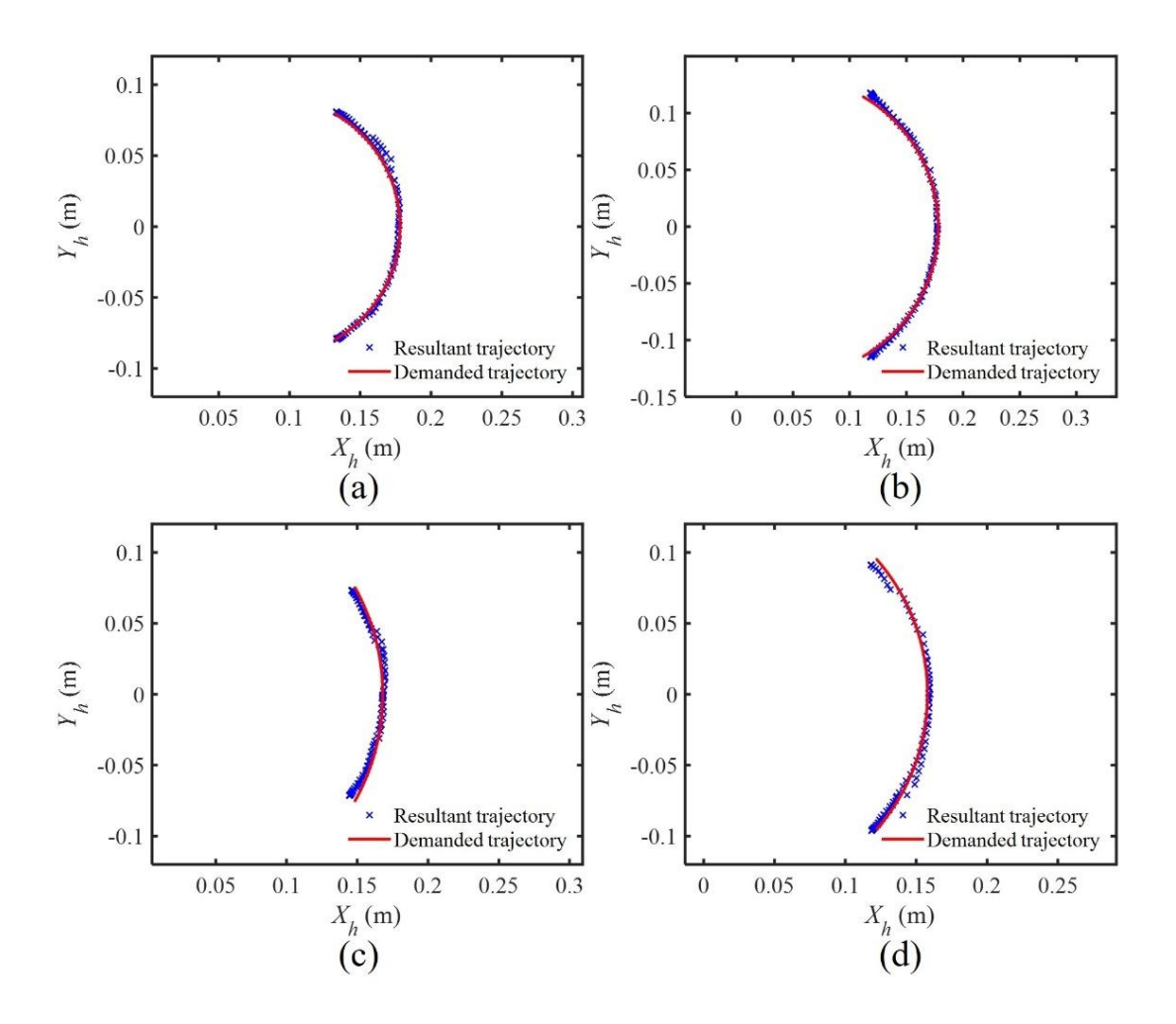


Fig. 5.16: Comparisons between the demanded and resultant control trajectories. (a) Monostable mode: $\gamma = 6 \text{ cm}$, $\alpha_c = 60^\circ$. (b) Monostable mode: $\gamma = 2 \text{ cm}$, $\alpha_c = 60^\circ$. (c) Bistable mode: $\Delta L = 1 \text{ cm}$. (d) Bistable mode: $\Delta L = 2 \text{ cm}$.

5.4.2 Forward swimming

We explored the forward swimming performance of the robot when the tail flaps with different trajectories. Due to the structure limitations ($\theta_1 < 77^\circ, \theta_2 > -77^\circ$), the reachable parameter space of each trajectory needs to be investigated. Fig. 5.14 shows the results of reachable spaces for trajectories of both monostable and bistable modes. The reachable space presents the maximum value of α_c for each trajectory of the monostable mode and the allowable precompression length ΔL of the elastic spine for the bistable mode. Six different

trajectories are selected for the forward swimming tests as shown in Fig. 5.15. Three trajectories belong to the monostable mode, and the trajectory with larger γ is not included because the amplitude is too small to get good performance on the speed. The other three trajectories pertaining to the bistable mode have different precompression of the elastic spine. The resultant trajectories were measured and compared with the demanded trajectories as shown in Fig. 5.16, which indicates the consistency between the inputs and outputs of control.

Fig. 5.17(a) demonstrates the swimming speed comparison between bistable ($\Delta L = 2$ cm) and monostable ($\gamma=2$ cm, $\alpha_c=60^\circ$) modes in the time domain at the frequency of 1 Hz. In the steady part of the speed, the minimum instantaneous speeds of two modes are almost same, while the maximum instantaneous speed of bistable mode is much higher than that of monostable mode. As a result, the average swimming speed of bistable mode is higher. The results of the swimming speed under various tail beat trajectories and frequencies are shown in Fig. 5.17(b). For the monostable locomotion mode, the speed increases with the decrease of the value of γ , this is because with the same control angle α_c , the amplitude is larger for the trajectory with smaller γ . The maximum average swimming speed of the monostable mode is around 0.65 m/s when the robot swims with the trajectory of $\gamma = 2$ cm and the frequency of 3.5 Hz and 4 Hz. More speed comparisons of each trajectory with different amplitudes for the monostable mode are provided in Fig. A3 (see Appendix A). As for the bistable swimming mode, the average speed is dramatically increased compared to the monostable mode. With a higher compression rate of the elastic spine, more improvement of the speed can be achieved. The reason is that a larger compression rate induces more prestored elastic strain energy of the spine, which will boost more thrust. The highest average swimming speed that can be achieved by the bistable mode is about 0.80 m/s at the frequency

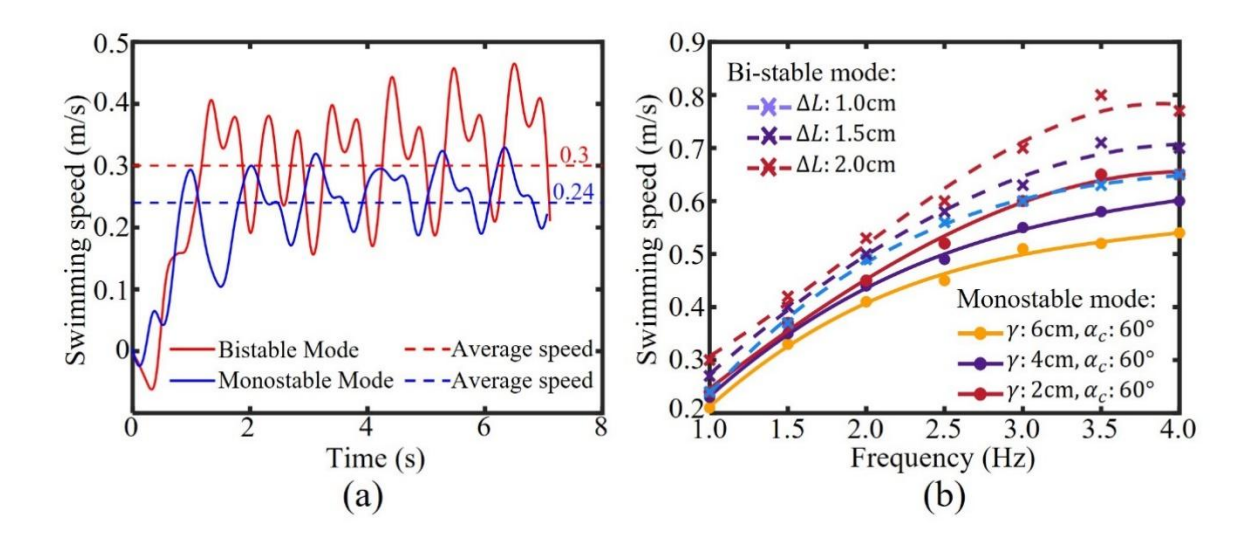


Fig. 5.17: Comparison of swimming speed between the bistable and monostable modes. (a) Comparison of swimming speed between the bistable and monostable modes at 1 Hz in the time domain. (b) Average forward swimming speed comparisons of the robot with different control trajectories in the frequency domain.

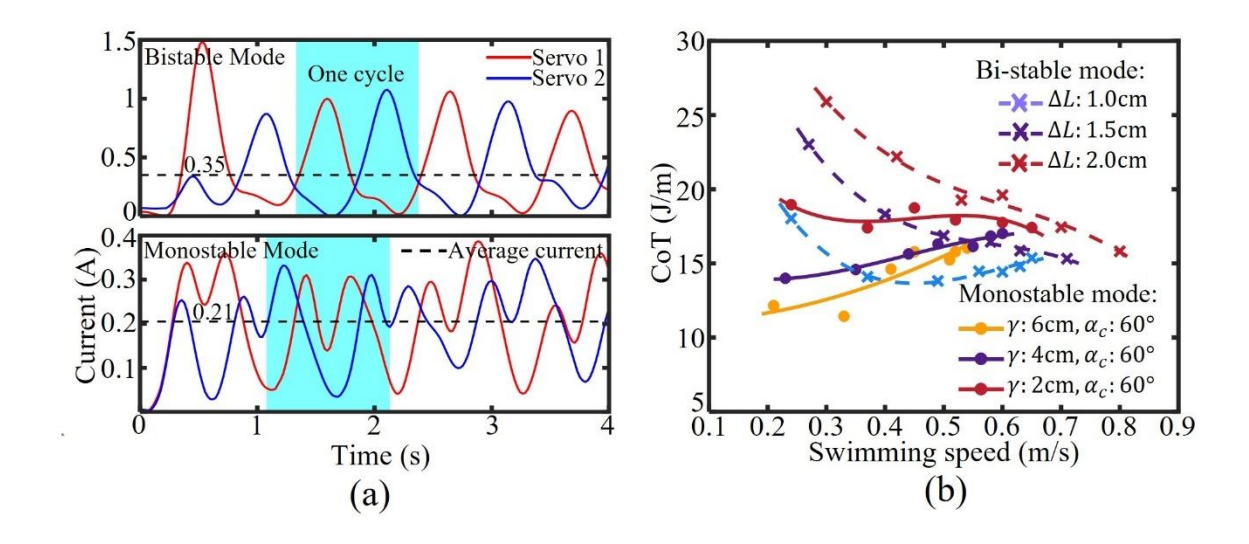


Fig. 5.18: Comparison of energy consumption between the bistable and monostable modes. (a) Comparison of consumed current between the bistable and monostable modes at 1 Hz in the time domain. (b) Cost of transport comparisons of the robot with different control trajectories in the frequency domain.

The consumed currents of two servos for bistable ($\Delta L = 2$ cm) and monostable ($\gamma = 2$ cm, $\alpha_c = 60^\circ$) modes at the frequency of 1 Hz are illustrated in Fig. 5.18(a). There is one

peak current for each motor in one bistable motion cycle. During one half of the motion cycle, the current consumed by one motor reaches its maximum value, while the current consumed by the other motor reaches its minimum value. It is opposite in another half motion cycle. The results indicate that generating the needed torque to overcome the energy barrier for achieving snapping motion on one side mainly relies on one motor. The curve shape of the consumed current in one monostable motion cycle is significantly different from that of bistable motion, which exhibits two peak values for each motor. In a half motion cycle, two motors both reach the maximum current and contribute equally. The average current value of bistable mode is higher. Because the working load on the motors increases due to the precompression of the elastic spine. It is worth noting that higher current cannot be always considered a drawback. According to the torque-speed-efficiency characteristic of a servo motor, the working efficiency of the motor shows the first rising and then dropping trend with the current increasing. Thus, the proposed fishtail mechanism could allow the motor to operate with high efficiency when the tail swing trajectory is properly selected. Fig. 5.18(b) compares the results of CoT when the robot swims with different tail-flapping trajectories. When the robot swims in the monostable mode, the trajectory with a large γ exhibits a higher energy efficiency than that of the trajectory with a small γ . The trajectory of $\gamma = 6$ cm is more energy efficient than the other two trajectories. Regarding the bistable locomotion mode, a large compression rate of the elastic spine leads to higher energy consumption. Among the three trajectories of the bistable mode, the one with the compression length ΔL of 1 cm achieves the lowest CoT. Through further comparisons between the CoT of the monostable and bistable modes, we find that the robot can swim energy efficiently with the monostable mode at low speed and with the bistable mode at high speed. For example, it is better for the robot to use the monostable mode with the trajectory of $\gamma = 2$ cm when the swimming speed

is below 0.40 m/s and to use the bistable mode with the trajectory of $\Delta L = 1$ cm when the swimming speed is higher than 0.40 m/s. Fig. 5.19 shows the snapshots of swimming comparison between the bistable and monostable modes under the frequency of 1 Hz.



Fig. 5.19: Comparison of the swimming between the bistable (Top) and monostable modes (Bottom). The tail beat frequency is 1Hz. For bistable mode, the precompression length ΔL is 2 cm, and for monostable mode, the γ of the trajectory is 2 cm.

According to the computation method described in equations (5.29) and (5.30), the specific swimming performance improvement of the bistable mode relative to the monostable mode under diverse frequencies was calculated and summarized in Table 5.2. There is an improvement of about 10% to 25% in swimming speed across the entire range of testing frequencies, benefiting from the bitable mode. While the monostable mode is more energy efficient at a frequency lower than 1.5 Hz. When the frequency is over 2 Hz, the swimming efficiency of bistable mode obtains an improvement about 5% to 10% compared to that of the monostable mode. Other than the forward swimming speed and swimming efficiency, the thrusts of both bistable ($\Delta L = 2$ cm) and monostable ($\gamma = 2$ cm, $\alpha_c = 60^{\circ}$) modes were also tested as shown in Fig. 5.20. Fig. 5.20(a) illustrates the comparison of thrust in one motion cycle between the bistable monostable modes. There are three local thrust peaks for both modes during a half motion cycle. The first two local thrust peaks of the bistable mode are much higher than those of monostable mode, which are the main sources of the higher

average thrust. Particularly, the second local thrust peak of the monostable mode is almost negligible. According to one article [78], the second local thrust peak occurs at the transition stage of the caudal fin's attack angle. During this transition stage, the snap-through motion happens. Thus, the thrust results prove that the energy storage and release offered by bistability is also the source of thrust gains. Fig. 5.20(b) demonstrates that the average thrusts are higher than those of the monostable mode under various frequencies. Fig. 5.20(c) illustrates the thrust improvement of the bistable mode compared to the monostable mode. At 1 Hz, the bistable mode gains the largest thrust improvement. And the average value of the thrust improvement of all tested frequencies is about 30.6%. The calculation method is depicted in equations (5.31) and (5.32).

Table 5.2: Swimming performance improvement of the bistable mode relative to the monostable mode

Frequency	IND_V	IND_C
1 Hz	25%	-48.3%
1.5 Hz	13.5%	-23.3%
2 Hz	17.8%	5.5%
2.5 Hz	15.4%	8.3%
3 Hz	16.7%	5.3%
3.5 Hz	23.1%	6.3%
4 Hz	18.5%	4.1%

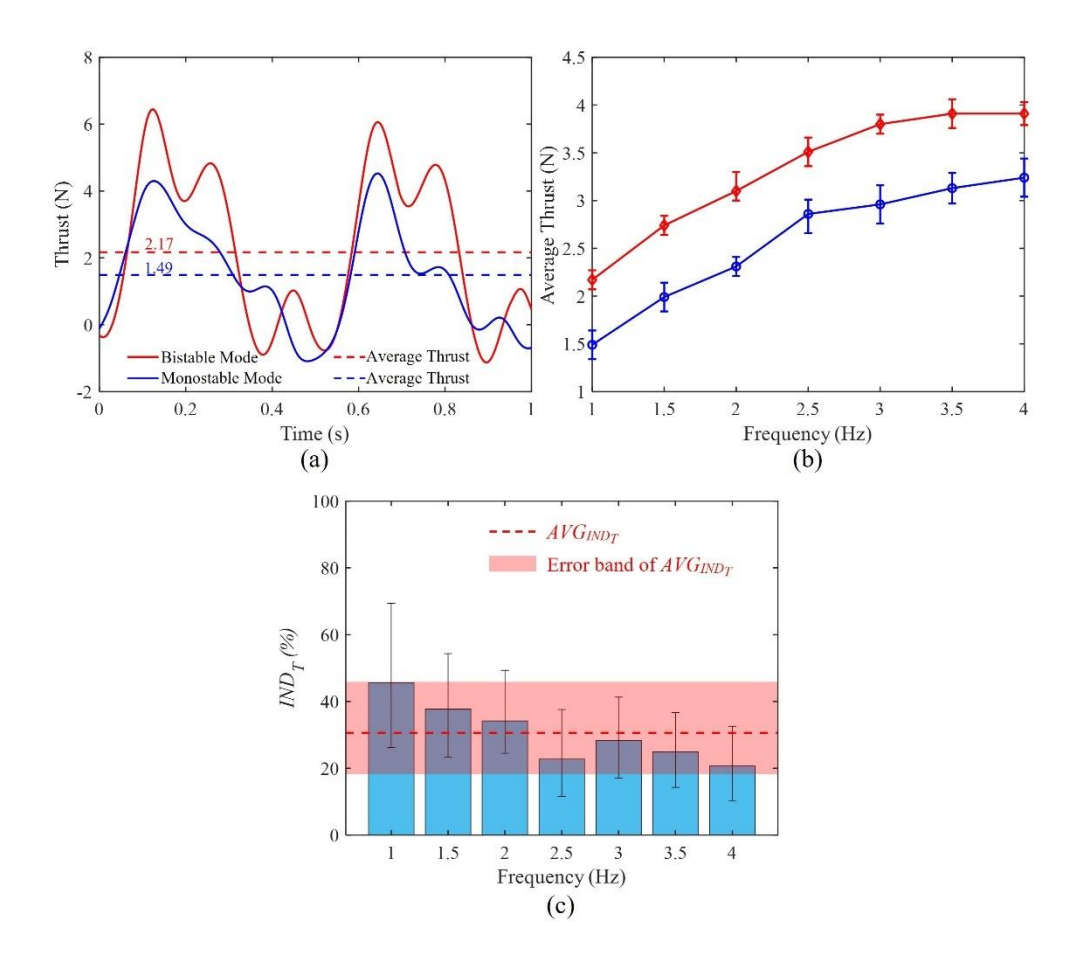


Fig. 5.20: Thrust comparison between the bistable ($\Delta L = 2 \text{ cm}$) and monostable ($\gamma = 2 \text{ cm}$, $\alpha_c = 60^\circ$) modes. (a) Thrust in one motion cycle at a frequency of 1 Hz. (b) Average thrust under various frequencies. (c) Thrust improvement of the bistable mode relative to the monostable mode under various frequencies.

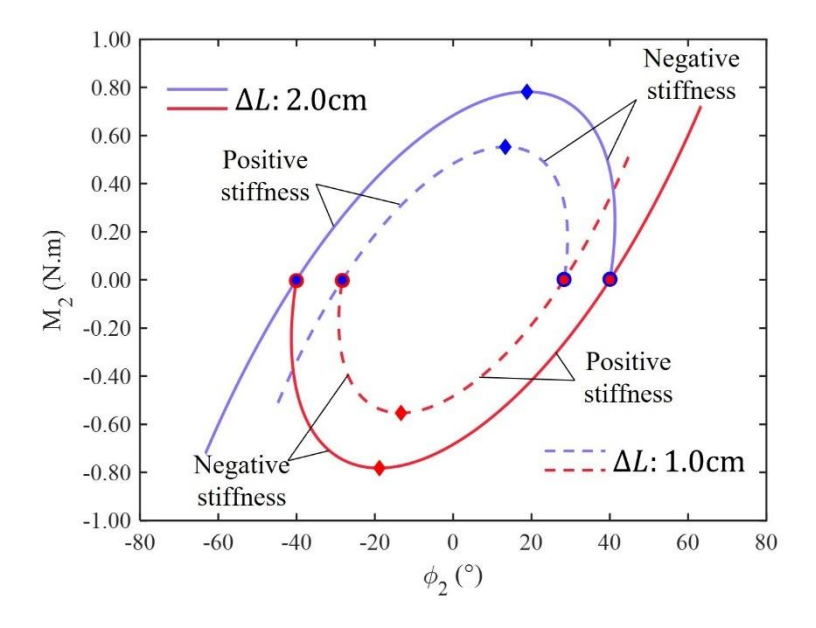


Fig. 5.21: Relation of moment and passive rotational joint's angle.

To explore the impact of the precompressed length of the spine on the passive rotation joint's stiffness, the relation of moment and rotational angle under different precompression length was calculated as shown in Fig. 5.21, whose slope represents stiffness. During one cycle of bistable motion, the stiffness is alternately positive and negative, and there are positive and negative stiffness mutations, which results in the snap-through motion. Comparing the curves of two precompression lengths, the stiffnesses are almost same at each motion stage, while more compression rate leads to larger snapping angle and more strain energy. Thereby, the interaction between the caudal fin and the surrounding water is stronger and generates larger fluid force.

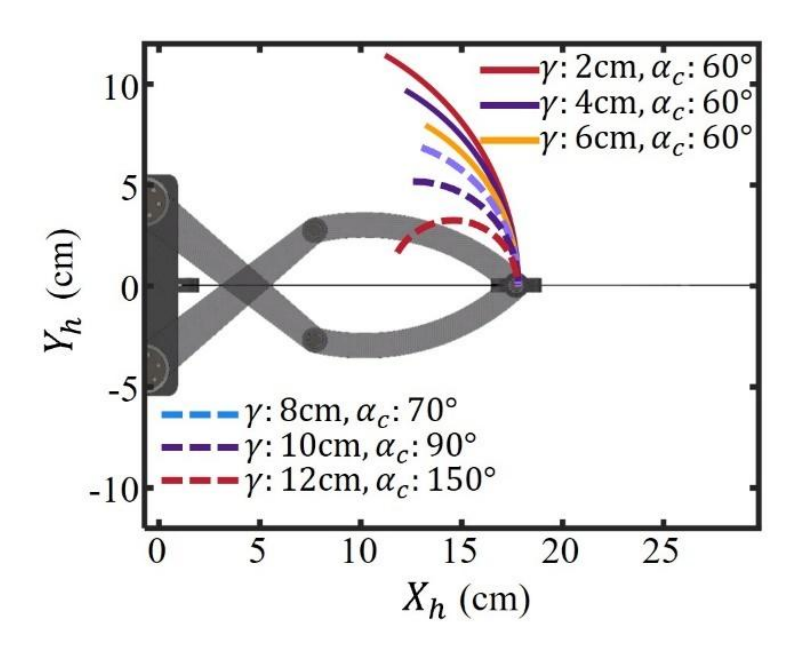


Fig. 5.22: Different control trajectories for turning.

5.4.3 Turning performance

Next, we compared the turning performance of the robot with different tail beat trajectories. Six trajectories are selected with γ varying from 2 cm to 12 cm for the turning performance exploration as shown in Fig. 5.22. Only the results of the trajectories with their

maximum control angle α_c are presented here, and the comparisons for several trajectories with different α_c are described in Fig. A4 (see Appendix A).

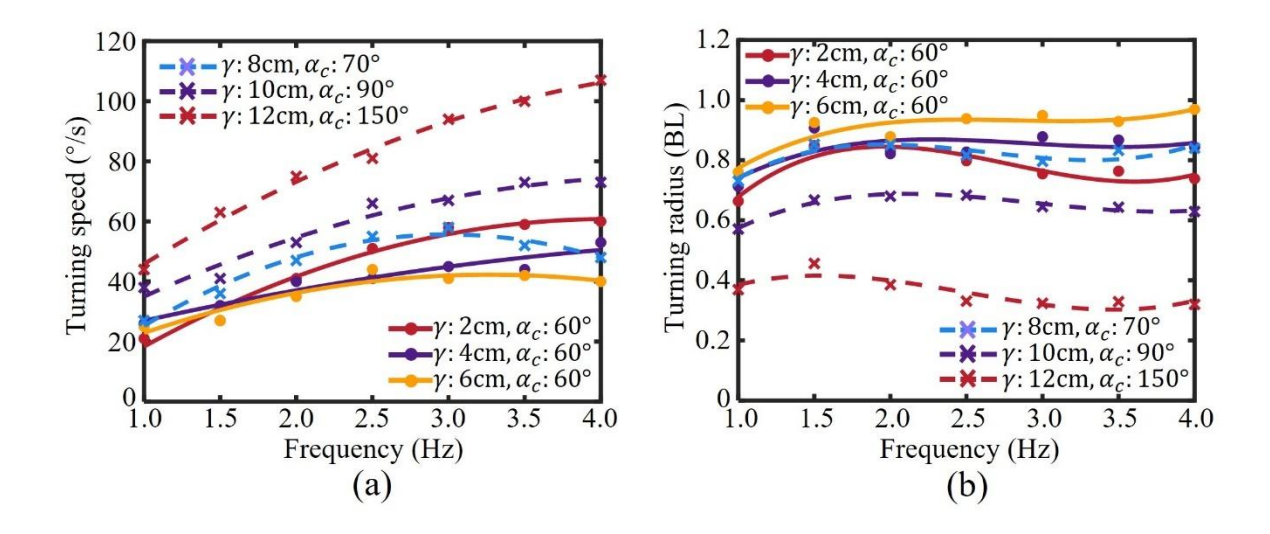


Fig. 5.23: Comparison of turning performance between the bistable and monostable modes. (a) Average turning speed comparisons of the robot with different control trajectories. (b) Turning radius comparisons of the robot with different control trajectories.

Fig. 5.23(a) shows the results of the average turning speed for the robot under various control trajectories. We find that the variation trend of the average turning rate drops initially and then goes up significantly with the decrease in the radius of the tail beat trajectory. The maximum turning speed can be achieved by the trajectory of $\gamma = 6$ cm is the smallest than that of the other trajectories. And among all trajectories, the highest average turning speed is around 107 °/s when the robot turns with the trajectory of $\gamma = 2$ cm and the frequency of 4 Hz. Similar to the effect of the tail trajectory on the turning rate, the turning radius presents an earlier increase and later decrease trend (Fig. 5.23(b)). The robot turns in the path with the largest radius when the γ of the trajectory is 6 cm, while the robot driven by the trajectory of $\gamma = 2$ cm shows the minimum turning radius at the frequency of 4 Hz. The minimum turning radius is 17 cm, equivalent to 0.31 body length per second.

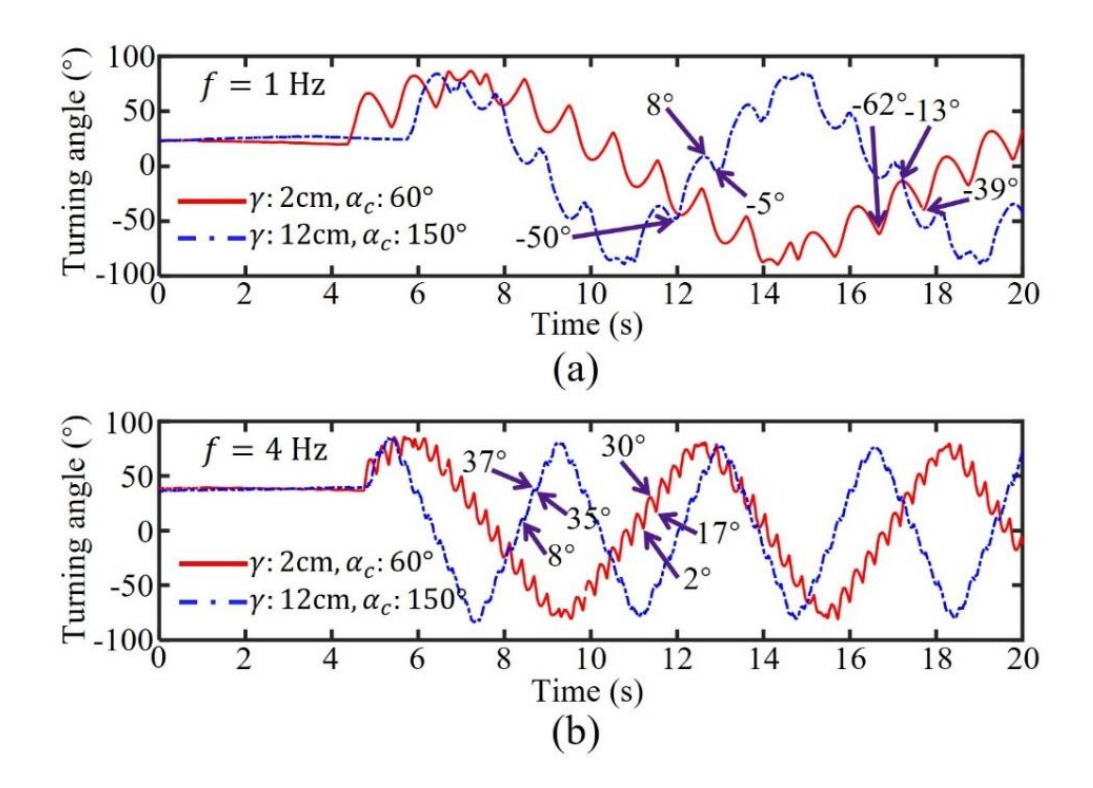


Fig. 5.24: Comparisons of the turning angle in the time domain between the trajectory of 2 cm γ and 60° α_c and the trajectory of 12 cm γ and 150° α_c when tail beat frequencies are 1 Hz (a) and 4 Hz (b) respectively.

Fig. 5.24 further compares the turning angle in the time domain between the robot driven by the trajectories of large ($\gamma=2$ cm) and small ($\gamma=12$ cm) radius. At the frequency of 1 Hz, one cycle of the tail flapping can generate 49° of the turning angle during the loading stroke with a recovery angle of 26° during the return stroke for the robot with the control trajectory of $\gamma=2$ cm. While for the trajectory of $\gamma=12$ cm, the robot can turn 58° with one stroke of the tail flapping, and the recovery angle is just a half compared to the robot turns under the trajectory of $\gamma=2$ cm. When the frequency is 4 Hz, one stroke of the tail flapping generates almost the same turning angle for the robot with the control trajectories of $\gamma=2$ cm and $\gamma=12$ cm (28° and 29° , respectively). However, during the return stroke, the recovery angle of the trajectory of $\gamma=12$ cm is much less than that of the trajectory of $\gamma=2$ cm, which are 2° and 13° , respectively. Fig. 5.25 demonstrates the snapshots of the turning

performance comparison between the robot turns with the tail beat trajectories of large and small radii under the frequency of 4 Hz.

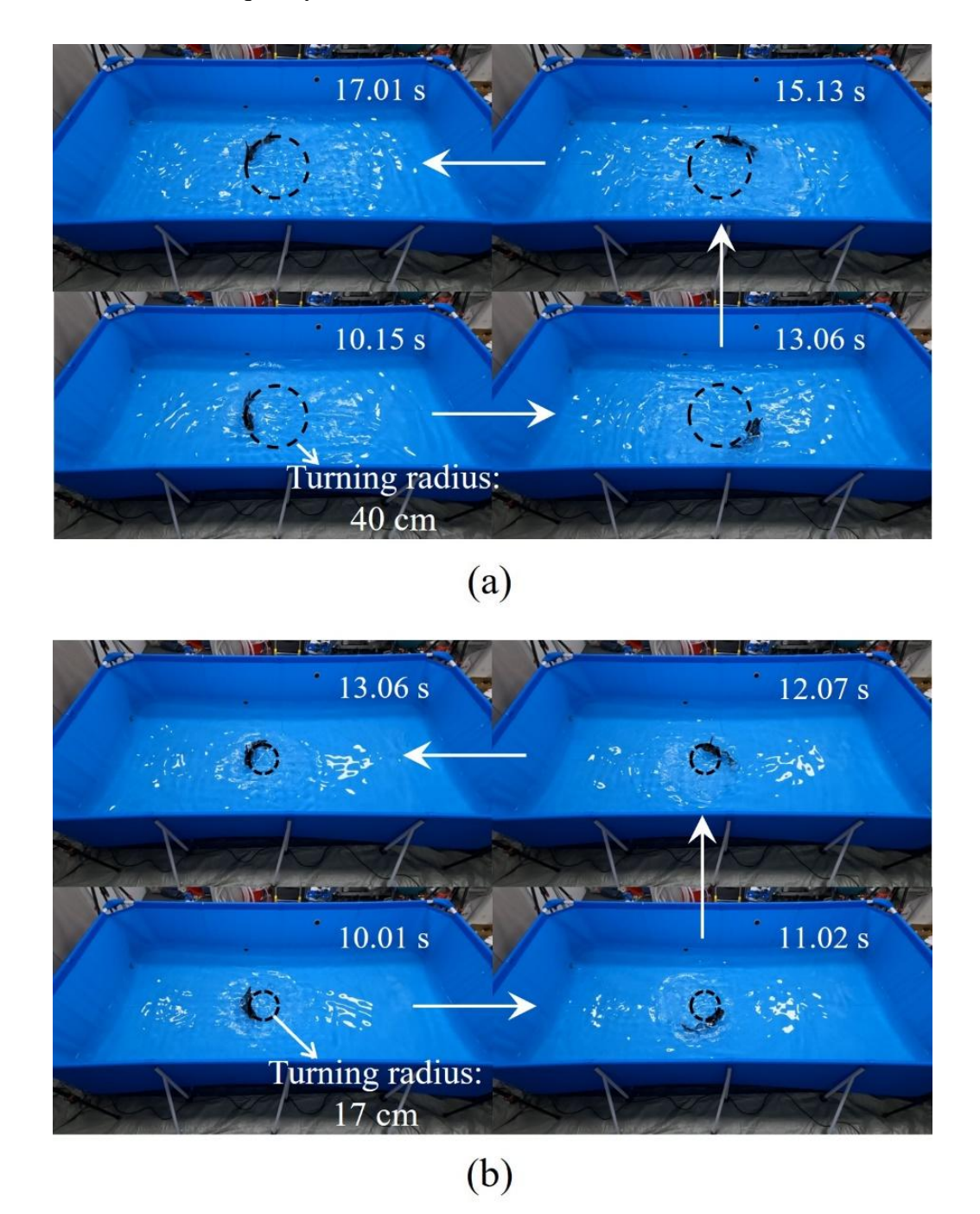


Fig. 5.25: Comparison of the turning between the trajectory of a large radius (a) and the trajectory of a small radius (b). The tail beat frequency is 4 Hz. For the trajectory of a large radius, $\gamma = 2$ cm, and for the trajectory of a small radius, $\gamma = 12$ cm.

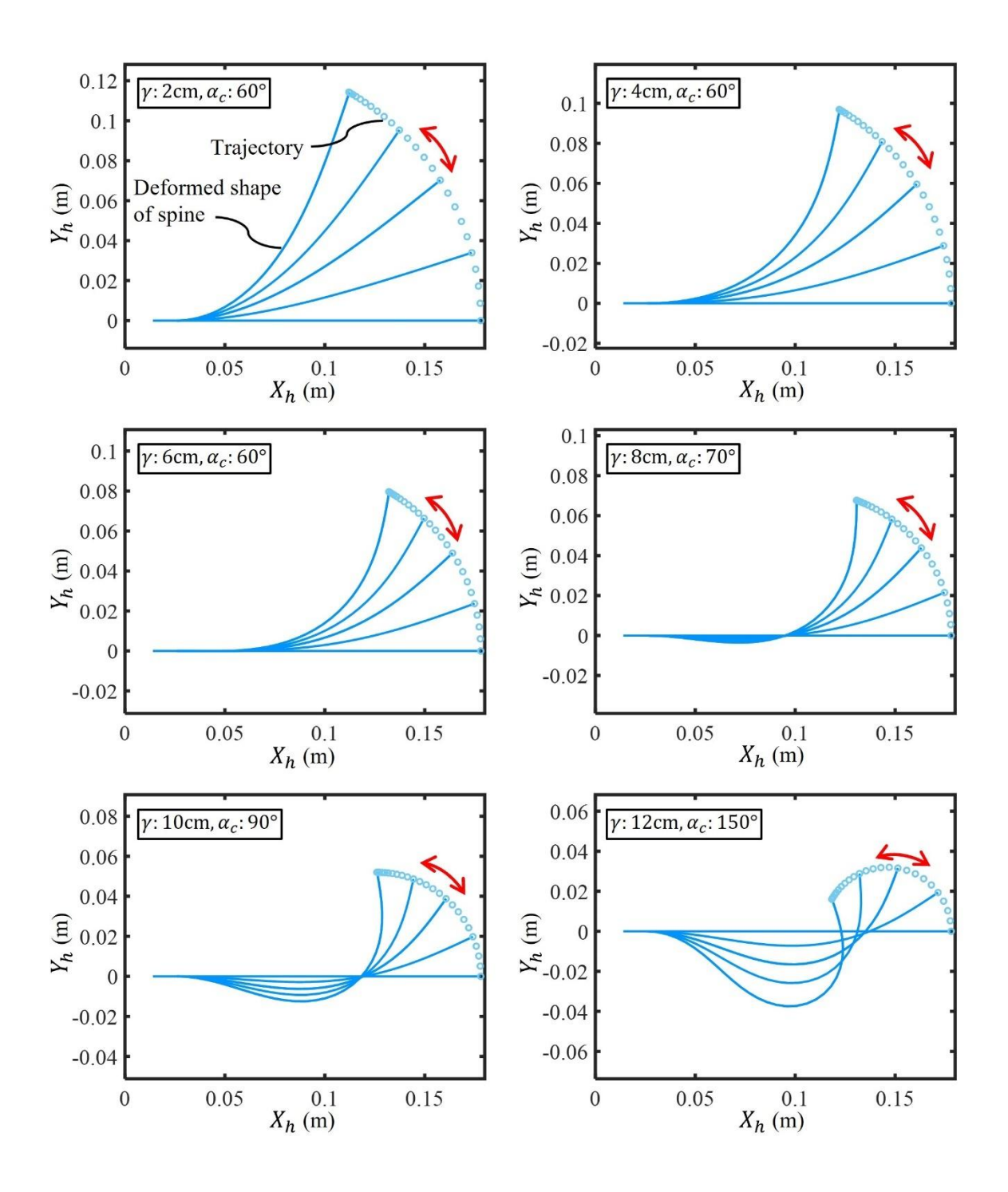


Fig. 5.26: Deformed shapes of the elastic spine under different control trajectories of point E for turning.

Furthermore, the deformed shapes of the elastic spine under different control trajectories of point E for the turning motion are shown in Fig. 5.26. According to the results, as the values of both γ and α_c increase, the elastic spine exhibits increased curvature and decreased swing amplitude. The different deformed shapes of the elastic spine result in reorienting

forces generated by the caudal fin. Larger curvature and smaller tail beat amplitude can reorient forces to achieve smaller forward thrust and generate a larger bending angle, which is beneficial for enhancing angular velocity and decreasing the turning radius, thus improving maneuverability. This advantage is due to the high controllability, continuous morphology, and elasticity of the spine, which is challenging to achieve using either discrete rigid structures or passive compliant mechanisms.

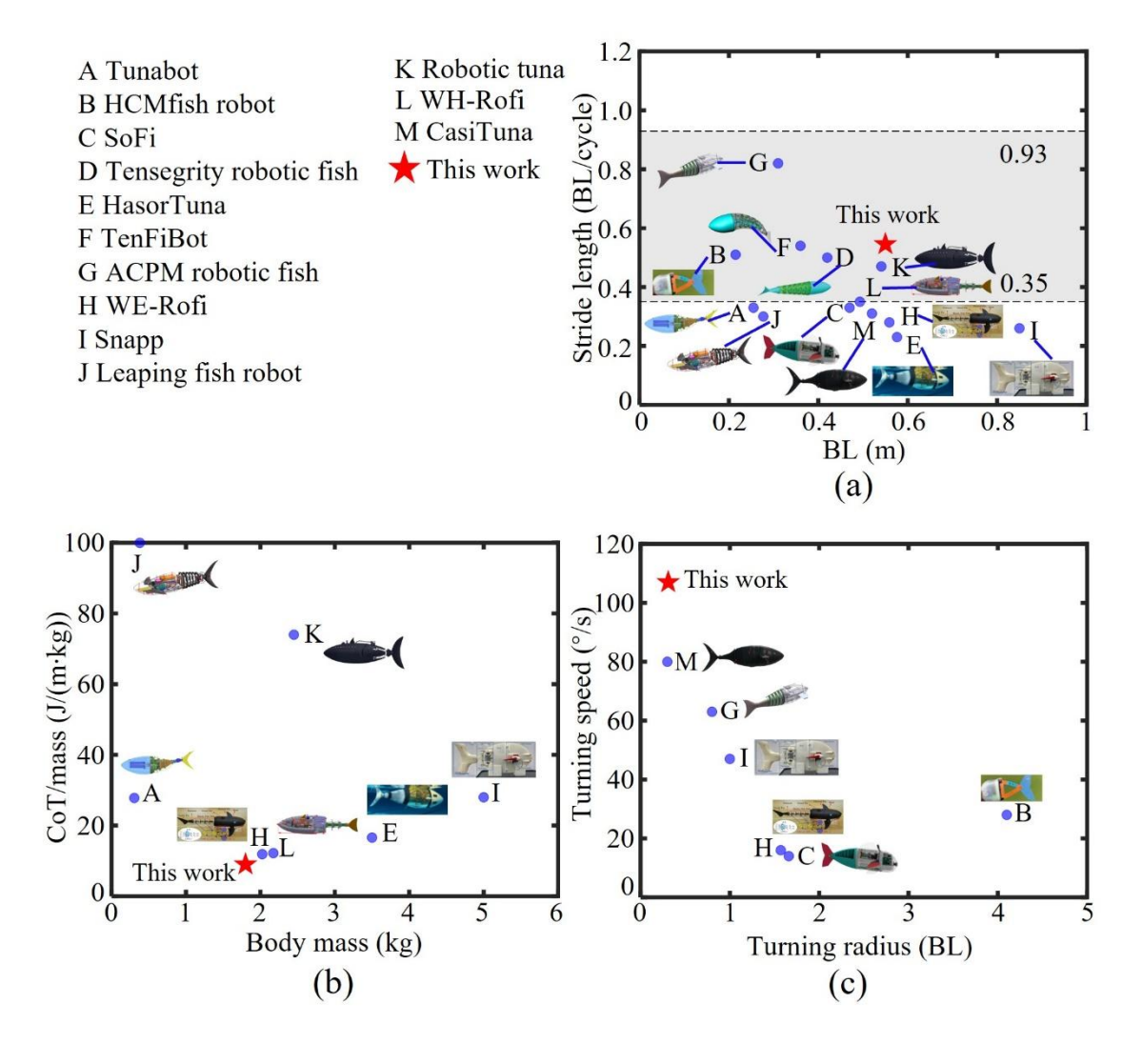


Fig. 5.27: Performance comparisons between the robotic fish in this study and similar robotic swimmers in literature. (a) Comparison of stride length versus tail beat frequency. The part in grey color (0.35-0.93) is the average stride length of fish in nature. (b) Comparison of energy consumption for moving a unit mass over per unit distance (CoT/mass) versus body mass at the maximal average swimming speed of the robots. (c) Comparison of maneuverability in terms of turning speed and turning radius.

5.5 Comparisons with Reported Robotic Fish

The performance of the robot in this chapter is compared with several similar reported robotic swimmers [26, 62, 67, 69, 78-80, 122, 141, 149-152]. The performance indicators include swimming speed, energy efficiency, turning speed, and turning radius. To make the evaluation benchmark more reasonable, the differences in the achievable maximum tail beat frequency and the mass of robots need to be taken into consideration. We use the stride length (SL = V/f) to reflect the swimming speed of the robotic swimmers, which denotes the traveled distance of the robot during one complete tail beat period [153]. Energy efficiency is characterized by the consumed energy for moving a unit mass over a unit distance (CoT/mass) [129].

Fig. 27(a) shows the comparison of the stride length. The average SL of fish varies from 0.35 to 0.93 BL/cycle [75], the part highlighted by the grey color in the figure. Our robotic swimmer achieves the fastest average swimming velocity in the bistable locomotion mode when the precompression length of the spine is 2 cm. Thus, the maximum SL under each tested tail beat frequency ranges from 0.35 to 0.55 BL/cycle, which shows comparable swimming speed with the real fish in nature. And the maximum stride length (0.55 BL/cycle) achieved at the frequency of 1 Hz is higher than most compared platforms and only lower than one platform, ACPM robotic fish [149]. But the length of the ACPM robotic fish is much smaller than that of our robot. Fig. 5.27(b) compares the energy efficiency when the robots swim at their maximum velocity. It is clear to see that the robotic swimmer in this work consumes the minimal energy at its maximum average swimming speed when compared to other platforms, which means our designed robot can achieve fast speed with a high energy efficiency. Our robot also exhibits excellent maneuverability when compared with other robotic swimmers (Fig. 5.27(c)). The fastest turning rate with the minimal turning radius

demonstrates that its maneuverability is strongly superior to other platforms.

5.6 Concluding Remarks

In this study, we developed a compliant robotic fish tail based on the bistable nonlinear mechanism, which combines a parallel linkage mechanism and an elastic spine. The active controlled elastic spine endows the robot tail with high controllability and flexibility, which allows the robot to swim and turn with different predefined tail beat trajectories. The tunable and controllable bistability of the robot tail can perform two different motion modes freely and accurately (monostable and bistable modes).

Firstly, the study on different stiffness combinations of the elastic spine and the caudal fin reveals that the spine thickness and caudal fin stiffness are two fundamental factors for improving swimming performance (see Figs. A1 and A2), and it is noted that a soft spine combined with a soft caudal fin performs better in both speed and CoT when compared to a soft spine combined with other two stiffer caudal fins (see Figs. A1(top) and A2(top)). It is also noted that a stiff spine with a caudal fin of medium stiffness enables the robot to swim faster (see Fig. 5.12(a) and Fig. 5.13(a)), but no combination can exhibit the best energy efficiency over a wide range of swimming speeds (see Fig. 5.12(b) and Fig. 5.13(b)). At a lower speed, the robot with a soft spine and a soft caudal fin (compared to stiff or medium ones in Fig. 5.11(b)) is more energy efficient, while at a higher speed, the energy efficiency of the robot with a stiff spine and a moderately stiff caudal fin is better.

Secondly, tunable tail beating modes, benefiting from the accurately controlled spine, not only enable the robotic fishtail to take advantage of the bistability for effectively amplifying the thrust force (see Fig. 5.20) by altering the caudal fin's kinematics, such as varying the angle of the passive joint (ϕ_2) through different compressed length of the spine

and producing snapping motion, but also allow the robot to maintain higher energy efficiency at different swimming speed through switching modes (see Fig. 5.18(b)). Compared to the traditional soft swimmers either using passive compliant tail [115] or actuated by hydraulic soft tail [26], our robot shows much better propulsive performance owing to its controllability of the tail trajectory and nonlinear stiffness. Compared with other bistable swimmers [69], the tunable and controllable bistability makes the robot tail more flexible and powerful, which is beneficial to real applications.

Thirdly, the maneuverability of the robotic swimmer can be largely enhanced through selecting the most suitable tail beat trajectory for turning. The active controlled spine allows the robot to simulate the smooth and continuous motion morphology of fish, which is difficult to be realized by other robotic fish built by discrete rigid linkages [45]. This property enables the robot to turn with the most efficient tail motion morphology like a real fish (the red dashed tail beat trajectory in Fig. 5.21). Based on the results of turning tests, the tail beat trajectory of a small radius and a large bending angle empower the robotic swimmer to have a faster turning rate (see Fig. 5.23(a)) and a smaller turning radius (see Fig. 5.23(b)).

The robotic swimmer successfully demonstrates its superior performance in terms of swimming speed, maneuverability, and energy efficiency through extensive comparisons with other similar robots in the literature (see Fig. 5.27). In the comparisons, several platforms have similar tail actuation mechanisms but can only realize single motor-actuated reciprocating motion with high tail beat frequency [78-80, 150, 151]. Thus, the swimming speed of these robots can be faster. However, robots of this kind are difficult to achieve turning motion, as a result, their maneuverability is relatively worse and some even can only swim forward. Moreover, most electronic components of a platform, Tunabot [78], are placed

outside the robot. All these mentioned drawbacks pose significant restrictions on practical applications. It is noted that the robot of this study can achieve a reasonable forward speed (although not the fastest because of the tail beat frequency), and it is more applicable to the marine environments due to these features as discussed before including self-contained compact system, high energy efficiency, and excellent maneuverability.

In comparing the performance of the two robots discussed in this and the previous chapters, it is evident that the robot featured in this chapter exhibits significantly improved performance in terms of swimming speed, energy efficiency, and maneuverability. However, a notable challenge with this robot is the difficulty in deriving its dynamic model for the bistable motion mode, attributed to the strong nonlinearity of the buckling spine. This complexity poses challenges for performance optimization and control, necessitating resolution in future research.

Therefore, the proposed tail mechanism provides a more reliable way for reproduction of real fish swimming skills and the results unveil a benchmark solution to the development of soft actuation of underwater robots. For example, using two such tails to imitate frog swimming, or using three or four tails to simulate the motion of octopus, etc., which will be investigated in further studies.

Chapter 6

Conclusions and Future Work

The research in this thesis strives to devise and investigate innovative solutions for designing better bio-inspired underwater robots with improved performance including swimming speed, energy efficiency, and maneuverability, thereby narrowing the gap of swimming performance between biomimetic swimming robots with their biological counterparts and enhancing their applicability in practice. The major contributions and findings of this work are summarized as follows,

A robotic tadpole is developed utilizing the multi-joint mechanism and flexible fin, and its dynamic model is derived for performance analysis and validated through extensive experiments. A critical assessment indicator, i.e., active-joint ratio, is proposed and thus the impact of control parameters on the performance of the tail with different active-joint ratios is thoroughly investigated based on the well-developed dynamic model and numerous experiments. An optimization process is provided to determine the optimal control parameters of each tail, together with an in-depth study on the dimension-related stiffness distribution of the flexible fin. The analysis and testing results in the water with currents verify the reliability of results in real-world environments. This study reveals that (i) there is an optimal active-joint ratio, which can enable the robot to swim efficiently; and (ii) with the same area of contact surface, a longer fin with a wide leading edge and a narrow trailing edge can achieve faster and more energy-efficient swimming. The findings in this

study provide new insights and guidance for the design of biomimetic swimming robots.

- 2) Inspired by the fish's ability to leverage muscle activity to tune tail stiffness for efficient swimming, a novel robotic fish capable of online modulating stiffness of its tail is proposed. Combining a parallel mechanism, an elastic steel strip, and a slider mechanism for constructing the fishtail can achieve stiffness adjusting through the endpoint trajectory control of the parallel mechanism without introducing extra actuators and any other power sources, which is the prominent difference compared with other existed stiffness adjustable biomimetic underwater platforms. The dynamic model of the robot is established and validated for performance prediction. Simulations and extensive experiments are conducted to examine the effectiveness of the proposed method. The results indicate that the proposed mechanism can maintain efficient swimming across a broader range of frequencies (0 to 4 Hz) compared to most servo-actuated platforms with tunable stiffness reported in the literature. The robot exhibits enhanced performance, including a maximum average speed of 1.46 BL/s, a minimum cost of transport (CoT) of 8.3 J/m/kg, a maximum average angular speed of 61°/s, and a minimum turning radius of 0.32 BL (15.9 cm). This approach offers a novel and alternative perspective on the design of stiffness modulation mechanisms for swimming robots.
- 3) In nature, fish are able to flexibly and precisely control their tail, which allows them to freely transform between the smooth flapping and the motion of rapid response so that they can move with dexterity. Here, inspired by the versatile motion abilities of fish, a novel robotic fish is developed through taking advantage of the nonlinear mechanism, featuring the capability of adjustable bistability. Through tuning the

bistability, the robot can acquire two locomotion modes, namely monostable and bistable modes. And it can also swim at different energy barriers that need to be overcome to achieve bistable motion. The theoretical models are derived to facilitate the control of the robot and the understanding of its nonlinear behaviors. The impact of the tunable bistability on the swimming and turning performance is investigated through extensive experiments. Experimental results show that the new bistable fishtail can achieve a faster speed of its size (up to an average speed of 0.8 m·s⁻¹) with associated higher energy efficiency (corresponding CoT as low as 9 J·m⁻¹·kg⁻¹), and greater maneuverability (with an average turning speed of up to 107 °/s at a much smaller turning radius of 0.31 BL). The results effectively demonstrate the robotic fish's capability to swiftly and efficiently swim through mode switching, enabled by its tunable bistability. This feature is essential for underwater robots to perform tasks in intricate environments. This study brings new insights into designing agile and efficient biomimetic underwater robots through making use of nonlinear properties.

Based on the work in this thesis, several points are discussed below that can help indicate possible future directions,

1) The capability of free swimming in 3D underwater space is crucial for robots to carry out underwater tasks. However, the work in this thesis focuses on the performance exploration of robots in 2D plane swimming. Therefore, the study should be extended to investigate 3D agile biomimetic swimming robots. For example, adding actively controlled pectoral fins or dorsal fins to the robots, designing effective buoyancy adjustment mechanisms, and so on.

- 2) Apart from the propulsion mechanism (fishtail), a fish's morphology has a significant influence on its swimming performance. Therefore, model-based morphology optimization, such as that of the robot's head, should be considered for further improvement in swimming performance.
- 3) Intelligent algorithms, such as deep reinforcement learning (DRL), can be leveraged for motion control and optimization in future work. For example, DRL can be applied to the proposed stiffness modulation mechanism to explore the impact of variable swing trajectories within one period for optimizing forward swimming and turning. Additionally, DRL can be used to train the designed robotic fish with tunable bistability, enabling it to intelligently select the best swing control trajectory under different environmental conditions.

Appendix

Appendix A

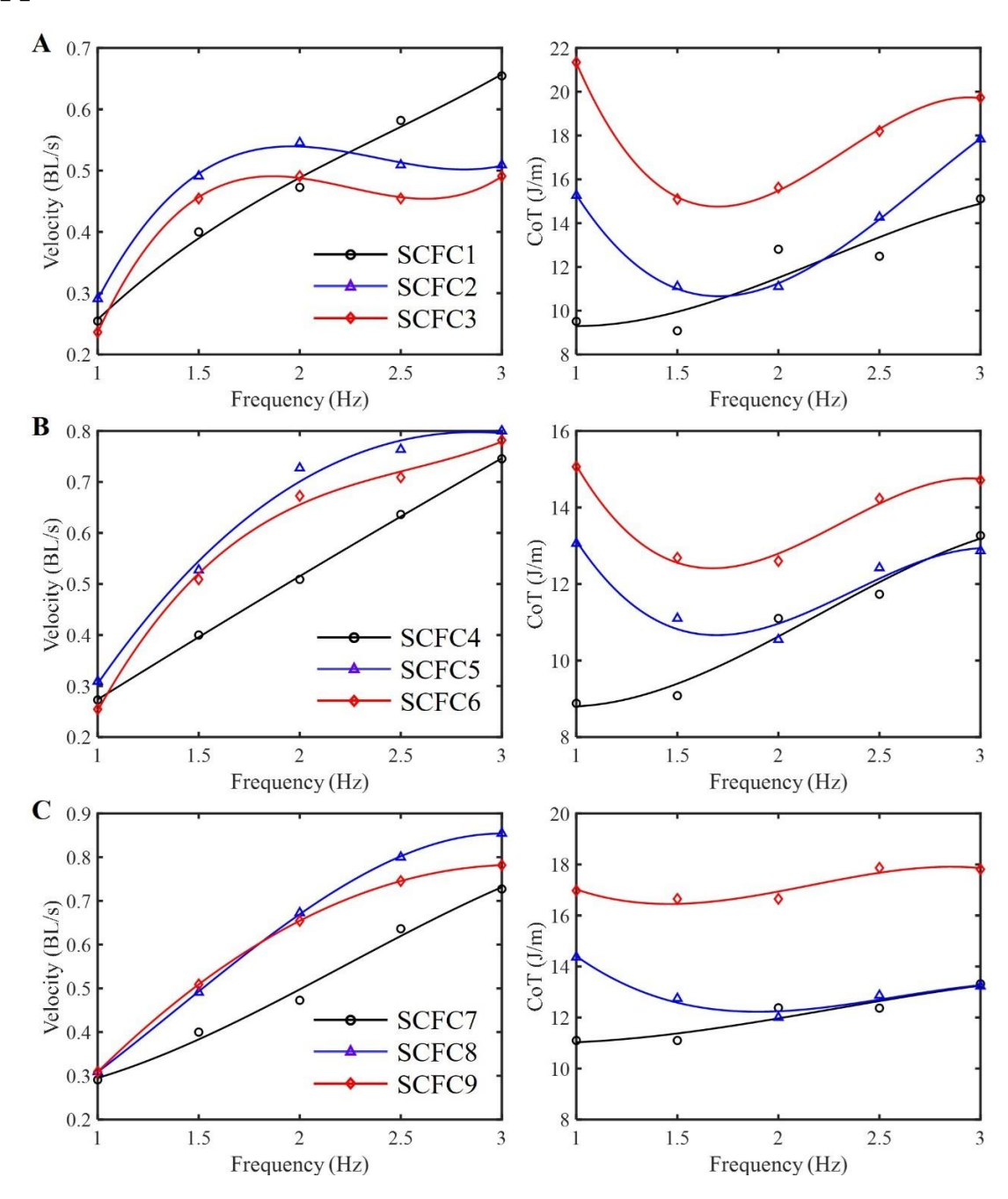


Fig. A1: Comparison of the swimming velocity and CoT in the frequency domain between the robot with different thickness combinations of the elastic spine and the caudal fin for the monostable swimming mode. (A) The thickness of the spine is 0.25 mm. SCFC1 performs better in velocity and CoT. (B) The thickness of the spine is 0.3 mm. SCFC5 performs better in velocity and CoT. (C) The thickness of the spine is 0.35 mm. SCFC8 performs better in velocity and CoT.

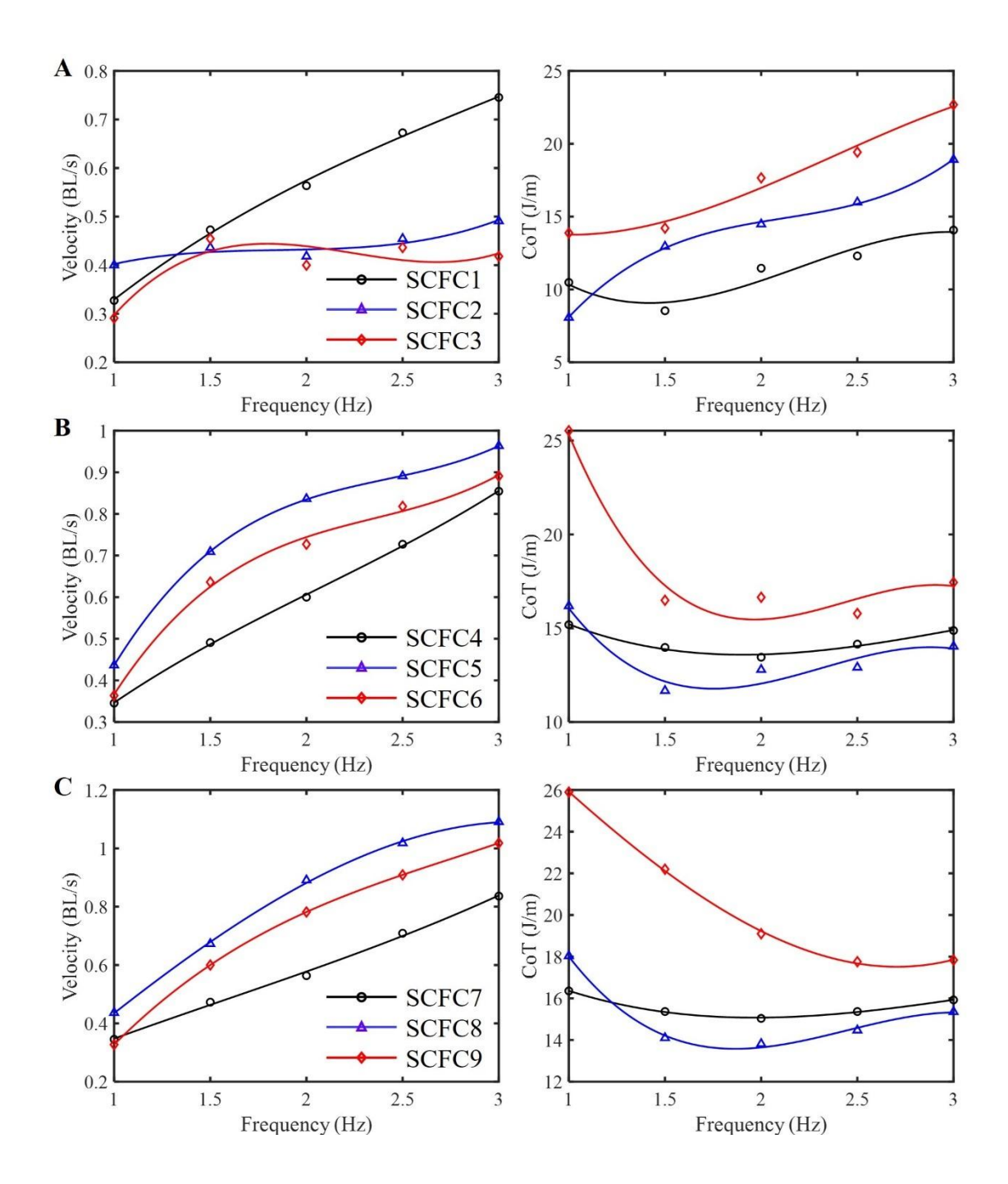


Fig. A2: Comparison of the swimming velocity and CoT in the frequency domain between the robot with different thickness combinations of the elastic spine and the caudal fin for the bistable swimming mode. (A) The thickness of the spine is 0.25 mm. SCFC1 performs better in velocity and CoT. (B) The thickness of the spine is 0.3 mm. SCFC5 performs better in velocity and CoT. (C) The thickness of the spine is 0.35 mm. SCFC8 performs better in velocity and CoT.

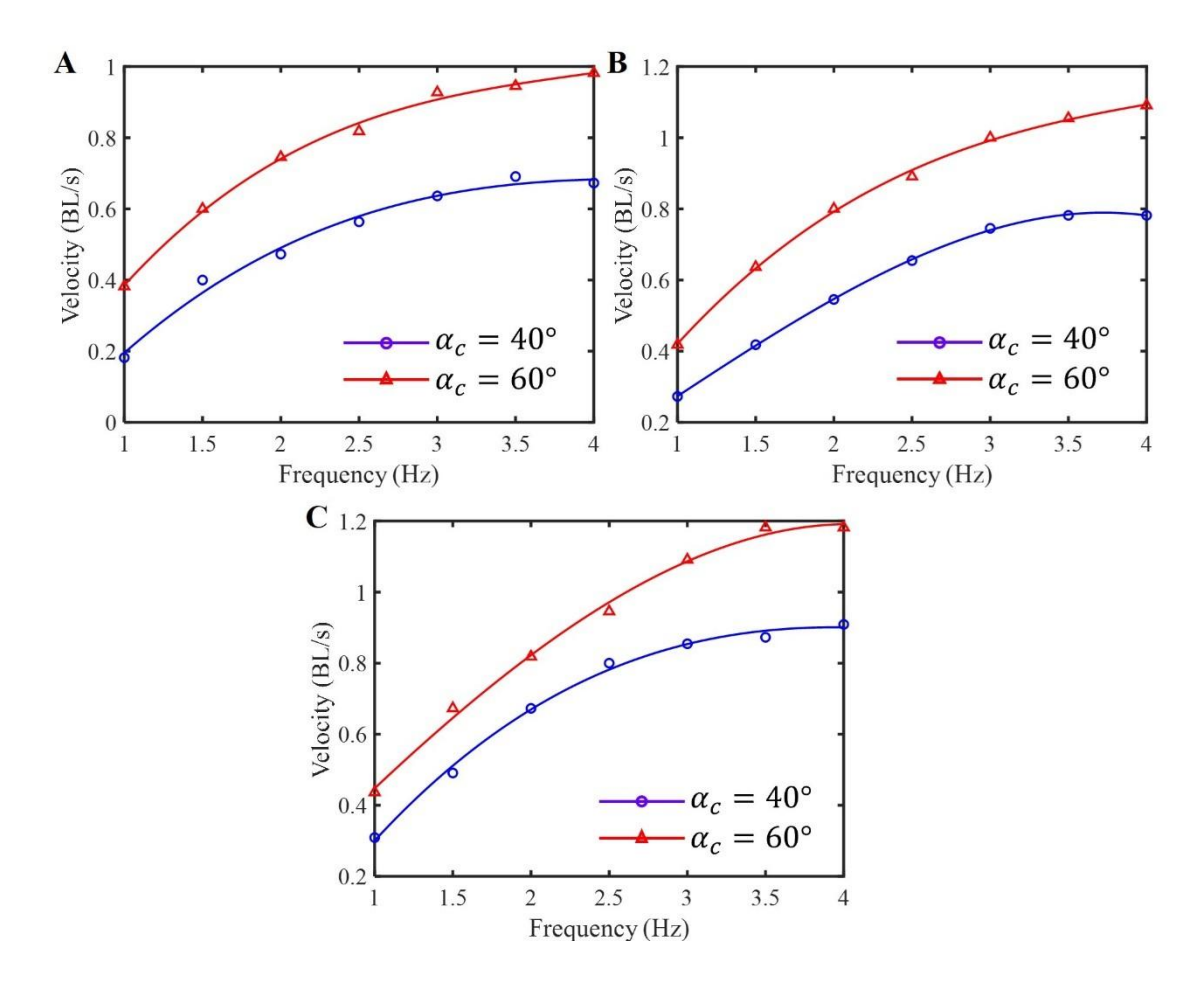


Fig. A3: Comparison of the swimming velocity in the frequency domain between the robot with different tail beat amplitudes for each trajectory of monostable mode. (A) γ of the trajectory is 6 cm. (B) γ of the trajectory is 4 cm. (C) γ of the trajectory is 2 cm.

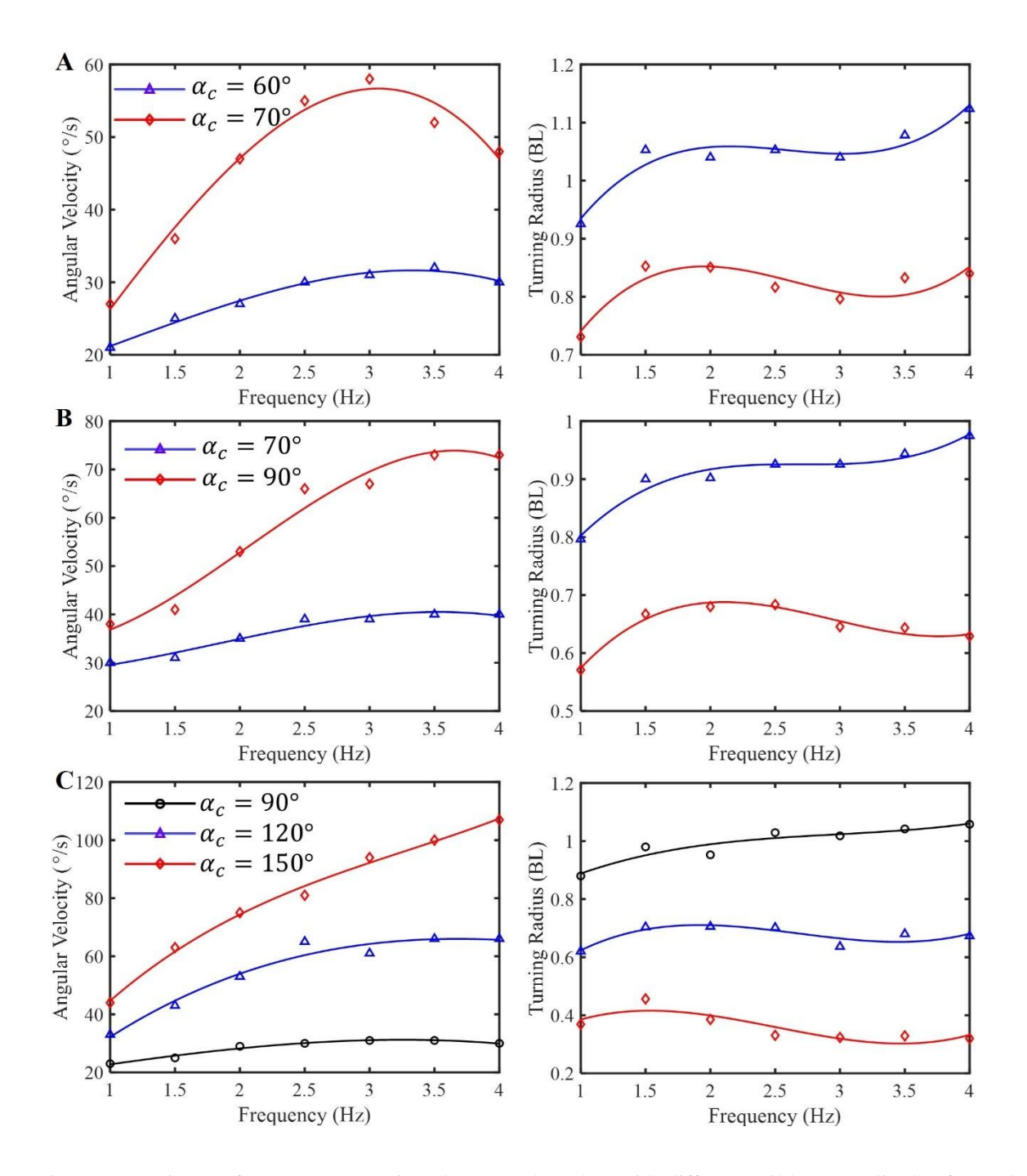


Fig. A4: Turning performance comparison between the robot with different tail beat amplitudes for each control trajectory. (A) γ of the trajectory is 8 cm. (B) γ of the trajectory is 10 cm. (C) γ of the trajectory is 12 cm.

Bibliography

- [1] M. D. Smith *et al.*, "Sustainability and global seafood," *Science*, vol. 327, no. 5967, pp. 784-786, 2010.
- [2] F. Fao, "Food and agriculture organization of the United Nations," *Rome, URL:* http://faostat. fao. org, pp. 403-403, 2018.
- [3] T. Wilberforce, Z. El Hassan, A. Durrant, J. Thompson, B. Soudan, and A. G. Olabi, "Overview of ocean power technology," *Energy*, vol. 175, pp. 165-181, 2019.
- [4] L. Hammar, M. Gullström, T. G. Dahlgren, M. E. Asplund, I. B. Goncalves, and S. Molander, "Introducing ocean energy industries to a busy marine environment," *Renewable and Sustainable Energy Reviews*, vol. 74, pp. 178-185, 2017.
- [5] S. D. Scott, "Marine minerals: their occurrences, exploration and exploitation," in *OCEANS'11 MTS/IEEE KONA*, 2011: IEEE, pp. 1-8.
- [6] A. Shukla and H. Karki, "Application of robotics in onshore oil and gas industry—A review Part I," *Robotics and Autonomous Systems*, vol. 75, pp. 490-507, 2016.
- [7] R. Costanza, "The ecological, economic, and social importance of the oceans," *Ecological economics*, vol. 31, no. 2, pp. 199-213, 1999.
- [8] P. C. Reid *et al.*, "Impacts of the oceans on climate change," *Advances in marine biology*, vol. 56, pp. 1-150, 2009.
- [9] G. R. Bigg, T. D. Jickells, P. S. Liss, and T. J. Osborn, "The role of the oceans in climate," *International Journal of Climatology: A journal of the Royal Meteorological Society*, vol. 23, no. 10, pp. 1127-1159, 2003.
- [10] A. Couper, *The geography of sea transport*. Routledge, 2015.
- [11] M. Visbeck, "Ocean science research is key for a sustainable future," *Nature communications*, vol. 9, no. 1, p. 690, 2018.
- [12] J. Das *et al.*, "Data-driven robotic sampling for marine ecosystem monitoring," *The International Journal of Robotics Research*, vol. 34, no. 12, pp. 1435-1452, 2015.
- [13] Z. E. Teoh *et al.*, "Rotary-actuated folding polyhedrons for midwater investigation of delicate marine organisms," *Science Robotics*, vol. 3, no. 20, p. eaat5276, 2018.

- [14] N. W. Xu, "Squid-inspired robots perform swimmingly," *Science Robotics*, vol. 6, no. 50, p. eabf4301, 2021.
- [15] E. Ramirez-Llodra *et al.*, "Deep, diverse and definitely different: unique attributes of the world's largest ecosystem," *Biogeosciences*, vol. 7, no. 9, pp. 2851-2899, 2010.
- [16] G. Li *et al.*, "Bioinspired soft robots for deep-sea exploration," *Nature Communications*, vol. 14, no. 1, p. 7097, 2023.
- [17] F. Kong, Y. Guo, and W. Lyu, "Dynamics modeling and motion control of an new unmanned underwater vehicle," *IEEE Access*, vol. 8, pp. 30119-30126, 2020.
- [18] E. C. De Souza and N. Maruyama, "Intelligent UUVs: Some issues on ROV dynamic positioning," *IEEE Transactions on Aerospace and Electronic Systems*, vol. 43, no. 1, pp. 214-226, 2007.
- [19] R. B. Wynn *et al.*, "Autonomous Underwater Vehicles (AUVs): Their past, present and future contributions to the advancement of marine geoscience," *Marine geology*, vol. 352, pp. 451-468, 2014.
- [20] D. L. McLean *et al.*, "Enhancing the scientific value of industry remotely operated vehicles (ROVs) in our oceans," *Frontiers in Marine Science*, vol. 7, p. 220, 2020.
- [21] S. Jin, J. Kim, J. Kim, and T. Seo, "Six-degree-of-freedom hovering control of an underwater robotic platform with four tilting thrusters via selective switching control," *IEEE/ASME Transactions on mechatronics*, vol. 20, no. 5, pp. 2370-2378, 2015.
- [22] F. S. Hover *et al.*, "Advanced perception, navigation and planning for autonomous inwater ship hull inspection," *The International Journal of Robotics Research*, vol. 31, no. 12, pp. 1445-1464, 2012.
- [23] L. Paull, S. Saeedi, M. Seto, and H. Li, "AUV navigation and localization: A review," *IEEE Journal of oceanic engineering*, vol. 39, no. 1, pp. 131-149, 2013.
- [24] E. Galceran, R. Campos, N. Palomeras, D. Ribas, M. Carreras, and P. Ridao, "Coverage path planning with real time replanning and surface reconstruction for inspection of three dimensional underwater structures using autonomous underwater vehicles," *Journal of Field Robotics*, vol. 32, no. 7, pp. 952-983, 2015.
- [25] J. D. Hernández, E. Vidal, M. Moll, N. Palomeras, M. Carreras, and L. E. Kavraki,

- "Online motion planning for unexplored underwater environments using autonomous underwater vehicles," *Journal of Field Robotics*, vol. 36, no. 2, pp. 370-396, 2019.
- [26] R. K. Katzschmann, J. DelPreto, R. MacCurdy, and D. Rus, "Exploration of underwater life with an acoustically controlled soft robotic fish," *Science Robotics*, vol. 3, no. 16, p. eaar3449, 2018.
- [27] Z. Li, X. Chao, I. Hameed, J. Li, W. Zhao, and X. Jing, "Biomimetic omnidirectional multi-tail underwater robot," *Mechanical Systems and Signal Processing*, vol. 173, p. 109056, 2022.
- [28] T. Kim, J. Kim, and S.-C. Yu, "Development of Bioinspired Multimodal Underwater Robot "HERO-BLUE" for Walking, Swimming, and Crawling," *IEEE Transactions on Robotics*, 2024.
- [29] L. Rojano-Doñate, L. Lamoni, J. Tougaard, and C. R. Findlay, "Effect of Vessel Noise on Marine Mammals and Measures to Reduce Impact," in *The Effects of Noise on Aquatic Life: Principles and Practical Considerations*: Springer, 2023, pp. 1-17.
- [30] C. Erbe, S. A. Marley, R. P. Schoeman, J. N. Smith, L. E. Trigg, and C. B. Embling, "The effects of ship noise on marine mammals—a review," *Frontiers in Marine Science*, vol. 6, p. 606, 2019.
- [31] V. Di Santo *et al.*, "Convergence of undulatory swimming kinematics across a diversity of fishes," *Proceedings of the National Academy of Sciences*, vol. 118, no. 49, p. e2113206118, 2021.
- [32] D. Scaradozzi, G. Palmieri, D. Costa, and A. Pinelli, "BCF swimming locomotion for autonomous underwater robots: a review and a novel solution to improve control and efficiency," *Ocean Engineering*, vol. 130, pp. 437-453, 2017.
- [33] X. Chao, I. Hameed, D. Navarro-Alarcon, and X. Jing, "Untethered Bimodal Robotic Fish with Tunable Bistability," in 2024 IEEE International Conference on Robotics and Automation (ICRA), 2024: IEEE, pp. 1491-1497.
- [34] R. Wang, S. Wang, Y. Wang, L. Cheng, and M. Tan, "Development and motion control of biomimetic underwater robots: A survey," *IEEE Transactions on Systems, Man, and Cybernetics: Systems*, vol. 52, no. 2, pp. 833-844, 2020.
- [35] I. FISH, "FORM, FUNCTION, AND LOCOMOTORY HABITS," Locomotion, 1979.

- [36] M. Sfakiotakis, D. M. Lane, and J. B. C. Davies, "Review of fish swimming modes for aquatic locomotion," *IEEE Journal of oceanic engineering*, vol. 24, no. 2, pp. 237-252, 1999.
- [37] R. Du, Z. Li, K. Youcef-Toumi, and P. V. y Alvarado, *Robot fish: Bio-inspired fishlike underwater robots*. Springer, 2015.
- [38] F. E. Fish, "Advantages of aquatic animals as models for bio-inspired drones over present AUV technology," *Bioinspiration & biomimetics*, vol. 15, no. 2, p. 025001, 2020.
- [39] G. Picardi, M. Chellapurath, S. Iacoponi, S. Stefanni, C. Laschi, and M. Calisti, "Bioinspired underwater legged robot for seabed exploration with low environmental disturbance," *Science Robotics*, vol. 5, no. 42, p. eaaz1012, 2020.
- [40] A. S. Barbosa and M. M. da Silva, "Macro fiber composite-actuated soft robotic fish: a gray box model-predictive motion planning strategy under limited actuation," *Soft Robotics*, vol. 10, no. 5, pp. 948-958, 2023.
- [41] G. Li, G. Liu, D. Leng, X. Fang, G. Li, and W. Wang, "Underwater undulating propulsion biomimetic robots: A review," *Biomimetics*, vol. 8, no. 3, p. 318, 2023.
- [42] O. Akanyeti *et al.*, "Fish-inspired segment models for undulatory steady swimming," *Bioinspiration & Biomimetics*, vol. 17, no. 4, p. 046007, 2022.
- [43] M. S. Triantafyllou and G. S. Triantafyllou, "An efficient swimming machine," *Scientific american*, vol. 272, no. 3, pp. 64-70, 1995.
- [44] Q. Yan, Z. Han, S.-w. Zhang, and J. Yang, "Parametric research of experiments on a carangiform robotic fish," *Journal of Bionic Engineering*, vol. 5, no. 2, pp. 95-101, 2008.
- [45] A. Crespi and A. J. Ijspeert, "Online optimization of swimming and crawling in an amphibious snake robot," *IEEE Transactions on robotics*, vol. 24, no. 1, pp. 75-87, 2008.
- [46] Z. Huang, D. Kong, C. Ren, S. Li, and S. Ma, "Performance study of an underwater snake-like robot with a flexible caudal fin," in 2019 IEEE international conference on mechatronics and automation (ICMA), 2019: IEEE, pp. 1-5.
- [47] Z. Huang et al., "Impact of caudal fin geometry on the swimming performance of a

- snake-like robot," Ocean Engineering, vol. 245, p. 110372, 2022.
- [48] E. Kelasidi, A. M. Kohl, K. Y. Pettersen, B. Hoffmann, and J. T. Gravdahl, "Experimental investigation of locomotion efficiency and path-following for underwater snake robots with and without a caudal fin," *Annual Reviews in Control*, vol. 46, pp. 281-294, 2018.
- [49] E. D. Tytell *et al.*, "Body stiffness and damping depend sensitively on the timing of muscle activation in lampreys," *Integrative and comparative biology*, vol. 58, no. 5, pp. 860-873, 2018.
- [50] Y.-J. Park, U. Jeong, J. Lee, S.-R. Kwon, H.-Y. Kim, and K.-J. Cho, "Kinematic condition for maximizing the thrust of a robotic fish using a compliant caudal fin," *IEEE Transactions on Robotics*, vol. 28, no. 6, pp. 1216-1227, 2012.
- [51] R. M. Shelton, P. J. Thornycroft, and G. V. Lauder, "Undulatory locomotion of flexible foils as biomimetic models for understanding fish propulsion," *Journal of Experimental Biology*, vol. 217, no. 12, pp. 2110-2120, 2014.
- [52] K. N. Lucas, P. J. Thornycroft, B. J. Gemmell, S. P. Colin, J. H. Costello, and G. V. Lauder, "Effects of non-uniform stiffness on the swimming performance of a passively-flexing, fish-like foil model," *Bioinspiration & biomimetics*, vol. 10, no. 5, p. 056019, 2015.
- [53] C. Zheng, J. Ding, B. Dong, G. Lian, K. He, and F. Xie, "How non-uniform stiffness affects the propulsion performance of a biomimetic robotic fish," *Biomimetics*, vol. 7, no. 4, p. 187, 2022.
- [54] T. Y.-T. Wu, "Hydromechanics of swimming propulsion. Part 1. Swimming of a two-dimensional flexible plate at variable forward speeds in an inviscid fluid," *Journal of Fluid Mechanics*, vol. 46, no. 2, pp. 337-355, 1971.
- [55] D. B. Quinn, G. V. Lauder, and A. J. Smits, "Scaling the propulsive performance of heaving flexible panels," *Journal of fluid mechanics*, vol. 738, pp. 250-267, 2014.
- [56] A. R. BLIGHT, "The muscular control of vertebrate swimming movements," *Biological Reviews*, vol. 52, no. 2, pp. 181-218, 1977.
- [57] J. H. Long Jr, "Muscles, elastic energy, and the dynamics of body stiffness in swimming eels," *American zoologist*, vol. 38, no. 4, pp. 771-792, 1998.

- [58] B. E. Flammang and G. V. Lauder, "Speed-dependent intrinsic caudal fin muscle recruitment during steady swimming in bluegill sunfish, Lepomis macrochirus," *Journal of Experimental Biology*, vol. 211, no. 4, pp. 587-598, 2008.
- [59] Q. Zou, B. Lu, Y. Fu, X. Liao, Z. Zhang, and C. Zhou, "Dynamic modeling and optimization of robotic fish based on passive flexible mechanism," in *2021 IEEE International Conference on Mechatronics and Automation (ICMA)*, 2021: IEEE, pp. 622-627.
- [60] B. Lu, C. Zhou, J. Wang, Y. Fu, L. Cheng, and M. Tan, "Development and stiffness optimization for a flexible-tail robotic fish," *IEEE Robotics and Automation Letters*, vol. 7, no. 2, pp. 834-841, 2021.
- [61] Q. Zou, C. Zhou, B. Lu, X. Liao, and Z. Zhang, "Tail-stiffness optimization for a flexible robotic fish," *Bioinspiration & Biomimetics*, vol. 17, no. 6, p. 066003, 2022.
- [62] B. Chen and H. Jiang, "Body stiffness variation of a tensegrity robotic fish using antagonistic stiffness in a kinematically singular configuration," *IEEE Transactions on Robotics*, vol. 37, no. 5, pp. 1712-1727, 2021.
- [63] B. Lu, C. Zhou, J. Wang, Z. Zhang, and M. Tan, "Toward swimming speed optimization of a multi-flexible robotic fish with low cost of transport," *IEEE Transactions on Automation Science and Engineering*, 2023.
- [64] Q. Zhong *et al.*, "Tunable stiffness enables fast and efficient swimming in fish-like robots," *Science Robotics*, vol. 6, no. 57, p. eabe4088, 2021.
- [65] I. Ju and D. Yun, "Hydraulic variable stiffness mechanism for swimming locomotion optimization of soft robotic fish," *Ocean Engineering*, vol. 286, p. 115551, 2023.
- [66] C. Qiu, Z. Wu, J. Wang, M. Tan, and J. Yu, "Locomotion optimization of a tendon-driven robotic fish with variable passive tail fin," *IEEE Transactions on Industrial Electronics*, vol. 70, no. 5, pp. 4983-4992, 2022.
- [67] S. Liu, C. Liu, Y. Liang, L. Ren, and L. Ren, "Tunable stiffness caudal peduncle leads to higher swimming speed without extra energy," *IEEE Robotics and Automation Letters*, 2023.
- [68] D. Marcheseandrew and D. Onalcagdas, "Autonomous soft robotic fish capable of escape maneuvers using fluidic elastomer actuators," *Soft robotics*, 2014.

- [69] Z. Xiong, Y. Su, and H. Lipson, "Fast untethered soft robotic crawler with elastic instability," in 2023 IEEE International Conference on Robotics and Automation (ICRA), 2023: IEEE, pp. 2606-2612.
- [70] Y. Tang *et al.*, "Leveraging elastic instabilities for amplified performance: Spine-inspired high-speed and high-force soft robots," *Science advances*, vol. 6, no. 19, p. eaaz6912, 2020.
- [71] X. Yang, Z. Wu, and J. Yu, "Design and implementation of a robotic shark with a novel embedded vision system," in 2016 IEEE International Conference on Robotics and Biomimetics (ROBIO), 2016: IEEE, pp. 841-846.
- [72] Z. Huang, S. Ma, H. Bagheri, C. Ren, and H. Marvi, "The impact of dorsal fin design on the swimming performance of a snake-like robot," *IEEE Robotics and Automation Letters*, vol. 7, no. 2, pp. 4939-4944, 2022.
- [73] Y. Zhong, Z. Hong, Y. Li, and J. Yu, "A general kinematic model of fish locomotion enables robot fish to master multiple swimming motions," *IEEE Transactions on Robotics*, 2023.
- [74] R. Thandiackal *et al.*, "Emergence of robust self-organized undulatory swimming based on local hydrodynamic force sensing," *Science robotics*, vol. 6, no. 57, p. eabf6354, 2021.
- [75] J. Videler and C. Wardle, "Fish swimming stride by stride: speed limits and endurance," *Reviews in Fish Biology and Fisheries*, vol. 1, pp. 23-40, 1991.
- [76] R. Bainbridge, "The speed of swimming of fish as related to size and to the frequency and amplitude of the tail beat," *Journal of experimental biology*, vol. 35, no. 1, pp. 109-133, 1958.
- [77] R. J. Clapham and H. Hu, "iSplash: Realizing fast carangiform swimming to outperform a real fish," *Robot fish: bio-inspired fishlike underwater robots*, pp. 193-218, 2015.
- [78] J. Zhu, C. White, D. K. Wainwright, V. Di Santo, G. V. Lauder, and H. Bart-Smith, "Tuna robotics: A high-frequency experimental platform exploring the performance space of swimming fishes," *Science Robotics*, vol. 4, no. 34, p. eaax4615, 2019.
- [79] D. Chen, Z. Wu, Y. Meng, M. Tan, and J. Yu, "Development of a high-speed swimming robot with the capability of fish-like leaping," *IEEE/ASME Transactions*

- on Mechatronics, vol. 27, no. 5, pp. 3579-3589, 2022.
- [80] T. J. Ng, N. Chen, and F. Zhang, "Snapp: An agile robotic fish with 3-D maneuverability for open water swim," *IEEE Robotics and Automation Letters*, 2023.
- [81] C. Laschi, B. Mazzolai, and M. Cianchetti, "Soft robotics: Technologies and systems pushing the boundaries of robot abilities," *Science robotics*, vol. 1, no. 1, p. eaah3690, 2016.
- [82] D. Q. Nguyen and V. A. Ho, "Anguilliform swimming performance of an eel-inspired soft robot," *Soft Robotics*, vol. 9, no. 3, pp. 425-439, 2022.
- [83] C. A. Aubin, S. Choudhury, R. Jerch, L. A. Archer, J. H. Pikul, and R. F. Shepherd, "Electrolytic vascular systems for energy-dense robots," *Nature*, vol. 571, no. 7763, pp. 51-57, 2019.
- [84] W. Zhou and Y. Li, "Modeling and analysis of soft pneumatic actuator with symmetrical chambers used for bionic robotic fish," *Soft Robotics*, vol. 7, no. 2, pp. 168-178, 2020.
- [85] H. Yuk, S. Lin, C. Ma, M. Takaffoli, N. X. Fang, and X. Zhao, "Hydraulic hydrogel actuators and robots optically and sonically camouflaged in water," *Nature communications*, vol. 8, no. 1, p. 14230, 2017.
- [86] T. Tao, Y.-C. Liang, and M. Taya, "Bio-inspired actuating system for swimming using shape memory alloy composites," *International Journal of Automation and Computing*, vol. 3, pp. 366-373, 2006.
- [87] M. Aureli, V. Kopman, and M. Porfiri, "Free-locomotion of underwater vehicles actuated by ionic polymer metal composites," *IEEE/ASME transactions on mechatronics*, vol. 15, no. 4, pp. 603-614, 2009.
- [88] J. Lou *et al.*, "Effects of actuator-substrate ratio on hydrodynamic and propulsion performances of underwater oscillating flexible structure actuated by macro fiber composites," *Mechanical Systems and Signal Processing*, vol. 170, p. 108824, 2022.
- [89] S. Wang, B. Huang, D. McCoul, M. Li, L. Mu, and J. Zhao, "A soft breaststroke-inspired swimming robot actuated by dielectric elastomers," *Smart Materials and Structures*, vol. 28, no. 4, p. 045006, 2019.
- [90] G. Li et al., "Self-powered soft robot in the Mariana Trench," Nature, vol. 591, no.

- 7848, pp. 66-71, 2021.
- [91] R. Wang *et al.*, "Fast-Swimming Soft Robotic Fish Actuated by Bionic Muscle," *Soft Robotics*, 2024.
- [92] S.-D. Gravert *et al.*, "Low-voltage electrohydraulic actuators for untethered robotics," *Science Advances*, vol. 10, no. 1, p. eadi9319, 2024.
- [93] J.-S. Koh *et al.*, "Jumping on water: Surface tension–dominated jumping of water striders and robotic insects," *Science*, vol. 349, no. 6247, pp. 517-521, 2015.
- [94] M. Noh, S.-W. Kim, S. An, J.-S. Koh, and K.-J. Cho, "Flea-inspired catapult mechanism for miniature jumping robots," *IEEE transactions on robotics*, vol. 28, no. 5, pp. 1007-1018, 2012.
- [95] S. Nishikawa, Y. Arai, R. Niiyama, and Y. Kuniyoshi, "Coordinated use of structure-integrated bistable actuation modules for agile locomotion," *IEEE Robotics and Automation Letters*, vol. 3, no. 2, pp. 1018-1024, 2018.
- [96] J. T. Overvelde, T. Kloek, J. J. D'haen, and K. Bertoldi, "Amplifying the response of soft actuators by harnessing snap-through instabilities," *Proceedings of the National Academy of Sciences*, vol. 112, no. 35, pp. 10863-10868, 2015.
- [97] Y. Cao, M. Derakhshani, Y. Fang, G. Huang, and C. Cao, "Bistable structures for advanced functional systems," *Advanced Functional Materials*, vol. 31, no. 45, p. 2106231, 2021.
- [98] A. Arrieta, P. Hagedorn, A. Erturk, and D. J. Inman, "A piezoelectric bistable plate for nonlinear broadband energy harvesting," *Applied Physics Letters*, vol. 97, no. 10, 2010.
- [99] F. Cottone, L. Gammaitoni, H. Vocca, M. Ferrari, and V. Ferrari, "Piezoelectric buckled beams for random vibration energy harvesting," *Smart materials and structures*, vol. 21, no. 3, p. 035021, 2012.
- [100] T. Chen, O. R. Bilal, K. Shea, and C. Daraio, "Harnessing bistability for directional propulsion of soft, untethered robots," *Proceedings of the National Academy of Sciences*, vol. 115, no. 22, pp. 5698-5702, 2018.
- [101] Y. Chi, Y. Hong, Y. Zhao, Y. Li, and J. Yin, "Snapping for high-speed and high-efficient butterfly stroke-like soft swimmer," *Science Advances*, vol. 8, no. 46, p.

- eadd3788, 2022.
- [102] C. Zhu *et al.*, "A variable stiffness fishlike propeller with compressible flexible bionic spine," *Ocean Engineering*, vol. 316, p. 119780, 2025.
- [103] B. Kwak, S. Choi, and J. Bae, "Development of a Stiffness Adjustable Articulated Paddle and its Application to a Swimming Robot," *Advanced Intelligent Systems*, vol. 5, no. 5, p. 2200348, 2023.
- [104] M. Lighthill, "Note on the swimming of slender fish," *Journal of fluid Mechanics*, vol. 9, no. 2, pp. 305-317, 1960.
- [105] J. Yu, M. Tan, S. Wang, and E. Chen, "Development of a biomimetic robotic fish and its control algorithm," *IEEE Transactions on Systems, Man, and Cybernetics, Part B* (*Cybernetics*), vol. 34, no. 4, pp. 1798-1810, 2004.
- [106] J. Liu and H. Hu, "Biological inspiration: from carangiform fish to multi-joint robotic fish," *Journal of bionic engineering*, vol. 7, no. 1, pp. 35-48, 2010.
- [107] K. Soltan, J. O'Brien, J. Dusek, F. Berlinger, and R. Nagpal, "Biomimetic actuation method for a miniature, low-cost multi-jointed robotic fish," in *OCEANS* 2018 MTS/IEEE Charleston, 2018: IEEE, pp. 1-9.
- [108] A. J. Ijspeert, A. Crespi, and J.-M. Cabelguen, "Simulation and robotics studies of salamander locomotion: applying neurobiological principles to the control of locomotion in robots," *Neuroinformatics*, vol. 3, pp. 171-195, 2005.
- [109] M. MacKay-Lyons, "Central pattern generation of locomotion: a review of the evidence," *Physical therapy*, vol. 82, no. 1, pp. 69-83, 2002.
- [110] A. I. Selverston, "Invertebrate central pattern generator circuits," *Philosophical Transactions of the Royal Society B: Biological Sciences*, vol. 365, no. 1551, pp. 2329-2345, 2010.
- [111] A. J. Ijspeert, "Central pattern generators for locomotion control in animals and robots: a review," *Neural networks*, vol. 21, no. 4, pp. 642-653, 2008.
- [112] A. J. Ijspeert, A. Crespi, D. Ryczko, and J.-M. Cabelguen, "From swimming to walking with a salamander robot driven by a spinal cord model," *science*, vol. 315, no. 5817, pp. 1416-1420, 2007.
- [113] R. Tian, L. Li, W. Wang, X. Chang, S. Ravi, and G. Xie, "CFD based parameter

- tuning for motion control of robotic fish," *Bioinspiration & Biomimetics*, vol. 15, no. 2, p. 026008, 2020.
- [114] R. Zangeneh and S. M. Musa, "Hydrodynamic Analysis of Biomimetic Robot Fish Using OpenFOAM," in 2021 IEEE Conference on Technologies for Sustainability (SusTech), 2021: IEEE, pp. 1-5.
- [115] V. Kopman, J. Laut, F. Acquaviva, A. Rizzo, and M. Porfiri, "Dynamic modeling of a robotic fish propelled by a compliant tail," *IEEE Journal of Oceanic Engineering*, vol. 40, no. 1, pp. 209-221, 2014.
- [116] D. Chen, Z. Wu, H. Dong, M. Tan, and J. Yu, "Exploration of swimming performance for a biomimetic multi-joint robotic fish with a compliant passive joint," *Bioinspiration & Biomimetics*, vol. 16, no. 2, p. 026007, 2020.
- [117] J. Wang and X. Tan, "A dynamic model for tail-actuated robotic fish with drag coefficient adaptation," *Mechatronics*, vol. 23, no. 6, pp. 659-668, 2013.
- [118] A. Wiens and M. Nahon, "Optimally efficient swimming in hyper-redundant mechanisms: control, design, and energy recovery," *Bioinspiration & biomimetics*, vol. 7, no. 4, p. 046016, 2012.
- [119] C. E. Jordan, "Coupling internal and external mechanics to predict swimming behavior: a general approach," *American Zoologist*, vol. 36, no. 6, pp. 710-722, 1996.
- [120] X. Zheng, M. Xiong, R. Tian, J. Zheng, M. Wang, and G. Xie, "Three-dimensional dynamic modeling and motion analysis of a fin-actuated robot," *IEEE/ASME Transactions on Mechatronics*, vol. 27, no. 4, pp. 1990-1997, 2022.
- [121] R. Tong *et al.*, "Design and optimization of an untethered high-performance robotic tuna," *IEEE/ASmE Transactions on mechatronics*, vol. 27, no. 5, pp. 4132-4142, 2022.
- [122] X. Liao, C. Zhou, Q. Zou, J. Wang, and B. Lu, "Dynamic modeling and performance analysis for a wire-driven elastic robotic fish," *IEEE Robotics and Automation Letters*, vol. 7, no. 4, pp. 11174-11181, 2022.
- [123] J. Wang, P. K. McKinley, and X. Tan, "Dynamic modeling of robotic fish with a base-actuated flexible tail," *Journal of dynamic systems, measurement, and control*, vol. 137, no. 1, p. 011004, 2015.
- [124] T. Fossen, "Guidance and Control of Ocean Vehicles. John Willey & Sons," Inc., New

- York, 1994.
- [125] A. Banerjee and S. Nagarajan, "Efficient simulation of large overall motion of beams undergoing large deflection," *Multibody System Dynamics*, vol. 1, no. 1, pp. 113-126, 1997.
- [126] R. W. Clough and J. Penzien, "Dynamics of structures. Berkeley," *CA: Computers and Structures*, 2003.
- [127] J. Yu, J. Yuan, Z. Wu, and M. Tan, "Data-driven dynamic modeling for a swimming robotic fish," *IEEE Transactions on industrial electronics*, vol. 63, no. 9, pp. 5632-5640, 2016.
- [128] V. Kopman and M. Porfiri, "Design, modeling, and characterization of a miniature robotic fish for research and education in biomimetics and bioinspiration," *IEEE/ASME Transactions on mechatronics*, vol. 18, no. 2, pp. 471-483, 2012.
- [129] T. Bujard, F. Giorgio-Serchi, and G. D. Weymouth, "A resonant squid-inspired robot unlocks biological propulsive efficiency," *Science Robotics*, vol. 6, no. 50, p. eabd2971, 2021.
- [130] E. D. Tytell, C.-Y. Hsu, T. L. Williams, A. H. Cohen, and L. J. Fauci, "Interactions between internal forces, body stiffness, and fluid environment in a neuromechanical model of lamprey swimming," *Proceedings of the National Academy of Sciences*, vol. 107, no. 46, pp. 19832-19837, 2010.
- [131] R. E. Shadwick and G. V. Lauder, Fish physiology: fish biomechanics. Elsevier, 2006.
- [132] A. P. Summers and J. H. Long Jr, "Skin and bones, sinew and gristle: the mechanical behavior of fish skeletal tissues," *Fish physiology*, vol. 23, pp. 141-177, 2005.
- [133] M. W. Westneat and S. A. Wainwright, "7. Mechanical design for swimming: muscle, tendon, and bone," *Fish physiology*, vol. 19, pp. 271-311, 2001.
- [134] M. H. Dickinson, C. T. Farley, R. J. Full, M. Koehl, R. Kram, and S. Lehman, "How animals move: an integrative view," *science*, vol. 288, no. 5463, pp. 100-106, 2000.
- [135] K. Shoele and Q. Zhu, "Leading edge strengthening and the propulsion performance of flexible ray fins," *Journal of Fluid Mechanics*, vol. 693, pp. 402-432, 2012.
- [136] K. H. Low, C. W. Chong, and C. Zhou, "Performance study of a fish robot propelled by a flexible caudal fin," in 2010 IEEE International Conference on Robotics and

- Automation, 2010: IEEE, pp. 90-95.
- [137] B. Yin and H. Luo, "Effect of wing inertia on hovering performance of flexible flapping wings," *Physics of Fluids*, vol. 22, no. 11, 2010.
- [138] D. Quinn and G. Lauder, "Tunable stiffness in fish robotics: mechanisms and advantages," *Bioinspiration & Biomimetics*, vol. 17, no. 1, p. 011002, 2021.
- [139] L. L. Howell, S. P. Magleby, B. M. Olsen, and J. Wiley, *Handbook of compliant mechanisms*. Wiley Online Library, 2013.
- [140] C. Zhou and K. H. Low, "On-line optimization of biomimetic undulatory swimming by an experiment-based approach," *Journal of Bionic Engineering*, vol. 11, no. 2, pp. 213-225, 2014.
- [141] B. Chen and H. Jiang, "Swimming performance of a tensegrity robotic fish," *Soft robotics*, vol. 6, no. 4, pp. 520-531, 2019.
- [142] Z. Wolf, A. Jusufi, D. Vogt, and G. Lauder, "Fish-like aquatic propulsion studied using a pneumatically-actuated soft-robotic model," *Bioinspiration & biomimetics*, vol. 15, no. 4, p. 046008, 2020.
- [143] M. Nakabayashi, R. Kobayashi, S. Kobayashi, and H. Morikawa, "Bioinspired propulsion mechanism using a fin with a dynamic variable-effective-length spring-evaluation of thrust characteristics and flow around a fin in a uniform flow," *Journal of Biomechanical Science and Engineering*, vol. 4, no. 1, pp. 82-93, 2009.
- [144] Y. Liu, H. Jiang, and Z. Xu, "Development of novel fish-inspired robot with variable stiffness," *Ocean Engineering*, vol. 305, p. 118047, 2024.
- [145] D. Chen, Y. Xiong, B. Wang, R. Tong, Y. Meng, and J. Yu, "Performance optimization for bionic robotic dolphin with active variable stiffness control," *Biomimetics*, vol. 8, no. 7, p. 545, 2023.
- [146] F. Ma and G. Chen, "Chained Beam-Constraint-Model (CBCM): a powerful tool for modeling large and complicated deflections of flexible beams in compliant mechanisms," in *International Design Engineering Technical Conferences and Computers and Information in Engineering Conference*, 2014, vol. 46360: American Society of Mechanical Engineers, p. V05AT08A027.
- [147] F. Ma and G. Chen, "Modeling large planar deflections of flexible beams in compliant

- mechanisms using chained beam-constraint-model," *Journal of Mechanisms and Robotics*, vol. 8, no. 2, p. 021018, 2016.
- [148] L. Tissot-Daguette, H. Schneegans, E. Thalmann, and S. Henein, "Analytical modeling and experimental validation of rotationally actuated pinned–pinned and fixed–pinned buckled beam bistable mechanisms," *Mechanism and Machine Theory*, vol. 174, p. 104874, 2022.
- [149] Y. Zhong, Z. Li, and R. Du, "A novel robot fish with wire-driven active body and compliant tail," *IEEE/ASME Transactions on Mechatronics*, vol. 22, no. 4, pp. 1633-1643, 2017.
- [150] X. Wang, C. Zhou, J. Wang, J. Fan, Z. Zhang, and M. Tan, "Toward Propulsive Performance Evaluation of a Robotic Tuna Based on the Damping-Elastic Composite Mechanism," *IEEE/ASME Transactions on Mechatronics*, 2023.
- [151] X. Liao, C. Zhou, J. Wang, and M. Tan, "A Wire-Driven Dual Elastic Fishtail With Energy Storing and Passive Flexibility," *IEEE/ASME Transactions on Mechatronics*, 2023.
- [152] S. Du, Z. Wu, J. Wang, S. Qi, and J. Yu, "Design and control of a two-motor-actuated tuna-inspired robot system," *IEEE Transactions on Systems, Man, and Cybernetics: Systems*, vol. 51, no. 8, pp. 4670-4680, 2019.
- [153] C. H. White, G. V. Lauder, and H. Bart-Smith, "Tunabot Flex: A tuna-inspired robot with body flexibility improves high-performance swimming," *Bioinspiration & Biomimetics*, vol. 16, no. 2, p. 026019, 2021.